Thermal Transport in Tungsten and Applications to Miniaturised Adiabatic Demagnetisation Refrigerators

Matthew Justin Hills

Mullard Space Science Laboratory

Department of Space and Climate Physics

University College London

A thesis submitted to University College London

for the degree of Doctor of Philosophy

June 2015

I, Matthew Hills, confirm that the work presented in this thesis is my own. Where information has been derived from other sources, I confirm that this has been indicated in the thesis.

Abstract

This thesis addresses the miniaturisation of Adiabatic Demagnetisation Refrigerators (ADRs) for cooling photon detectors that operate below 1 K. Such detectors offer vastly improved energy resolution and the potential to count individual photons, which make them attractive for both astronomical and ground-based applications. The primary focus of the thesis is on the heat switches used in ADRs. These components provide a strong thermal link to a pre-cooling bath during the magnetisation part of the ADR's refrigeration cycle and – ideally – thermal isolation during the demagnetisation (cooling) part. In ADRs configured to provide continuous cooling, it is the heat switches which ultimately limit the efficiency of the ADR and the cooling power that can be obtained for a given size of refrigerator.

Tungsten is an attractive material for constructing heat switches in ADRs because its thermal conductivity at liquid helium temperatures can be reduced by several orders of magnitude on application of a magnetic field. While the fields required are of the order of a few Tesla, they are very similar to those provided by superconducting magnets used in ADRs already. Moreover, the fact that tungsten switches are solid state devices, without moving parts or working fluids, makes them ideally suited to miniaturisation.

Thermal transport in tungsten on the scales appropriate to miniature ADRs is investigated in both theoretical and experimental terms. Theoretical relationships between tungsten's thermal conductivity and applied field are presented and verified by experimental studies on a variety of samples. The effects of different sample purity, crystal orientation and field orientation relative to the sample are also discussed. These findings are then incorporated into a thermal mathematical model which provides predictions of the performance of a miniature ADR and identifies key factors for optimising it. Finally, the future developments necessary to make a miniature ADR a reality are summarised.

Contents

List of Figures

List of Tables

Index of Symbols

Where not specified in the text, symbols used have the following definitions. To avoid departures from conventional notation, one symbol sometimes has multiple meanings; in these cases the intended meaning is either stated explicitly in the text or implied by the theme of a particular section.

a	Lattice constant
A	Area
b	Internal magnetic field
$\boldsymbol{B}$	Magnetic field
c	Particle heat capacity
c	Speed of light
C	Heat capacity
d	Sample diameter/thickness
e	Electron charge (= 1.60219×10^{-19} C)
$\boldsymbol{E}$	Electric field
$f, \Delta f$	Frequency, frequency bandwidth
$f_{\boldsymbol{k}}$	k-space distribution function
$f_{\boldsymbol{k}}^{0}$	Equilibrium k-space distribution function
F	Helmholtz free energy
$\boldsymbol{F}$	Force
g	Landau splitting factor
$g_{\mathbf{k}}$	Deviation from the equilibrium k-space distribution function
G	Thermal conductance
G	Lattice rigidity
$\mathbf{G}$	Reciprocal lattice vector
$\dot{\mathrm{G}}$	Irradiation
h	Planck's constant (= 6.62620×10^{-34} Js)
$\hbar$	$h/2\pi$ (= 1.05459×10^{-34} Js)
$\boldsymbol{H}$	Auxiliary magnetic field

I	Electric current
j	Electric current density
J	Total angular momentum quantum number
$\boldsymbol{J}$	Total angular momentum vector
j̇	Radiosity
$\mathbf{k}$	Electron wavevector
k_B	Boltzmann constant (= 1.38062×10^{-23} J/K)
L	Length
L	Orbital angular momentum quantum number
$\mathbf{L}$	Orbital angular momentum vector
L_0	Lorenz number
L	Inductance
L_i	Mean vector distance travelled by an electron
m_c^*	Effective cyclotron mass
m_e	Electron mass (= 9.10956×10^{-31} kg)
m_l	Mass of the lth atom
M	Molar mass
M	Magnetisation
n	Particle concentration (= N/volume)
n	Lattice mode number
n	Magnetic field exponent
N	Number of particles
p	Fraction of carriers specularly reflected from a surface
$\mathbf{p}$	Momentum
P	Power
P	Probability
$\dot{q}$	Rate of heat flow per unit area
$\mathbf{q}$	Phonon wavevector
Q	Transition probability
Q	Heat energy

$\dot{Q}$	Rate of heat flow
$\mathbf{r}$	Position vector
r_0	Particle radius
r_B	Cyclotron/Larmor radius
R	Resistance
R	Gas constant (= 8.314 J/mol K)
R	Surface scattering transition probability
R_{Bd}	Boundary resistance
S	Entropy
S	Spin quantum number
$\mathbf{S}$	Spin vector
S_c	Cross–sectional area
S_F	Fermi surface area
t	Time
T	Temperature
T_c	Superconducting transition temperature
T_F	Fermi temperature
T_N	Néel temperature
U	Internal energy
$\mathbf{v}$	Velocity
v	Speed of sound
$\bar{\mathbf{v}}$	Average velocity
V	Voltage
V	Volume
V	Potential energy
w	Sample width
$\mathbf{x}$	Atomic position vector
Z	Partition function
Z	Acoustic impedance

α	Phonon transmission probability
α	Absorptivity
β	Thermal boundary resistance constant
γ	Thermal resistivity
Δ	Superconducting energy gap
ϵ	Energy
ϵ_F	Fermi energy
ε	Emissivity
η	Thermodynamic efficiency
η	Asperity parameter
θ	Scattering angle
θ_D	Debye temperature
ϑ	Angle between electron motion and magnetic field
κ	Thermal conductivity
κ_0	Thermal conductivity in zero magnetic field
κ_e	Electronic part of the thermal conductivity
κ_l	Lattice conductivity
λ	Wavelength
Λ	Mean free path
μ	Chemical potential
μ_B	Bohr magneton
μ_0	Permeability of free space (= $4\pi \times 10^{-7}$ N/A^2)
ξ	Number of atoms per unit cell
ρ	Density
ρ	Electrical resistivity
ρ	Reflectivity
σ	Number of accessible states for a system
σ	Electrical conductivity
σ	Stefan–Boltzmann constant (= 5.67×10^{-8} W/m^2 K^4)
σ_0	Scattering cross-section

σ_{el-el}	Electron-electron scattering cross-section
τ	Relaxation time
τ	Transmission
φ	Azimuthal angle (in a spherical coordinate system)
ϕ	Phase variable for electron orbits in high magnetic fields
Φ	Magnetic flux
χ	Magnetic susceptibility
ψ	Electron wavefunction
ω	Angular frequency
ω_c	Cyclotron frequency
Ω	Solid angle

List of Acronyms

ADR	Adiabatic Demagnetisation Refrigerator
AM	Additive Manufacture
AMM	Acoustic Mismatch Model
AMR	Active Magnetic Refrigeration
ATHENA	The Advanced Telescope for High ENergy Astrophysics
BCS	Bardeen, Cooper, Schrieffer
CADR	Continuous Adiabatic Demagnetisation Refrigerator
CCD	Charge Coupled Device
CMB	Cosmic Microwave Background
COP	Coefficient of Performance
CPA	Chromic Potassium Alum
CTE	Coefficient of Thermal Expansion
DMLS	Direct Metal Laser Sintering
DMM	Diffuse Mismatch Model
DGG	Dysprosium Gallium Garnet
DR	Dilution Refrigerator
FAA	Ferric Ammonium Alum
FDM	Frequency Division Multiplexing
FET	Field Effect Transistor
FIR	Far Infra-Red
FWHM	Full Width Half Maximum
GGG	Gadolinium Gallium Garnet
GMCE	Giant MagnetoCaloric Effect
GSFC	Goddard Space Flight Center
HEMT	High Electron Mobility Transistor
HFI	High Frequency Instrument
HIFI	Heterodyne Instrument for the Far-Infrared
HST	Hubble Space Telescope
HTS	High Temperature Superconductor
IR	Infra-Red
ISO	Infrared Space Observatory
JAXA	Japanese Aerospace Exploration Agency
JFET	Junction Field Effect Transistor
JPL	Jet Propulsion Laboratory

JT	Joule-Thomson
LFI	Low Frequency Instrument
MCE	MagnetoCaloric Effect
MIR	Mid Infra-Red
mKCC	milli-Kelvin Cryo-Cooler
MKID	Microwave Kinetic Inductance Detector
MMC	Metallic Magnetic Calorimeter
MSSL	Mullard Space Science Laboratory
NASA	National Aeronautics and Space Administration
NEP	Noise Equivalent Power
NIR	Near Infra–Red
NIS	Normal-Insulator-Superconductor
PID	Proportional Integral Derivative
PIXIE	Primordial Inflation Explorer
PTR	Pulse Tube Refrigerator
SPICA	Space Infrared Telescope for Cosmology and Astrophysics
SQUID	Superconducting QUantum Interference Device
STJ	Superconducting Tunnel Junction
STP	Standard Temperature and Pressure
SXS	Soft X-ray Spectrometer
TDM	Time Division Multiplexing
TMM	Thermal Mathematical Model
UV	Ultra-Violet
X-IFU	X-ray Integral Field Unit

Acknowledgements

"No man can make a greater mistake than he who did nothing because he himself could only do a little." – Edmund Burke (1729-1797)

Thanks to my supervisor, Ian Hepburn: for giving me the opportunity to do this PhD in the first place, for all his guidance along the way and for providing numerous useful comments on drafts of this thesis. Thanks too to my second supervisor, Dhiren Kataria.

A big thank you to Jo Bartlett: for helping to answer my questions as I found my way in the world of ADRs (and for introducing me to the "pleasures" of cold water swimming). I'm also extremely grateful to Graham Hardy, both for his practical advice in the lab and for listening to my frustrations at running cryogenic experiments without complaint.

Thanks to Tom Bradshaw: for starting me off down this cold path, for advice along the way and for providing several helpful comments on drafts of the early chapters. I would also like to thank Andrew Fisher and Meera Parish for providing invaluable advice on the solid state physics aspects during the initial stages and, in Meera's case, for reading and giving helpful comments on drafts of chapters 3 and 4.

A special thank you to John and Kathryn for providing me with a standard of accommodation that was well above what the stipend would normally allow: not only are you the best landlord and landlady I've ever had, you're even better friends.

I'm hugely grateful to many others too: my brother, Dan, for giving me the benefit of his solid state physics knowledge and for being kind enough to delay his PhD submission so that we could go through the writing-up process together; my sister-in-law, Steph, for showing us both how it should be done; my friends, for distracting me from work, but still remembering to ask me what I was doing – even when for three years they got different versions of the same answer; and everyone at MSSL, who made it such a great place to spend 3 years.

Last, but of course not least, thanks to my parents for giving me the same support in this that they have in everything else I've done – and for so much more.

General Introduction and Overview

The part of the temperature scale below 1 K has been fertile ground for research since the first demonstrations of magnetic cooling were made in the 1930s [1–3]. The techniques employed in these early experiments – along with other advances [4–7] – have been developed to the extent that the achievement of such temperatures is no longer restricted to specialist laboratories, and commercially available equipment has opened up sub-Kelvin experiments to scientists in a variety of fields outside dedicated low temperature research.

Now that reaching the sub-Kelvin regime has become more routine, a number of technologies have been – and are being – developed that require milli-Kelvin temperatures (or lower) as a prerequisite. However, while laboratory systems may be readily available to meet these needs, sub-Kelvin coolers which can be scaled appropriately and adapted to the demands of a particular technology have yet to be realised. This thesis looks at how one of the main low temperature refrigeration technologies, Adiabatic Demagnetisation Refrigerators (ADRs), can be designed in a flexible way that can be both easily miniaturised and scaled-up for higher cooling power applications. It does this by considering in detail the thermal transport mechanisms involved and the materials challenges that currently make such designs of ADRs difficult to accomplish.

High sensitivity photon detectors are the main application currently driving the miniaturisation of sub-Kelvin coolers and the thesis begins with a short review of these. It goes on to look at the cryogenic systems that permit their operation, before the focus is shifted to Adiabatic Demagnetisation Refrigerators specifically and how the use of solid state tungsten heat switches within them offers the potential to make these refrigerators more compact and adaptable.

Chapter 1 describes some of the current sensors which are capable of detecting single photons and extracting spectrographic information, illustrating why their operating principles require temperatures below 1 K. It then reviews the cryogenic technologies used

to reach these temperatures with a particular focus on those applicable to spaceflight, since this is where sub-Kelvin cryogenic detectors are most likely to be used in the short term. To assemble a cryogenic system that cools to below 1 K from room temperature requires the combination of at least two of these cooling techniques. The importance of reducing the size of the cryogenic refrigeration system to bring it more in line with the size of the detectors is then highlighted.

Chapter 2 reviews the theory of operation of ADRs. The physics of reducing temperature through an adiabatic demagnetisation process is described, followed by a discussion of the principles used in the construction of current ADRs. One of the major issues affecting the use of the basic ADR is that it must spend some time being "recycled" between cooling cycles and no refrigeration is available during this period. This is addressed in Continuous ADRs (CADRs). Both the "tandem" and "sequential" CADR concepts are reviewed and it is shown that only the tandem configuration provides true continuous cooling. The tandem CADR consists of two ADRs in parallel, both connected to a common cold stage; while one provides cooling the other is recycling. This method of operation means that each individual ADR need only be sized to provide cooling for sufficient time for its partner ADR to be recycled. If the recycle time can be reduced, then the whole refrigerator can shrink. A second crucial aspect is limiting the parasitic heat loads onto the cold stage, so that these do not force the size of the CADR upwards. These two factors combine to make the control of heat flow within the ADR the key parameter in achieving miniaturisation. This, then, puts the focus of miniaturisation firmly on the ADR heat switches, which open and close to ensure demagnetisation is adiabatic and to dump heat during recycling, respectively. A brief review of current heat switch technologies for ADRs is also given in this chapter.

The theoretical background to heat transport in ADRs is given in Chapter 3. Heat transport by electrons and phonons is covered, along with the scattering mechanisms that limit both. The formal methods for calculating thermal conductivity are also introduced. In finite, composite structures – as found in ADRs – interfaces and surfaces can play a limiting role in

conduction and this is discussed. The final part of the chapter deals with how an applied magnetic field can influence the heat conduction process, since this method of altering the thermal conductivity is used in ADR heat switches. Some particular phenomena seen in magnetic fields at low temperatures are also introduced here as they are important in explaining the results of the following chapters.

Chapter 4 uses the theory of the preceding chapter to develop an equation for the transverse[1] thermal conductivity of tungsten below 6 K in zero-, low- and high-fields. It then presents the results of measurements made on different tungsten samples which show that the expression models the thermal conductivity extremely well under all fields tested. In fitting the data, it is found that some parameters are not exactly in line with theoretical expectations. Reasons for this are examined, leading to a discussion of phenomena beyond pure magnetoresistance.

In Chapter 5, the zero to high-field magnetoconductivity expression is generalised to cases other than transverse. Experimental results to verify this generalisation are then presented and, overall, the agreement is good. A special case here is the longitudinal conductivity for which the thermal current is parallel to the applied magnetic field. The results in this case are important because they are made use of in the following chapter and because they are not what would be expected from the magnetoresistance theory described in Chapter 3. The reasons for this are discussed.

Chapter 6 takes the equations developed and tested in the preceding two chapters and uses them in a Thermal Mathematical Model of a tandem CADR. This model predicts the temperatures and heat flows within a tandem CADR of the type described in Chapter 2. It is used to show how tungsten heat switches could be employed in a miniature CADR based on current magnet and pill technology. A set of preliminary design parameters for such a

[1] Magnetic field perpendicular to direction of heat flow.

miniature CADR is extracted and some methods to achieve further size reduction are modelled.

Finally, Chapter 7 outlines the future developments that would be required to realise a miniaturised ("micro") ADR in practice. It also discusses future research into tungsten heat switches that would provide a better understanding of their magnetoresistive properties and could potentially lead to even more effective heat switches. It concludes with a summary of the thesis.

Chapter 1 – Sub-Kelvin Cryogenics and Space Applications

Astronomy is one of the main fields currently making use of sub-Kelvin temperatures and the major driver for this is cryogenic detectors. This chapter introduces the detection methods used and reviews some of the detector technologies, focussing in particular on those which require milli-Kelvin temperatures.

The second part of the chapter outlines the cryogenic cooling technologies which facilitate their use. To reach the milli-Kelvin regime from room temperature requires several stages of cooling operating across different temperature ranges. Therefore, to design a complete cryogenic system it is necessary to combine sub-Kelvin cooling technologies with one, or more, operating at higher temperatures. For this reason, the different refrigeration methods used at each temperature range are each summarised in section 1.4.

1.1 Demand for sub-Kelvin Cryogenics in Space

The use of sub-Kelvin temperatures in space research is primarily connected with observational satellites where cryogenically cooled photon detectors confer advantages in terms of both increased sensitivity (through reduction of thermal noise in the detector) and better energy resolution (determined from the ratio $E/\Delta E$ where ΔE is the FWHM of the detector response) [8]. These advantages have been used in missions operating across a large part of the electromagnetic spectrum, from X-ray (e.g. Astro-E) to far infra-red (FIR e.g. ISO, Herschel), although those in the lower energy end of the spectrum have historically benefitted most.

Due to the complexity and mass of cryogenic systems operating below 1 K, detectors requiring them are usually only justified for scientific satellites where the high sensitivity is necessary to achieve the mission's science goals. Recent examples include the Herschel and

Planck missions, launched together in 2009. The lowest instrument temperatures on these satellites were 0.3 K and 0.1 K, respectively. These temperatures allowed them to make observations in the infra-red and sub-millimetre wavelengths that revealed the details of galaxy and star formation (Herschel) and in the microwave and FIR that provided the most precise measurement of the fluctuations in the Cosmic Microwave Background (CMB) to date (Planck).

Several future missions requiring sub-Kelvin cooling are currently proposed or in design, including ESA's Athena+ (Advanced Telescope for High Energy Astrophysics) mission and JAXA's (Japanese Space Agency) Astro-H mission, both of which will use cryogenically cooled detectors operating below 1 K to observe the X-ray universe.

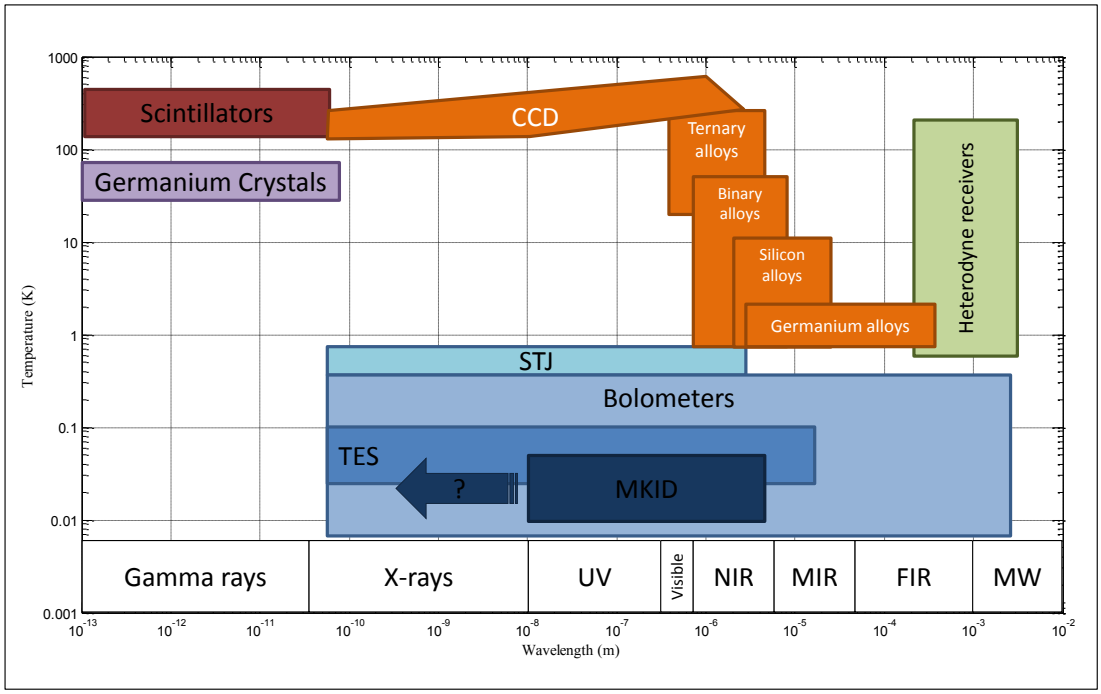

Figure 1.1: Overview of solid-state photon detectors for different wavelengths. Operating temperature is shown on the y-axis. The orange boxes refer to different types of photoconductor (adapted from [9]).

Figure 1.1 and Table 1.1 summarise the operating parameters of the main detector types used on spacecraft. Solid-state detectors are more prevalent than other alternatives at present and it is these to which the table and figure are restricted. As Figure 1.1 illustrates, certain detector types can only be operated in the cryogenic temperature range and, furthermore,

sub-Kelvin temperatures open up the use of totally new detector technologies, such as Transition Edge Sensors (TESs), Superconducting Tunnel Junctions (STJs) and Microwave Kinetic Inductance Detectors (MKIDs), which can be used across a broad frequency range. These technologies are all described in more detail below.

Detector type	**Temperature range (K)**		**Dissipation range (W)**		**Detector Size**		**Wavelength**
	Min.	**Max.**	**Min.**	**Max.**	**Pixel (μm)**	**Array (n × n)**	
CCDs	150	300	0.1	20	10-30	10^6	X-ray/Vis
Ge crystals	50	100	0	0	10000	<10	Gamma
Photoconductors (NIR)	30	100	0.01	0.02	30-50	10^6	NIR
Photoconductors (MIR)	2	20	0.01	0.02	50-100	$<10^4$	MIR
Photoconductors (FIR)	1	2	0.001	0.003	50-100	$<10^3$	FIR
Sub-mm bolometers	0.1	0.3	10^{-9}	10^{-8}	100-500	$<10^2$	Sub-mm
STJs	0.01	1	10^{-9}	10^{-6}	20-50	$<10^3$	X-ray-UV-Vis-NIR
MKIDs	0.05	0.3	10^{-11}	10^{-9}	100-200	<100	UV, Vis, (X-ray)
μ-Calorimeter	0.05	0.3	10^{-12}	10^{-11}	100	<100	X-ray
TESs	0.05	0.3	10^{-11}	10^{-9}	100	<100	X-ray-UV-Vis-NIR

Table 1.1: Characteristics of typical photon detectors used in astronomy (adapted from [8]).

The sensitivity of current cryogenic detector technologies is such that they can make ground breaking measurements in modestly sized arrays – and are doing so already [10–12]. However, their real benefits are expected to be realised when they can be assembled into the large arrays presently only associated with semiconductor technology (e.g. CCDs). This follows from the fact that the time required to observe a given section of sky to a certain

sensitivity scales as (sensitivity)^2/(number of pixels) [13]. The latest cryogenic detector technologies are approaching the sensitivity limits imposed by sky backgrounds (such as scattered sunlight and the CMB [13]) and so further gains will only be made through greater numbers of pixels. From a cryogenic standpoint, the main challenge associated with building these large arrays is to provide sufficient cooling power at low temperatures without the size of the cryogenic sub-system making the overall detector array impractical.

1.1.1 Detector Noise

The reason for the higher sensitivity of cryogenic detectors is substantially reduced noise. Electrical noise in detectors comes from a number of sources; the one for which reductions can be achieved through cooling is thermal noise and this is the type that is central to discussions of the benefits of cryogenic detectors. It is caused by spontaneous fluctuations in voltage generated by thermal agitation of the electrons (or other charge carriers), which will occur at any temperature above 0 K. These were first observed by J. B. Johnson and explained by H. Nyquist [14] leading to the term "Johnson–Nyquist" noise. The mean square of the voltage fluctuations as derived by Nyquist [14], is given by:

$$\langle V^2 \rangle = 4Rk_B T\Delta f, \tag{1.1}$$

where R is the resistance of the conductor and k_B is the Boltzmann constant. It is clearly seen from this equation that the fluctuations are linearly proportional to the absolute temperature, T, and the frequency bandwidth within which the fluctuations are measured, Δf. Using $\langle V^2 \rangle / R$, the relationship leads to the following expression for the power dissipated as a result of these fluctuations:

$$P = 4k_B T\Delta f. \tag{1.2}$$

Photon detectors must be operated at a low enough temperature that the number of photo-generated carriers is much larger than the number of thermally generated carriers. Quantitatively, $k_B T$ must be sufficiently below the excitation energy hc/λ_c, where λ_c is the

long wavelength limit (cut-off wavelength) for the detector [15]. This sets fundamental constraints on detector operating temperatures and is why many require cryogenic cooling.

1.2 Detector Types

There are a variety of detector technologies used in space missions. The main detector technologies requiring sub-Kelvin temperatures are reviewed below, but first the different detector types are briefly summarised; these fall into three categories: photoconductors, thermal detectors (bolometers) and coherent detectors.

1.2.1 Photoconductors

Photons can change the conductivity of semiconducting materials via three mechanisms [16]:

i. Electron–hole pair creation through inter-band transitions caused by absorption of photons;
ii. Excitation of electrons (or holes) from "donor" (or "acceptor") impurities into the conduction band;
iii. Absorption by free charge carriers.

These phenomena are made use of in photoconductors. The creation of electron–hole pairs (case i) is referred to as "intrinsic" photoconduction. It occurs when the photon energy is greater than the band gap energy, which is typically ~ 1 eV (e.g. 1.1 eV for silicon [16]). However, the addition of alloying elements can extend this to 0.1–10 eV, depending on the elements used. This corresponds to wavelengths from 0.1 to 10 μm, in the UV to NIR range.

Impurities can be added to semiconductors which create new states within the band gap (case ii). For "donor" impurities, electron states will be created close to the conduction band allowing excitation of electrons into this band by much lower energy photons. In the case of "acceptor" impurities, hole states are created close to the valence band and again excitation

across the band gap requires much lower energy photons. These are referred to as "extrinsic" photoconductors. Excitation across the band gap for this type of photoconductor typically occurs at energies from 5–50 meV, corresponding to wavelengths from ~ 200–20 μm and covering parts of the both the MIR and FIR range.

Photons with energies below a certain value (i.e. with wavelengths greater than a certain value) will be unable to excite electrons across the band gap. The wavelength at which this occurs is known as the "cut-off wavelength" of the detector. The process of adding impurities is one way to change this wavelength; another is to stress the material which also modifies the band gap energy.

In case iii, no new charge carriers are created, but the conductivity increases due to a change in the carrier mobility resulting from photon absorption. It has been known for some time that this effect can be utilised for the detection of millimetre and sub-millimetre wavelengths [17] when the device is cooled to liquid helium temperatures.

The importance of reducing thermal noise is clear from the method of operation of photoconductors: should the temperature be high enough that there is sufficient thermal energy in the lattice to excite an electron into the conduction band, the signal from absorbed photons may be lost amongst the signal resulting from these thermal excitations. In general, photoconductors use cooling to temperatures from as low as 1 K up to 100 K depending on whether they are constructed for FIR or Near Infra-Red (NIR) – the range of application is summarised in Table 1.1.

1.2.2 Bolometers

Bolometers (or thermal detectors) measure incoming radiation by detecting a change in the temperature of an absorbing material. A schematic is shown in Figure 1.2. The absorbing element, with heat capacity C, is connected to a heat sink through a thermal conductance, G, and its temperature, T_B, rises according to [15]:

$$\frac{dT_B}{dt} = P/C, \tag{1.3}$$

where P is the power of the incident radiation. The temperature of the absorbing element approaches the following limiting value [15] according to the thermal time constant of the system:

$$T_B = T_S + P/G, \tag{1.4}$$

where T_S is the temperature of the sink. This temperature change is normally measured by an associated change in electrical resistance, either directly through the absorbing material (such as in chip – or "hot electron" – bolometers where the incoming photons excite the electron population resulting in a change in resistance), or through a separate thermometer in thermal equilibrium with the absorber.

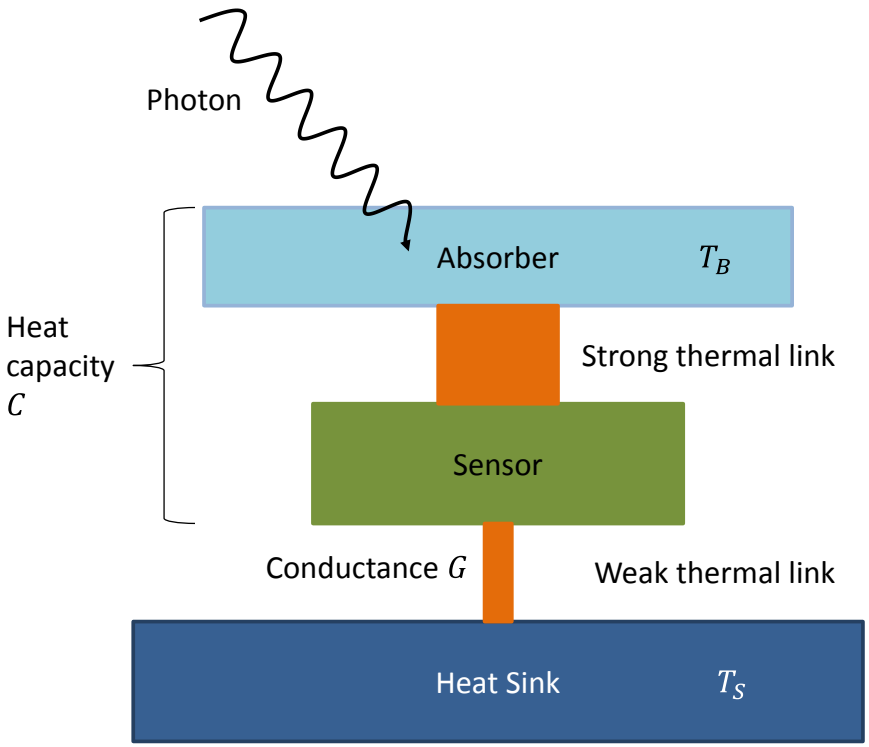

Figure 1.2: Bolometer schematic.

The commonly used figure of merit is the Noise Equivalent Power (NEP), defined as the signal power, P_S, required to produce a signal current, I_S, equal to the square root of the sum of squares of all the noise currents in a bandwidth of 1 Hz [18]:

$$NEP = P_S \frac{\sqrt{\sum_i I_{n_i}^2 \Delta f}}{I_S}. \quad (1.5)$$

Obviously this figure is improved by reducing any sources of background noise in the detector assembly. Johnson–Nyquist noise will be one such source and hence the requirement to cool bolometers. In order to detect lower energy photons in the IR and sub-mm portion of the spectrum, sub-Kelvin temperatures become necessary.

Bolometers of various types have been used on several astronomical satellites (e.g. Planck, Astro-E2 [19,20]) and ground based telescopes (e.g. SCUBA [21]).

1.2.3 Coherent Detectors

A photon stream is associated with a varying electro-magnetic field. Ideally, the frequency of changes in this field (the wave) would be measured directly, but the oscillations are too rapid for direct electronic measurement. Coherent detectors get around this by mixing the electric field signal from the incoming photons with that from an oscillator integrated with the detector ("local oscillator"). The superposition of the two signals generates a signal whose properties are much easier to handle electrically. The original high frequency components are filtered out of the combined signal, but frequency and phase information can still be extracted from the lower frequency components.

This detection technique was used on Herschel's Heterodyne Instrument for the Far–Infrared (HIFI), where STJs (see 1.3.1) were employed as the "mixers", combining the signal from the incoming photon with that from a local oscillator.

1.2.4 Signal Amplification

The output signal from a detector will usually be too weak to be used directly and will therefore need to be amplified. The amplifiers commonly used are based around Junction Field Effect Transistors (JFETs) – see Figure 1.3. These devices consist of either a hole (p-type) or electron (n-type) doped semiconductor connecting the source and drain terminals with an oppositely doped semiconductor at the gate terminal. Between the two types is a region with a depletion of charge carriers – the depletion layer – arising from the fact that electrons are attracted from the n-type material towards to p-type material by its excess of holes and vice versa. Current flowing between the source and drain terminals is modulated by a voltage applied to the gate, which increases the number of charge carriers in the gate semiconductor, thereby attracting more carriers of opposite charge to the gate. This increases the width of the depletion layer and, since the depletion layer acts like an insulator, reduces the amount of current that can pass between the source and drain. The principle is analogous to reducing the flow through a hose by squeezing it.

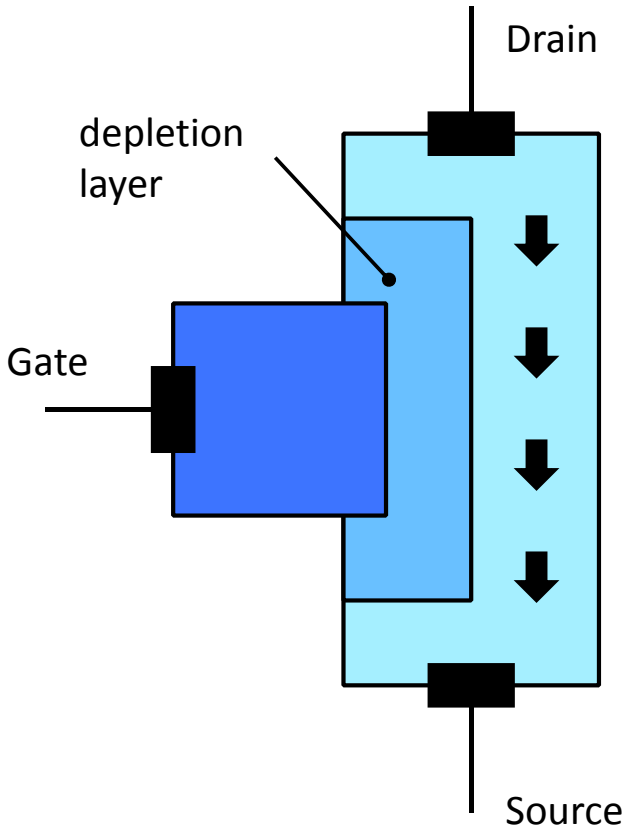

Figure 1.3: JFET Schematic.

The circuit for a common source JFET amplifier is shown in Figure 1.4. The detector signal is fed into the JFET's gate terminal so that it modulates the voltage drop between the drain and ground; this, in turn, modulates the voltage drop between the supply (V_{DD}) and the source which controls the output signal.

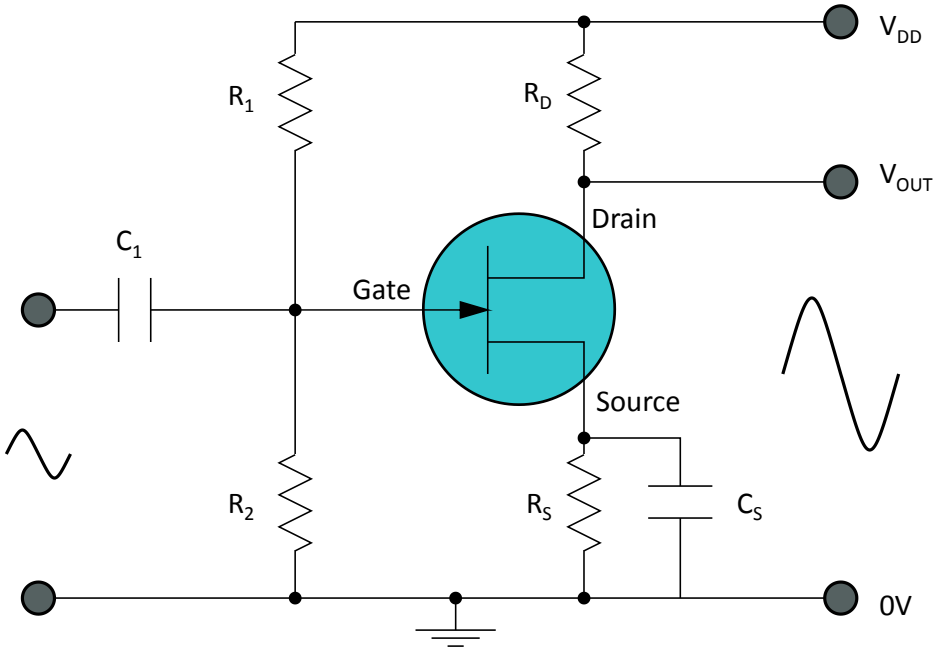

Figure 1.4: Common Source JFET amplifier circuit.

JFETs are particularly suitable for the amplification of weak signals due to their high input impedance and low noise output. However, their temperature must be controlled near to their noise minimum, which is typically of the order of 100 K [20]. Furthermore, they should ideally be placed near to the detectors so that rigid leads which minimise microphonics can be used. Detector arrays thus require a large number of JFETs positioned close to the detector array and in a location that affords the level of cooling necessary to maintain their operating temperature. These complications can be a significant barrier to the construction of large bolometer arrays.

Signal amplification and detector read-out in general are important factors in assessing how easily large arrays can be constructed from a particular detector technology. For this reason, multiplexing schemes are discussed for each of the detector technologies described below.

1.3 Sub-Kelvin Detector Technologies

1.3.1 Superconducting Tunnel Junctions

Superconducting Tunnel Junctions (STJs) employ the quantum tunnelling effect across a Josephson junction to produce a current that is related to the absorbed energy. A Josephson junction is a type of potential barrier created by separating two superconducting electrodes with a thin insulating layer; STJs are micro-fabricated in this format. There are two ways in which electrical transport across the barrier can take place:

i. Cooper pairs can tunnel across the barrier. This happens as a consequence of the Uncertainty Principle: if the position of the particle is well known, its energy is uncertain to the extent that it can attain values in excess of the constraining potential (even though this may be more than its classical energy limit).

ii. Quasi-particles can traverse the barrier in similar manner. The creation of these is associated with a rise in temperature which breaks up the Cooper pairs.

The "Josephson current", consisting of tunnelling Cooper pairs, is suppressed by placing the detector in a uniform magnetic field of a few milli-Tesla. The supercurrent is then related to the quasi particles and is proportional the absorbed energy, which, in turn, can be used to determine photon energy.

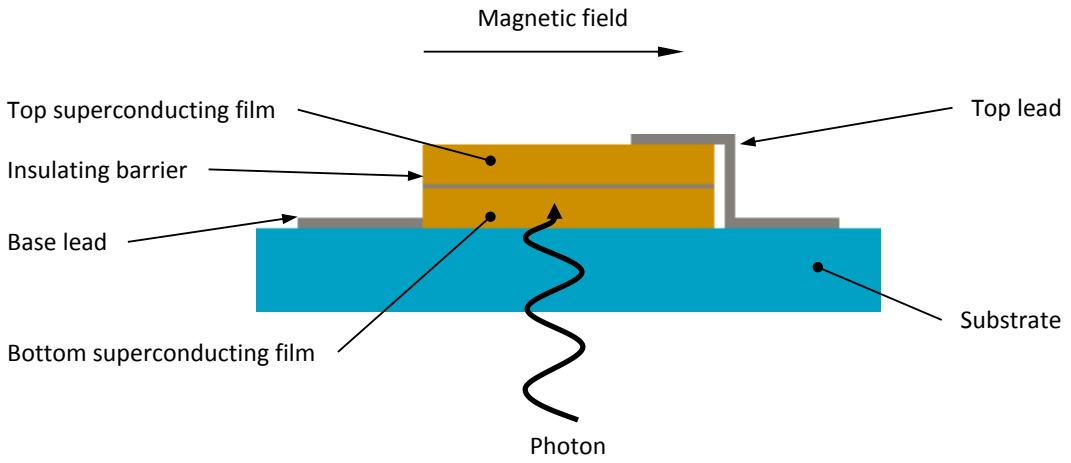

Figure 1.5: Superconducting Tunnel Junction schematic.

To register a signal, the number of quasi-particles must exceed those resulting from the thermal background and for this to occur the temperature must be such that $T/T_c \approx 0.1$ [22], where T_c is the critical temperature of the superconductor. This translates to operating temperatures of between 100 and 500 mK [8]. STJs can observe photons from the X-ray, UV, visible and NIR portions of the spectrum and because of their sensitivity they can also be used as calorimeters. The energy resolution ($= E/\Delta E$) of a STJ is proportional to the square root of the photon energy [23]; theoretical values of $\Delta E = 80$ meV and $\Delta E = 1$ eV at $E = 1$ eV and $E = 1$ keV, respectively, are reported [22].

Progress has been made in recent years on producing STJ arrays and a read-out scheme based on grouping electrodes in rows and columns has shown a way to reduce the number of wafer connections and amplifier chains for an N × N array to 2N, instead of the N^2 normally required [24,25]. This arrangement leads to a small increases in the effect of amplifier noise, but a more serious drawback is to do with biasing the junctions [25]. As noted above, the Josephson current in a STJ must be supressed with a magnetic field; small manufacturing differences result in the required field being slightly different for each junction, meaning that it can never be optimum for all the pixels in an array and some current will persist. In a matrix readout scheme, the biasing current must then be sufficient to exceed the sum of all the Josephson currents in a row (or column), which leads to increased noise on the read-out line.

1.3.2 Transition Edge Sensors

Transition Edge Sensors (TESs) comprise thin films which have a sharp superconducting-to-normal transition, typically in the range 70–130 mK, with the transition width being less than 1 mK [23]. The sensor is cooled whilst being supplied with a bias voltage to maintain it within the superconducting-to-normal transition by virtue of the resulting Joule heating. The Joule heating ($\propto V^2/R$) provides intrinsic stability through a negative feedback mechanism: an increase in sensor temperature increases its resistance and thus decreases the Joule heating; similarly, a decrease in temperature increases the Joule heating. An incident photon

can push the sensor into the normally conducting regime and the resulting change in resistance can be measured.

TESs can be used as either calorimeters (in response to a pulse of energy) or as bolometers (in response to an input power). A schematic of the arrangement when using them as bolometers is shown in Figure 1.6. They have a range of applications from gamma-ray and X-ray spectroscopy to infrared bolometry.

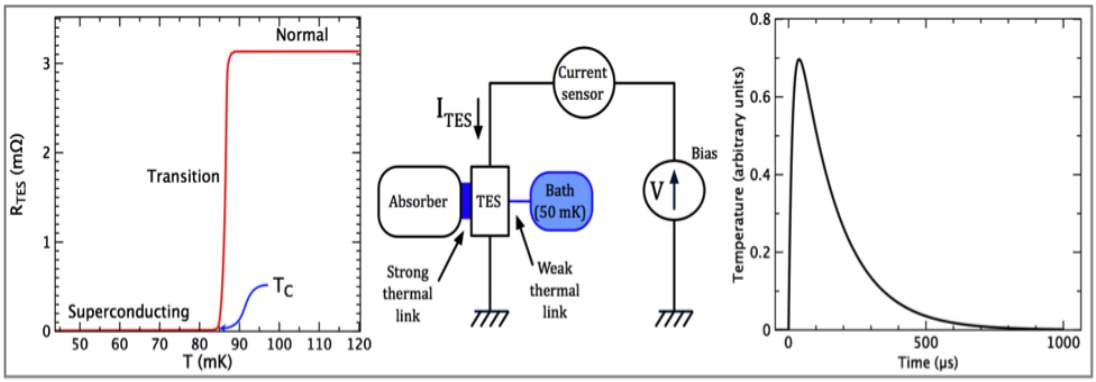

Figure 1.6: TES Operating principle [26].
Left panel: the TES is cooled to the transition region between its normal and superconducting states. Middle panel: photon absorption heats the absorber and TES. Right panel: the change in temperature (or resistance) with time during photon absorption.

In current instrument designs [27] they are read out with SQUIDs (Superconducting QUantum Interference Devices). SQUIDs for this application are constructed by placing two Josephson junctions in a superconducting loop. These junctions are indicated in the right half of Figure 1.7 by crosses. In the absence of a magnetic field, the supercurrent splits evenly between the two branches. If a magnetic field is applied, however, a screening current will flow in the superconducting loop which acts to cancel the external flux. Should this cause the total current in either branch to exceed the critical current, the loop will go normal and a voltage can be measured. The amount of flux in the loop can only be an integer value of the flux quantum, Φ_0; if the external flux is $> (n + 1/2)\Phi_0$ it will be energetically favourable for the screening current to flow in the direction that increases the external flux. When the SQUID is operated with a sufficient bias current that it is always

resistive, this effect causes oscillations in the measured voltage which are extremely sensitive to changes in the external flux.

An example read-out circuit from the X-IFU (X-ray Integral Field Unit) instrument proposed for Athena+ is shown in Figure 1.7 below [27]. Changes in the resistance of the TES cause current to flow in the inductance L; this produces a flux imbalance in the SQUID and the resulting changes in voltage can be measured.

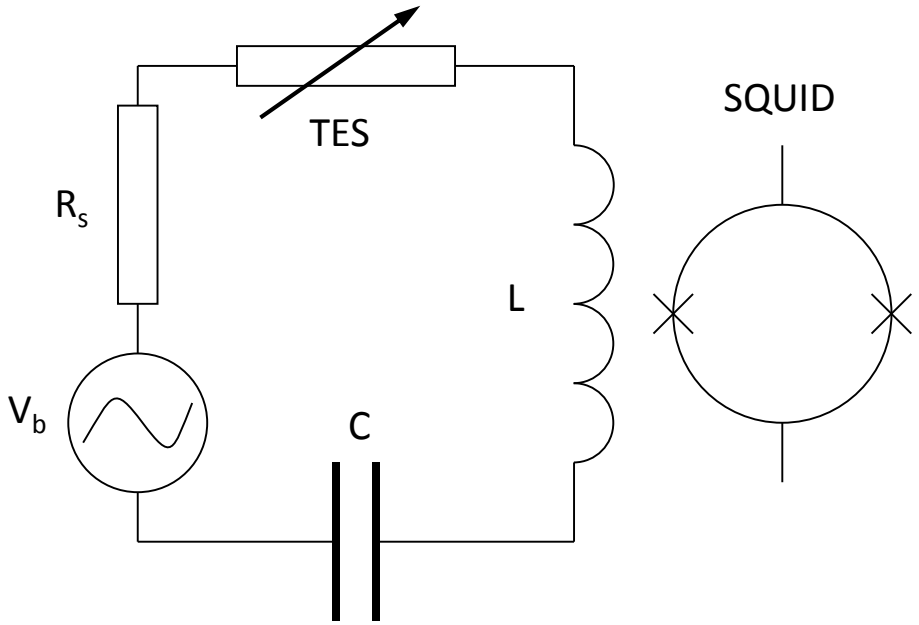

Figure 1.7: Schematic of TES read-out electronics using a SQUID (reproduced from [27]).

TESs are usually used to measure the temperature rise in an isolated heat capacity which provides a direct measure of photon energy [23]. This is to be contrasted with the STJ, whose output signal is proportional to number of quasiparticles created by the incident photon. Both STJs and TESs offer the potential of close to 100% detection efficiency, intrinsic spectroscopic capability and good imaging resolution. Whereas the energy resolution of a STJ scales with the root of the energy, the resolution of a TES scales with the square root of the detector's saturation energy [23] – values of $\Delta E = 0.15$ eV at $E = 1$ eV are reported, with TES performance tending to outstrip that of STJs at higher energies [23].

TES arrays may be read out using either time or frequency domain multiplexing. In the latter case, the sensors are biased with a comb of sinusoidal frequencies and each sensor is placed in a parallel RLC circuit which passes the designated bias frequency for that particular sensor and suppresses all the others. The circuit functions like a pure LC circuit, containing an inductance, L, and a capacitance, C. As the capacitor discharges through the inductor, magnetic field is built up and energy is then transferred from this field back to the current carriers as the potential from the capacitor dies away; the capacitor is thus charged with the opposite polarity. When the capacitor is fully charged, it discharges again; this time causing current to flow in the opposite direction, storing energy in the inductor and eventually charging the capacitor with the initial polarity once again. In a pure LC circuit, current will oscillate around the loop indefinitely. The effect of the resistance is merely to damp out these oscillations. There is a characteristic time associated with the oscillations, depending on the relative sizes of the inductance and capacitance; the circuit will resonate under application of an alternating current with frequency $1/(2\pi\sqrt{LC})$, which makes the inductive and capacitive reactances equal. The TES takes the place of the resistor in the RLC circuit and a change in its resistance leads to a change in the amplitude of sinusoidal bias signal. The modulated frequency comb can then be read out through a single SQUID [28]. Frequency domain multiplexing has been used to read out arrays of 1000+ bolometers on the South Pole Telescope [11].

To achieve time domain multiplexing requires a SQUID for each TES. The SQUIDs are connected in series and biased with a pulse train ("boxcar modulation functions"), with the pulses offset in time for each device; this effectively switches successive SQUIDs on and off at high frequency [29]. By using common output voltage and feedback lines for a column of N sensors, an M × N array may be wired with 2M output leads, 2M feedback leads and N+1 address lines – a significant saving on the 6 lines per SQUID required in a conventional configuration and one that makes it possible to contemplate large arrays [30]. Time division

multiplexing has been used in the 32 × 40 pixel TES arrays demonstrated on SCUBA-2 [31].

1.3.3 Metallic Magnetic Calorimeters

Metallic Magnetic Calorimeters (MMCs) are a type of bolometer where the temperature change in the absorber is measured through the change in magnetisation of a paramagnetic material. This concept was originally developed for particle detection [32], but has gone on to find application in X-ray and gamma-ray measurements [33].

MMCs' principle of operation follows that of a bolometer, with the role of the temperature sensor being played by the paramagnet, which is in close thermal contact with the absorber. Both the absorber and the paramagnet are weakly thermally coupled to a cold sink. The paramagnet is placed in a weak magnetic field and its magnetisation is then related to the temperature change according to the following expression:

$$dM = \frac{\partial M}{\partial T} dT. \tag{1.6}$$

This change in magnetisation will usually be very small and is therefore measured using a SQUID, where this change is reflected by a change in magnetic flux ($d\Phi$) in the loop. This change in flux is then related to energy deposited in the absorber ($d\epsilon$) using the heat capacities of the absorber (C_a) and the sensor (C_s) [34]:

$$d\Phi = \frac{\partial M}{\partial T} \frac{d\epsilon}{C_a + C_s}. \tag{1.7}$$

Recent MMCs have been micro-fabricated from erbium doped gold films, where it is the erbium spins which are affected by a change in magnetic field. It has been shown that these should be capable of achieving energy resolutions below 1 eV for energies up to 10 eV, although further work remains to optimise the energy resolution and the make the fabrication reliable [34].

Arrays of MMCs are based on time division multiplexing, following the same principles used for TESs [35]. The main challenge is that, by turning on individual pixels successively, the sampling rate for each pixel is limited by the number of pixels multiplexed through a single read-out line and the speed with which the switching is performed. This reduces the bandwidth for each pixel and can cause high frequency noise (usually coming from the SQUID read-out) to be included in the measurement of the lower frequency signal ("aliasing"). The problem is addressed by using two stages of SQUID read-out, separated by a low pass filter; reducing noise in the second stage SQUIDs is a key requirement for realising larger arrays [35].

A 5 × 5 array has recently been demonstrated, suitable for detection of X-rays between 0.2 and 10 keV [36]. With the readout of two pixels multiplexed (TDM) a resolution of 4.1 eV was achieved at an X-ray energy of 6 keV and it is suggested that up to 32 pixels could be multiplexed in this way with minimal further loss of resolution [36].

1.3.4 Microwave Kinetic Inductance Detectors

Microwave Kinetic Inductance Detectors (MKIDs) are a comparatively new form of low temperature detector, originally developed by Caltech and NASA's Jet Propulsion Laboratory (JPL) [37,38]. They make use of the fact that, while a superconductor can pass a direct current without resistance, it has a non-zero impedance for alternating currents. This is due to kinetic energy being stored in the Cooper pairs on application of an electric field; energy which must be extracted upon reversal of the electric field. Energy may also be stored in the magnetic field existing within the penetration depth of the superconductor. The flow of energy between the superconductor and its magnetic field gives rise to a surface impedance [39]. Photons are detected through changes in this surface impedance.

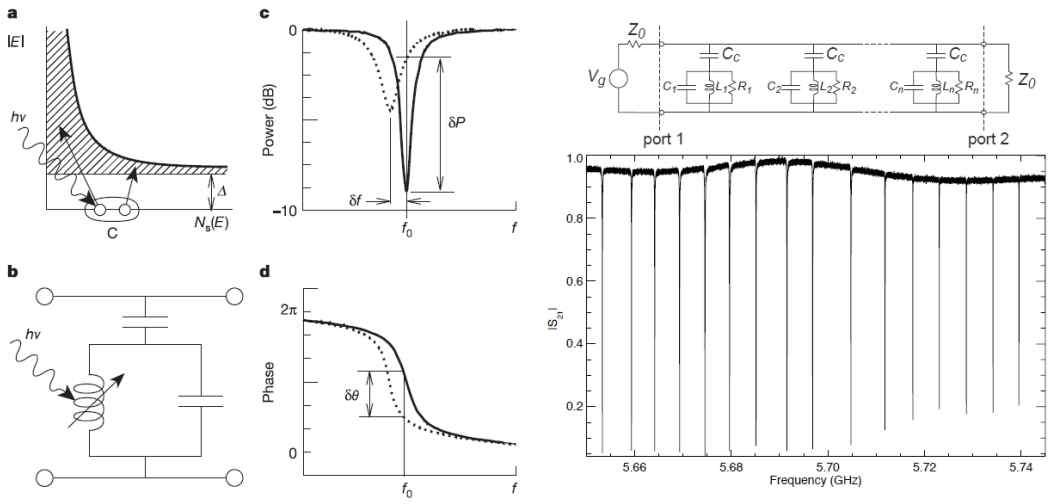

Figure 1.8: Operation of a MKID [40].
(a) A photon of sufficient energy to break a Cooper pair at the Fermi level is absorbed, creating two quasiparticles capable of bridging the superconducting energy gap. This changes the surface impedance of the device. (b) The MKID is placed as the inductor in an LC resonator circuit where its inductance is altered by the absorption of a photon and the creation of quasiparticles. The photon absorption is seen in the amplitude (c) and phase (d) changes of the resonance of the LC circuit and these can be used to determine photon energy. The right panels show how MKIDs can be multiplexed by passing a comb of microwave frequencies through a series of individually tuned resonant circuits.

The process of photon detection using MKIDs is illustrated in Figure 1.8. Photon absorption in a superconductor can break the Cooper pairs responsible for the superconductivity if two quasiparticle excitations are created with sufficient energy to cross the superconducting energy gap. The quasiparticle excess will temporarily change the surface inductance of the superconductor. To measure this change in inductance, the MKID is placed as the inductor in an LC, or resonant, circuit, similar to that described in section 1.3.2. The change in surface impedance of a MKID can therefore be measured through the change in amplitude and phase of the circuit's resonant peak. The phase change can be shown to be related to the photon energy [38] and this allows MKIDs to be used as very accurate calorimeters. The resonator circuits are typically tuned to microwave frequencies; hence the term Microwave Kinetic Inductance Detector.

The sensitivity of a MKID is dependent on the energy gap in the superconductor used [39]; energy resolution should therefore be at least as good as STJs or TESs and theoretical values of 100 ($= E/\Delta E$) have been reported [41]. They can be used across the electromagnetic

spectrum from UV to IR and their timing resolution is also excellent, being of the order of a microsecond – up to six orders of magnitude better than CCDs [12]. However, the main attraction of these devices is the simplicity with which they can be multiplexed using low cost, low power electronics developed for wireless communications [39]. The only low temperature parts of the electronics are HEMT (High Electron Mobility Transistor) amplifiers, greatly simplifying cryogenic wiring and the load on the low temperature cooler.

The technology is still in a relatively early stage of development and some problems exist with manufacturing the arrays with a uniform transition temperature and easily distinguishable resonant frequencies. However, a 2024-pixel array has recently been constructed from titanium nitride films [41] and testing of the device at the Palomar Observatory revealed a 70% yield of good pixels.

1.4 Cryogenic Technologies used in Space Missions

While space itself is very cold (~ 3 K), radiative heating[2] and the requirement for much of the electronics on a spacecraft to operate in the vicinity of room temperature, make cryogenic cooling in space fairly complex. To achieve sub-Kelvin temperatures requires several stages of cooling operating at various steps from approximately 300 K downwards. Each cooling stage will usually be provided by a separate cooler and these are assembled into a "cryogenic chain" to reach the ultimate temperature required. The cooler types appropriate to each temperature range are shown in Figure 1.9.

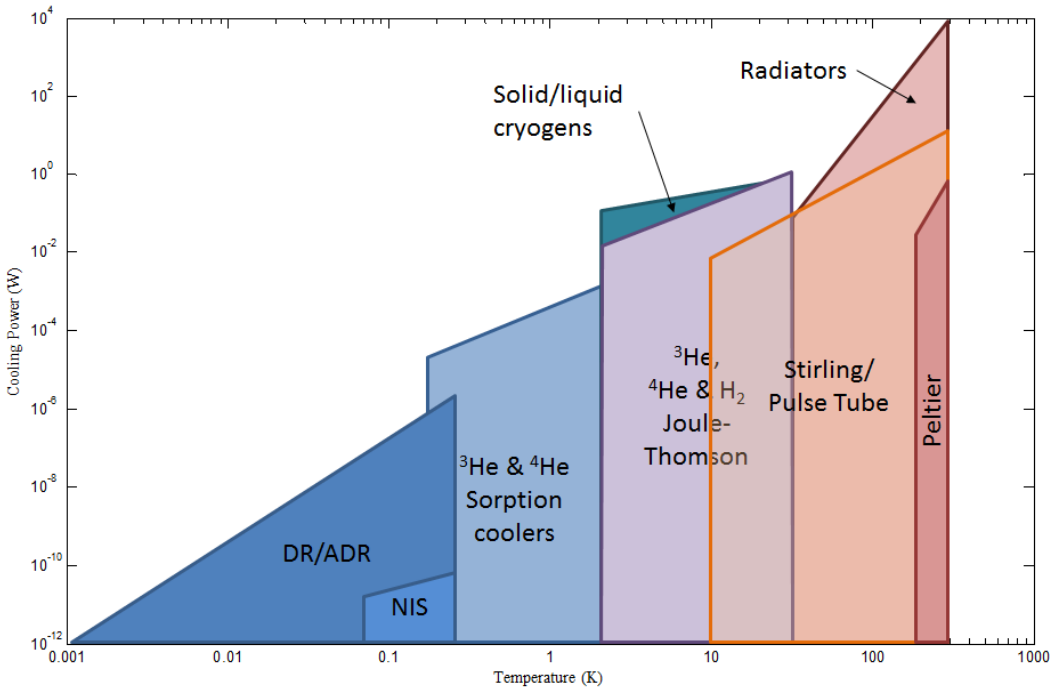

Figure 1.9: Operating range of different space coolers plotted in temperature–cooling power space. DR = Dilution Refrigerator, ADR = Adiabatic Demagnetisation Refrigerator NIS = Normal-Insulator-Superconductor cooler (adapted from [9]).

Combining the technologies in Figure 1.9 to reach temperatures below 1 K can result in a complex cryogenic system. The cooling system used on the Planck satellite to reach 0.1 K is a prime example and a schematic is shown in Figure 1.10. Planck's orbit around the second Earth–Sun Lagrangian point (L2) protected it from much of the Sun's radiation and allowed

[2] Sources of this may include the Sun and albedo radiation, depending on the spacecraft orbit.

the shields shown in the diagram to provide passive cooling to around 50 K. Three separate coolers were then used to reach 0.1 K (for the High Frequency Instrument) from this temperature: a sorption-pumped hydrogen Joule-Thomson (JT) cooler providing cooling at 18 K (which also provided cooling for the Low Frequency Instrument), a helium JT cooler providing 4.5 K and, finally, a Dilution Refrigerator (DR) to reach 0.1 K. These technologies (and others) are briefly reviewed in this section.

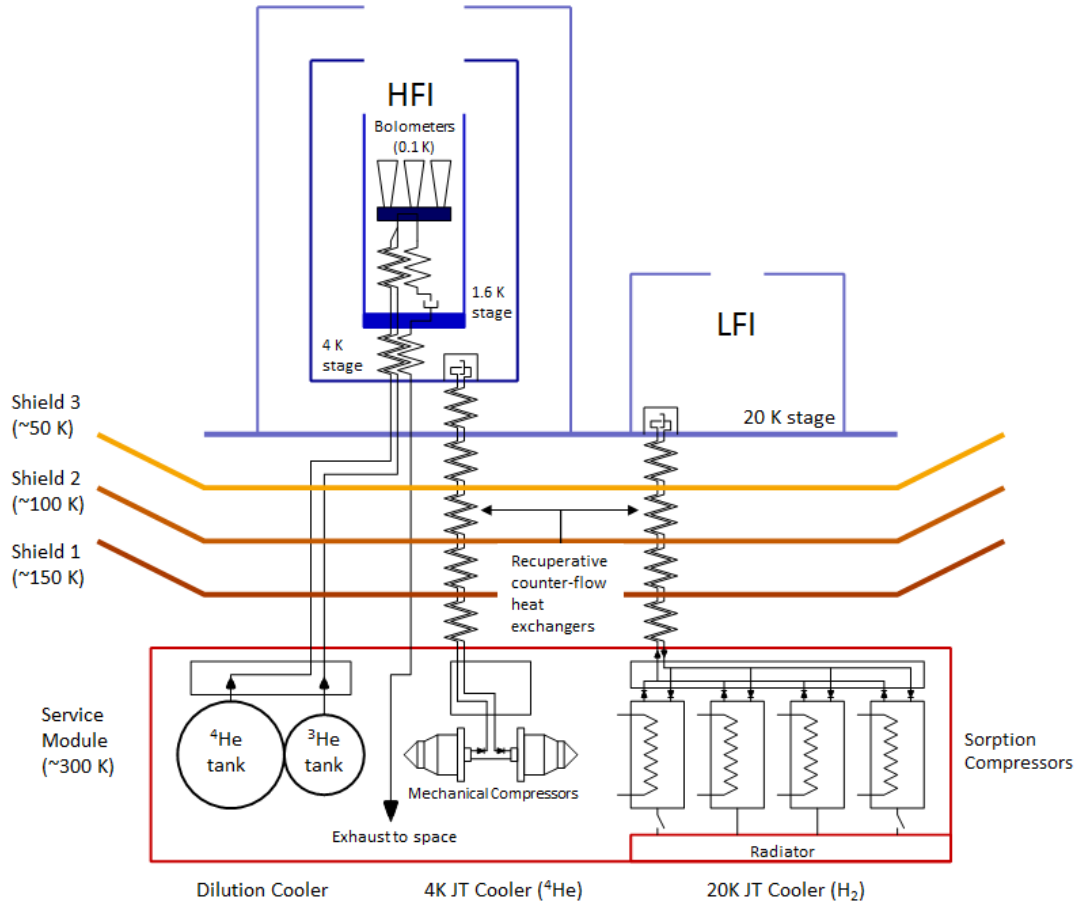

Figure 1.10: Schematic of the Planck cooling chain
(adapted and augmented from [42]).

1.4.1 Radiative Cooling

Radiant cooling makes use of the low temperature of space as a heat sink. As with any radiant heat transfer, the cooling power, $\dot{Q}$, is proportional to the difference between the fourth powers of the source and sink temperatures:

$$\dot{Q} = \varepsilon\sigma A(T_R^4 - T_S^4), \tag{1.8}$$

where ε is the emissivity of the radiator's surface, σ is the Stefan-Boltzmann constant, A is the radiator's area, T_R is its temperature and T_S is the temperature of space.

As noted above, this radiated power will be counteracted by incoming radiation loads, such as from the Sun, or albedo and infra-red radiation from the Earth. Radiant cooling is therefore most effective when these can be minimised and spacecraft orbits are chosen to achieve this. The design and positioning of a radiant cooler must be cognisant of the spacecraft's orbit and pointing; ideally it will be able to radiate to deep space for as large a proportion of the orbit as possible and shield cold surfaces from all unwanted incoming radiation. The surfaces of the radiators are produced in high emissivity material and shielded, as much as possible, from incoming radiation by surfaces of high reflectivity. Optimum results are usually achieved by using multiple stages, in which higher temperature radiators shield lower temperature ones and reduce parasitic loads.

In deep space orbits (e.g. L2) where heat loads from the Sun and Earth are minimised, radiative cooling can be used to achieve temperatures down to approximately 50 K [43]. This is higher for geostationary orbits, where between 75 K and 90 K can be achieved, and higher still for low Earth orbits, where only around 100 K is possible [8]. Sometimes these temperatures are sufficient for radiators to be the only cooling system on a spacecraft, but for the types of detector described above they must be augmented by other coolers.

1.4.2 Liquid Cryogens

Before the relatively recent progress in mechanical coolers for space (see 1.4.4), flying cryostats was the only way to reach cryogenic temperatures on spacecraft. Helium is the fluid used almost exclusively and it is contained in the cryostat by means of a porous plug (phase separator). Although becoming less favoured, one such cryostat has been used recently on ESA's Herschel mission, which carried approximately 2400 L of superfluid helium for its mission lifetime of four years [44].

There are several design considerations particular to spaceflight cryostats which mark them out from normal laboratory cryostats:

i. No pumped vacuum jacket is needed once in orbit;
ii. The absence of gravity means the fluid must be maintained by a phase separator;
iii. Launch loads require additional support of the liquid vessel; the fill/vent neck cannot be used as the only support;
iv. Boil-off can be vented to space through a restriction to provide further cooling (e.g. to shields), but this must be done so as not to impart unwanted momentum on the spacecraft;
v. It may not be necessary to have radiation shields that completely enclose the Dewar as heat can be radiated to space;

Using liquid cryogens offers a number of advantages: they provide a stable temperature that is not significantly impacted by short-term spikes in the heat load; the evaporating gas can be used to provide cooling at higher temperatures; and the electrical requirements are minimal, with only power for temperature measurement and control being necessary. A benefit particular to use on spacecraft is that no additional pump is required to reduce the temperature since the vacuum of space can serve this purpose.

The main drawback of using liquid cryogens is that the operating period is limited by the amount of cryogen that can be stored on the spacecraft. To achieve desired lifetimes (usually > 3 years), the size of the cryostat will be so large that it will dominate the spacecraft. This situation can be improved by the addition of mechanical coolers to achieve zero boil-off systems, albeit at the expense of additional mass. Cryostats are also unable to provide a continuous spectrum of temperatures; rather discrete points fixed by the saturation temperatures of the various cryogenic fluids.

In addition to the Herschel spacecraft, Dewars have been flown on NASA's COBE (COsmic Background Explorer) mission, where 80kg of liquid helium was maintained at ~1.5 K to

allow nearly one year of observations [43], and on the Infrared Space Observatory (ISO), where 265 kg of liquid was maintained at 1.8 K for over 2 years [43].

1.4.3 Solid Cryogens

Solid cryogens can be used to negate the need for a phase separator. Where cryogens are stored in both solid and liquid phase, a range of temperatures is possible from one system. The optimal design can often be to use two cryogens; the first one reducing parasitic loads by absorbing heat at higher temperatures and a second one to achieve the required operating point.

On the Japanese X-ray mission, Astro-E2, solid neon at 17 K was used in this way to insulate the helium Dewar [45] and solid nitrogen has been used on the NICMOS (Near Infrared Camera and Multi-Object Spectrometer) instrument aboard the Hubble Space Telescope.

1.4.4 Mechanical Coolers

Mechanical coolers may be either "recuperative" or "regenerative". In recuperative coolers two steady fluid streams exchange heat across a boundary; in regenerative systems one fluid stream moves back and forth in the same porous heat exchanger, alternately loosing and absorbing heat.

1.4.4.1 Stirling Coolers

In the same way that work is extracted from heat input in the traditional Stirling engine [46], work input can allow it to extract heat and cool below ambient temperature. The theoretical cycle has an efficiency equal to that of the Carnot cycle.

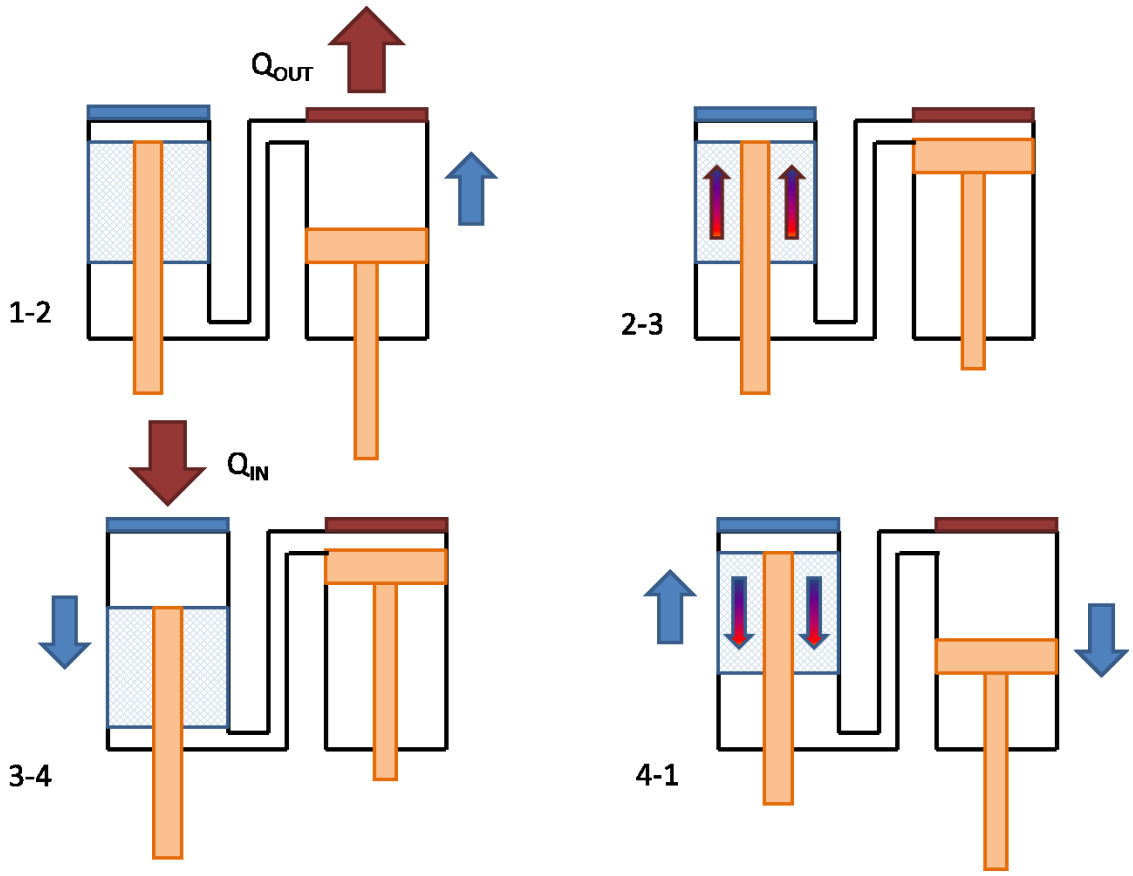

Figure 1.11: Schematic representation of a Stirling cooler in the four stages of the cycle.

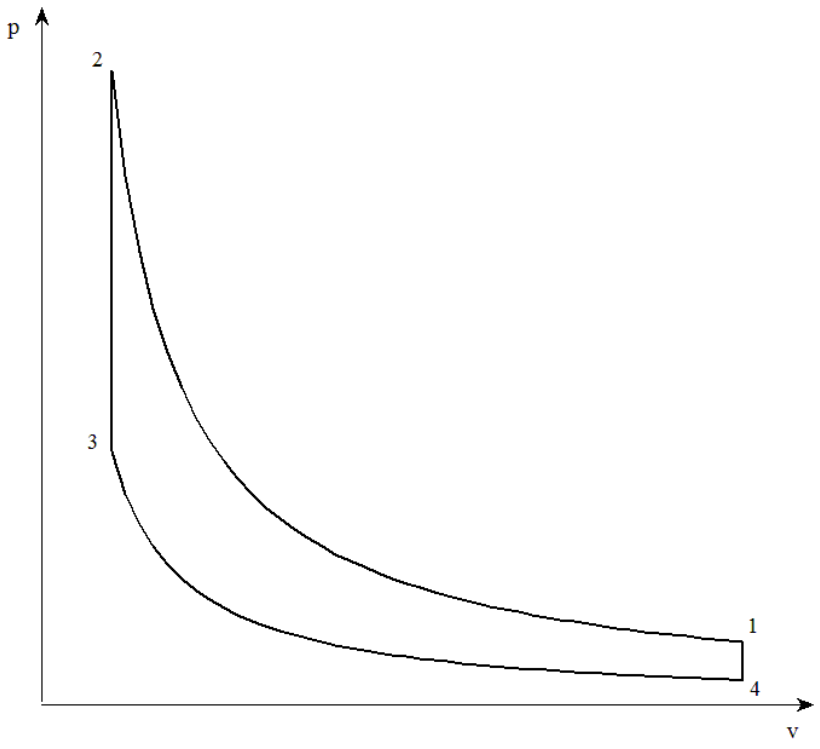

Figure 1.12: p-v diagram of the Stirling cycle.

The schematic layout of a typical Stirling cooler is shown in Figure 1.11. It consists of a compressor (on the right of the diagrams) and a displacer (on the left of the diagrams). These can be driven by either rotary or linear motors; the latter are more widespread in space applications since their design eliminates contact between moving parts. This is achieved through the use of radially stiff, but axially compliant, diaphragm springs, which accurately centre the piston and allow a small enough clearance between the piston and bore to create a gas seal. The absence of rubbing surfaces permits much longer lifetimes than can normally be achieved in rotary machines. Where rotary compressors are used, the required pressure swing is created by one-way valves. This arrangement is employed in commercial Gifford-McMahon cryocoolers.

Between the compression and expansion spaces is the regenerator: a fine matrix of material designed to absorb and reject heat in as close to a reversible fashion as possible. The usual arrangement is to design the regenerator into the displacer piston (as shown in Figure 1.11) although other configurations are possible. The displacer is often separated from the compressor to allow more flexibility in the overall spacecraft architecture; in this way the compressors, which may be a source of vibration, can be situated away from the instrument to be cooled.

The cycle is characterised by the following stages, illustrated by Figure 1.11 and Figure 1.12.

1-2: The gas is compressed isothermally, rejecting heat to the hot sink

2-3: The warm gas passes through the regenerator, to which it dumps heat, resulting a pressure drop that theoretically takes place at constant volume. In the ideal cycle, this occurs reversibly.

3-4: The gas expands isothermally, absorbing heat from the cold sink.

4-1: The cool gas passes through the regenerator, absorbing heat from it as it does so. In the ideal cycle this results in a pressure increase at constant volume.

During cool-down, the heat rejected to the regenerator results in the gas arriving at the cold end at a slightly lower temperature than in the previous cycle, allowing progressive cooling.

Stirling coolers are the most ubiquitous mechanical cooler for space and have been flown on many missions, such as ESA's ENVISAT, INTEGRAL and Rosetta spacecraft [9]. Typical cooling powers and operating temperatures can vary depending on the size of the cooler and whether multiple stages are employed, but are of the order of hundreds of mW at anything from 10 to 80 K.

1.4.4.2 Pulse Tube Coolers

Pulse Tube coolers are a variation of Stirling coolers where the task of the displacer is performed instead by an oscillating pressure wave in the pulse tube section. The combination of a buffer with an orifice (or flow impedance) act in a similar way to a capacitor and resistor in an electrical circuit, producing a phase shift between the pressure (voltage) and mass-flow (current) waveforms [47].

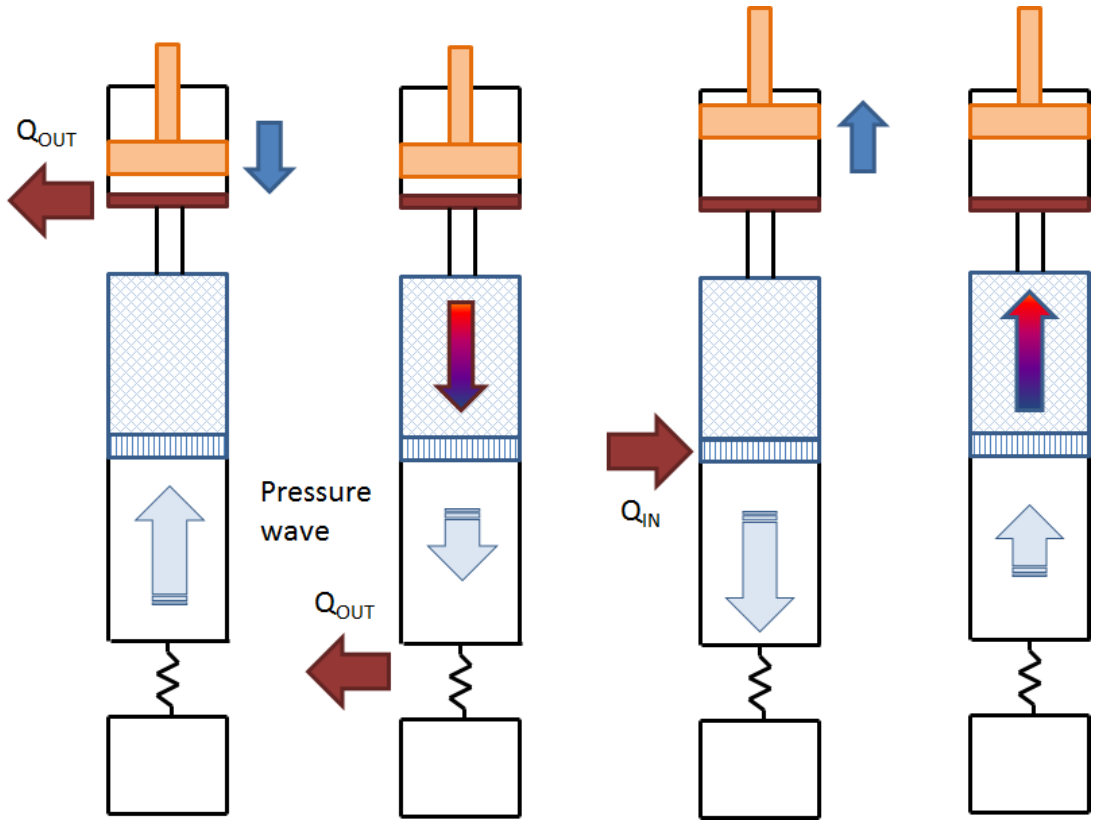

Figure 1.13: Schematic of a Pulse Tube cooler in the different stages of its cycle.

The sequence can be explained with reference to Figure 1.13 as follows.

1-2: The gas is compressed isothermally, rejecting heat to the hot sink.

2-3: The pressure wave in the pulse tube acts in the same direction as the gas flow causing it to pass through the regenerator, to which it rejects heat. Gas flows into the buffer and this also exchanges heat with the warm surroundings.

3-4: The pressure wave and compressor now act in opposing directions, causing an isothermal expansion of the gas. Heat is absorbed at the cold sink.

4-1: The pressure wave and compressor direction align again, returning gas back to the compressor, though the regenerator, from which heat is absorbed.

Gas in the central portion of the pulse tube never leaves the tube and can be thought of as a "gas displacer". To promote this state, which thermally insulates the two ends of the pulse

tube, turbulence inside the tube must be minimised – flow straighteners at the two ends are often used for this purpose.

Various different configurations of pulse tube refrigerator have been developed to optimise the phasing between the mass flow and pressure for maximum efficiency [47]: the flow impedance may be realised using either an orifice or an inertance tube (or both), or some of the compressed gas can be bypassed directly to the warm end of the pulse tube in the so-called "Double Inlet" arrangement. All of these modifications are aimed creating a small phase lag between the flow and pressure at the cold end with the flow at the warm end leading the pressure. These differences minimise the amplitude of the mass flow in the regenerator which reduces pressure drops and increases heat exchange [47]. The "Double Inlet" configuration contains a line and orifice which directly connect the compressor to the warm end of the pulse tube. In addition to promoting the correct phasing, this also reduces regenerator losses be reducing the amount of gas that passes through it. The expansion work in a pulse tube cannot be recovered as it can in an ideal Stirling cooler; instead it is dissipated as a small amount of entropy production, seen as heat at the orifice [43].

Pulse tube coolers are popular for cooling applications where vibration might affect the object to be cooled because they do not contain moving parts in the cold end. Exported vibrations can still be an issue, however, as they can arise from movement of gas within the pulse and inertance tubes. The absence of moving parts at the cold end also makes them attractive for applications where there may be high magnetic fields associated with the low temperature region. Their use in space is relatively rare to date, but examples have been flown on the Space Shuttle (delivering 50 mW at 100 K) and NASA's Aqua mission (delivering 1.75 W at 55 K) [9].

1.4.4.3 Joule-Thomson Coolers

Joule-Thomson expansion refers to free expansion of a gas. Its use in a cooling cycle is based around adiabatic expansion of gas through a nozzle or orifice. For a perfect gas, this

process would happen reversibly and would result in no change in temperature. However, for a real gas, irreversibilities arise from two sources:

i. The expansion of the gas increases the average distance between molecules and does work against the van der Waals forces to increase the potential energy of the gas. For an adiabatic process, no heat is transferred so that the increase in potential energy implies a decrease in kinetic energy and thus cooling.

ii. The increase in the average distance between molecules reduces the collision rate. During collisions kinetic energy is converted to potential energy, so fewer collisions results in lower average potential energy. As in i, if no external work is done, the adiabatic process implies conservation of energy; hence, a lower average potential energy implies a higher average kinetic energy and thus heating.

Which of the above two processes dominates depends on the "inversion temperature" of the gas. Above the inversion temperature, the second process dominates and the temperature of the gas increases; below the inversion temperature, the first process is dominant and cooling can be achieved. It can be shown using van der Waals theory of interacting particles [14] that the inversion temperature at atmospheric pressure is expected to be 27/4 times the critical temperature, which for helium-4 gives a value of ~ 35 K. The true inversion temperature is usually below this.

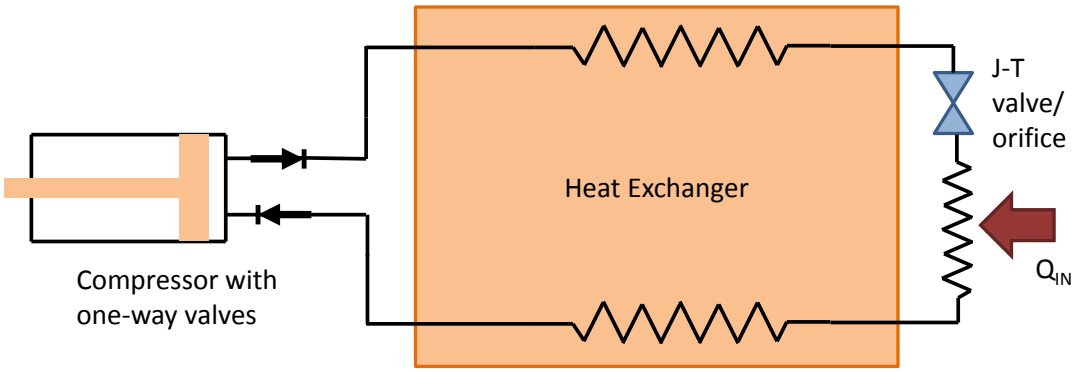

Figure 1.14: Schematic of a Joule-Thomson cooler.

The cycle requires a high pressure upstream of the orifice and low pressure downstream. This is typically achieved using linear compressors with non-return valves to achieve uni-directional flow (see Figure 1.14). A heat exchanger is also employed to allow the returning gas to cool the incoming stream and improve efficiency. Where necessary, pre-cooling of the gas to below its inversion temperature takes place here too. An open cycle system can be constructed by driving the gas flow from high pressure gas stores rather than using compressors.

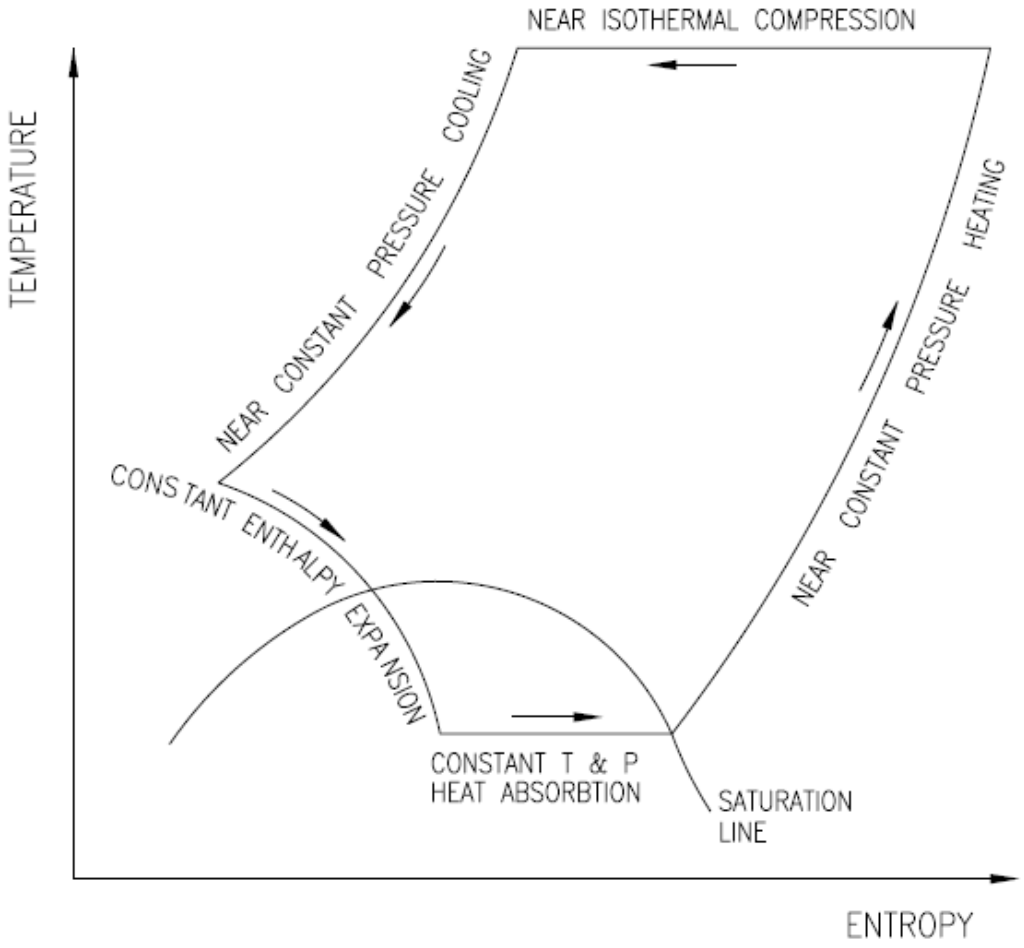

Figure 1.15: Idealised JT cycle shown on a T-S diagram [48].

The cooling rate depends on the mass flow through the orifice and the enthalpy difference between the high and low pressure sides. The full cycle is summarised below with reference to Figure 1.15 [43].

1-2: Isothermal compression

2-3: Recuperative cooling of the gas in the counter-flow heat exchanger

3-4: Isenthalpic expansion through the orifice

4-5: Isothermal heat absorption

5-1: Recuperative warming of the gas in the counter-flow heat exchanger

Two examples of this type of system were flown on the Planck spacecraft [49,50]. The first [51] used sorption pumps (see 1.4.5 below) based on metal hydrides to drive the hydrogen through a JT orifice. The metal hydrides evolved hydrogen gas when heated and absorbed it when cooled, with heat generated by the pumps being radiated to space. Cooling powers of 1 W at approximately 20 K were achieved to cool the Low Frequency Instrument (LFI) and provide the first stage cooling on the High Frequency Instrument (HFI).

The second was based on linear compressors and used ^{4}He, achieving up to 19 mW at 4.5 K [50]. This was used to pre-cool the 100 mK dilution stage on the HFI and act as a reference temperature for the LFI. An evolution of this cooler is currently being developed to operate at 2 K by reducing the pressure at the outlet of the JT orifice and making use of the lower vapour pressure of helium-3 [52].

1.4.4.4 Turbo-Brayton Coolers

Turbo-Brayton coolers achieve cooling by expansion of gas in a high speed turbine (or turbo-expander). The turbines are designed to achieve an expansion process which is as close as possible to perfectly reversible. Closed cycle operation is achieved by re-compression of the gas and passing it through a recuperative heat exchanger. The Brayton (or Joule) cycle is illustrated in Figure 1.16 (b) and can be explained with reference to the schematic in Figure 1.16 (a). The stages are as follows:

1-2: Gas is compressed

2-3: The heat of compression is rejected to a sink

3-4: The gas is further cooled by gas from the expansion stage in a counter-flow heat exchanger

4-5: Gas is expanded in the turbine

5-6: Heat is absorbed from the cold end

6-1: The cooled gas returns to the compressor through the counter-flow heat exchanger

The working fluid depends on the required operating temperature: helium is the usual choice, although other gases can be used for temperatures above 5 K.

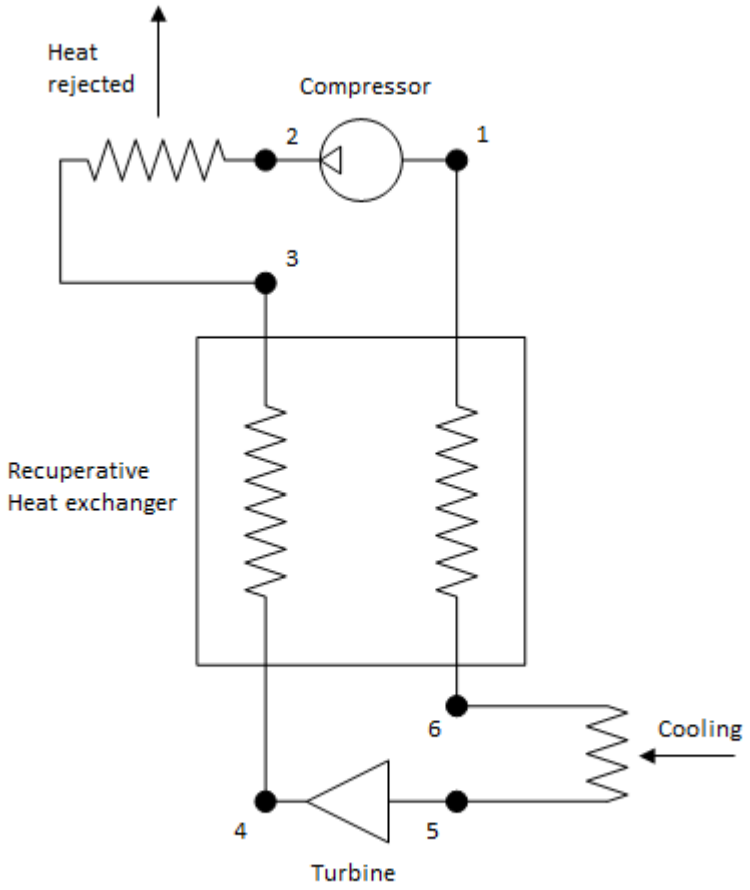

(a)

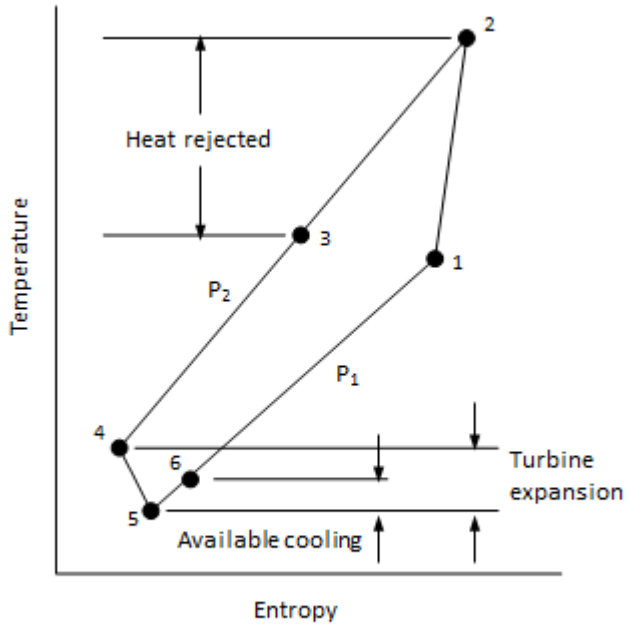

(b)

Figure 1.16: (a) Schematic of Turbo-Brayton cooler (b) T-S diagram of the cycle (after [43]).

The basic system may be extended to one of almost arbitrary complexity with multiple compression and expansion stages operating at different temperatures. They are most efficient for higher cooling powers (several W) since low powers imply smaller turbines and many of the losses associated with these devices do not scale with size [43]. Successful engineering of the turbines is crucial in these coolers; the turbines run at speeds in excess of 500 000 rpm and operate on gas bearings which require high precision manufacture. For space missions, a particular issue is protecting the turbine and bearings against launch vibrations. With such small clearances in the bearings, it is difficult to consider running the cooler during launch, but this exacerbates the problem because the gas bearings are unable to provide restraint when stationary. Notwithstanding these difficulties, Turbo-Brayton coolers can have maintenance free operating lives of between 5 and 20 years if designed and manufactured properly [43].

An example of this type of cooler, developed at NASA's GSFC, was tested on a Shuttle mission and eventually went on to revive the NICMOS instrument on the Hubble Space Telescope after its original solid-nitrogen coolant had prematurely evaporated. The cooler provided around 5 W at 65 K.

1.4.5 Sorption Coolers

Sorption coolers make use of the property of certain materials (e.g. zeolites or active charcoal) to adsorb gas at one temperature and desorb it at another. This provides pumping action, which can then be used to expand gas and achieve cooling.

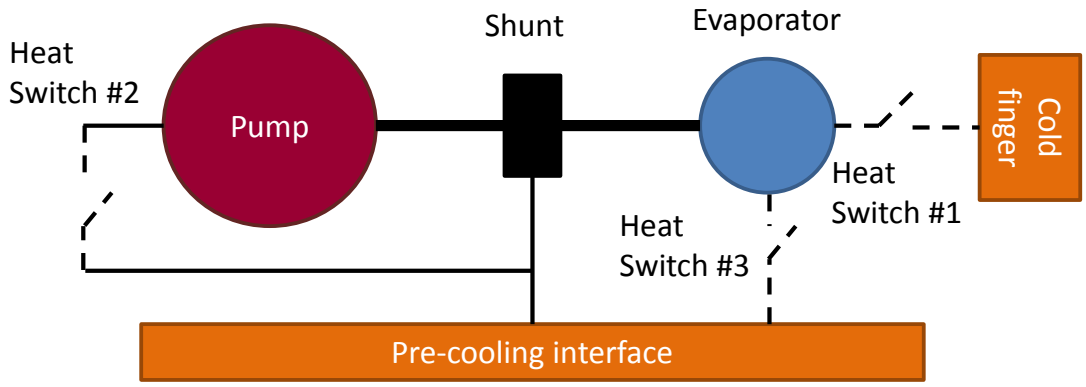

Figure 1.17: Schematic of an evaporative sorption cooler.

In the basic layout (see Figure 1.17), a sorption pump is connected to an evaporator, which is thermally linked to the object to be cooled. Both the pump and evaporator are linked to a pre-cooler through heat switches. Cooling is achieved through the following sequence:

i. The heat switches to the pre-cooling interface (#2 and #3) are closed and the cooler reaches thermal equilibrium with the pre-cooler. All the gas is adsorbed in the pump.

ii. The heat switch to the pump (#2) is opened and the pump is heated. This releases gas from the pump which condenses in the evaporator.

iii. The heat switch to the evaporator (#3) is opened and heat switches to the pump and cold finger (#1 and #2) are closed. This causes the temperature of the pump to drop and it starts to re-adsorb the gas.

iv. The vapour pressure of the gas in the evaporator reduces and the liquid begins to evaporate, providing cooling.

v. When all the liquid has been evaporated and adsorbed by the pump, the cycle re-starts.

The working fluid is usually ^{3}He, for which an operating temperature of 300 mK can be achieved with pre-cooling at 3 K. Operation can be across a broader temperature range by combining two or more sorption coolers, using different working fluids, into a multi-stage refrigerator. A two-stage version (using ^{4}He and ^{3}He) has been constructed operating

between 5 K and 260 mK [53] and, elsewhere, this concept has been extending by adding a further ^{3}He stage operating down to 234 mK [48,54].

Sorption coolers have no moving parts and therefore do not introduce vibrations as mechanical coolers inevitably will. However, the evaporative system cannot provide continuous cooling because of the need to raise the system temperature when gas is being pumped into the evaporator.

Sorption coolers have been flown on the Infrared Telescope in Space (IRTS) aboard JAXA's Space Flyer Unit (SFU) mission [55] and more recently on the Photo-conductor Array Camera and Spectrometer (PACS) and Spectral and Photometric Imaging REceiver (SPIRE) instruments on Herschel. The Herschel flight model sorption coolers achieved cooling powers of the order of 50 mW at 300 mK and demonstrated hold times of in excess of 60 hours with a 10 μW applied load [56]. The cooler could be recycled in less than 2 hours.

1.4.6 Dilution Refrigerators

The Dilution Refrigerator (DR) and the Adiabatic Demagnetisation Refrigerator (considered in 1.4.7) are the only established devices for reaching temperatures below 100 mK. The DR is based on the special properties of helium-3 and helium-4 mixtures that occur at low temperatures.

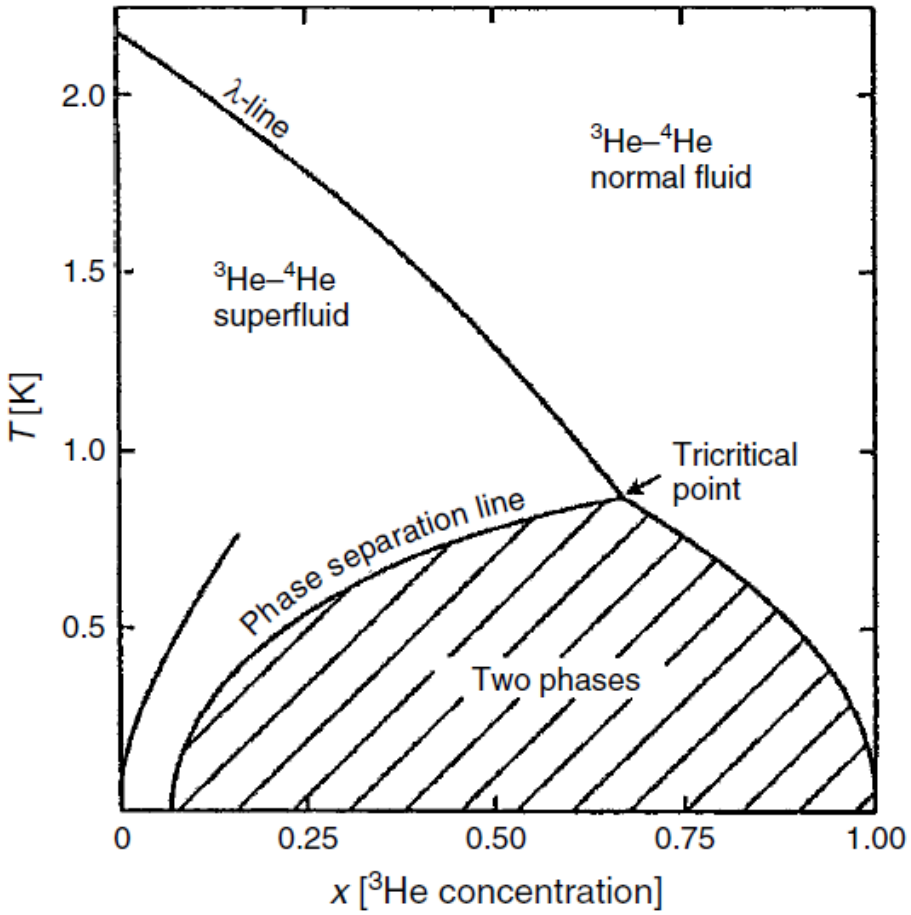

Figure 1.18: Phase diagram for ^{3}He–^{4}He mixtures at the saturated vapour pressures [57].

Figure 1.18 illustrates the phases of a ^{3}He-^{4}He mixture below 2 K. At temperatures above 0.87 K, the mixture forms a single phase with any degree of concentration, x. Below this temperature, at certain concentrations, the mixture will separate into two phases. When this happens, the ^{3}He rich phase will float on the denser ^{4}He phase with a distinct interface between them [58]. As the temperature approaches absolute zero, the ^{3}He rich phase becomes almost pure ^{3}He, while the ^{4}He rich phase remains dilute with a ^{3}He concentration of approximately 6%. It is the properties of this dilute phase which are crucial for the cooling effect.

At temperatures below 1 K, the ^{4}He behaves as a Bose-Einstein gas having effectively zero heat capacity, entropy and viscosity, and a chemical potential equal just to its binding energy [7]. It can be thought of as just a background medium to the ^{3}He. The ^{3}He itself behaves

like a degenerate Fermi gas (i.e. its pressure results almost exclusively from the Pauli Exclusion Principle[3]). These properties create a situation where the binding energy of the ^{3}He in the dilute phase is less than the concentrated ^{3}He phase; the result is an osmotic pressure which drives ^{3}He atoms across the interface between the phases [7]. The enthalpy of the dilute phase is higher than the pure ^{3}He phase, so energy is absorbed from the walls of the chamber to facilitate the process and it is from this that the cooling arises. It is analogous to evaporative cooling with the dilute phase acting as the vapour and the ^{3}He rich phase as the liquid. Even as the temperature approaches 0 K, the osmotic pressure driving the flow of ^{3}He remains greater than the ^{3}He vapour pressure and it is therefore always possible to drive ^{3}He across the boundary to sustain the dilution process.

[3]No two particles can occupy the same quantum state.

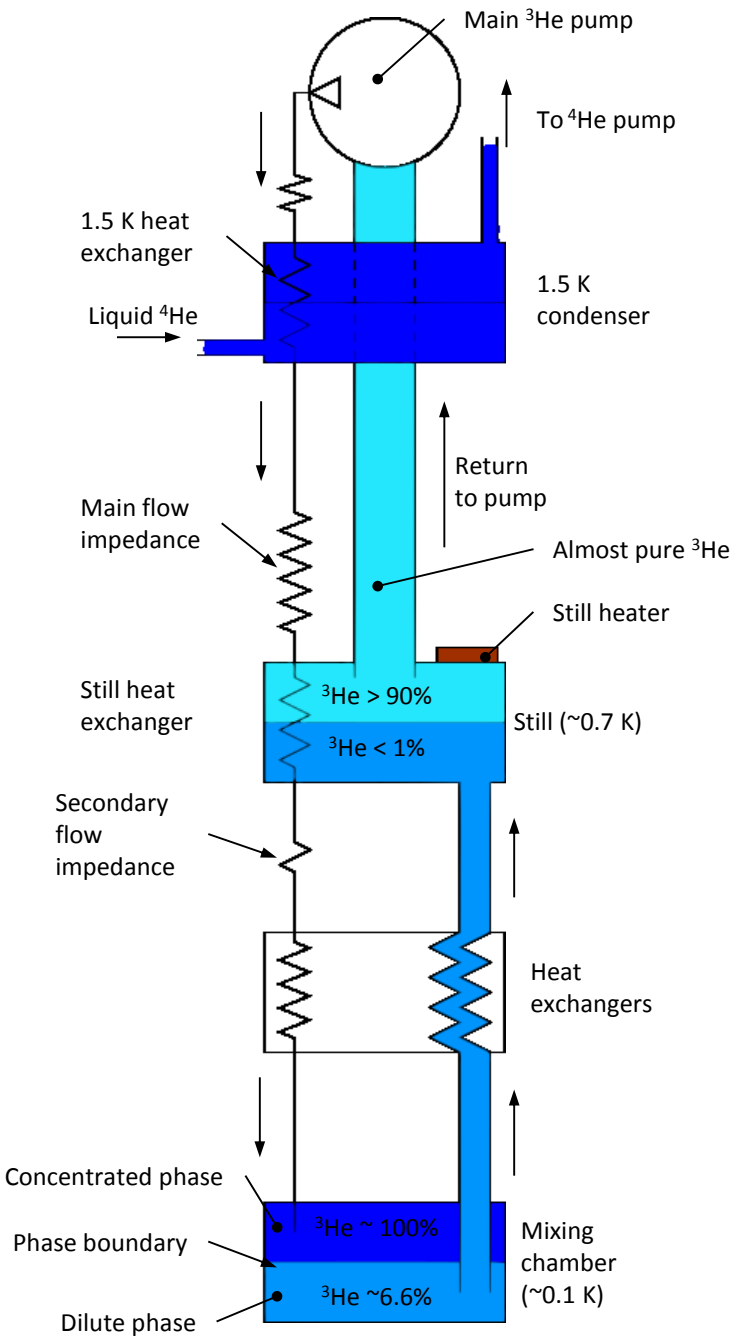

Figure 1.19: Dilution cooler schematic (adapted from [57]).

A simplified illustration of the implementation of the dilution effect is shown in Figure 1.19. Gaseous ^{3}He is supplied from a pump into a 1.5 K heat exchanger, which is cooled by pumping on a small pot of liquid ^{4}He. The condensed liquid ^{3}He then passes through an impedance which maintains sufficient pressure in the 1.5 K heat exchanger to achieve condensation. The liquid is further cooled by passing through the Still, which is maintained

at approximately 0.7 K, before entering a counter-flow heat exchanger which leads to the mixing chamber. At the mixing chamber, the ^{3}He comes into contact with ^{4}He and the dilution process occurs. The dilute phase then flows into the Still. The flow of ^{3}He is maintained by the pump and by heating the Still, where the different vapour pressures of ^{3}He and ^{4}He allow the ^{3}He to be recovered from the mixture.

A dilution refrigerator of the type described above requires the presence of gravity to separate the phases and a substantial pumping system to circulate the ^{3}He. On this basis, they would appear unsuitable for use in space. However, these problems have been largely addressed in open cycle dilution coolers [59]. In this design, dilution is achieved by mixing continuous streams of ^{4}He and ^{3}He, with the vacuum of space providing a low enough pressure to pump the ^{3}He across the phase boundary. The phases are mixed in small capillaries, where surface tension creates an alternating sequence of concentrated and dilute droplets [59]. The need for a pumped volume of ^{4}He in the condensing pot is negated by Joule-Thomson expansion of the mixture after dilution. This flows through a heat exchanger which pre-cools the incoming streams to around 1.5–1.6 K. Such a system has been flown on the Planck mission [60] for which it was able to provide 100 nW of cooling at 100 mK for 2.5 years.

The drawback of the Planck DR was that its lifetime was limited by the amount of the helium isotopes that could be stored on the spacecraft. The 2.5 year lifetime was achieved with 10560L (at STP) of ^{3}He and 31680L (STP) of ^{4}He [61]. To provide the higher cooling powers and longer lifetimes required for future missions would lead to an impractical amount of isotopes. A closed cycle system is under development [61] which is able to get around this problem by recycling the helium. Two main challenges have to be addressed in this cooler: the first is that a method to separate the isotopes in the Still must be found that does not rely on gravity; the second is that a suitable space-qualified compressor must be found to pump off the ^{3}He and return it to the mixing chamber. The first difficulty has been solved by the use of a porous material (e.g. alumina sponge) in the Still, which confines the

liquid phase through capillary action. The latter remains to be fully addressed; several candidate compressors are under consideration based on either linear, rotary (e.g. Holweck) or sorption, but at the time of writing the cooler is yet to be demonstrated with either of these. Using a standard laboratory pump, performance of 1 μW at 51 mK has been achieved with a ^{3}He flow of approximately 30 μmol/s and a ^{4}He flow of approximately 350 μmol/s [62].

1.4.7 Adiabatic Demagnetisation Refrigerators

Adiabatic Demagnetisation Refrigerators (ADRs) cool by reducing the entropy of a paramagnetic material through ordering the magnetic dipoles in a strong magnetic field. The term given to the change in entropy resulting from a change in applied magnetic field is the Magnetocaloric Effect (MCE). The physics and engineering of these coolers is the subject of the following chapter.

Along with dilution refrigerators, ADRs are the only type of cooler available for space that can reach temperatures below 100 mK. They have the advantage of being insensitive to zero-gravity and having a lifetime which is not limited by the amounts of stored coolant on the spacecraft. However, the basic ADR is unable to provide continuous cooling and creates high magnetic fields which may be detrimental to surrounding instruments if not adequately shielded.

An ADR was flown as part of the X-ray spectrometer on board JAXA's Suzaku satellite, but, unfortunately, a failure of the liquid helium Dewar vacuum space just a month after launch caused the helium to boil off and rendered the ADR inoperable. ADRs are currently in design for number of future mission including Athena+ (ESA's second L-class mission in its Cosmic Vision 2015–25 plan), SPICA (Space Infrared Telescope for Cosmology and Astrophysics) and Japan's next generation X-ray observatory, Astro-H.

1.4.8 High Temperature Magnetic Refrigeration

Although a relatively new area, concepts are being developed to extend the range of magnetic refrigeration above 10 K. This offers the potential to utilise the inherent high efficiency of magnetic cooling in high temperature stages, all the way up to temperatures compatible with the use of radiative cooling (~ 50 K). The basis of this development is twofold: first is the investigation of materials which show large magnetocaloric effect above 10 K; second is a technique known as Active Magnetic Refrigeration (AMR) [63]. AMR allows a much larger span between the operating and bath temperatures than is possible in a normal ADR.

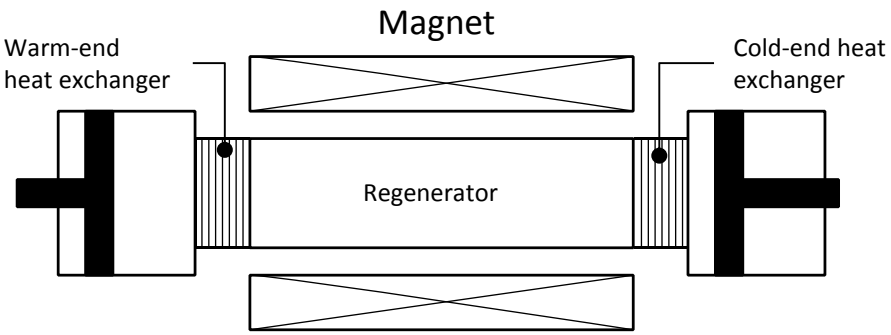

Figure 1.20: Schematic diagram of a (static) AMR (after [63]).

The architecture of an AMR cooler is shown in Figure 1.20. It is able to perform many cycles of cooling using "active regenerator" through which gas is shuttled. The process is analogous to a more traditional Stirling cycle and has the following stages [64]:

i. The regenerator is magnetised isothermally.

ii. Gas absorbs heat at the cold end and flows from the cold to the warm end cooling the regenerator as it passes through.

iii. The regenerator is demagnetised isothermally.

iv. Gas is shuttled back from the warm to cold end. It is cooled by the regenerator as it passes through, thus starting its next cycle at a lower temperature

The "cascade" process is illustrated on a temperature-entropy plot in Figure 1.21. Just like a Stirling cycle, it allows a large temperature difference to develop across the regenerator, even though the amount of entropy removed in each cycle is small. In contrast, the cooling effect comes not from expansion of the gas, but active (magnetic) cooling of the regenerator.

To allow practical versions of this type of cooler to be constructed requires materials which display a significant magnetocaloric effect over wide temperature ranges, particularly at the higher temperatures not normally associated with magnetic refrigeration. A number of rare-earth ferromagnetic compounds show promise in this respect and recent interest has been generated by the discovery of a so-called Giant Magnetocaloric Effect (GMCE) in $Gd_5(Si_2Ge_2)$ associated with a ferromagnetic phase transition at 276 K [65]. The large magnetocaloric effect of lanthanum-magnesium-oxide compounds at ~ 270 K has also been investigated [66].

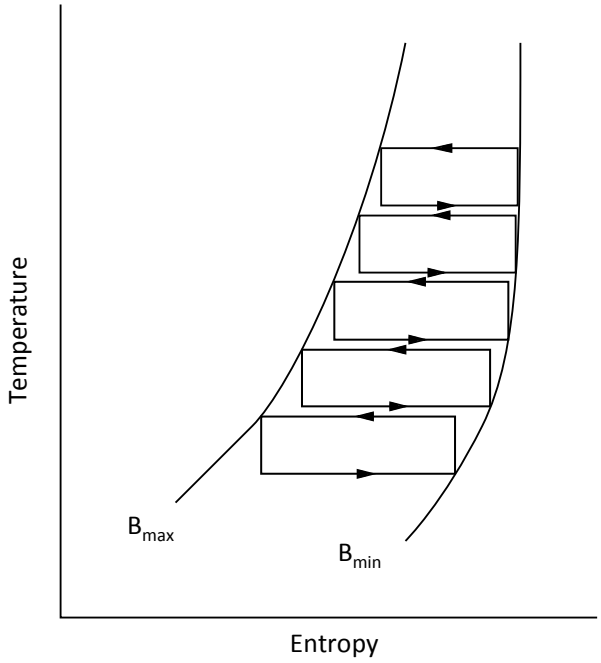

Figure 1.21: The cascade Carnot cycle of an AMR (after [63]).

1.4.9 Other Solid State Cooling Effects

Changing the applied magnetic field is not the only way that entropy can be manipulated in a solid substance; other methods of doing this include controlling the applied electric field, the

applied pressure, or the applied strain, and each has a caloric effect associated with it. While these effects are not used in space cryogenics at present, they are all active areas of research and, crucially, offer the possibility of solid state cooling without the drawback of large magnetic fields.

Since few real refrigerators based on these effects have been built to date, performance data given below are in terms of the adiabatic temperature change that can be achieved in a material upon removal of a field of a given strength. Equivalently, the isothermal entropy change may be used as an alternative. Rather than make direct measurements, it is common for these values to be calculated from measurements of the parameter that is directly influenced by the field (e.g. electrical polarisation) and compute the temperature or entropy change from the appropriate Maxwell relation.

1.4.9.1 Barocaloric and Elastocaloric Effects

The caloric effects associated with changing either the pressure or strain applied to a material are known as the barocaloric and elastocaloric effects, respectively. Although promising research has been conducting into both for refrigeration at room temperature – mainly based around shape memory alloys [67,68], which can be forced through a martensitic transition by pressure or strain – no results at cryogenic temperatures have so far been reported. One material which shows the potential for exhibiting a barocaloric effect at cryogenic temperatures is $Pr_{1-x}La_xNiO_3$ [69]. Both rhombohedral and orthombic phases exist in this material and the fraction of a sample in each phase can be controlled by the applied pressure. Calculations on the two phases suggest that entropy differences between them of > 5 J/mol K will persist below 1 K [69]. In principle, it should be possible to make use of this for sub-Kelvin cooling, but no such demonstration has so far been made.

1.4.9.2 Electrocaloric Effect

After the magnetocaloric effect, the electrocaloric effect has perhaps the most promise for the manufacture of practical solid-state refrigerators. It refers to the effect in which an applied electric field is used to increase the polarisation in a material and thereby reduce its

entropy. Subsequent adiabatic removal of the field allows the temperature to be reduced. It has been a subject of research since it was discovered in the 1930s [70], but has attracted particular attention recently with the discovery of the "Giant Electrocaloric Effect" in thin films of PZT (Lead Zirconate Titanate) [71] and ferroelectric polymers [72]. The use of thin films permits very high electric fields to be achieved with the sort of modest voltages that could be provided by a battery (~ 25 V). Adiabatic temperature changes of 12 K were reported in both the studies mentioned, but these occurred well above room temperature and are therefore not directly applicable for cryogenic cooling.

However, materials that show the electrocaloric effect at cryogenic temperatures have been found [73]. Lawless identified electrocaloric behaviour in $KTaO_3$ at 2–15 K, but the adiabatic temperature change was of the order of 100 mK for an electric field of 15.6 kV/m [74]. Hegenbarth has investigated the ferroelectric ceramics Strontium Titanate and Cadmium Titanate, with the former showing the largest adiabatic temperature changes: between 6 mK (at 78 K) and 60 mK (at 17.5 K) in a field of 800 kV/m. Kapphan and Lüty [75] and Lombardo and Pohl [76] have both studied the effect in the alkali halides. Again, the adiabatic temperature changes barely exceeded 100 mK, even in fields of ~ 10^4 kV/m.

Refrigerators based on the electrocaloric effect have only reached the earliest prototype stage. "Single-shot" systems have been constructed whereby a crystal displaying the electrocaloric effect is attached to a helium bath through a heat switch [77]. An electric field is applied with the switch closed so that heat generated during polarisation of the crystal is dumped to the bath. The switch is then opened and the electric field removed, reducing the temperature of the crystal to below that of the bath. However, cooling cannot continue after the electric field has been reduced to zero and the field must be re-applied for further refrigeration. This technique is exactly analogous to the operation of Adiabatic Demagnetisation Refrigerators (1.4.7 and Chapter 2). An obvious drawback is the small adiabatic temperature change that electrocaloric materials can provide and it has been suggested that use of them as the regenerator material in an active refrigerator (as described

in 1.4.8) could improve the temperature reduction achievable [77]. Beyond this, the recent discovery of the effect in commercial multi-layer capacitors [78] offers the potential of on-chip cooling devices, but, thus far, results have only been achieved in the room temperature range.

1.4.9.3 Multicaloric Effect

The multicaloric effect refers to the possibility that more than one caloric effect could occur simultaneously in certain materials. In other words, an applied field of one sort (e.g. magnetic) can change both the associated parameter (e.g. magnetisation) and one, or more, others (e.g. the electrical polarisation). This cross-coupling offers the potential of much larger entropy changes for a given applied field than would otherwise be possible. The thermodynamic theory has been presented by Vopson [79,80] and, based on this method, it has been suggested that some cross-coupling is already present in certain magnetocaloric materials [80,81]. For example, it has been shown that ferroelectric effects in $NdCrTiO_3$ are enhanced in magnetic fields up to 7 T [82] and by applying the theory of multiferroic materials to these data, Vopson has predicted that an adiabatic temperature change of 6.9 K could be achieved around 21 K [79], where the ferroelectric and antiferromagnetic transition temperatures of this material coincide. It is calculated that approximately 0.6 K of this temperature change would be attributable to multicaloric coupling [79]. Recently, a multicaloric effect, arising from the electro- and elastocaloric effects, has also been predicted in PZT thin films [83].

To take advantage of the multicaloric effect in a refrigerator, materials must be found which have more than one caloric effect in the vicinity of the desired operating temperature of the refrigerator. Furthermore, suitable materials would need to have low magnetic and electric hysteresis (to minimise losses during the refrigeration cycle) and good thermal conductivity. Candidate materials are likely to be found amongst those known to have large single-caloric effects and the possibility of creating composite multiferroic structures from such materials has been suggested [80].

At present, the multicaloric effect has yet to be confirmed experimentally, but as part of the expanding field of multiferroics – currently receiving much attention amongst condensed matter researchers – it is likely that there will be many further developments in the coming years.

1.4.10 Normal–Insulator–Superconductor Junctions

Using NIS junctions for refrigeration was first demonstrated in the 1990s [84] and has subsequently been developed to achieve pW cooling in the 100 mK temperature region [85,86]. They utilise the fact that a NIS junction can be controlled to selectively allow only the higher energy electrons to tunnel across the barrier by modifying the Fermi level in the normal conductor relative to the energy gap in the superconductor. The process is illustrated in Figure 1.22. The normal part of the junction is biased with a voltage (V) such that the Fermi energy (ϵ_F) is just within the superconducting energy gap (Δ). The presence of the gap means that there are no available states for the majority of electrons in the normal metal to tunnel into; only those at the top of the Fermi-Dirac distribution – with the highest energies – can traverse the insulating barrier. In this way, electrons with energies above ϵ_F are selectively removed from the metal. The charge is replenished through a superconducting contact connected to the normal side when a Cooper pair from the superconductor combines with hole from the normal metal to produce an electron. These electrons are of energy ϵ_F and so the net result is a reduction in the temperature of the electron gas within the normal metal.

NIS junction refrigerators are normally fabricated with two superconducting electrodes. One provides the refrigeration, whilst the other is used to measure the temperature, making use of the fact that tunnelling current will be a function of the temperature in the normal metal. In practice, the thermometer voltage is measured for a constant bias current.

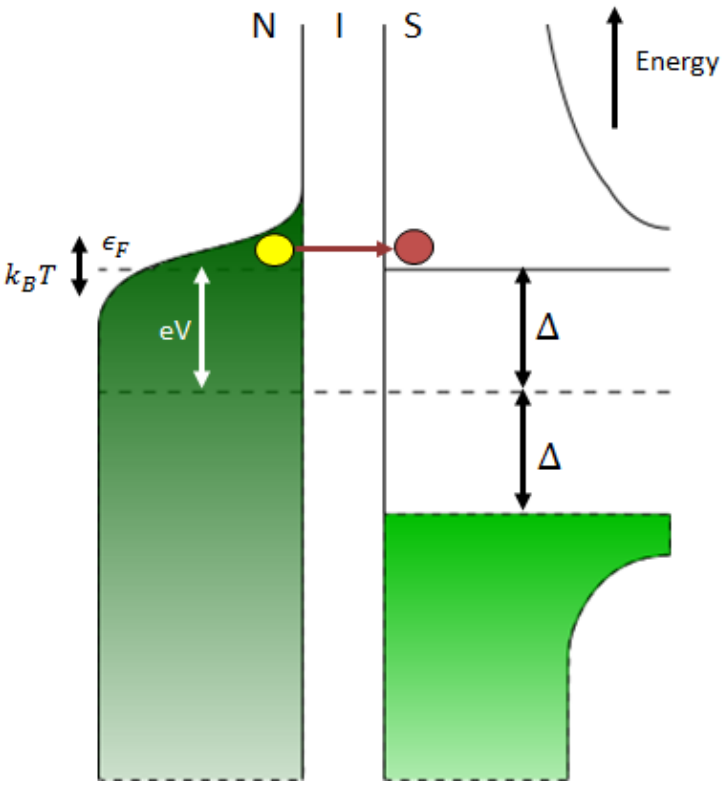

Figure 1.22: Energy level diagram for an NIS refrigerator junction showing the form of the electron energy distributions on the normal (N) and superconducting (S) sides (after [87]).

The fact that NIS junction can be fabricated on the μm scale using the same lithographic processes as micro-calorimeters offers great potential for "on-chip" cooling. NIS junctions have been coupled to TESs and a temperature reduction of 110 mK (from 300 mK to 190 mK) was achieved resulting in an energy resolution of 9.5±0.3 eV (FWHM) at 5.9 keV [88].

Much recent progress has been made on devices where a second junction is placed in series with the first to form a Superconductor–Insulator–Normal–Insulator–Superconductor (SINIS) junction [85]; one junction removes hot electrons, while the other removes hot holes. Improvements in the manufacture of this configuration to optimise electrode dimensions has resulted in a refrigerator that can cool from 260 mK to 130 mK and is predicted to absorb 10 pW at 140 mK [89]. This concept has been developed into a complete cooling platform to accept arbitrary payloads [90,91].

There is some doubt as to these devices' effectiveness below 100 mK, where electron-electron and electron-phonon interactions may be so limited that the electron energy no longer follows a Fermi-Dirac distribution. This, combined with a non-zero density of states in the gap of the superconductor, may limit the ultimate minimum temperatures achievable [92]. Nevertheless, recent work has shown that, with a 100 mK bath, temperatures of around 50 mK may be possible [93].

1.4.11 Superfluid Coolers

Some development has taken place on coolers that follow the thermodynamic cycle of conventional Stirling coolers, but use a dilute solution of ^{3}He in ^{4}He as the working fluid [94]. At temperatures below 2.2 K the ^{4}He becomes a superfluid (a Bose liquid), having zero entropy and, effectively, a vacuum for the ^{3}He atoms, which behave like a classical gas. By using microscopically porous "super-leak pistons" it is possible to pump on just the ^{3}He in the mixture, compressing and expanding it to provide cooling in much the same way as a conventional Stirling cooler. Cooling to 168 mK has been demonstrated in this way [94].

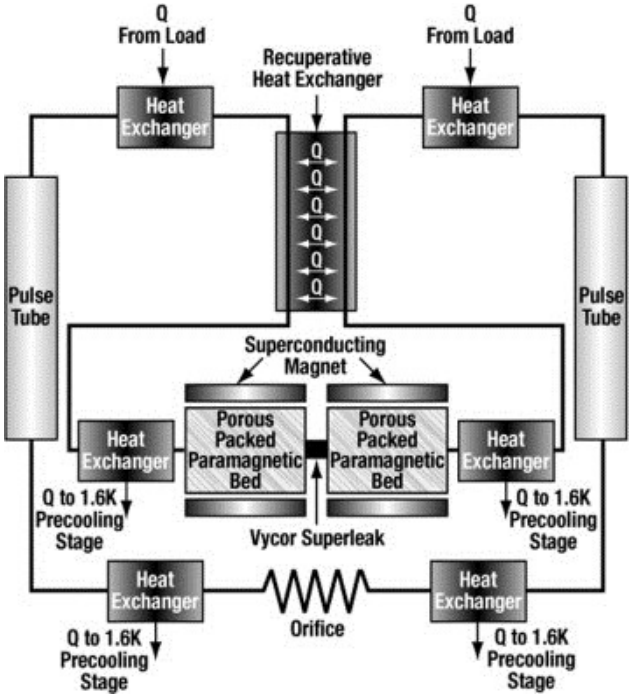

Figure 1.23: Schematic diagram of a superfluid pulse tube refrigerator [95].

However, construction of the super-leak pistons required moving bellows assemblies to contain the fluid and these were deemed sufficiently unsuitable for operation in space that further development along these lines was curtailed. Nevertheless, a recent concept aims to obviate these difficulties by using the principles above to construct a pulse tube cooler driven by a fountain effect pump (see Figure 1.23). The fountain effect pump is constructed from two canisters of paramagnetic material connected by a super-leak. Each canister is placed in a superconducting magnet. The current, and therefore magnetic field, of one magnet is increased, while it is decreased in the other. In high field, the magnetic entropy of the paramagnetic material decreases transferring heat to the surrounding fluid. This causes high pressure fluid to flow out of the canister at high field, through conventional pulse tube components: heat exchangers, a pulse tube and an orifice. Continuity is maintained by superfluid from the low temperature canister flowing through the super-leak connection. Flow is reversed by changing the fields in the magnets in opposite directions, creating the oscillating flow required for a pulse tube. In fact, the design places two pulse tubes in parallel (see Figure 1.23), so that fluid flow in one direction drives expansion on one pulse tube and compression in the other, and the two systems run 180° out of phase. This technique is used as helium itself is the only material with sufficient entropy at these temperatures to make an effective regenerator and by using two systems running out of phase, the helium from one cycle is able to act as the regenerator for the other cycle.

Although this system is yet to be built, modelling shows a predicted performance of around 40 μW at 100 mK [95].

1.5 The Need for Miniaturisation

The emerging low temperature detector technologies described at the beginning of this chapter are driving a growing desire to reduce the size, weight and power consumption of cryogenic systems described in the second part. Linder *et al* [8] identify very low

temperature coolers (< 1 K) and miniaturisation as two of the key developments for the future of space cryogenics:

"Very Low Temperature (VLT) coolers (T < 1 K) are becoming more and more important to space missions due to the use of very sensitive cryogenic detectors. A large effort is required to develop closed-loop, space-qualified coolers (such as ADR, DR, Sorption Coolers) providing sub-Kelvin temperatures and offering reliable performances and long lifetimes."

"Miniaturisation also represents an important trend, since it should allow the reduction of heat losses, power consumption and sensitivity to vibrations. New activities are aimed at verifying the possibility of using micromachining technologies to develop both active and solid-state miniature coolers."

The prevalence of micro-fabricated, solid state detectors is firmly switching the focus of attempts to reduce instrument mass on to the cooling chain. In the X-IFU instrument proposed for Athena+, the cryogenic cooling chain is estimated to be nearly 250 kg compared to 150 kg for the rest of the instrument [26]. Clearly reducing the size and mass of cryogenic systems offers the potential for significant gains in terms of accommodating more instruments and getting greater science output from missions. The research described in the following chapters is aimed at achieving this miniaturisation at the sub-Kelvin end of the cooling chain.

Chapter 2 – Adiabatic Demagnetisation Refrigerators

In this chapter, the theory and engineering of Adiabatic Demagnetisation Refrigerators are considered in detail. It begins with the theory of magnetic cooling and goes on to look at how this applies in a real paramagnetic material. Attention is then turned to the use of the effect in ADRs and the main elements of their design. Heat switch technologies are given particular consideration as this is the focus for the work presented in Chapters 4 and 5. Finally, the advantages and disadvantages of different ADR configurations are summarised.

2.1 Magnetic Cooling

Any cooling process can be thought of as a way to reduce a system's entropy and any refrigerator can be thought of as an "entropy squeezer" [6]. Since entropy cannot usually be manipulated directly, advantage must be taken of the fact that it will be a function of some other parameter of the system, in addition to the temperature. In an isolated system, reducing the entropy of one part of it must increase the entropy of another (by the second law of thermodynamics) and the system must be connected to some external reservoir to facilitate an overall entropy reduction. In cooling of a gas, for example, the external parameter is the pressure: a pressure increase (by volume reduction) will lead to an entropy reduction as long as the heat of compression is removed; subsequent adiabatic or isentropic expansion can then provide cooling to below the starting temperature. In certain solids with significant magnetic disorder, the applied magnetic field can be an equally suitable parameter with which to control the system's entropy and hence temperature.

Magnetic cooling requires a material that has a high degree of magnetic disorder in its natural state, yet is capable of becoming ordered in a magnetic field. The disorder comes from the magnetic moments within the material and it is this entropy which is reduced by an external magnetic field. Either the electronic dipoles (arising from the electron spins and

orbital motions) or the nuclear dipoles (arising from the nuclear spins) may be used. The latter is referred to as "nuclear demagnetisation" and is only effective for cooling in the temperature range of μK to a few mK [96]. Since these temperatures are not currently required for sub-Kelvin detectors, it is not considered further here.

The "adiabatic demagnetisation" discussed in this chapter is achieved using the magnetic moments of electrons occurring in atoms whose outer shell electrons are unpaired. Importantly, in the paramagnetic materials used for magnetic cooling, the interaction of these moments with each other is small compared with the thermal energy $k_B T$ and thus each dipole is free to take up a random orientation. Cooling is achieved by ordering the dipoles through the application of a magnetic field – thus reducing their entropy – extracting the heat produced, and then removing the magnetic field; this last step allows the dipoles to become disordered again and take up entropy (heat) from the surrounding material. The process is particularly applicable at low temperatures because a significant amount of entropy can persist in a paramagnet's spin system below the temperature at which disorder in the lattice has almost entirely disappeared. In this situation, the magnetic entropy is the dominant contributor to the system's overall entropy.

That such a technique could be used for cooling was independently proposed by Debye [97] and Giauque [98] in the 1920s. By the early 1930s several researchers, including Giauque, [1,3,99] had put the idea into practice, making systematic study of the temperature range below 1 K possible for the first time. The initial emphasis was purely on reaching low temperatures, determining an absolute temperature scale below 1 K [100] and on study of the paramagnetic materials being used. Since then, sub-Kelvin temperatures have gone on to be widely used – both to investigate properties of matter in this regime and to research technologies that make use of these properties.

2.2 Paramagnetism and Energy Level Splitting

Magnetic moments in atoms and ions arise from the spin and orbital motion of unpaired electrons [58]. An electron has spin angular momentum, **S**, and orbital angular momentum, **L**, which combine to form the total angular momentum $\boldsymbol{J} = \mathbf{L} + \mathbf{S}$. In many paramagnetic materials, the spin and orbital angular momentum are assumed to couple such that **S** and **L** are not individually conserved, but $\boldsymbol{J}$ is. This so-called "spin-orbit interaction" arises from relativistic considerations: in the inertial frame that moves with the electron, the nucleus orbits the electron and this motion gives rise to a magnetic field at the origin (i.e. the electron's location). This magnetic field interacts with the electron's own spin and gives rise to an additional term in the expression for the energy of the electron [101].

This type of interaction is referred to as Russell-Saunders, or L-S, coupling [58]. It assumes that the spin-orbit interaction is a weak perturbation on the electrostatic interactions that control the L and S values[4]. Using this assumption, the spin angular momentum and orbital angular momentum of unpaired electrons in an ion are coupled separately before being combined to form a resultant total angular momentum. Coupling between electron spins gives an ion a resultant spin vector **S** which takes a magnitude $(\mathrm{S}(\mathrm{S}+1))^{1/2}$ determined by the spin quantum number, S. Likewise, the orbital angular momentum of individual electrons couple to produce an orbital angular momentum vector **L** which takes a magnitude $(\mathrm{L}(\mathrm{L}+1))^{1/2}$ determined by its associated quantum number, L. These vectors then combine to give a total angular momentum vector $\boldsymbol{J}$ with an associated quantum number J, which has a magnitude defined by $(J(J+1))^{1/2}$. This vector precesses about the direction of an applied field and may only take up a finite number of orientations with respect to it. The projection of $\boldsymbol{J}$ on the direction of the applied magnetic field corresponds to a particular state or energy level [102].

[4] This may not be a good assumption in atoms with a high atomic number [101].

In a paramagnetic material the magnetic ions only interact weakly, such that their interaction energy is smaller than the average thermal energy $k_B T$. In this scenario, the dipoles, rather than naturally order as in a ferro–magnet, are free. J may take any integer (or half integer) value between $-J$ and $+J$ so that the possible orientations of the dipoles (vector $\boldsymbol{J}$) may be listed as the series $-J, -J+1, \ldots J-1, +J$ and the total number of combinations are $(2J+1)$. This gives rise to a magnetic contribution to the entropy (per mole) of

$$S_m = R \ln(2J+1). \tag{2.1}$$

The total entropy of the paramagnetic material is a combination of this, the entropy associated with the lattice, $S_{lattice}$, and the electronic entropy, S_e [96]. Hence,

$$S = S_m + S_{lattice} + S_e. \tag{2.2}$$

At low enough temperatures, the contribution from the magnetic entropy dominates over the other two. In this regime, further cooling can be produced by ordering of the dipoles. Rather than equating an increase of magnetic entropy with a decrease in thermal entropy of the lattice, the absolute temperature should be considered in its statistical aspect:

$$\frac{1}{T} = k_B \left(\frac{\delta S}{\delta U}\right)_{N,V}. \tag{2.3}$$

The reciprocal of the temperature is proportional to the derivative of the entropy with respect to internal energy at constant volume and constant number of particles. The entropy, *S*, is defined by:

$$S = \ln \sigma, \tag{2.4}$$

where there are σ accessible states of the system [14]. Hence the temperature of the system is controlled by changing the number of states accessible to it.

The process of ordering the dipoles can be described with reference to Figure 2.1. The different allowed dipole orientations (i.e. energy levels) are represented by the thin

horizontal lines and the dipole population in each level is indicated by the length of the thicker lines. From left to right, the states before application of a field, with field applied and after the field is removed are shown.

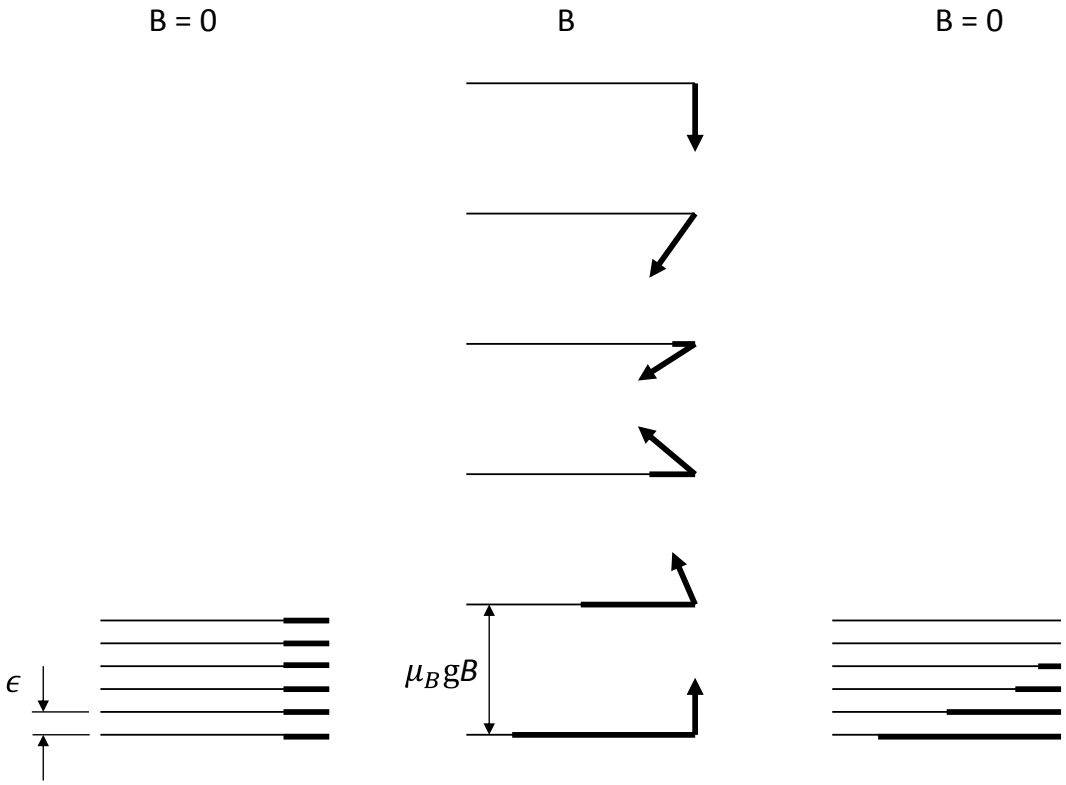

Figure 2.1: Energy level splitting in a paramagnetic material (after [103]).

In the initial state, at low temperature and with no applied field, the dipoles are essentially free to take up any orientation and there is only a small difference in the energy level of any orientation[5]. As a result, the dipoles are evenly distributed between the possible orientations. The Boltzmann factor

$$\exp\left(-\frac{\epsilon}{k_B T}\right) \tag{2.5}$$

can be used to determine the probability that a dipole will take up a certain orientation. In this case the energy is given by [101]:

[5] The small difference may arise from any internal field in the material.

$$\epsilon = \mu_B \mathrm{g} B \tag{2.6}$$

and is a function of the Landé splitting factor, g, the Bohr magneton, μ_B, and the magnetic field, B. The Landé splitting factor accounts for different relative contributions of spin and orbital angular momenta in real atoms. Its value is found from a quantum mechanical calculation of this interaction [101]:

$$\mathrm{g} = \frac{3}{2} + \frac{\mathrm{S}(\mathrm{S}+1) - \mathrm{L}(\mathrm{L}+1)}{2J(J+1)}. \tag{2.7}$$

The Bohr magneton is defined as the magnitude of the magnetic dipole moment of an orbiting electron that has an orbital angular momentum $\hbar$:

$$\mu_B = \frac{e\hbar}{2m_e}. \tag{2.8}$$

With no applied field, ϵ will be much lower than $k_B T$ and from equation (2.5) it can be seen that the probability of occupation of a given state will be high and almost equal for all energy levels.

When a field is applied only ions with higher energies can take orientations which are not aligned (or nearly aligned) to the applied field and occupation of the lower energy levels increases, with a corresponding decrease in occupation of the higher levels. This is reflected in the decrease in the Boltzmann factor for higher values of B. If the field is removed isentropically, the degree of order must be maintained; the dipoles keep their orientations with a bias towards the lower energy levels, which are now all much closer together. Since the entropy of the dipoles is equal before and after demagnetisation, the Boltzmann factors must also be equal:

$$\exp\left(-\frac{\mathrm{g}\mu_B B_1}{k_B T_i}\right) = \exp\left(-\frac{\mathrm{g}\mu_B B_0}{k_B T_f}\right), \tag{2.9}$$

where T_i and T_f are the temperatures before and after demagnetisation. The temperature after magnetisation is deduced from this to be:

$$T_f = \frac{B_0 T_i}{B_1}. \tag{2.10}$$

Equation (2.10) violates the third law of thermodynamics if the external field is reduced to zero, but this is prevented in reality by interactions between the dipoles which maintain a small internal field. The interactions may be complex, but the situation can be represented by the relationship below which includes a contribution from the internal field, b:

$$T_f = \frac{({B_0}^2 + b^2)^{1/2}}{({B_1}^2 + b^2)^{1/2}} T_i. \tag{2.11}$$

Here an "effective field" has been defined by [104]:

$$B_{eff} = \sqrt{B^2 + b^2}. \tag{2.12}$$

2.3 Magnetic Cooling in a Real Paramagnet

The ideal magnetic cooling cycle is a Carnot cycle operating between a cold object at T_f and a warm sink at T_i. It is illustrated by the dashed lines in Figure 2.2, which show the process of adiabatic demagnetisation refrigeration for a typical paramagnetic material, whose temperature-entropy curves are shown for magnetic fields of 0 T and 2 T. The paramagnetic material is often referred to as a "salt pill" in reference to the fact that paramagnetic salts

formed in pill shapes were used for the original experiments.[6]

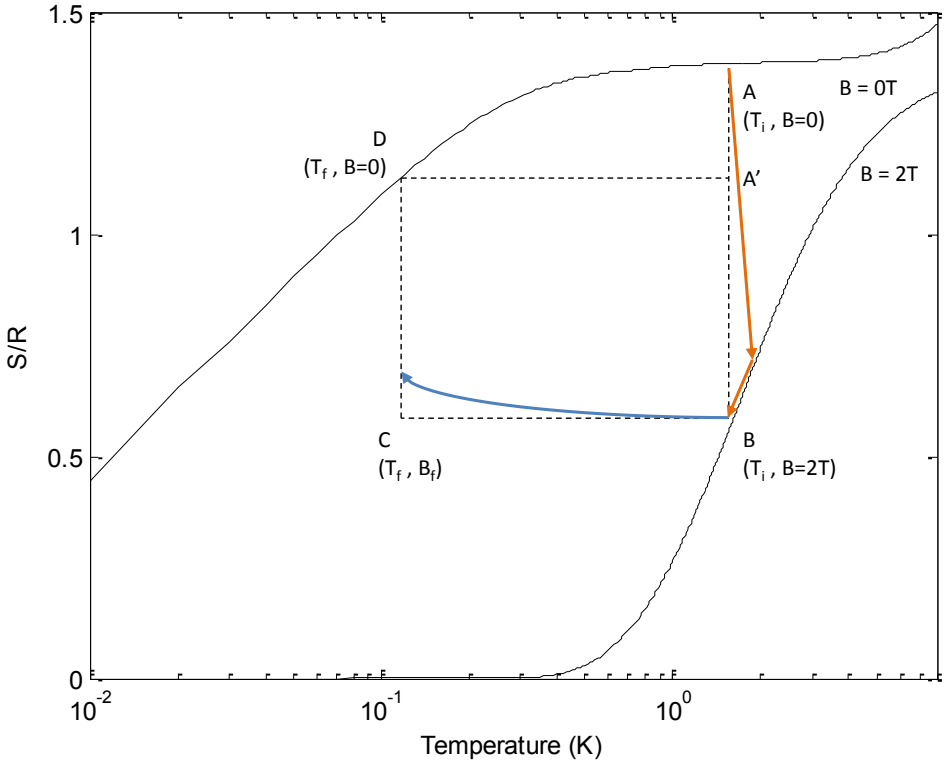

Figure 2.2: Temperature-entropy curves for a typical paramagnetic salt.
Dashed lines show an ideal cooling cycle; the arrows illustrate the real scenario with finite conductivity and parasitic heat loads.

The stages in the magnetic refrigeration cycle are as follows:

1. The salt pill is pre-cooled to a few Kelvin in zero magnetic field (this can be done with a helium bath or a mechanical cooler).

2. The salt pill is magnetised adiabatically. The heat of magnetisation is absorbed by the bath. (A–B)

3. The field is removed. The salt pill cools isentropically to the desired temperature (T_f). (B–C)

[6] The ovoid – or "pill" – shape permitted the temperature to be calculated from the magnetisation using Curie's law ($\chi \propto 1/T$) [100]; the magnetisation could be found using a set of measuring coils and, at the time, this was the preferred way to determine temperatures in this range. Although the majority of the paramagnetic materials discussed here are neither salts, nor shaped into pills, the historical terminology is retained for lack of a succinct alternative.

4. At T_f the magnetic field can be reduced at a controlled rate to balance the parasitic heat loads and maintain the desired temperature. This stage can continue until zero-field is reached; the time taken is the "hold time". (C–D)

5. The salt pill is re-magnetised causing it to warm until it reaches a sufficiently high temperature to dump heat to the bath again. (D–A')

6. The pill is fully magnetised and the cycle may be re-started. (A'–B)

The theoretical cycle will have an efficiency equal to the Carnot efficiency and its Coefficient of Performance (COP) will be [46]:

$$\mathrm{COP}_{\mathrm{ideal}} = \frac{T_f}{T_i - T_f}. \tag{2.13}$$

The thermodynamic efficiency of the real cycle can then be found by comparing the real COP with the ideal one [104]:

$$\eta = \frac{\mathrm{COP}}{\mathrm{COP}_{\mathrm{ideal}}}. \tag{2.14}$$

Differences between the real and theoretical cycles arise from two sources. Firstly, the magnetisation (A–B) is not truly adiabatic due to finite conductivity of the link between the pill and the bath (illustrated by the orange arrows in Figure 2.2). As a consequence, time must be allowed after magnetisation for the pill to come into thermal equilibrium with the bath. Of course, the link can never be perfect and demagnetisation will begin at some small increment above the bath temperature. This will limit the entropy capacity of the cycle. Secondly, demagnetisation (B–C) will not be perfectly isentropic due to parasitic heat loads, the effect of which is shown by the blue arrow in Figure 2.2. Additionally, there will be entropy losses from: extra heat capacities attached to the pill (e.g. detectors); eddy current dissipation in metallic structures in the pill; and temperature gradients within the salt pill [105].

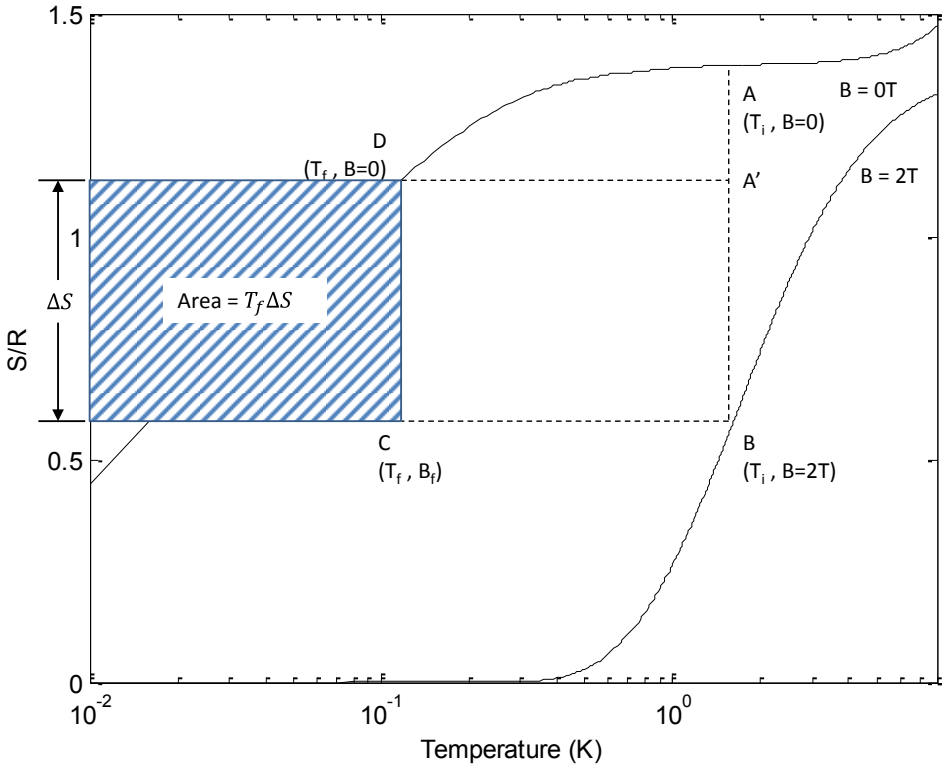

Figure 2.3: Energy absorbed in adiabatic demagnetization of typical paramagnetic salt.

The energy absorbed during the ADR's hold-time depends on the hold temperature and the entropy change, and is given by:

$$Q = \int T dS. \tag{2.15}$$

Figure 2.3 illustrates this graphically for an ideal demagnetisation.

One of the main attractions of magnetic cooling, and something that helps it to achieve high efficiencies, is that the change in temperature of the salt pill is reversible. Therefore, temperature control does not need to be a dissipative process, as it usually is for other cooling technologies, where a heater is used to balance whatever excess cooling power is provided by the refrigerator. Temperature stability at the micro-Kelvin level, or better [105], can be achieved using temperature as the input to a feedback loop for which either magnet current or voltage is the output. In the latter case, a set voltage produces a current ramp rate proportional to the magnet's inductance. Using voltage has the advantage that it is a more

slowly varying function of time when holding a fixed heat load at constant temperature [105,106].

2.4 ADR Design

Adiabatic Demagnetisation Refrigerators are the practical embodiment of the theory described in the preceding sections. Any ADR design is comprised of three functional elements: the paramagnetic material (or "salt pill"), the magnet and the heat switch. These are described in more detail in the following sections.

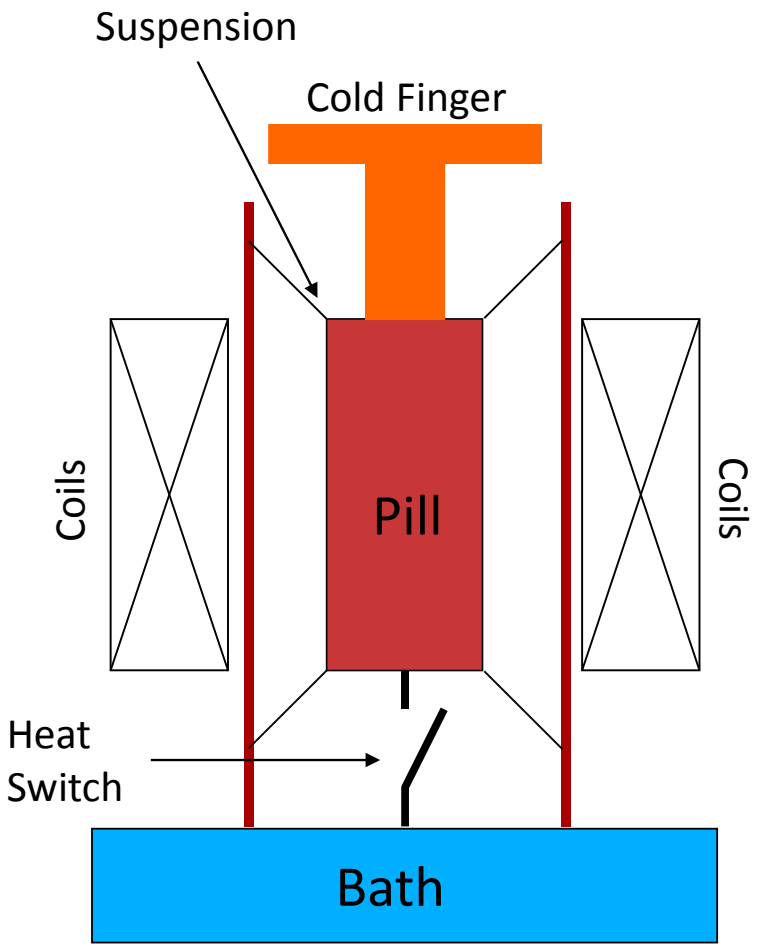

Figure 2.4: Basic ADR schematic.

Figure 2.4 shows the arrangement of these elements in an ADR with the pill thermally linked to a cold stage (the "cold finger") which would support the detectors, or other items to be cooled. The thicker black lines indicate the heat switch, linking the pill to the bath, and the pill is shown supported by thin wires made from a material with low thermal conductivity (Kevlar® is usually used) to minimise parasitic heat loads.

2.4.1 Salt Pills

The salt pill is constructed from a material which contains paramagnetic ions exhibiting dipole interactions of the type discussed in section 2.2, arising from unpaired electrons in the outer shells. Suitable paramagnetic ions have been found in the rare earth elements (e.g. Cerium, Gadolinium, Neodymium and Dysprosium) where the 4f shell is incomplete and the transition elements (e.g. Chrome, Manganese, Cobalt and Nickel) where the 3d shell is incomplete. These are mixed with atoms of other elements, which act to reduce the magnetic interactions through the addition of non-magnetic ions and – in the case of hydrated salts, where crystals form in an aqueous solution – water. Although salts were the traditional mixing substance, both garnets (O_{12} compounds) and perovskites (AlO_3 compounds) are now also used [96].

For hydrated salts, where the ions are separated sufficiently to ignore interactions, the free-ion approximation can be applied and the entropy will be given by (see Appendix A):

$$S = R\left\{x\coth(x) - (2J+1)x\ \coth[(2J+1)x] + \ln\left[\frac{\sinh[(2J+1)x]}{\sinh(x)}\right]\right\}, \quad (2.16)$$

where

$$x = \frac{g\mu_B B}{2k_B T}. \quad (2.17)$$

To achieve high cooling powers for minimum mass of refrigerant, the paramagnetic salt should have a large magnetocaloric effect in the relevant temperature range. This happens when [104]:

i. The total angular momentum number, J, and the Landé splitting factor, g, are large.

ii. The refrigerant's ordering temperature is close enough to the operating range for it to exhibit a large $\partial M/\partial T$, but far enough away that spontaneous ordering will not take place.

All paramagnetic materials have a temperature at which a spontaneous ordering of the dipoles into the ferro- or anti-ferromagnetic state occurs. If the transition is of the first type, it is called the Curie temperature; in transitions of the second type, it is referred to as the Néel temperature [104]. Below this temperature, the dipoles are not free to take up different orientations; their spin system enters its lowest entropy state and they are no longer useful as refrigerants. In the vicinity of the ordering temperature $(\partial M/\partial T)_B$ will be large and the magnetocaloric effect will therefore also be large.

While the free-ion approximation shown above provides a good basis for calculating the entropies of several paramagnetic materials, it is important to note that it is an incomplete description of the temperature–entropy relationship in these substances. Its use implies that the zero-field entropy is entirely independent of temperature (see equation (2.1)); something that does not allow for any interaction effects. These will result in splitting of the energy levels even at zero-field (see Figure 2.1) and may take several forms. Firstly, however well separated the electronic dipoles are, there must be some interaction between them. Secondly, there will be some interaction between the electronic dipoles and the crystal lattice. This is a result of the fact that charge distribution in surrounding ions causes certain electron states to be associated with higher energies than others, even with no external field. Thirdly, the electronic dipoles can interact, albeit weakly, with the nuclear dipoles; because these dipole moments are so weak, the resulting energy level splitting is extremely small and is referred to as "hyperfine structure" [101].

It is possible to incorporate the above effects into entropy calculations; the exact form of the expressions depend on whether the energy level splitting is $> g\mu_B B$ (the weak-field case), or $\ll g\mu_B B$ (the strong-field case) [102]. A simple way to account for interaction effects is to introduce an external field (as described in 2.2) and Hagmann *et al.* [107] suggest this can be expressed in terms of an internal temperature, T_{int}, below which the interactions between the dipoles become significant enough to cause ordering:

$$b = kT_{int}/2Jg\mu_B. \tag{2.18}$$

This can then be combined with the applied field using equation (2.12) and the result used in equation (2.16).

In addition to the ordering temperature, a second important property of a paramagnetic salt is its specific heat, which is effectively a measure of the energy level splitting. This is reflected in the Landé splitting factor (see equation (2.7)). It governs the entropy change for a given applied field and hence the temperature that can be obtained upon demagnetisation. Equally importantly, it reflects the temperature rise from a given heat leak and consequently the "hold time" of the pill. To some extent, the properties of a paramagnetic material can be tuned by dilution [6] so as to increase the distance between the magnetic ions. This has the effect of decreasing the magnetic interaction and therefore the splitting of the energy levels. The result is a reduction in the temperature that can be achieved upon demagnetisation, but this comes with a reduction in the specific heat capacity as the density of the dipoles is less.

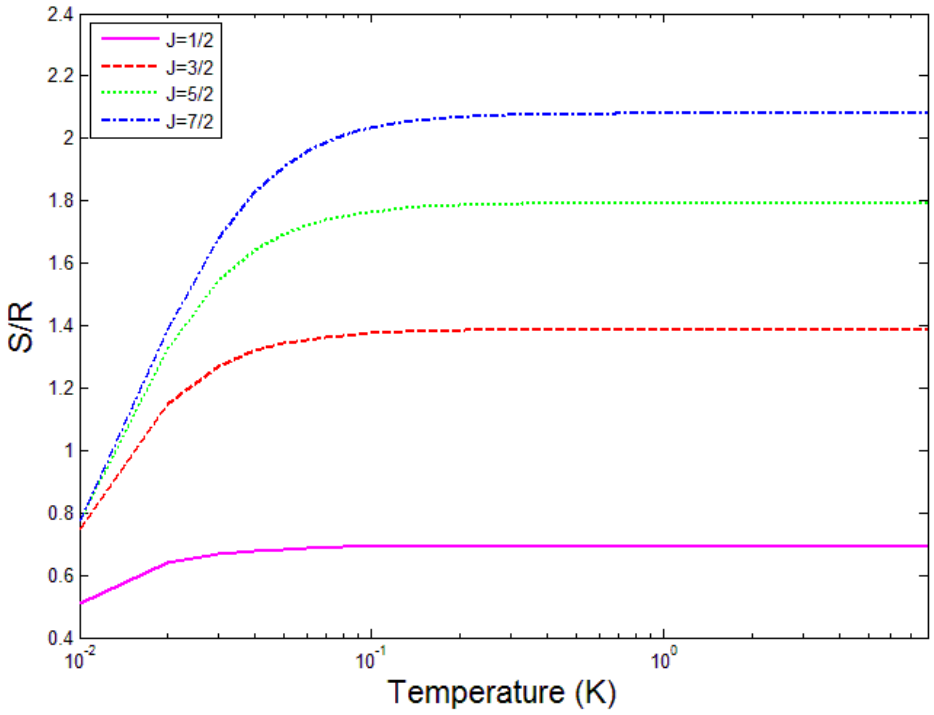

Figure 2.5: Effect of different J values on the zero-field entropy of a paramagnetic material

A larger J value increases the entropy of the paramagnetic material at zero-field and hence offers greater potential for entropy reduction upon application of a field. This is illustrated in Figure 2.5, which is a plot of equation (2.16) for different values of J. The lines are calculated by using a low value for the magnetic field to approximate the internal field.

Real entropy data as a function of temperature for a paramagnetic material may be obtained either by measurements of the specific heat, or the magnetisation. If it is the former, the entropy can be found from equation (2.19) [104], readily derived from the definition of specific heat at constant magnetic field.

$$S = \int_0^T \left(\frac{C}{T}\right)_B dT \qquad (2.19)$$

If it is the magnetisation that is measured (which can be done accurately using SQUIIDs), the following equation is used [104].

$$\Delta S = \int_0^B \left(\frac{\partial M}{\partial T}\right)_{B'} dB' \tag{2.20}$$

Magnetisation of the salt is performed at two temperatures. Providing these are sufficiently close, equation (2.20) can be re-written as:

$$\Delta S = \frac{1}{T_1 - T_2} \int_0^B (M(T_1) - M(T_2)) dB'. \tag{2.21}$$

The entropy change is then found from the area between two magnetisation curves. Since this is only an entropy *change*, some specific heat data is needed to find absolute values. It should be noted that these methods will only give the total entropy data; it is not possible to split out contributions from the lattice and the spin system.

The parameters of some commonly used salts are shown in Table 2.1 [108]. It can be seen that in general the Alums (e.g. CPA, CCA) are better suited to low temperature stages with their lower ordering temperatures, whilst the Garnets (e.g. GGG, DGG) will be the preferred option for higher temperature stages due to their larger J values. In addition to the information in Table 2.1, practical considerations must also be borne in mind. For example, FAA may appear the ideal choice for a low temperature pill because of its high J value and low ordering temperature. However, it is corrosive to copper and this makes construction of the thermal bus difficult and expensive, since gold wires must usually be used.

Salt	Chemical Composition	J	g	To (mK)	n	M (g/mol)	ρ (g/cm^3)	Data T_{min} (mK)
CMN (Cerium Magnesium Nitrate)	$Ce_2Mg_3(NO_3)_{12}\ 24H_2O$	1/2	2	1.5	2	1529.6	2.1	0.6
CPA (Chromic Potassium Alum)	$CrK(SO_4)_2\ 12H_2O$	3/2	2	9	1	499.4	1.83	17
CCA (Chromic Caesium Alum)	$CrCs(SO_4)_2\ 12H_2O$	3/2	2	10	1	593.2	2.06	50
FAA (Ferric Ammonium Alum)	$Fe(SO_4)_2NH_4\ 12H_2O$	5/2	2	26	1	482.2	1.71	22
MAS (Manganese Ammonium Sulphate)	$Mn(SO_4)_2(NH_4)_2\ 6H_2O$	5/2		170	1	391.2	1.81	95
DGG (Dysprosium Gallium Garnet)	$Dy_3Ga_5O_{12}$	15/2[7]	8	373	3	1028.1	7.3	37
GGG (Gadolinium Gallium Garnet)	$Gd_3Ga_5O_{12}$	7/2	2	380[8]	3	1012.3	7.08	200

[7] Below 1 K, the spin of DGG is better approximated by J=1/2

[8] In a 1 T magnetic field. In the absence of magnetic field, no long range order has been observed down to 25 mK [104].

Salt	Chemical Composition	J	g	To (mK)	n	M (g/mol)	ρ (g/cm^3)	Data T_{min} (mK)
GLF (Gadolinium Lithium Fluorine)	$GdLiF_4$	7/2	2	480	1	240.2	5.34	500
ErOA (Erbium Aluminate Perovskite)	$ErAlO_3$	1/2	9	~600	-	-	-	-
YbOA (Ytterbium Aluminate Perovskite)	$YbAlO_3$	1/2	7	~800	-	-	-	-
DOA (Dysprosium Aluminate Perovskite)	$DyAlO_3$	1/2	14	~3500	-	-	-	-
GOA (Gadolinium Aluminate Perovskite)	$GdAlO_3$	7/2	2	~3800	-	-	-	-

Table 2.1: Physical properties of some common paramagnetic refrigerant (data combined from [96] and [108]).
T_o is the magnetic ordering temperature, n is the number of moles of the ion per moles of the salt, M is the molar mass ρ is the density and T_{min} is the lowest temperature at which the data were taken. Other symbols are as defined above. Dashes indicate no data available.

The salt pill may be constructed in a number of ways [6]:

i. Grown as a single crystal;

ii. By compressing powder into a solid rod;

iii. By packing loose powder in a glass, plastic or metal container to which oil or helium is added to increase the heat transfer;

iv. Forming a solid cylinder by mixing the salt with epoxy resin.

Which method is chosen depends on the properties of the salt. Garnets and Perovskites are large dense crystals and these can be bonded to the thermal bus using an epoxy. Hydrated salts (Alums) are formed in an aqueous solution by slow evaporation of the water and can either be grown directly onto the thermal bus, or grown in a vessel and then compressed with the wires before sealing the container. In the particular case of CMN, for which the crystal orientation relative the magnetic field is important [109], a further requirement is starting the growth process by cementing a seed crystal in position with the correct orientation.

In addition to the method of construction, a number of other factors should be taken into account in salt pill design. For the hydrated salts, such as the Alums, it is important to prevent water loss, which occurs naturally at room temperature and is accentuated in a vacuum. Ideally the salt will be enclosed in a hermetic container which is closed with a weld. Thin-walled stainless steel tubes are regularly used, but care must be taken not to introduce a large mass of this material because a Schottky anomaly causes its heat capacity to rise below 0.1 K [110] and this additional heat capacity will hinder the cooling effect of the salt.

If conductive materials are used in the pill's construction, it is important to minimise eddy currents. Eddy currents will be induced during magnet ramping when loops of conducting material are present in the field. Ideally, insulating materials (e.g. G-10) will be used to contain the salt, but it can be difficult to eliminate all the conductive material from a pill design; where it is used, it is vital to avoid complete loops. For example, a small lengthwise

cut in a solid rod will reduce eddy current dissipation by more than a factor of two and a similar cut in a cylindrical tube will be even more effective [111]. Making cuts all the way down a tube or rod may not be practical, but the design can be such that any unbroken conducting loops are kept outside the highest fields.

In the low temperature stages for which the Alums are typically used, boundary resistance between the salt and the thermal bus is a key consideration. This necessitates a large area of contact between the pill and the thermal bus, which is achieved by constructing the thermal bus either from large bundles of wires (see Figure 2.6) or by wire-cutting a solid billet of copper (see Figure 2.7). The wires should be spaced so that the distance between them is less than the typical salt crystal size to minimise phonon scattering at grain boundaries. Reducing boundary resistance is also important to reduce the time lag between a change in magnetic field and a change in temperature; this both helps reduce recycling time and permits better temperature control during operation.

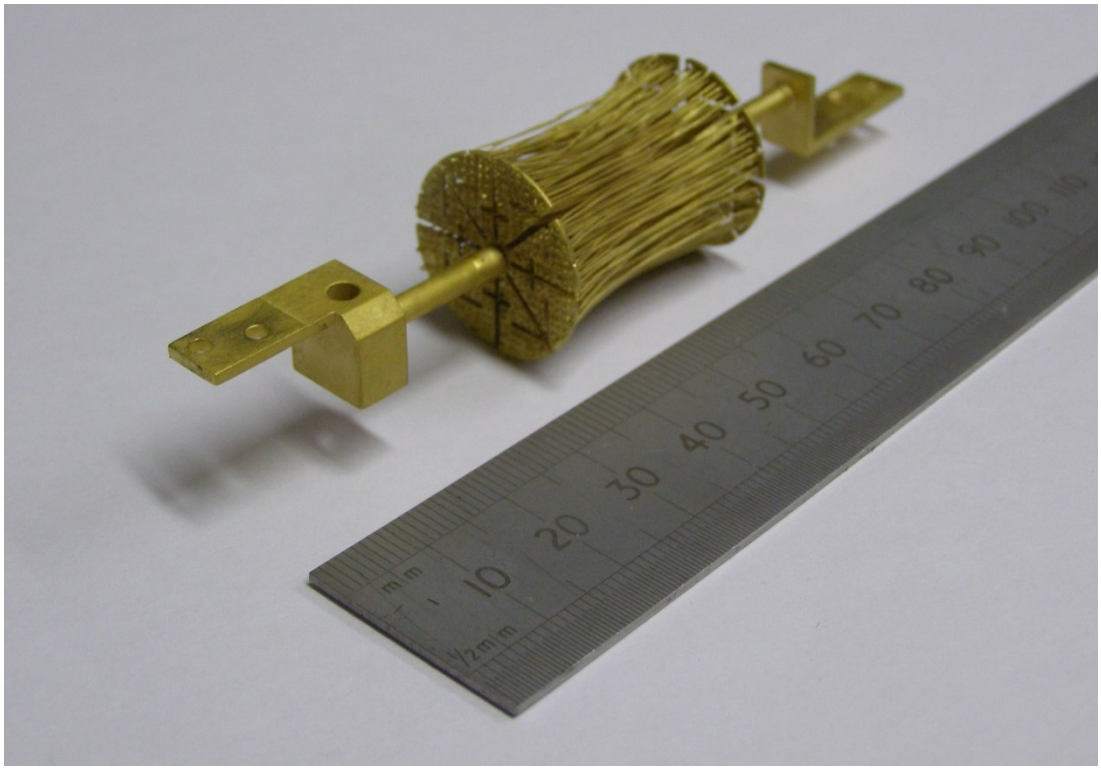

Figure 2.6: MSSL thermal bus for a CPA pill.
The construction method is to thread ~250 0.25 mm diameter copper wires through 0.5 mm thick end plates. Gold plating is applied as a final process. [112]

Figure 2.7: Example of a thermal bus for a low temperature salt pill manufactured using wire electron discharge machining [111].

The interaction of the wire and boundary thermal resistances can be used to optimise pill design [111]. The wire resistance goes as T^{-1}, while the boundary resistance goes as T^{-3}. Consequently, while a large number of small diameter wires may be necessary at low temperatures where the boundary resistance dominates, a small number larger diameter wires is preferable at higher temperature. This is because the heat of magnetisation should be conducted away as quickly as possible to minimise the recycling time and this can only be done with a cross-sectional area that would require a prohibitive number of small diameter wires. Furthermore, the boundary resistance at magnetisation temperatures is usually smaller than the wire thermal resistance. On this basis, two different wire diameters may be used in the thermal bus. Such a construction has the additional advantage that the support structure and heat switch (through which the majority of heat load normally enters the pill) can be coupled to the high temperature bus, whose small contact area with the pill

provides a higher resistance at low temperature. This part of the bus is then separated from the low temperature part, thus minimising the heat load on the cold stage.

For pills designed for higher temperature operation, the boundary resistance should no longer be as critical and compression or bonded joints to the thermal bus can be used. These also work well with the fabrication of the pill itself, which is usually either grown as a single crystal, or compressed into pill form from powder.

The final salt pill assembly must be robust and have excellent long term stability [111] – especially for space applications. It should avoid: mismatches between the coefficients of thermal expansion of materials used that could lead to thermal cycling failure; unsaturated solution in voids that may freeze and dislodge the salt from the bus; and seal breaches which could dehydrate the salt in vacuum.

2.4.2 Heat Switches

The heat switch in an ADR performs the role of allowing heat to flow to the bath during magnetisation and of isolating the salt pill during demagnetisation. In the former case, a high thermal conductance is desired to keep the magnetisation process as isothermal as possible. In the latter case, the switch must have a low thermal conductance to prevent parasitic heat leaks as the pill cools. The ratio of the two values is known as the *switching ratio* and as high a value as possible is desired.

In addition to the switching ratio, there are a number of other factors that influence the choice of heat switch and the details of its design: size, mass, speed with which the switch can be opened and closed, structural integrity and reliability of actuation. The latter two are particularly relevant for ADRs to be used in space. Depending on the switch type, consideration may also have to be given to parasitic heat loads arising from the switch support structure and wiring. It is useful, too, if the switch is highly conducting at high temperatures, so that the entire ADR may be rapidly pre-cooled to the bath temperature.

A number of methods have been employed to achieve the high switching ratios required to make an ADR effective and these are reviewed briefly in the following sections.

2.4.2.1 Mechanical Heat Switches

In a mechanical heat switch, an actuator (typically electro-magnetic) is used to open and close contacts on a thermal link. An example of this type of switch is shown in Figure 2.8. When closed, it exerts sufficient pressure on the joint to ensure good thermal conductance; when open, assuming a good vacuum, only radiative heat transfer is possible.

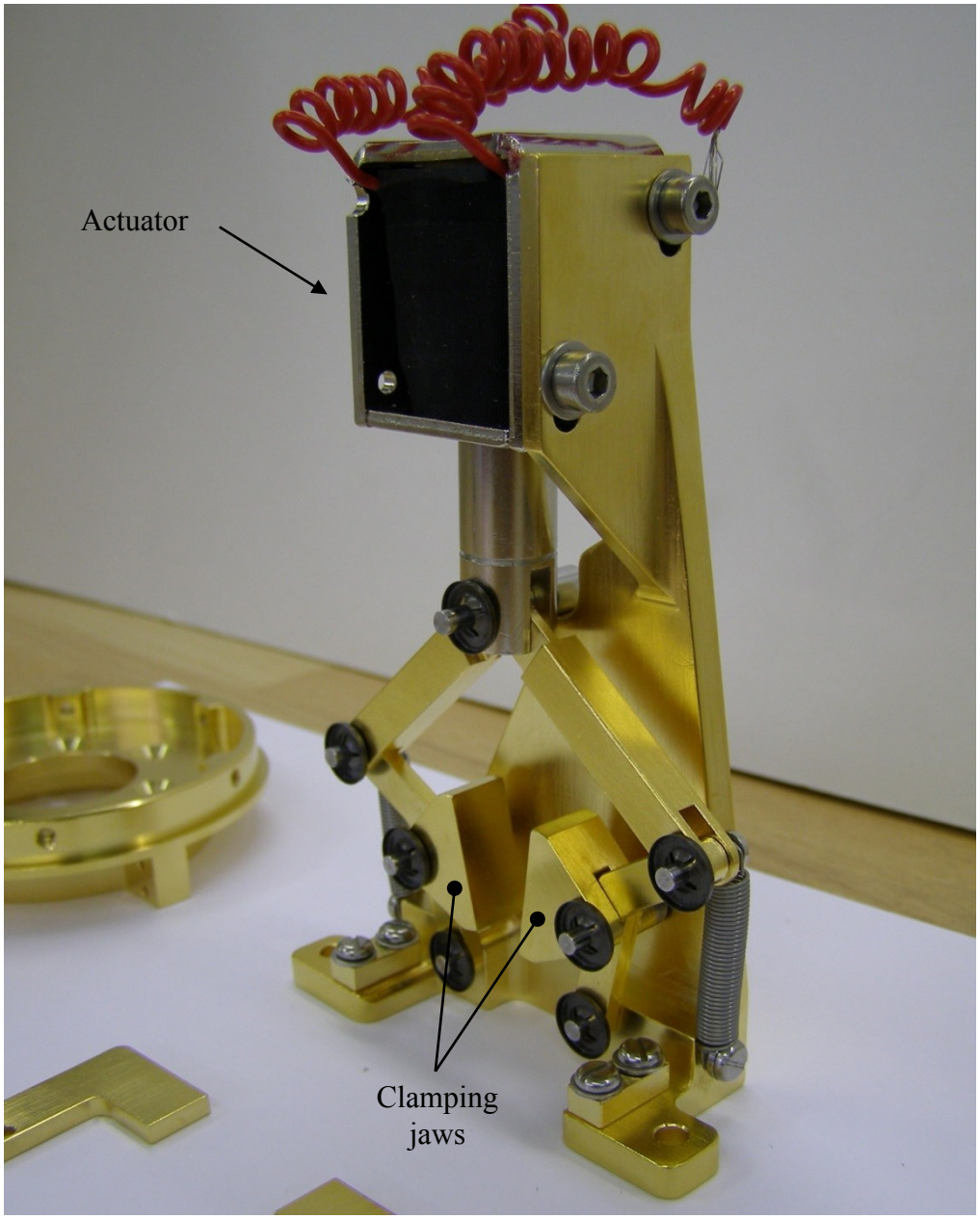

Figure 2.8: Electromagnetically actuated mechanical heat switch developed at MSSL (courtesy of Dr J. Bartlett).

Particular care must be taken with certain aspects to ensure a successful design. Contact resistance is a key consideration in achieving good thermal conductivity, especially at temperatures below 1 K. A soft material, such as indium, that will flow to match surface imperfections may be used in the switch jaws to improve contact area, although it is vital not to cool the indium below its superconducting transition (see section 2.4.2.3). Various

combinations of materials for the contact have been studied [113] with results suggesting that it is difficult to improve on a simple copper-copper interface.

Below 1 K, the breaking of the contact can generate a heat load [6,113] and this must not overwhelm the system. Some of this heat is associated with reducing the load on the contact and some with actually breaking the contact. To control the impact of the former, the load should be reduced gradually to allow any heat generated to be conducted away. Of course, this may be to the detriment of switching time. Minimising the latter is more difficult, but research suggests providing paths for heat generated by the moving parts of the switch to be conducted away will help, as will ensuring very good alignment of the contact surfaces [113].

If the above factors are properly addressed, mechanical switches can have high switching ratios. However, due to the number of moving parts, they come with the disadvantages of being bulky and mechanically complex. As such, they are generally considered too unreliable for space coolers. A recent attempt has been made to develop a mechanical switch by using a piezoelectric actuator, which could be qualified for space [114]. The design is quite simple: two high-purity copper blocks are separated by G-10 columns and Vespel® insulators, below one of which is a piezoelectric positioner capable of providing 8 N of force (see Figure 2.9). When a voltage is applied to the piezoelectric positioner it closes the gap between the contacts. In this case, the problem of contact resistance was handled by polishing the contact surfaces and coating with ~1 μm of gold which provided the necessary compliance. Initial tests showed a switching ratio between 100 (at 4 K) and 200 (at 10 K).

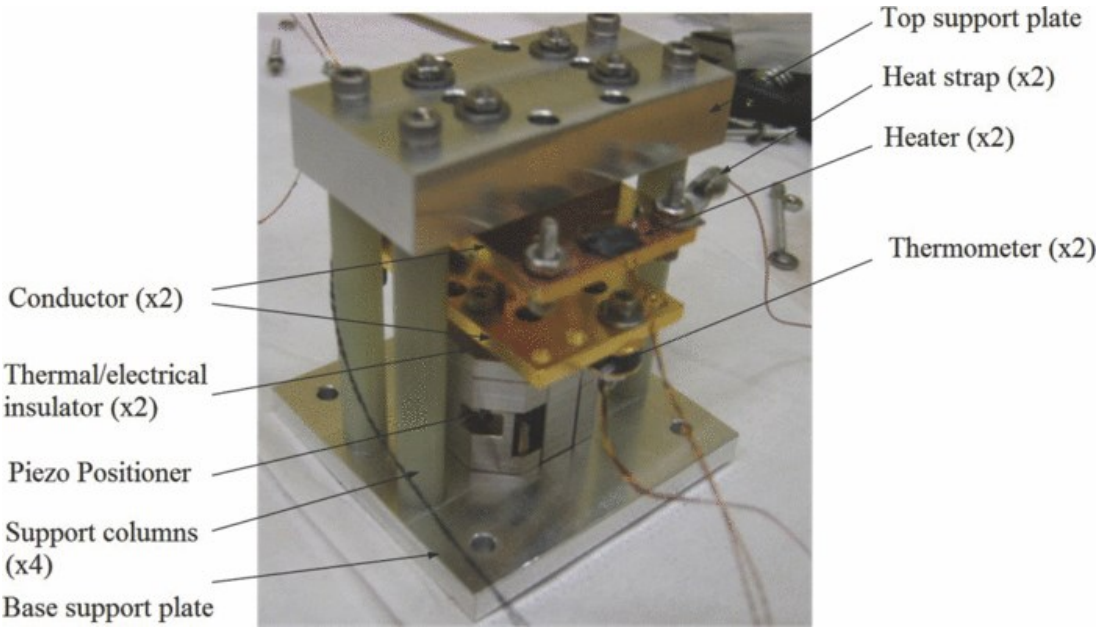

Figure 2.9: Piezoelectric heat switch prototype [114].

2.4.2.2 Gas-Gap Heat Switches

The use of exchange gas is one of the oldest and simplest techniques for transferring heat between different parts of cryogenic apparatus. A gas pressure of as little as 0.1 mbar can be sufficient for good heat transfer [115]. This principle is used in gas-gap heat switches. They operate by altering the gas pressure between two sets of heat exchanger plates. The thermal conductance of the gas will be comparatively low compared to conductance down the plates and the area-to-gap ratio must be high to overcome this. The gas pressure in the gap is controlled by the use of a "getter" made from a porous material such as charcoal. When the temperature of the getter is close to the condensation temperature of the gas, it is absorbed; conversely, the gas can be desorbed by raising the getter's temperature. Where single atomic layer films are formed on the getter surface, the vapour pressure has a very strong temperature dependence. At the temperatures appropriate to most ADRs (i.e. < 10 K), the gas used is usually either ^{3}He or ^{4}He, but ^{3}He is favoured due to higher conductance below 10K [116]. If using ^{4}He, it must be sufficiently well pumped that superfluid films cannot form as these would add a significant contribution to the heat transfer. H_2 may be used for temperatures above 5K.

A typical design of a gas-gap heat switch is shown in Figure 2.10.

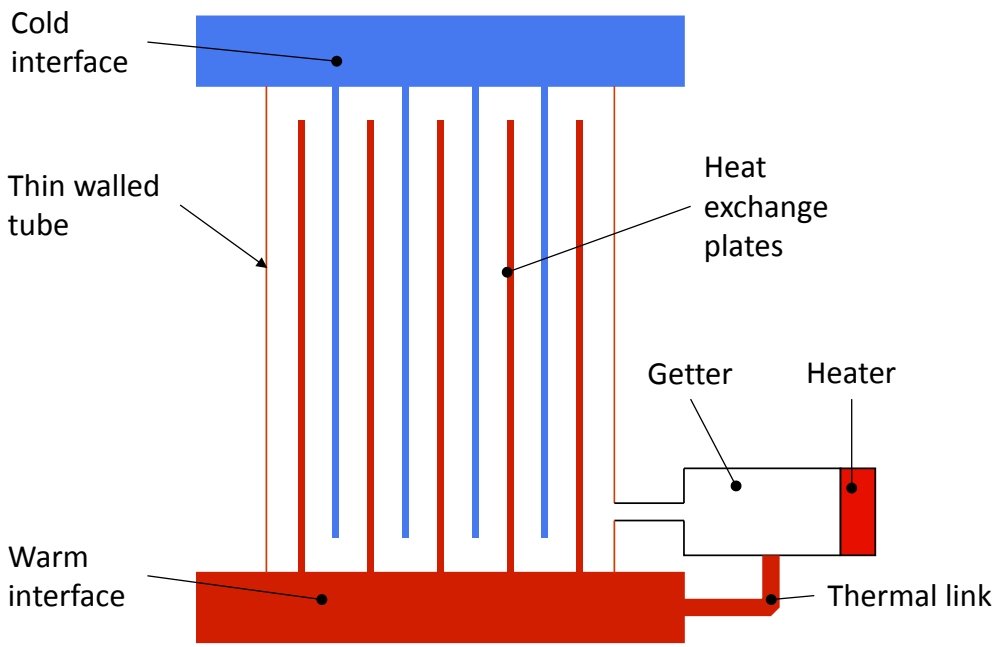

Figure 2.10: Schematic of a gas-gap heat switch.

The gas conduction can fall into either the laminar, molecular or transition regime [117]. In the laminar regime the mean free path of the gas molecules is less than the plate spacing by at least two orders of magnitude; in the molecular regime the mean free path is equal to, or greater than, the plate spacing; the transition regime occurs between the two. The amount of gas in the switch is usually set so that the working pressure is in the transition between molecular and laminar flow. Under these conditions, an increase in pressure (by heating the getter) increases the conductance considerably.

The design of the heat exchanger plates involves a trade-off: it is desirable to maximise both the plate area (to improve gas conduction and reduce the effect of the resistance at the gas-plate interface – the "Kapitza" resistance) and the fin thickness (for conduction to the switch interfaces), yet minimise the overall volume and mass. The final design must be one that is practical to machine and this often leads to arrangements of several long and relatively thin plates.

Hermetic gas containment can be a problem for some low conductivity materials used to separate the two heat exchanger plates (e.g. Vespel®) which may be slightly porous to helium. Typical design lives for ADRs used in space missions are around 5 years; given the small amounts of gas contained in the switch, this translates to leak rates that must usually be $< 5\times10^{-6}$ l/s [116]. One solution is to line spacer tubes with a foil, or cover them in epoxy [118]. At higher temperatures, thin metal sleeves may be suitable. Should the conductivity need to be reduced further, a bellows arrangement will increase the thermal path, but will then require some additional structural support (see Figure 2.11). A particular grade of titanium (Ti 15V–3Cr–3Sn–3Al) has been shown to be an effective spacer material at low temperatures because of its superconducting transition at 3.9K [119].

The speed with which the switch can be turned on and off depends on both how fast the getter can be heated or cooled and how quickly the gas can be pumped within the switch. The latter can be a problem in low temperature switches where the helium is less mobile and cannot reach open areas as quickly. Pumping speed can be increased by adding more getter material to improve adsorption, but it also increases the switch-on temperature because most of the helium is strongly bound to the surface. The switch-on/off time for the getter will be influenced by the heat capacity of the warm elements and therefore this should be kept small. It will also be limited by the amount of heat that can be absorbed by the higher temperature stage since any heat input to the getter must be dumped here.

Different adsorbing materials can be used depending on the temperature at which the switch is required to turn on. For example, charcoal or zeolite will have suitable adsorbing properties for use around 10 K, copper will work well at 4 K and neon plated on copper has been used around 1 K [117]. For charcoal getters, the “on” adsorption temperature is 7–14 K [116]. Since the heat switch may be operating below this temperature, heat from the getter must be intercepted before it reaches the switch interfaces. In general, the switch needs to turn on at a temperature which is not too high, but turn off at a temperature that does not take a long time to reach when the getter heater is turned off and the switch is

cooled (either by the bath, or – in the case of multi-stage ADRs – a higher temperature stage).

Figure 2.11: Example of a bellows sealed gas-gap heat switch [116].
The external support is Vespel® SP-1 and the diameter of the top and bottom flanges is 38 mm.

Gas-gap heat switches have the advantage over mechanical switches of no moving parts and therefore greater reliability. Their main disadvantage is the time taken to operate the switch between the on and off states, which allows heat leaks to occur during switching. Another is the fact that an additional heat input is introduced when operating the getter. This particular problem is addressed in passive gas-gap switches.

2.4.2.2.1 Passive Gas-Gap Heat Switches

In passive gas-gap heat switches, the getter is strongly thermally coupled to the low temperature end of the switch. The switch is then activated by the temperature rise associated with magnetising the salt pill and it is turned off when the salt pill cools during demagnetisation (thereby reducing the getter temperature). They operate in the molecular regime, utilising the fact that the conductivity of the gas is proportional to pressure under these conditions. The vapour pressure of the gas must be a strong function of temperature

near the desired switching point, which must occur when the temperature of the switch drops below the temperature of the bath (or higher temperature stage).

The heat exchanger fins themselves may be used as the adsorbing surface, so that a liquid film (in the case of ^{3}He or ^{4}He) or solid (in the case of H_2) is formed on the surface. In this scenario, the total amount of gas in the switch must be precisely controlled: it cannot be so much that the films will drip under gravity, or that bridges could form across the gaps between the plates; however, films must be thick enough that their vapour pressure is close to the saturated vapour pressure in the bulk gas.

In some laboratory systems, a variation on the passive gas-gap heat switch is implemented, whereby long, thin tubes of helium gas transfer heat to a cold stage [120]. The thermal conductivity of the tubes alone is very small, but heat is conducted down them effectively when they are filled with gas. The amount of gas in them is accurately controlled, so that when the cold end reaches liquid helium temperature, all the gas is liquefied out of the tube into the cold stage which is then well insulated from the warm parts of the apparatus. However, this arrangement is clearly only suitable in the vicinity of the ^{3}He or ^{4}He saturation temperature.

Passive gas-gap heat switches using ^{3}He have been shown to work well between 0.1 and 1 K [117], thus demonstrating that gas-gap heat switches are suitable for milli-Kelvin ADR stages.

2.4.2.3 Superconducting Heat Switches

Superconducting heat switches take advantage of the difference between the thermal conductivity of a type-I superconductor in its superconducting and normal states. The fact that the superconducting state can be destroyed by application of a magnetic field is used as the controlling mechanism.

In a superconductor, entropy decreases exponentially with temperature below T_c due to changes in the electron states. At the transition temperature, T_c, some electrons fall into a

lower energy ground state (i.e. form "Cooper pairs"); and from the transition temperature down to 0 K electrons may be thermally excited out of the ground state with probability proportional to $\exp(k_B T/\Delta)$ [121] where Δ is the energy gap, given by BCS theory as [122]:

$$\Delta = 1.76 k_B T_c. \tag{2.22}$$

It can therefore be seen that the number of electrons in the normal state falls exponentially with temperature below T_c. While the ground state can carry electrical current without dissipation, it has zero entropy, meaning that it is unable to carry heat. As it becomes increasingly populated, the only mechanism of heat transport is by phonons (which are almost entirely absent at such low temperatures) and the thermal conductivity of the superconductor drops. To obtain a sufficiently low conductivity in the "off" state, the switch must be operated significantly below the transition temperature ($\sim 0.1 T_c$). When the magnetic field is turned on, the switch is driven normal and electrons are free to take part in the conduction along with the phonons, causing an increase in conductivity. This might lead to the conclusion that type-II superconductors, with their higher transition temperatures, could be used to good effect. However, they are not as suitable for heat switches because of the fact that they maintain regions of superconductivity above a lower critical field and the superconductivity is not entirely destroyed until some much higher upper critical field is reached.

Material	T_c (K)	H_c (T)	T_{upper} (K)
Zinc	0.85	0.0053	< 0.1
Aluminium	1.2	0.0105	0.1
Indium	3.4	0.0293	0.5
Tin	3.7	0.0309	0.52
Lead	7.2	0.0803	0.5

Table 2.2: Critical temperatures (T_c) and fields (H_c) of superconducting materials commonly used in heat switches.
T_{upper} indicates the practical maximum temperature of operation (reproduced from [116]).

Several pure metals can be used for the switch material (see Table 2.2). As is clear from the table, only moderate magnetic fields (0.01–0.1 T) are required to destroy the superconducting state, which means the magnets used in these switches can be relatively compact. Helmholtz coils are often used (see Figure 2.12) as they provide uniform field, minimise end effects that could generate eddy currents in copper interfaces and can be easily configured to orient the magnetic field perpendicular to the direction of heat flow. The latter point is important because as the material returns to its superconducting state on removal of the field, flux may remain trapped inside maintaining normal regions below T_c [123]. Should these flux lines align with the temperature gradient in the switch, they provide a direct path for heat to flow from the warm to cold ends. A further consideration for the choice of material is that thermal conductance in the "on" state can be limited by magnetoresistance effects (see section 2.4.2.4), so materials for which this phenomenon is small are preferred.

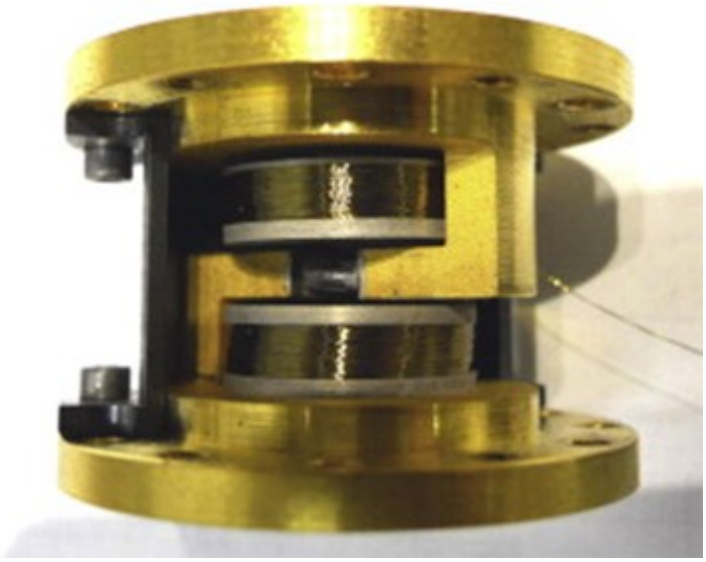

Figure 2.12: Example of a superconducting heat switch for use below 0.35 K [116].
The field is provided by a vertically stacked Helmholtz coil and Vespel® spacers are used to separate the top and bottom flanges.

Switching ratios can be several orders of magnitude if the temperature is low enough. For tin, for example, a ratio of 60 at 0.5 K rises to 10^5 at 0.01 K [100]. The low operating temperatures of superconducting heat switches restrict their use to the low temperature

stages of ADRs. Nevertheless, they offer high switching ratios without heat generation or moving parts.

2.4.2.4 Magnetoresistive Heat Switches

Magnetoresistive (MR) heat switches take advantage of the magnetoresistance that occurs in certain metals. Under the application of a high magnetic field the motion of heat carrying electrons is inhibited and, given low phonon conduction, the thermal conductivity of the switch is reduced. Removal of the magnetic field raises the thermal conductivity to the normal value for the metal. Although magnetoresistance is observed to some extent in most metals, the effect can be extremely large in certain cases.

Initial investigations of the low temperature thermal conductivity of a range of metals in magnetic fields by Mendelssohn and Rosenberg [124] suggested that a number of materials might be suitable for magnetoresistive heat switches, particularly cadmium, which they found to have resistance over 1000 times its zero-field value at 1.85 T. It was recognised from this early stage that largest effects were seen in high purity specimens where the zero-field conductivity was high.

Laudy and Knol followed up this work by testing a cadmium crystal formed into the kind of "meander" geometry necessary to obtain the small (area)/(length) (≡ A/L) ratio required for a practical heat switch [125]. Their results showed that switching ratios in excess of 50 could be achieved up to 5 K in fields of 2 T.

Work has also been done on high purity, single crystal gallium [126,127] for which thermal conductivity changes of over four orders of magnitude are reported at 1.37 T and for temperatures below 3 K. Engels *et al.* [127] constructed and tested a gallium heat switch. By choosing the optimum crystal orientation with respect to the applied field and forming the crystal into geometry which gave a small A/L ratio, they obtained an "off" conductivity of 10^{-6} W/K at 1 K in 1.5 T and an "on" conductivity of nearly 10^{-2} W/K at the same temperature in zero-field; the resulting switching ratio was 8000. Their design took

advantage of the low melting temperature of gallium (~ 30°C) to form the meander geometry and to attach thermal contacts. Such a low melting temperature, however, makes gallium heat switches rather impractical and certainly unsuitable for space applications.

Single crystal beryllium has been investigated by Radebaugh [128] who found a change in thermal conductivity of over three orders of magnitude in fields of 1.2 T. His data could be closely fitted to a B^2 dependence, indicating that even greater switching ratios could be achieved with higher fields.

MR switches have many of the advantages of superconducting heat switches whilst also operating at higher temperatures; they can be used up to 4 K to allow direct linking to a helium bath. They do require relatively high fields (of the order of a few Tesla), but these are usually available from superconducting magnets of the same design as those used to magnetise the pill. As noted above, the material must be chosen so that phonon conduction is low, which can be inferred from a high Debye temperature (see 3.6.1). It is also necessary that the material temperature never drops below its superconducting transition temperature; if it does, the conductance will drop as it would in a superconducting heat switch. These two parameters are listed for some magnetoresistive materials in Table 2.3.

Material	T_c (K)	θ_D (K)
Beryllium	0.026	1440
Cadmium	0.56	209
Gallium	1.083	320
Molybdenum	0.92	450
Thallium	2.39	78.5
Tin	3.72	200
Tungsten	0.015	400
Zinc	0.85	327

Table 2.3: Superconducting transition temperature (T_c) and Debye temperature (θ_D) for a selection of magnetoresistive materials.
Data from [129].

Since ADRs are usually required to cool to at least 100 mK, only beryllium and tungsten from the list above will be suitable for the lowest temperature stages. If temperatures of 25 mK or below are not required, beryllium would seem to be the better choice, since its high Debye temperature indicates very low phonon conduction at low temperatures (as confirmed by Radebaugh [128]). However, it presents practical difficulties because of its toxicity: small particles must not be breathed in, making machining a complex operation. As a result of this, tungsten (see Figure 2.13) has become the optimum choice and there has been considerable recent research to optimise its use in heat switches [130,131].

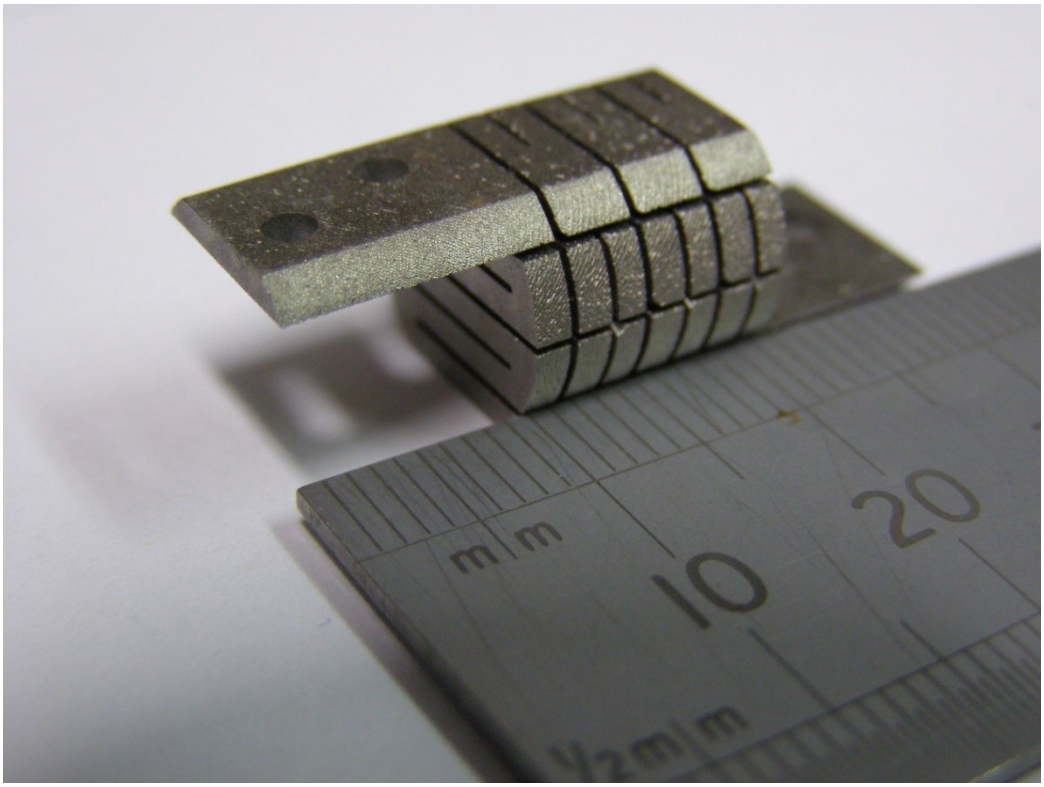

Figure 2.13: A tungsten heat switch manufactured use in an MSSL ADR (courtesy of Dr J. Bartlett).

In addition to material choice, there are particular design challenges to constructing a magnetoresistive heat switch: even in fields of several Tesla, the "off" conductivity is still high enough that small A/L ratios are needed to keep heat loads to acceptable levels, and this leads to geometries that can be difficult to manufacture and inherently weak.

2.4.3 Magnets

Magnetic fields of several Tesla are required to produce an appreciable magnetic cooling effect. Provision of these fields has been made easier by the advent of commercially available superconducting magnets that can be cooled by conduction. Conduction cooling simplifies the overall design by allowing magnets to be thermally linked to a helium bath, or low temperature stage of a cryocoolers, so that immersion in liquid is not necessary and cryogen free systems are possible. Niobium-titanium (NbTi) is commonly used since wires can be produced with small filament sizes leading to good stability. Furthermore, it can be supplied and wound in sub-mm cross sections, allowing production of small, high field magnets. This enables the fast magnet ramping times that are desirable for rapidly cycling multi-stage ADRs (see 2.5.3).

Reaching higher fields will increase the cooling effect, but in most magnetocaloric materials the gains become marginal above 3 T. Moreover, fundamental limits of the superconducting materials used are quickly reached as operating temperatures rise above 4 K. The critical field in a superconductor is fairly well approximated by a $1 - (T/T_c)^2$ relationship [122]. For niobium-titanium (T_c = 9.2 K), for example, the critical field is around 8 T at 4.2 K, but drops to 4 T at 6 K [105]. This makes it increasingly difficult to build magnets that achieve sufficient field to generate a useful magnetocaloric effect as temperature rises. Naturally, this has led to investigation of materials with higher T_c, such as niobium-tin (Nb_3Sn). This offers the benefit of operating the magnet up to 10 K, potentially simplifying the pre-cooling system, and magnets of this type have been demonstrated in ADRs [132].

The two main system engineering aspects that must be addressed in an ADR magnet design are the stray fields they create and the parasitic heat load from their current leads. Sufficient shielding must be incorporated in the design so that stray field will not affect other parts of the system or the item being cooled. Maximum allowable fields at detector locations can be as low as 5 μT [133], although a working value of 100 μT is used for the TESs in the

SAFARI instrument [134]. Where especially stringent requirements apply to the detectors, it can be better to protect them with their own dedicated shield [135].

The simplest shielding method is to surround the solenoid with an iron cylinder that will provide a return path for the flux exiting the solenoid. More flux can be contained by increasing the thickness, thus reducing the remnant field outside the shield. If practical, capping – or partial capping – of the cylinder will improve the shielding further. The use of iron comes with relatively high size and mass penalties, however, and this has motivated the use of other materials with a high relative permeability, such as mumetal or silicon steel [135]. Multi-shield designs have also been developed that use different materials to reduce fields to the micro-Tesla level [136].

An alternative is to use either passive or active superconducting shielding. The passive form consists of a cylinder of a type-I superconductor placed around the magnet leaving a gap between the magnet coils and the field. Since the superconductor is perfectly diamagnetic below its transition temperature, field lines are directed into the gap between the magnet and the shield leaving minimal stray flux. The superconducting material used (e.g. Ni_3Sn powder [137]) will likely require a dedicated container or support structure and any influence from this must also be considered.

In active superconducting shielding, the field lines are contained by a second set of superconducting coils, which can be powered in series with the main coils, but with polarity reversed. The field seen by a salt pill will be reduced by this type of shielding, requiring the size of the main coil and/or its operating current to be slightly increased.

The use of toroidal magnet arrangements has been experimented with for ADRs [137,138]. An ideal toroid has no external field and so no additional shielding is required. However, practical designs are composed of many small coils, allowing some flux to escape. Moreover, the total size and mass may exceed that of a shielded solenoid. Measurements from a real toroid used in an ADR showed that the magnetic field dropped from 3 T within

the magnet to < 100 μT at 15 cm – over two orders of magnitude better than an unshielded solenoid [138].

The current lead issue must be addressed with proper heat sinking. This is vital to avoid excessive heat loads which risk driving either the magnet or leads normal, or overwhelming the cooling power of the ADR and its pre-cooler. Usually, the heat load from the current leads ends up as a significant fraction of the overall load on the cooling system; hence achieving the required fields with more windings of a lower current wire is preferred. However, even when magnet currents are kept to a few amps, this can still induce significant heat loads on the higher temperature stages of a cryogenic cooling chain. Although copper current leads can be optimised to minimise this load [139], high-temperature superconductors are sometimes the only viable option. Commercially available YBCO coated conductors – cut down to 1mm widths to reduce heat leak – will be used on the SXS ADR for Astro-H [140] and these leads have successfully completed a flight qualification programme. In doing so, the particular design challenges associated with supporting the tapes had to be addressed: although they are strong in pure tension, a minimum bend radius must be observed and transverse stresses that could cause delamination must be avoided. These requirements were met by enclosing the conductors in Kapton tubes and supporting these on a carbon composite ribbon. It was also found that the thermal conductivity could be reduced by using tapes with a silver-gold alloy coating, instead of the regular silver one.

In addition to the aspects described above, magnet construction comes with its own challenges: winding the coil to the desired accuracy, potting it and making connections to the wire all require skill and care, and are key parts of ADR construction.

Since the magnets and associated shielding represent a large proportion of an ADR's size and mass, they are obvious targets for miniaturisation. The size of a solenoid magnet for a given field is reduced by increasing the density of current-turns – i.e. by increasing either (or both) the number of turns of the conductor in a given length, or the current in the wire. The

key to reducing magnet size and mass in ADRs is therefore smaller wire that maintains a high critical current density. Of course, practical issues must not be neglected, such as the wire's strength and the fact that smaller wire will increase the ratio of insulation to conductor in the coil pack and so may not lead to an overall reduction in size. Furthermore, increasing the density of current turns will increase the inductance and this will place bigger demands on any quench protection circuit, since the voltages generated for a given rate of change of current will be larger. Some of these considerations are returned to in Chapter 7.

Efforts to further miniaturise the magnets are likely to move towards producing superconducting structures with micro-fabrication techniques and progress is already being made in this area with the production of HTS coils through thin-film deposition [141].

2.4.4 Suspension System

An easily overlooked, but vital, part of an ADR's design is the suspension system for the pill. The target is to combine high strength with a minimal heat load. Shirron and McCammon [111] point out that the relevant figure of merit is the ratio of the suspension material's Young's modulus to its thermal conductivity, since heat load for given tensile strength can be reduced arbitrarily by lengthening the supports, whereas the Young's modulus gives information about the resonant frequency of the supports. This is crucial for two reasons on spaceflight ADRs: first, the arrangement must simultaneously withstand high vibrations from launch and minimise exported vibrations which could influence the detectors to be cooled; second, and more fundamentally, the vibrational heat input must be minimised. In addition to incurring an additional heat load, these vibrations can also introduce random temperature fluctuations which a control system will struggle to regulate. The most reliable way to minimise the effects of vibrations is to ensure that the first resonant frequency of the suspensions system is higher than that of any of its supporting structures.

Pills are traditionally supported using Kevlar® thread and this has been proven in a number of space-qualified designs [133,142,143]. The untwisted yarn is used for its low elongation

at breaking point [111], but this can make it challenging to achieve even tension in all fibres as running the yarn around curved edges can leave the inside fibres un-tensioned. One solution is to bond the Kevlar® into screws which can be used to set the tension and this is then maintained with springs, or spring washers [143]. Forged end fittings which can be fixed in adjustable mounts have also been shown to work [144]. Vespel® rods have been employed as a mechanically simpler alternative in laboratory based systems [145], but these have yet to be proven under loads equivalent to launch vibrations.

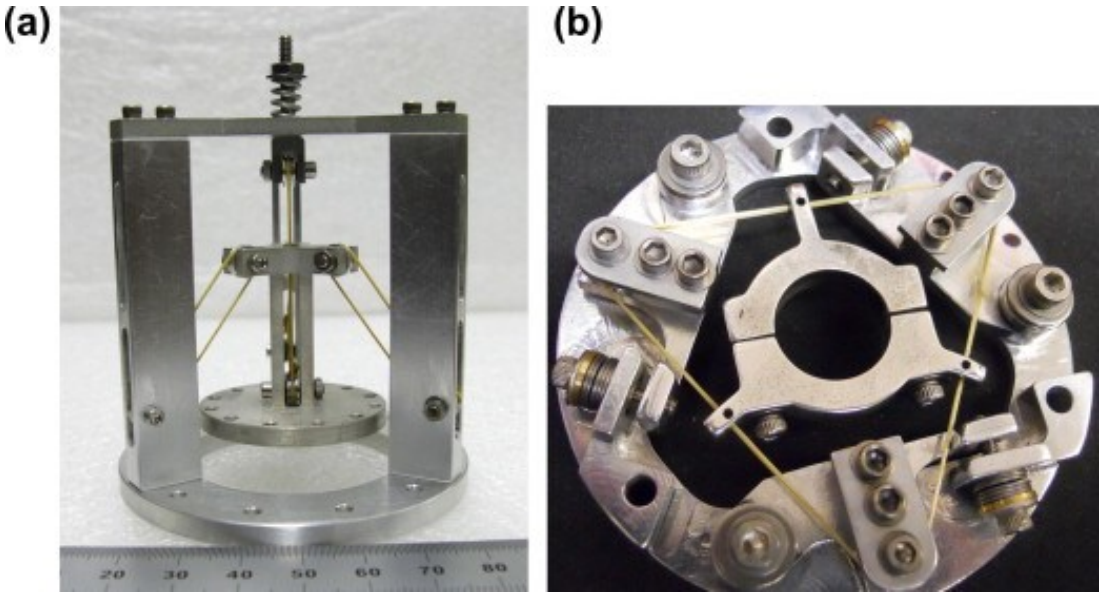

Figure 2.14: (a) Longitudinal and (b) lateral suspension assemblies used in the Astro-H ADR [146].

A further consideration is ensuring that the arrangement constrains all 6 degrees-of-freedom of the pill and some solutions use separate structures to constrain the translational and axial degrees-of-freedom (see Figure 2.14).

2.5 ADR Configurations

The basic ADR configuration presented in Figure 2.4 has a number of drawbacks. Firstly, the salt pill must cycle over the complete temperature range from bath to cold stage. While, in principle, this range can be expanded by increasing the magnetising field, if the ratio of bath to operating temperature exceeds a factor of around 30, the required field starts to

rapidly increase [105]. This brings increases in magnet size and mass, which are exacerbated by shielding requirements. The second problem with an increasing temperature ratio is that the parasitic heat loads coming though the suspension system and heat switches from the bath grow, usually following a relationship which is some power of the bath temperature. Maintaining the same operating temperature then requires a proportionally bigger salt pill. Finally, and perhaps most importantly, the basic ADR always needs to spend some period of time recycling, during which it is unable to provide cooling.

The shortcomings of the fundamental design can be addressed by modified configurations and these are described in the following sections. They all feature additional stages of refrigeration, which provide the following general advantages [105]:

i. each stage cycles over only a fraction of its operating range and so required fields are reduced;
ii. upper stages act as a guard to parasitic heat loads;
iii. refrigerants can be optimised for their temperature range (i.e. higher density refrigerants can be used for the upper stages to reduce salt pill volume).

2.5.1 2-Stage ADR

The layout of a 2-stage ADR is shown in Figure 2.15. A second ("high temperature") salt pill is used, which acts as a shield for the pill connected to the cold finger and limits the parasitic heat loads on this "low temperature" pill. The high temperature pill is constructed from a salt which has good heat capacity at temperatures just below the bath temperature, but cannot cool all the way to the desired operating temperature on demagnetisation. Each pill has its own heat switch to the bath. As is illustrated in the figure, this can result in a longer thermal path between the low temperature pill and the bath. The low temperature pill is mounted from shields linked to the high temperature pill and, in this way, the latter act as an intercept for both conductive and radiative loads. This increases the hold time at a given operating temperature.

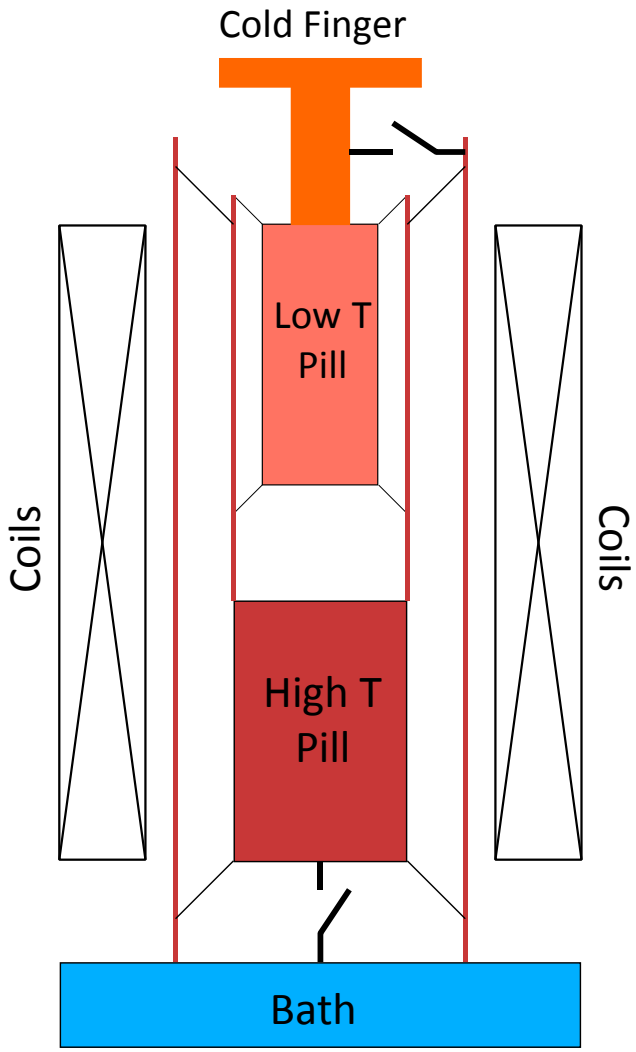

Figure 2.15: 2-stage ADR schematic.

The method of operation is exactly the same as the single stage ADR: both pills are magnetised with the heat switches closed and then demagnetised together after the heat switches have been opened, meaning only one set of coils is required.

This design was proposed by Hagmann and Richards [147] for the Space Infra-Red Telescope Facility (SIRTF), where they used gadolinium-gallium-garnet (GGG) for the high temperature stage and chromic-caesium-alum (CCA) for the low temperature stage. These pills were supported by Kevlar cords and linked to the bath through a single mechanical heat switch. Hold times of 24 hours or longer at 100 mK were achieved.

2.5.2 Double ADR

The layout of the Double ADR (shown in Figure 2.16) is very similar to the 2-stage ADR, with the exception that the low temperature pill is connected to the high temperature pill through a heat switch while the heat switch between the low temperature pill and the bath is removed. Each pill has its own set of coils for magnetisation and demagnetisation and these are controlled independently through separate power supplies.

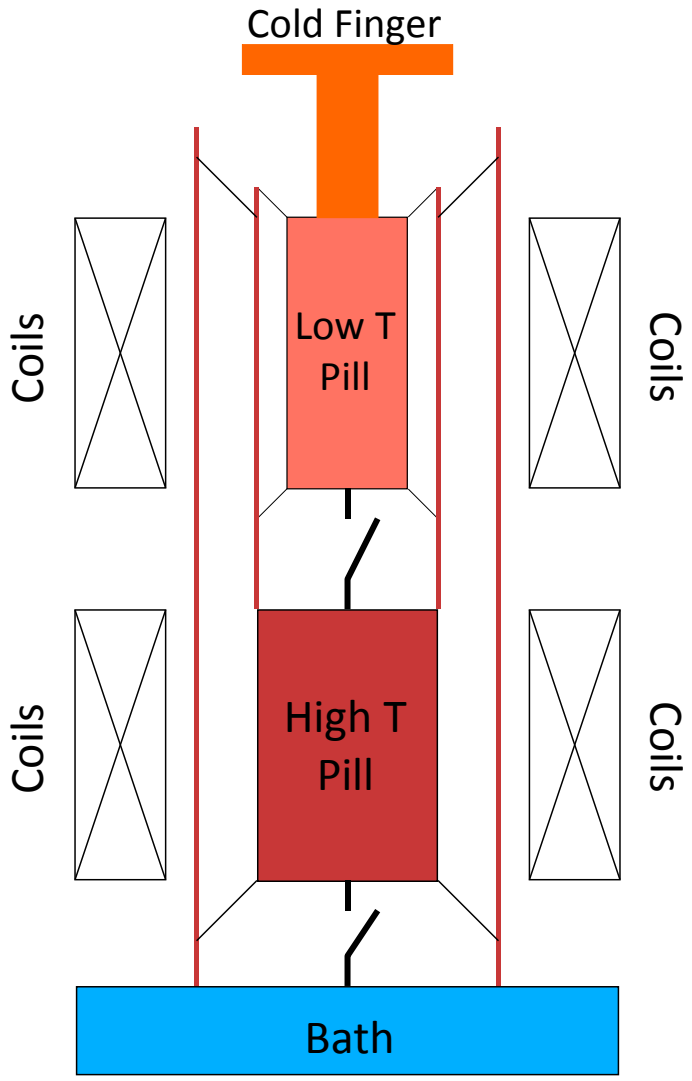

Figure 2.16: Double ADR schematic.

Having separate coils for each pill offers greater flexibility in modes of operation; there are two main sequences: parallel and series. In the descriptions below, the first stage is the high

temperature pill, while the second stage is the low temperature pill. The parallel sequence runs as follows:

i. Starting with both heat switches open, the pills are magnetised.
ii. As the pill temperatures rise above those of their respective sinks (the bath in the case of the first stage, or the high temperature pill in the case of the second stage) the heat switches are closed; the heat of magnetisation is dumped to the bath.
iii. The heat switch to the bath is opened and the high temperature pill is demagnetised, cooling both itself and the low temperature pill.
iv. The heat switch between the pills is opened.
v. The low temperature pill is demagnetised from below the bath temperature.

The series sequence has the following steps, which assume that at least one cycle has already been completed and the low temperature stage is colder than the high temperature stage:

i. With the heat switch between the pills left open to maintain the temperature of the second stage, the high temperature pill is magnetised.
ii. As the temperature of the first stage exceeds the bath temperature, the switch to the bath is closed.
iii. The high temperature pill comes into equilibrium with the bath.
iv. Assuming that the second stage is still colder than the first stage, both switches are opened while the first stage is demagnetised.
v. The second stage is magnetised and the heat switch between the stages closed as soon as the second stage temperature exceeds the first stage temperature.
vi. The second stage comes into equilibrium with the first stage.
vii. The heat switch between the pills is opened and the second stage is demagnetised to the desired operating temperature.

Further variations on the series method are possible [148]. The second stage can be recycled before the first, or the first stage can be recycled a second time before the hold period, but after the second stage recycling to dump this heat back to the bath. This can allow the size of the first stage to be reduced, since it only has to be sized for the larger of the two entropy loads (either the entropy of second stage magnetisation, or the entropy from parasitic loads during the hold time) rather than the sum.

The temperature at which heat is transferred between the stages becomes a parameter to be optimised in the series sequence. Decreasing it will increase the entropy capacity of the low temperature (i.e. second) stage because it will be magnetised at a temperature where there is a larger entropy difference between the zero-field state and the high-field state (see Figure 2.3). However, there will be an associated of penalty of reducing the entropy capacity of the high temperature (i.e. first) stage because its hold temperature will be at a point where there is less entropy difference between the high and zero-field states (again, see Figure 2.3). The optimum is the point where the combined mass of the salt pills and magnets for both stages is minimised [148]. If the transfer temperature is the same as the first stage hold-temperature, then the order of recycling will not be important. However, if it is greater, more entropy will be available if the second stage is recycled before the first (i.e. directly after the first stage hold time). This reason for this is illustrated in Figure 2.17 [148], which shows the cycle of the high temperature stage: in the left-hand plot, it is at its hold temperature (0.5 K) before accepting heat from the low temperature stage (at 0.8 K) which is recycled first; in the right-hand plot, the sequence is reversed. Comparison of the two clearly shows that when heat is transferred between the stages at a higher temperature than the hold temperature of the first stage, the left-hand sequence is optimum since more energy can be absorbed (illustrated by the shaded boxes).

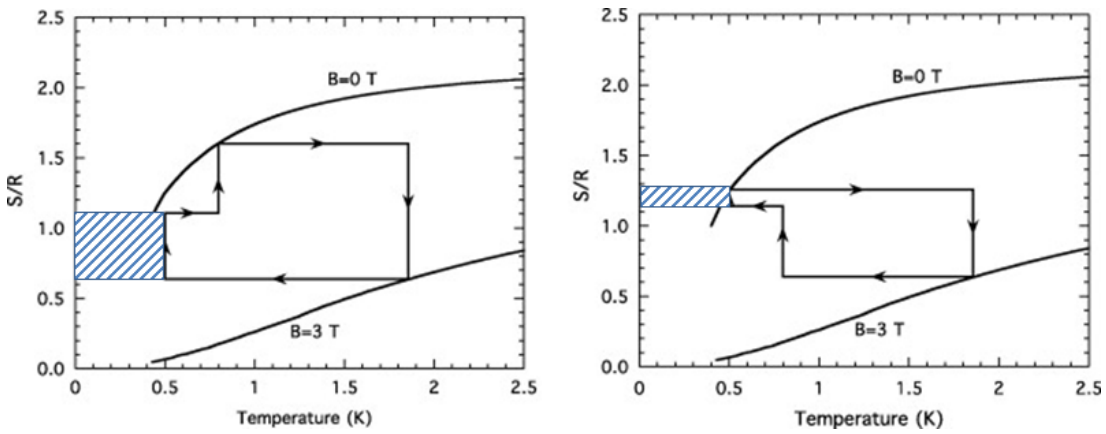

Figure 2.17: Temperature-entropy curves showing two alternatives for the operation of the high temperature stage during series recycling of a double-ADR [148].
The energy absorbed ($= \int TdS$) in each case is shown by the shaded box.

The double-ADR allows the use of salts which have lower ordering temperatures for the low temperature stage, but would not have sufficient entropy capacity to reach low temperature without an initial pre-cooling step. Whilst the high temperature stage must absorb all the entropy from the low temperature stage, materials suited for this purpose (i.e. higher entropy density and ordering temperature) may be used. The layout also maintains the benefits of the 2-stage ADR in terms of reduced parasitic heat loads.

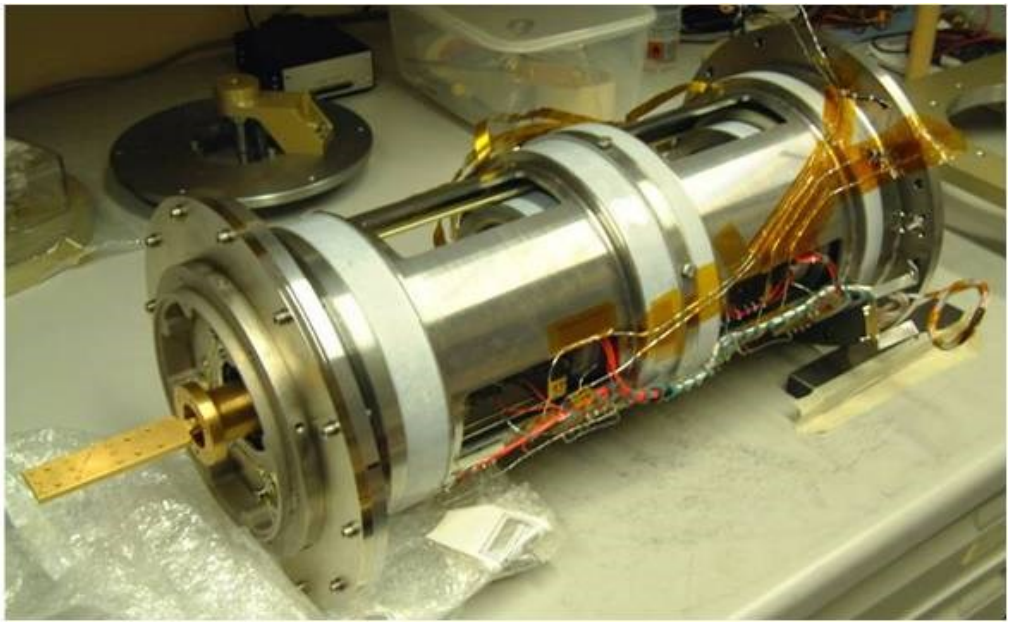

Figure 2.18: Double-ADR developed at MSSL
(photo courtesy of Dr J. Bartlett).

A space qualified double-ADR has been developed at MSSL for future ESA missions [136] using a single crystal of dysprosium-gallium-garnet (DGG) for the high temperature pill and Chromic-potassium-alum (CPA) for the low temperature pill (see Figure 2.18). The pills were connected by a superconducting lead heat switch and the switch to the bath was a gas-gap switch. In principle, many more stages may be added in series to the double-ADR configuration to extend operating range, with the purpose of providing additional intermediate cooling for instruments, or higher temperature heat intercepts.

A variation of this design uses a sorption cooler in place of the high temperature salt pill. Such a configuration has been developed for space and it is planned to be flown on the SAFARI instrument on board the SPICA satellite [149,150]. This cooler (see Figure 2.19) uses a slightly modified version of the series sequence of operation:

i. The sorption cooler is recycled by raising the temperature of the pump to ~ 30 K; this releases gas into the evaporator which is pre-cooled using the 4.5 K interface and ultimately liquefied by the 1.7 K interface (HS1 is open, HS2 and HS3 are closed).
ii. The heat switch to the 4.5 K interface (HS1) is closed, cooling the sorption pump and allowing it to adsorb gas; meanwhile, the heat switch to the 1.7 K interface (HS2) is opened, the temperature of the evaporator drops to ~ 350 mK.
iii. The ADR stage is recycled, increasing gas flow from the evaporator and rejecting heat to the sorption pump at ~ 4.5 K;
iv. The heat switch between the ADR and the evaporator (HS3) is opened and the ADR stage is a demagnetised to 50 mK.

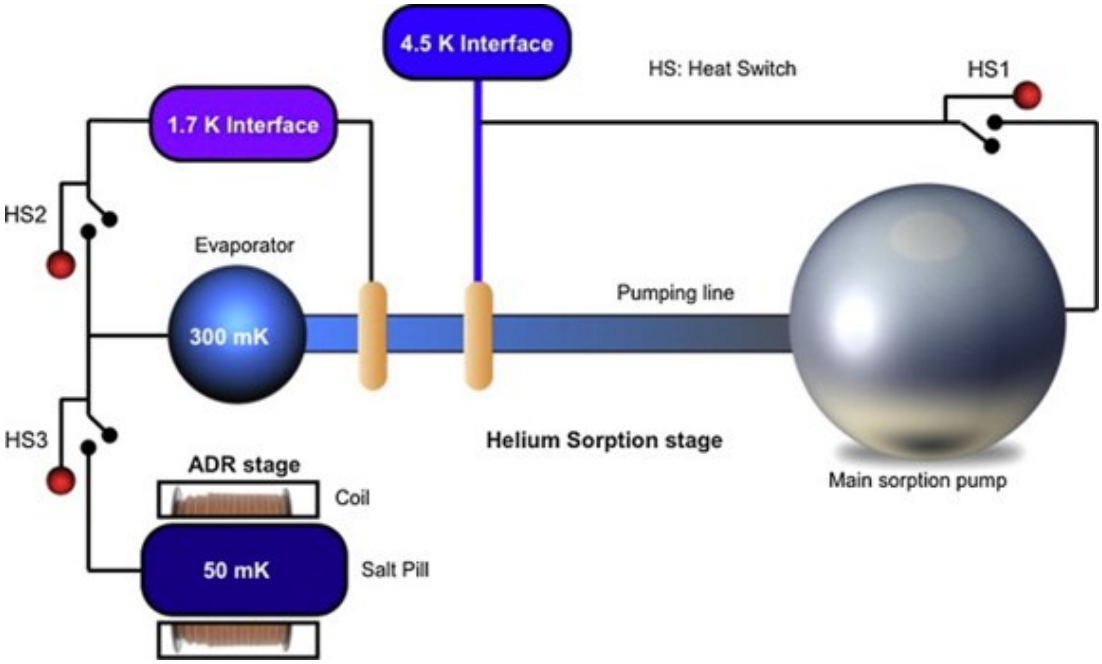

Figure 2.19: SAFARI Sorption/ADR hybrid [150].

Other multi-stage variations of the single stage ADR are possible and these may be adopted to satisfy certain system level demands. For example, it may be desirable to use one of the ADR stages to provide redundancy for another part of the cooling chain (e.g. the ADR for Soft X-ray Spectrometer for Astro-H [146]), or cooling from the ADR may be required at two distinct temperatures for different parts of the instrument (e.g. the hybrid ADR planned for the PIXIE mission [151]).

2.5.3 Continuous ADR

The Continuous ADR (CADR) addresses one of the main problems of conventional ADRs, namely that after a certain time zero-field is reached in the pill and for further cooling it must be re-magnetised ("recycled"). This means that the experiment being cooled cannot be maintained at its operational temperature continuously. In the case of detectors for telescopes, this introduces enforced breaks in the observational period which are generally undesirable.

Two main approaches have been taken to tackle this difficulty: the tandem ADR and the sequential multi-stage ADR. They both allow ADRs to achieve higher cooling powers

without unacceptable increases in mass. Furthermore, either technique is well suited for use with a mechanical cooler as the high temperature sink, since heat is dumped more steadily throughout the cycle instead of large loads for short time periods. An example of the tandem ADR configuration is shown in Figure 2.20; it essentially combines two ADRs in parallel and links them to a common cold finger. While one is demagnetising and providing cooling, the heat switch to the other is opened and it is recycled. One particular advantage of this arrangement is that the pills need only be sized for a hold time which is slightly greater than their recycling time. This allows size reductions in the magnets and other components and offers significant promise for overall size and weight reductions. A prototype cooler of this type is currently under construction at MSSL [145,152].

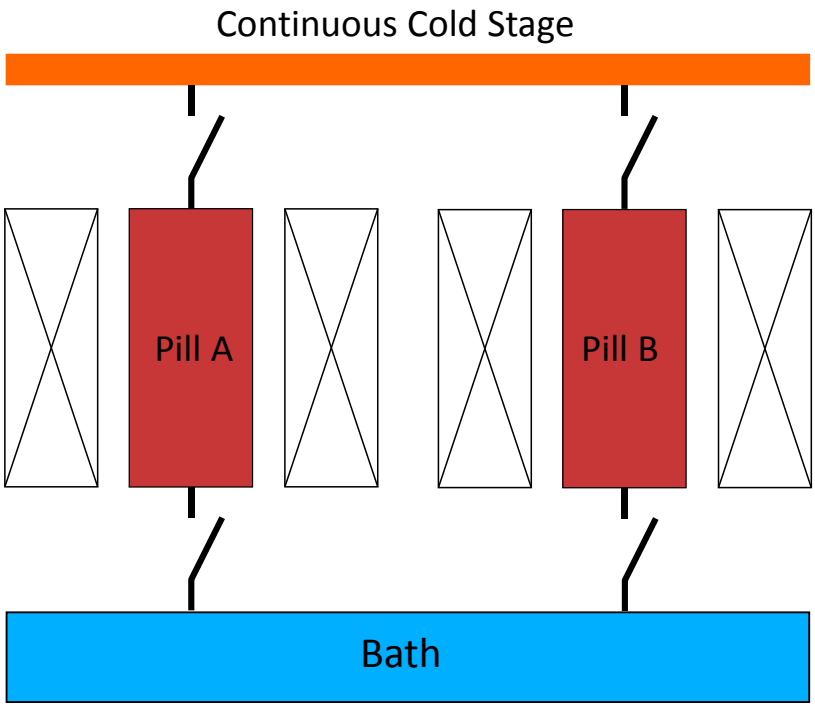

Figure 2.20: Tandem CADR schematic.

In the sequential multi-stage ADR, two (or more) pills are connected in series as shown in Figure 2.21.

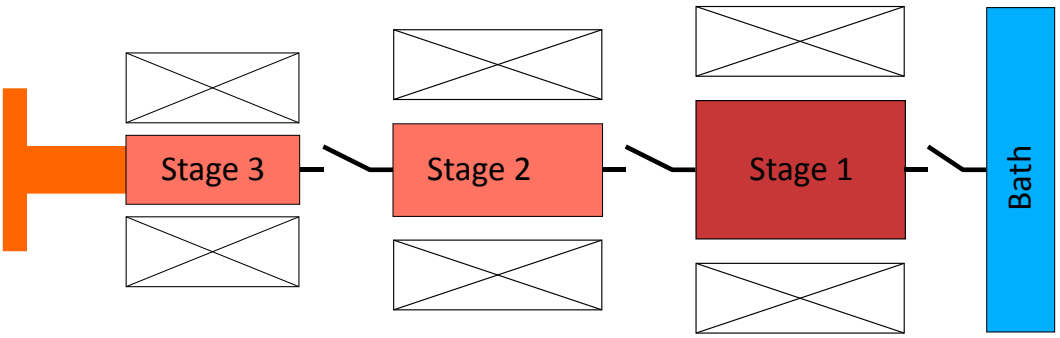

Figure 2.21: Sequential multi-stage CADR (adapted from [151]).

The pills are chosen so that there is an overlap in their operating temperatures and heat is shuttled between the stages. This translates to the following sequence of operation to maintain a constant cold end temperature:

i. Heat is absorbed from cold end through demagnetisation of the low temperature pill (stage 3) in the normal way. The heat switch to the higher temperature pill (stage 2) is kept open and this stage is demagnetised to just below the operating temperature of the cold stage.

ii. When the low temperature pill is fully demagnetised it is recycled by closing the heat switch between the stages 2 and 3 and magnetising. Heat is dumped to the higher temperature pill, which prevents the low temperature pill from rising above the required cold end temperature. The heat of magnetisation is absorbed by continued demagnetisation of stage 2.

iii. When stage 3 is fully magnetised, the heat switch between it and stage 2 is opened and it is free to be demagnetised in the usual way. While this is occurring, stage 2 can be recycled by closing the heat switch to next stage (stage 1) and re-magnetising.

iv. Once stage 2 is recycled, the switch between it and stage 1 is opened and stage 2 is partially demagnetised, ready to absorb heat from the recycling of stage 3. While stage 2 is demagnetising, stage 1 can be recycled to the bath.

By using this procedure the final stage becomes an isothermal stage, maintaining its temperature either through its own demagnetisation, or by dumping the heat to the lower stage. In principle, any number of stages can be used and this makes it possible to bridge the temperature gap to a 4 K (or higher) bath while still achieving sub-100 mK cold end temperatures. In some designs, the higher temperature pills are replaced by a sorption cooler operating at around 300 mK [153].

The main drawback of this layout is that heat is only being absorbed from the cold end for 50% of the cycle, while the tandem CADR provides true continuous cooling. The parallel configuration will always have a higher gross cooling power for this reason and this is illustrated in Figure 2.22, which compares the performance of 2-stage parallel and series ADRs operating with 3 T fields and a 4.5 K bath temperature [105].

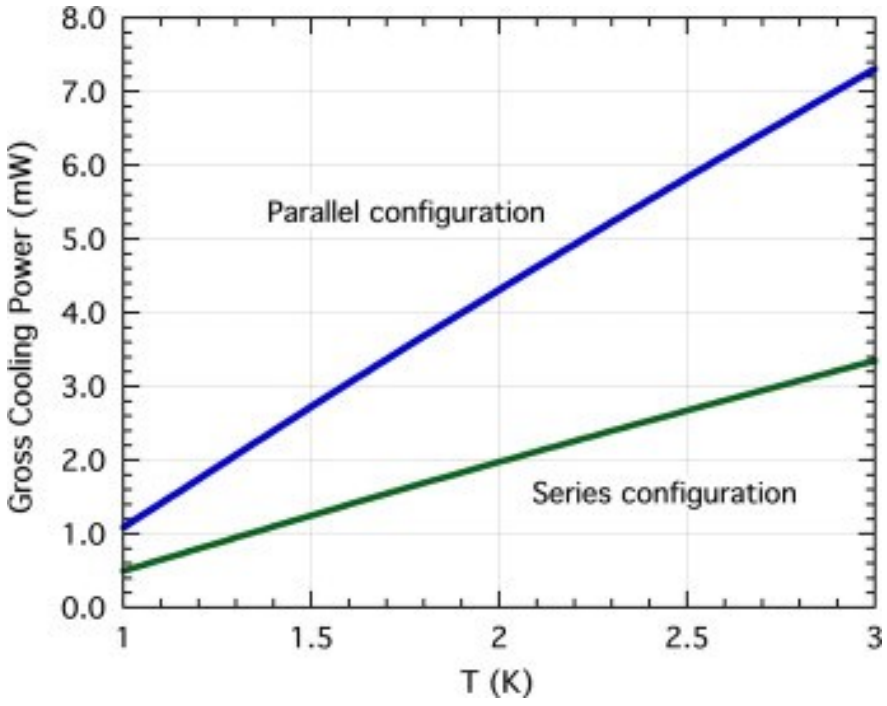

Figure 2.22: Gross cooling power of a 2-stage CADR, cooled form a 4.5 K bath, in parallel and series configurations [105].

The control algorithms can also be quite complex for the sequential ADR. However, fewer heat switches are required than in a tandem CADR with the same number of pills, which can potentially simplify the design.

Both types of CADR mentioned above change the driving factors of the ADR design, in that the size of the salt pill and the achievable magnetic fields are no longer so crucial; instead, it is more important that heat can be transferred quickly through the cooler's various stages and that the time for recycling and operating heat switches is minimised.

2.6 ADR Miniaturisation

The importance of miniaturisation of low temperature cryogenic coolers was highlighted in Chapter 1. The CADR concepts described above offer the potential to miniaturise ADRs because the salt pill no longer needs to be sized for an integrated heat load. This opens up the possibility of much higher cooling powers with a relatively low mass. Performance of a CADR, as noted above, is more dependent on the rate of heat transfer between the stages and the sink, and the times required for magnetisation and heat switch transitions.

Therefore, to make progress in miniaturisation it is vital to understand the mechanisms that limit heat flow on the microscopic scale. In the context of ADRs, this means understanding how heat is transported in the paramagnetic materials and the connecting heat switches. The paramagnetic material is effectively a "molecular refrigerant" and there would be no theoretical reason why a salt pill of just a few molecules could not be used as a refrigerant. It is then the limit on heat transport in this pill and the connecting materials that will constrain the ultimate size achievable for a "micro-ADR". These factors are explored in the next chapter.

2.7 Summary

This chapter has looked in detail at the theory of magnetic cooling and its use in Adiabatic Demagnetisation Refrigerators. The main components of an ADR are the paramagnetic refrigerant (the "salt pill"), the magnets and the heat switches that alternately link (or isolate) the paramagnetic refrigerant to (or from) its pre-cooling bath. The design and construction aspects of each of these elements have been reviewed, with particular focus being put on the heat switch technologies, since it is improvement in this area which will be the subject of Chapters 4 and 5. The various different ADR configurations that improve on the limitations of the basic system were described, leading up to Continuous ADRs, which address one of the most important of these – namely the inability of the basic ADR to provide continuous cooling. It has been shown that in CADRs the paramagnetic refrigerant no longer needs to be sized for the integrated heat load over the required hold time; instead, it need only be large enough to absorb sufficient heat to maintain the hold temperature while other parts of the refrigerator are recycled. This is what makes the performance of the ADR's heat switch so vital because its "on" conductivity helps determine the recycling time and its "off" conductivity is the dominant contributor to parasitic head loads which drive the size of the salt pill. It is for these reasons that improved heat switch performance can lead to smaller ADRs.

Chapter 3 – Thermal Transport in Adiabatic Demagnetisation Refrigerators

This chapter discusses aspects of the theory of heat conduction in solids which are applicable to ADRs. Particular attention is given to its application to tungsten since experiments on this material are the subject of the following two chapters. Starting from the simplified picture of kinetic theory (3.1), the more detailed semi-classical approach is developed (3.2 and 3.3); this recognises quantum mechanical effects, but – subject to certain restrictions – still allows the heat carriers to be thought of as particles.

Heat conduction in solids is governed by the ways in which heat carriers propagate through the medium. In metals, thermal currents are carried by two mechanisms: the movement of "hot" electrons down a thermal gradient and "cold" electrons up it; and phonons carrying thermal energy from the "hot" to the "cold" regions. In dielectrics, only phonons are involved. A steady-state heat flow is arrived at because these effects are balanced by the scattering of the carriers and it is the processes by which this occurs that set the limit on how much heat current can be passed for a given temperature difference. In many practical cases it is sufficient to subsume all the processes which limit the heat flow into one factor: the thermal conductivity, κ. The rate of heat transfer, $\dot{Q}$, can then be calculated for a known geometry and temperature difference using Fourier's law of conduction (in 1-dimension):

$$\dot{Q} = -\kappa A \frac{dT}{dx}, \tag{3.1}$$

where A is the sample area, κ its thermal conductivity and dT/dx the thermal gradient. The negative sign indicates that a positive heat flow is associated with a negative thermal gradient – i.e. heat flows down a thermal gradient. Usually κ will be a function of temperature and it will have to be integrated between the temperature limits to find the heat flow. Analysis and modelling of heat flow problems (as is performed in Chapter 6)

therefore requires knowledge of the form of $\kappa(T)$. Methods for determining the form of the conductivity are described in 3.4. Sections 3.2 and 3.6 focus on the heat carrying properties of electrons and phonons, respectively, and the scattering processes that affect them are examined in sections 3.5 and 3.7. The effects of surfaces and boundaries on both types of carrier are discussed in 3.8 and 3.9. In the final part of the chapter (3.10), the effects of a magnetic field on heat conduction are considered. As described in Chapter 2, it is these effects which are made use of in tungsten heat switches for ADRs.

3.1 Thermal Conductivity – The Kinetic Method

The kinetic method [154] is a natural starting point in tackling conduction problems and it can be an effective predictor despite its simplicity. It treats the heat carriers (either electrons or phonons) as particles, each with specific heat c. It therefore takes an energy $c\delta T$ per particle to change the local temperature of an assembly by δT. When a temperature gradient ∇T is established in a collection of particles (the sample), a particle travelling with velocity $\mathbf{v}$ from one region of the sample to another must therefore change its energy at the rate

$$\frac{\partial \epsilon}{\partial t} = c\mathbf{v} \cdot \nabla T \tag{3.2}$$

to stay in thermal equilibrium with its surroundings. Any particle moving through a medium will experience collisions (scattering events) which hinder its progress. In the kinetic method – and in the more detailed quantum descriptions that follow – these are dealt with by introducing the idea of a "relaxation time". The probability of a particle experiencing a collision in a time interval δt is taken to be $\delta t/\tau$, where τ is the relaxation time. If the probability that a particle has survived up to time t without a collision is $P(t)$, the probability of it being scattered between time t and time $t + \delta t$ is

$$P(t + \delta t) - P(t) = P(t)\frac{\delta t}{\tau}; \tag{3.3}$$

i.e.

$$\frac{P(t+\delta t)-P(t)}{\delta t}=\frac{\partial P}{\partial t}=-\frac{P(t)}{\tau}, \tag{3.4}$$

where the minus sign indicates that the scattering probability is decreasing as t increases. Rearranging and integrating both sides yields the form of $P(t)$:

$$P(t)=\mathrm{e}^{-t/\tau}. \tag{3.5}$$

Equation (3.5) shows that the relaxation time assumption (i.e. that the probability of a particle experiencing a collision in a time interval δt is $\delta t/\tau$) leads to the scattering probability decaying exponentially with time constant τ. It follows directly from the properties of the exponential function that the mean expected – or average – time between scattering events is τ.

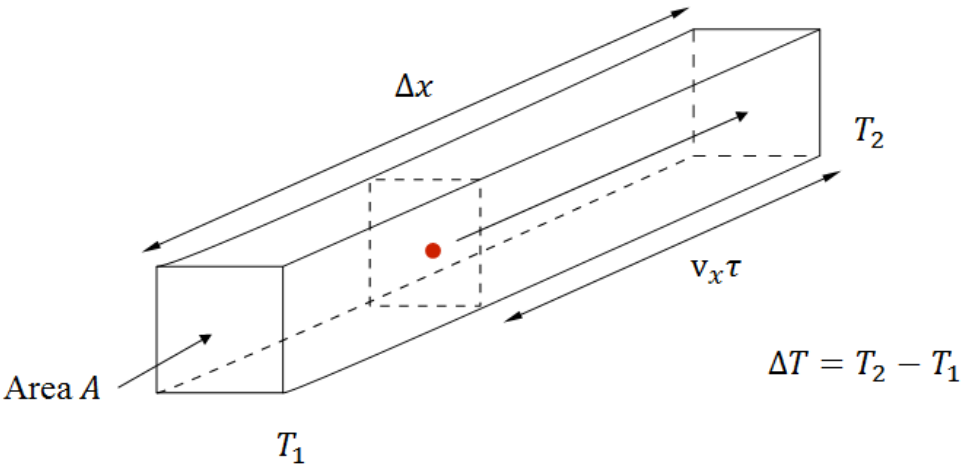

Figure 3.1: Thermal conductivity in 1-dimension according to kinetic theory

Consider Figure 3.1, showing a simple bar of cross-sectional area A and length Δx, with its two ends held at temperatures T_1 and T_2. By applying equation (3.2) in one dimension, it can be seen that a particle arriving at end 2 will bring with it an additional thermal energy $cl\,\Delta T/\Delta x$, where l is the distance it has travelled since its last scattering event (assumed to bring it into thermal equilibrium with the temperature of the sample at that point). The total

number of particles arriving at point 2 per unit time will be $nA\overline{v_x}$, where n is the number particles per unit volume and $\overline{v_x}$ is the average velocity of the particles in the x direction. Therefore the total thermal energy per unit time arriving at point 2 will be:

$$\dot{Q} = nc\overline{v_x}\tau\overline{v_x}\frac{\Delta T}{\Delta x}A, \tag{3.6}$$

where l has been replaced with the average distance travelled by each particle – i.e. $\overline{v_x}\tau$. To generalise equation (3.6) to three dimensions, it is assumed that the particle velocities are isotropic so that:

$$\bar{v}^2 = \overline{v_x}^2 + \overline{v_y}^2 + \overline{v_z}^2 = 3\overline{v_x}^2 \tag{3.7}$$

and $\overline{v_x}^2 = \bar{v}^2/3$. Equation (3.6) can now be re-written as:

$$\dot{Q} = \frac{1}{3}C\bar{v}\Lambda\frac{\Delta T}{\Delta x}A, \tag{3.8}$$

where $C = nc$ is the total specific heat for all the particles, $\bar{v}$ is the averaged velocity and $\Lambda = \bar{v}\tau$ is to be interpreted as the average distance travelled by a particle between collisions. Λ is referred to as the "mean free path." Comparison with equation (3.1) shows that the thermal conductivity is given by:

$$\kappa = \frac{1}{3}C\bar{v}\Lambda. \tag{3.9}$$

3.1.1 Wiedemann-Franz Law

Kinetic arguments can also be used to derive an expression for electrical conductivity [16]. An electric current, defined as the rate of flow of electric charge, can be expressed in terms of its current density, or rate of flow of charge per unit area:

$$\boldsymbol{j} = -ne\mathbf{v} = -\frac{ne}{m_e}\mathbf{p}, \tag{3.10}$$

where e, m_e and $\mathbf{p}$ are the electron's charge, mass and momentum, respectively. If the electron's momentum is examined over a short time interval δt, its increase resulting from an applied force $\boldsymbol{F}$, which is assumed to be constant in time, will be:

$$\delta \mathbf{p} = \boldsymbol{F} \delta t. \tag{3.11}$$

This will be correct only for electrons that have not experienced a collision in the time interval δt. Using the relaxation time approximation, the probability of an electron passing without collision in this time interval will be $(1 - \delta t/\tau)$. Hence, the contribution from these electrons to the average electron momentum is:

$$\mathbf{p}(t + \delta t) = (1 - \delta t/\tau)(\mathbf{p}(t) + \boldsymbol{F}(t)\delta t). \tag{3.12}$$

Ignoring terms of the order of $(\delta t)^2$, rearranging and taking the limit $\delta t \to 0$ gives:

$$\frac{d\mathbf{p}(t)}{dt} = -\frac{\mathbf{p}(t)}{\tau} + \boldsymbol{F}(t). \tag{3.13}$$

In the case of an applied electric field, the force $\boldsymbol{F}(t) = -e\boldsymbol{E}$. Taking the steady state, where $d\mathbf{p}(t)/dt = 0$, the momentum is then found to be:

$$\mathbf{p}(t) = -e\boldsymbol{E}\tau. \tag{3.14}$$

Substituting equation (3.14) into (3.10) and using the definition of the electrical conductivity $\boldsymbol{J} = \sigma \boldsymbol{E}$ leads directly to:

$$\sigma = \frac{ne^2\tau}{m_e}. \tag{3.15}$$

The concept of a mean free path can also be introduced into equation (3.15):

$$\sigma = \frac{ne^2\Lambda}{m_e \bar{\mathrm{v}}}. \tag{3.16}$$

The mean free path can then be eliminated from the ratio of the thermal and electrical conductivities by dividing (3.9) by (3.16):

$$\frac{\kappa}{\sigma} = \frac{1}{3}\frac{C m_e \bar{\mathrm{v}}^2}{n e^2}. \tag{3.17}$$

Following the classical relations from statistical mechanics (see Appendix B), the average energy of a particle is:

$$\bar{\epsilon} = \frac{1}{2} m_e \bar{\mathrm{v}}^2 = \frac{3}{2} k_B T \tag{3.18}$$

and the heat capacity of the free electron gas is:

$$C = n\frac{d\bar{\epsilon}}{dT} = \frac{3}{2} n k_B. \tag{3.19}$$

Inserting these into (3.17) leads to the *Wiedemann-Franz law*:

$$\frac{\kappa}{\sigma} = \frac{3}{2}\frac{{k_B}^2}{e^2} T = \mathrm{L_0 T}. \tag{3.20}$$

The law states that the ratio of the thermal and electrical conductivities will always be proportional to the absolute temperature, with the constant of proportionality $\mathrm{L_0}$, the Lorenz number.

3.2 Electronic Heat Transport

In quantum theory, the electron is described by a wavefunction obeying Schrödinger's equation:

$$-\frac{\hbar^2}{2m_e}\left(\frac{\partial^2}{\partial x^2} + \frac{\partial^2}{\partial y^2} + \frac{\partial^2}{\partial z^2}\right)\psi_{\mathrm{k}}(\mathbf{r}) = \epsilon_k \psi_{\mathrm{k}}(\mathbf{r}). \tag{3.21}$$

The waves must be confined within the limits of the sample, having dimensions L_x, L_y, L_z, and, since it is travelling wave solutions which are of interest for heat transport, they shall satisfy the following periodic boundary conditions:

$$\psi(x,y,z) = \psi(x+L_x,y,z) = \psi\big(x,y+L_y,z\big) = \psi(x,y,z+L_z). \tag{3.22}$$

When these boundary conditions are applied, equation (3.21) has solutions of the form:

$$\psi_{\mathrm{k}}(\mathbf{r}) = \mathrm{e}^{i\mathbf{k}\cdot\mathbf{r}}, \tag{3.23}$$

where the components of **k** take the form $k_x = 2\pi n/L_x$ and n is an integer.

In contrast to particles in a classical gas, the free electrons in a metal are fermions obeying the Pauli Exclusion Principle – i.e. no two electrons can occupy the same quantum state. The probability of a certain state (as defined by the wavevector **k**) being occupied is a function of its energy and is given by the Fermi-Dirac distribution function[9]:

$$f(\epsilon) = \frac{1}{\mathrm{e}^{(\epsilon-\mu)/k_BT}+1}. \tag{3.24}$$

This function gives the central properties of the electron gas in a solid. At 0 K all electron states up to energy μ are occupied and all states above this energy are empty. Temperatures above 0 K cause a small number of states above μ to become occupied, while a small number below μ are left empty. At 0 K, the chemical potential is equal to the Fermi energy, ϵ_F – i.e. the energy up to which all states are occupied at 0 K. In a typical metal, $\mu \approx \epsilon_F$ at all temperatures below its melting point [16]. In Figure 3.2 the Fermi distribution is plotted for a chemical potential of 10 eV at temperatures of 300 K and 5000 K. It is clear that for all temperatures up to room temperature, the Fermi distribution very closely approximates a step function. The spread of the step (the energy range over which the probability of occupation is neither 1 nor 0) is of the order of k_BT.

[9] Referred to hereafter for brevity as the Fermi distribution

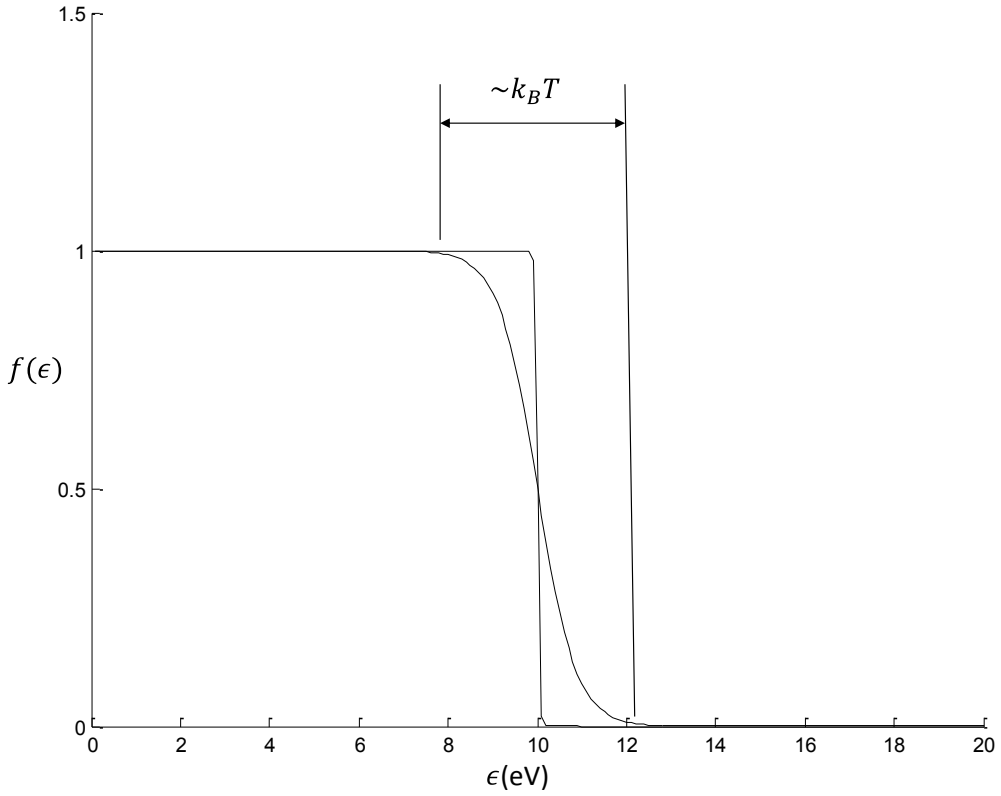

Figure 3.2: The Fermi function plotted for temperatures of 300 K and 10000 K.

One of the key implications of Fermi statistics is that only electrons within $k_B T$ of the Fermi energy can be excited thermally because only for these electrons can a thermal energy of $k_B T$ gain them access to unoccupied states. This is in stark contrast to the classical assumption that every electron gains an energy $\sim k_B T$ when a sample is heated. The fraction of electrons that can be thermally excited at temperature T is $k_B T/\epsilon_F$. Defining a Fermi "temperature" $T_F = \epsilon_F/k_B$, the total electronic thermal energy of an N electron Fermi gas at temperature T is therefore of the order of

$$U \approx (NT/T_F)k_B T, \tag{3.25}$$

which suggests the electronic heat capacity will be given by

$$C_{el} = \frac{\partial U}{\partial T} \approx N k_B (T/T_F). \tag{3.26}$$

A more detailed calculation (for $k_B T \ll \epsilon_F$) reveals, in contrast to equation (3.19), that the electronic heat capacity will be [129]:

$$C_{el} = \frac{1}{3}\pi^2 D(\epsilon_F) {k_B}^2 T = \frac{1}{2}\pi^2 N k_B \frac{T}{T_F}, \tag{3.27}$$

where $D(\epsilon_F)$ is the density of states at the Fermi energy, defined as:

$$D(\epsilon_F) = \frac{3N}{2k_B T_F}. \tag{3.28}$$

Equation (3.27) demonstrates the important result that the electronic heat capacity is proportional to T; this is reflected in the measured heat capacities of metals at low temperatures [16,129]. Inserting (3.27) into equation (3.9) and using $\epsilon_F = k_B T_F = \frac{1}{2} m_e {\mathrm{v}_F}^2$, the thermal conductivity of a Fermi gas can be written as:

$$\kappa_{el} = \frac{\pi^2}{3}\frac{n {k_B}^2 T}{m_e {\mathrm{v}_F}^2}\mathrm{v}_F \Lambda = \frac{\pi^2 n {k_B}^2 T \tau}{3 m_e}, \tag{3.29}$$

where $\Lambda = \mathrm{v}_F \tau$. This predicts a linear dependence of electronic thermal conductivity on temperature.

If the specific heat determined above (see equation (3.27)) is used in formulating the Wiedemann-Franz law, the constant of proportionality is modified slightly:

$$\frac{\kappa}{\sigma} = \frac{\pi^2}{3}\frac{{k_B}^2}{e^2} T = \mathrm{L_0 T}. \tag{3.30}$$

The value of the Lorenz number in this case is 2.45×10^{-8} $\mathrm{W\Omega K^{-2}}$ and this theoretical value is often in very good agreement with experimental results [155]. There are, however, many situations where the experimentally determined value differs from the theoretical one [156]. As shown in 3.5.2.1, the reason behind discrepancies with experiment is that the underlying assumption of the law (that the scattering processes have the same effect on both the electrical and thermal conductivities) is not always a good one.

3.2.1 The Effect of the Crystal Lattice

If interactions between the electrons and the crystal lattice are ignored (the "free electron" approximation), their energy is a continuous function of their wavevector:

$$\epsilon = \frac{\hbar^2 k^2}{2m_e}. \tag{3.31}$$

The "dispersion relation" (energy–wavevector relation) for this case is sketched on the left side of Figure 3.3:

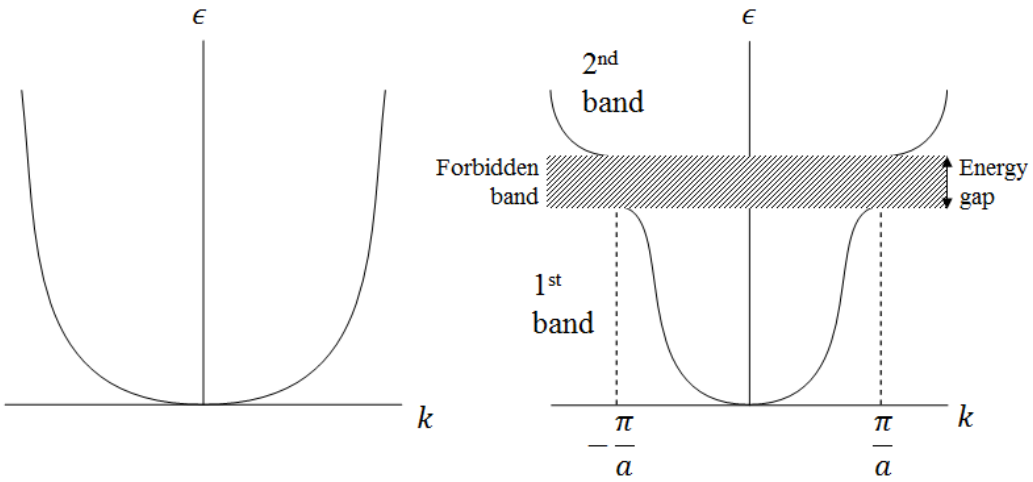

Figure 3.3: Formation of band gaps in k-space (after [129]).

Introducing the effects of the crystal lattice complicates this picture. One impact is the creation of a "band gap"; electrons will be Bragg reflected in a periodic crystal where when their wavevectors satisfy the following condition [16]:

$$\mathrm{G}^2 = 2\mathbf{k} \cdot \mathbf{G} \tag{3.32}$$

where $\mathbf{G}$ is the reciprocal lattice vector. In a 1-dimensional lattice with a repeating length a, electrons with wavevectors $k = \pm n\pi/a$ (where n is an integer) will be reflected at the crystal planes. For $n = 1$ such waves will be of the form $\mathrm{e}^{\pm i\pi x/a}$. The reflected waves combine to form standing waves and they can do so in two ways: either waves travelling in

the same direction will combine (indicated by $\psi(+)$ below), or waves travelling in opposite directions will combine ($\psi(-)$):

$$\psi(+) = \mathrm{e}^{i\pi x/a} + \mathrm{e}^{-i\pi x/a} = 2\cos(\pi x/a)$$
$$\psi(-) = \mathrm{e}^{i\pi x/a} - \mathrm{e}^{-i\pi x/a} = 2i\sin(\pi x/a). \tag{3.33}$$

Whether the constituent waves were travelling in the same or opposite directions will determine whether these standing tend to build up charge at, or between, the ion cores. Since the probability density is the square of the wavefunction

$$P(+) = |\psi(+)|^2 \propto \cos^2(\pi x/a)$$
$$P(-) = |\psi(-)|^2 \propto \sin^2(\pi x/a). \tag{3.34}$$

These probability densities are shown in Figure 3.4. The probability density that builds up charge at the ion cores, $P(+)$, will result in a lower potential energy than that which builds up charge away from the ion cores $P(-)$, since the electrostatic potential is lower in these locations. The two situations thus give rise to two distinct electron energies for a given wavevector and cause a discontinuity in the dispersion relation (a "band gap") whenever equation (3.32) is satisfied [129]. This is shown on the right side of Figure 3.3. There are no travelling wave solutions to Schrödinger's equation in this energy gap.

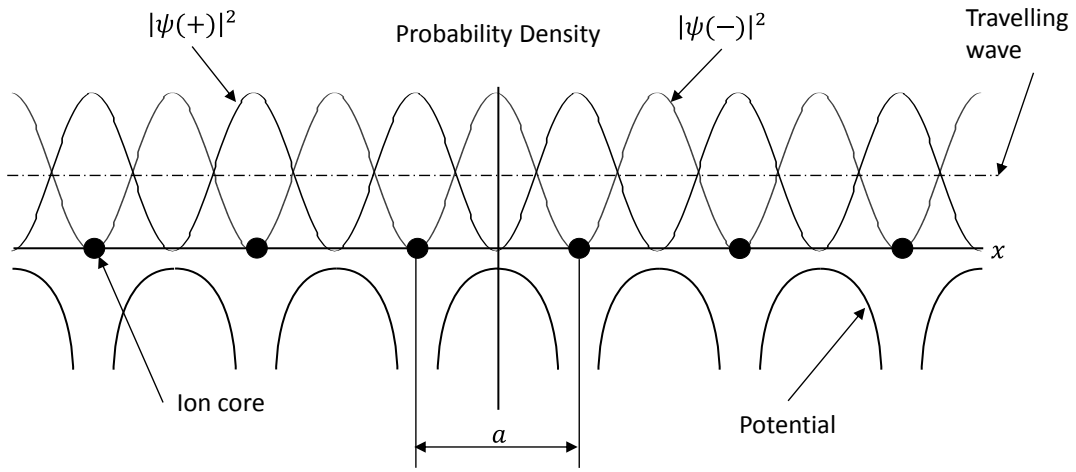

Figure 3.4: Probability density distributions for the two standing waves resulting from Bragg reflection and a travelling wave (after [129]).

Of concern for transport processes is the form of the wavefunction in a periodic potential for which travelling wave solutions of the Schrödinger equation *do* exist. Solving the Schrödinger equation for particles in a periodic potential leads to Bloch's theorem [16], which states that solutions must take the form:

$$\psi_{\mathrm{k}}(\mathbf{r}) = u_{\mathrm{k}}(\mathbf{r})\mathrm{e}^{i\mathbf{k}\cdot\mathbf{r}}, \tag{3.35}$$

where $u_{\mathrm{k}}(\mathbf{r})$ is a function with the same periodicity as the lattice. The significance of this result for electron transport is that the properties of the electron in a periodic potential are analogous to those of a free electron, for which $\mathbf{v} = \hbar\mathbf{k}/m_e$ [157]. Providing nothing disturbs the lattice's periodicity, a "Bloch electron" (i.e. an electron whose wavefunction is of the form (3.35)) can move through it unhindered and this leads to very long mean free paths when the periodicity of the crystal is unaffected by lattice imperfections or phonons. This unhindered motion is due to the wave nature of electrons: a wave can propagate without attenuation in a periodic array of scattering centres because of constructive interference between waves that are scattered [16]. Although the periodicity of any real crystal will never be perfect, high purity single crystals can approach this state and the long electron mean free paths that result can lead to very high conductivities. The mean free path (and therefore the conductivity) will be further enhanced at low temperatures where there are fewer phonons to disturb the lattice.

A wavefunction of the form of (3.35) can be written as a sum of plane waves ($\mathrm{e}^{i\mathbf{k}\cdot\mathbf{r}}$), each modulated by a function with the periodicity of the lattice. In this way, the electron may be represented as a wave-packet. The velocity of the wave-packet can therefore be expressed in terms of a group velocity. From the definition of group velocity [158]:

$$\mathbf{v} = \frac{d\omega}{d\mathbf{k}}, \tag{3.36}$$

where ω is the angular frequency, and using de Broglie's relation

$$\epsilon = hf = \hbar\omega, \tag{3.37}$$

the velocity of a Bloch electron can be expressed as:

$$\mathbf{v} = \frac{1}{\hbar}\frac{d\epsilon}{d\mathbf{k}} = \frac{1}{\hbar}\nabla_{\mathbf{k}}\epsilon. \tag{3.38}$$

Equation (3.38) shows that in a periodic crystal, the electron's velocity is proportional to the energy gradient in k-space and will therefore be directed normal to surfaces of constant energy in k-space (e.g. the Fermi surface).

3.2.2 Semi-Classical Transport Theory

Quantum theory is incorporated into electron transport through the "semi-classical model" [159]. Its applicability has the following restrictions:

i. the mean free path of a carrier must be greater than its wavelength;
ii. the spread of the wave-packet must be greater than the lattice spacing;
iii. any variation in applied fields must occur over much greater distances than the size of the wave-packet.

When the above conditions apply, it is acceptable to treat the electron wave-packets like particles. Provided their wavefunctions satisfy Bloch's theorem, interaction with the periodic potential from the ions has already been accounted for implicitly and it is permissible to follow their motion through the lattice as if they were free particles.

The Pauli Exclusion Principle dictates that each electron in a metal occupies a unique quantum state, determined by the components of its wavevector $(\mathrm{k}_1, \mathrm{k}_2, \mathrm{k}_3)$ and its spin. Fermi-Dirac statistics then determine how these states will be filled: at 0K all states up to the Fermi energy are filled, while those above it are empty; at temperatures above 0K, some states above the Fermi energy will become occupied, leaving some states below it empty. As noted above, the change in the distribution only occurs within a region of the order of $k_B T$ about the Fermi energy. Some states are associated with positive velocities and others

with negative velocities[10]. It is by considering the net result when all states are summed, that a flow of charge or energy (heat) is revealed.

Without any applied fields, the distribution of states is centred about $\mathbf{k} = 0$ and there is no net flow of charge. For charge transport, an electric field is applied to the electron gas, which exerts a force (equal to $-e\boldsymbol{E}$) on the individual electrons and modifies their wave vectors according to [16]:

$$\boldsymbol{F} = \hbar \frac{d\mathbf{k}}{dt}. \tag{3.39}$$

As a result of this, electrons at the Fermi surface acquire a small additional velocity on top of the Fermi velocity (the *drift velocity*). If their initial velocity was in the direction of the applied field, they will move up to slightly higher energy states and electrons from lower energies move up to fill the states vacated. The distribution of states is thus shifted in k-space and using (3.39) this change can be written [157]:

$$\frac{df}{dt} = \frac{\boldsymbol{F}}{\hbar} \cdot \frac{\partial f_{\mathbf{k}}^0}{\partial \mathbf{k}}, \tag{3.40}$$

where $f_{\mathbf{k}}^0$ is the equilibrium Fermi distribution. When all the states are summed there will be surplus of electrons with velocities in the direction of the field.

For the case of thermal transport, it is not an imbalance in the total number of electrons with velocities in one direction as opposed to another that occurs; rather it is the imbalance in their energies. A temperature difference along the sample creates a "hot" region at one end and a "cold" region at the opposite end. Electrons moving from the "hot" to the "cold" region have greater thermal energy than those moving in the opposite direction. The effect on the Fermi distribution is to spread the "step" on the side that corresponds to electron velocities in the direction of the temperature gradient (i.e. from "hot" to "cold") and sharpen

[10] Depending on the shape of the Fermi surface, it may be that positive wavevectors do not always correspond to positive velocities.

the "step" on the opposite side. This has important consequences for the scattering mechanisms (see 3.5.2.1).

In analysing both the electrical and thermal transport cases, the aim is not to follow the motion of individual carriers, but to observe changes to distribution of all the electron states in the sample. This statistical approach to calculating transport coefficients leads to the Boltzmann equation which is discussed in 3.3.

3.3 The Boltzmann Equation

The Boltzmann equation is a continuity equation describing the evolution in time of the distribution function of a group of carriers. In principle, it allows the mathematical formulation of any transport problem for any type of carriers in terms of their distribution function. The remainder of this section concentrates on its application to electrons and so the appropriate distribution is the Fermi function $f_{\mathbf{k}}(\mathbf{r})$, changes to which result from three effects: diffusion, external fields (electric and magnetic) and scattering. This can be expressed mathematically as follows:

$$\dot{f}_{\mathbf{k}} = \dot{f}_{\mathbf{k}}\big|_{diff} + \dot{f}_{\mathbf{k}}\big|_{field} + \dot{f}_{\mathbf{k}}\big|_{scatt}. \tag{3.41}$$

In steady-state the left hand side vanishes to give the Boltzmann equation in its general form [154]:

$$-\mathbf{v}_{\mathbf{k}} \cdot \frac{\partial f_{\mathbf{k}}}{\partial \mathbf{r}} - \frac{e}{\hbar}(\boldsymbol{E} + \mathbf{v}_{\mathbf{k}} \times \boldsymbol{B}) \cdot \frac{\partial f_{\mathbf{k}}}{\partial \mathbf{k}} = -\dot{f}_{\mathbf{k}}\big|_{scatt}. \tag{3.42}$$

The first term on the left hand side represents the changes to the distribution due to carrier diffusion, while the second term represents the effects of external fields. These are equated to the effects of scattering.

A small deviation from the equilibrium Fermi distribution ($f_{\mathbf{k}}^{0}$) in steady-state can be defined as:

$$g_{\mathbf{k}} = f_{\mathbf{k}} - f_{\mathbf{k}}^0 \tag{3.43}$$

and substituting (3.43) into (3.42) gives

$$\begin{aligned} -\mathbf{v}_{\mathbf{k}} \cdot \frac{\partial f_{\mathbf{k}}^0}{\partial T} \nabla T - \frac{e}{\hbar}(\boldsymbol{E} + \mathbf{v}_{\mathbf{k}} \times \boldsymbol{B}) \cdot \frac{\partial f_{\mathbf{k}}^0}{\partial \mathbf{k}} \\ = -\dot{f}_{\mathbf{k}}\big|_{scatt} + \mathbf{v}_{\mathbf{k}} \cdot \frac{\partial g_{\mathbf{k}}}{\partial \mathbf{r}} + \frac{e}{\hbar}(\boldsymbol{E} + \mathbf{v}_{\mathbf{k}} \times \boldsymbol{B}) \cdot \frac{\partial g_{\mathbf{k}}}{\partial \mathbf{k}}. \end{aligned} \tag{3.44}$$

The scattering term can be written as [160]:

$$\dot{f}_{\mathbf{k}}\big|_{scatt} = \int \{f_{\mathbf{k}'}(1 - f_{\mathbf{k}}) - f_{\mathbf{k}}(1 - f_{\mathbf{k}'})\} Q(\mathbf{k}, \mathbf{k}') d\mathbf{k}'. \tag{3.45}$$

This shows that the scattering rate depends on the transition probability $Q(\mathbf{k}, \mathbf{k}')$ of an electron from state $\mathbf{k}$ to $\mathbf{k}'$, weighted by the probability that state $\mathbf{k}$ is initially occupied and state $\mathbf{k}'$ is initially empty, and integrated over all k-states. The reverse process from state $\mathbf{k}'$ to $\mathbf{k}$ is also accounted for, with the sign convention set such that scattering from $\mathbf{k}$ to $\mathbf{k}'$ decreases $f_{\mathbf{k}}$.[11] The formulation also assumes elastic scattering. Transition probabilities are not usually known, so simplifications have to be made when tackling real conduction problems (see 3.3.1).

It is common to simplify (3.44) still further [154] by assuming that the deviation from equilibrium in the steady state will be small enough that the terms involving $g_{\mathbf{k}}$ on the right-hand side can be ignored. This leads to the linearised Boltzmann equation:

$$\begin{aligned} -\mathbf{v}_{\mathbf{k}} \cdot \frac{\partial f_{\mathbf{k}}^0}{\partial T} \nabla T - \frac{e}{\hbar}(\boldsymbol{E} + \mathbf{v}_{\mathbf{k}} \times \boldsymbol{B}) \cdot \frac{\partial f_{\mathbf{k}}^0}{\partial \mathbf{k}} \\ = \int \{f_{\mathbf{k}'}(1 - f_{\mathbf{k}}) - f_{\mathbf{k}}(1 - f_{\mathbf{k}'})\} Q(\mathbf{k}, \mathbf{k}') d\mathbf{k}'. \end{aligned} \tag{3.46}$$

An elementary solution of this equation exists under certain specific conditions:

[11] The principle of microscopic reversibility asserts that the transition probability between two states of a system is the same regardless of the direction of the transition. It is a consequence of the principle of detailed balance: for a system in equilibrium to maintain constant entropy $f_i Q_{ij} = f_j Q_{ji}$, where f_i is the probability of the system being in state i, Q_{ij} is the conditional transition probability between states i and j and likewise when the subscripts are swapped [161].

i. Energy surfaces in k-space are spherical such that $\mathbf{v_k}$ and $\mathbf{k}$ are both in the same direction. Therefore, the left hand side is the scalar product of $\mathbf{v_k}$ with a vector which is constant on a spherical surface and so is proportional to cosine of the angle between the two.

ii. Scattering probability depends only on the angle between $\mathbf{k}$ and $\mathbf{k}'$. This assumption leads to the definition of a *differential transition probability*, $Q(k,\theta)d\Omega$, which is the probability that a particle of momentum $\hbar k$ is scattered through the angle θ into the solid angle $d\Omega$.

The form of the resulting solution is [154]:

$$(f_{\mathbf{k}} - f_{\mathbf{k}}^0) = -\mathbf{v_k} \cdot \left(\frac{\partial f_{\mathbf{k}}^0}{\partial T} \nabla T - e \frac{\partial f_{\mathbf{k}}^0}{\partial \epsilon_{\mathbf{k}}} \boldsymbol{E} \right) \Big/ \int (1 - \cos\theta) Q(k,\theta) d\Omega. \quad (3.47)$$

A mixed scattering process (such as between electrons and phonons) fits just as well into the same formulation [154]. Hence, the approach of balancing the rate of changes in the distribution function provides a basis for analysing any general transport problem.

When the above simplifications cannot be made, the form of (3.45) leads to an integro-differential equation, solutions of which are not easily found. The "variational method" [154,162] may be used. This technique defines a "variational function" which must be minimised to obtain the best solution. The process starts by selection of a trial function of a certain number of arbitrary parameters, which are then varied to minimise the variational function. Even then, numerical solutions may still have to be used in order to calculate conductivities.

3.3.1 The Relaxation Time Solution

Using the concept of a relaxation time as introduced in 3.1, the scattering term in the Boltzmann equation can be written in a much simplified form:

$$-\frac{\partial f_{\mathbf{k}}}{\partial t}\Big|_{scatt} = \frac{f_{\mathbf{k}} - f_{\mathbf{k}}^0}{\tau} = \frac{g_{\mathbf{k}}}{\tau}. \tag{3.48}$$

With this definition of the scattering term, the linearised Boltzmann equation now takes the form

$$-\mathbf{v}_{\mathbf{k}} \cdot \frac{\partial f_{\mathbf{k}}^0}{\partial T}\nabla T - \frac{e}{\hbar}(\boldsymbol{E} + \mathbf{v}_{\mathbf{k}} \times \boldsymbol{B}) \cdot \frac{\partial f_{\mathbf{k}}^0}{\partial \mathbf{k}} = \frac{f_{\mathbf{k}} - f_{\mathbf{k}}^0}{\tau}. \tag{3.49}$$

The magnetic field term on the left hand side of this equation will cancel, as can be shown by re-writing the differential of the equilibrium Fermi distribution as follows [154]:

$$\frac{e}{\hbar}(\mathbf{v}_{\mathbf{k}} \times \boldsymbol{B}) \cdot \frac{\partial f_{\mathbf{k}}^0}{\partial \mathbf{k}} = \frac{e}{\hbar}(\mathbf{v}_{\mathbf{k}} \times \boldsymbol{B}) \cdot \frac{\partial \epsilon}{\partial \mathbf{k}}\frac{\partial f_{\mathbf{k}}^0}{\partial \epsilon} = \frac{e}{\hbar}(\mathbf{v}_{\mathbf{k}} \times \boldsymbol{B} \cdot \mathbf{v}_{\mathbf{k}})\hbar\frac{\partial f_{\mathbf{k}}^0}{\partial \epsilon} = 0. \tag{3.50}$$

The magnetic field therefore has no net effect on the equilibrium distribution, so it is dropped from the expressions from this point. Evaluating the differentials of the Fermi distribution function (see Appendix D) leads to:

$$\left(-\frac{\partial f_{\mathbf{k}}^0}{\partial \epsilon}\right)\mathbf{v}_{\mathbf{k}} \cdot \left(-\left(\frac{\epsilon - \mu}{T}\right)\nabla T + e\boldsymbol{E} - \nabla\mu\right) = \frac{f_{\mathbf{k}} - f_{\mathbf{k}}^0}{\tau}, \tag{3.51}$$

which permits an elementary solution for the non-equilibrium distribution function:

$$f_{\mathbf{k}} = f_{\mathbf{k}}^0 + \left(-\frac{\partial f_{\mathbf{k}}^0}{\partial \epsilon}\right)\tau\mathbf{v}_{\mathbf{k}} \cdot \left(-\left(\frac{\epsilon - \mu}{T}\right)\nabla T + e\boldsymbol{E} - \nabla\mu\right). \tag{3.52}$$

Using this method of solution carries further implicit assumptions [159]:

i. The distribution of electrons emerging from a collision does not depend on the non-equilibrium distribution function just prior to the collision. This asserts that collisions are completely effective in destroying information about the non-equilibrium distribution prior to the collision, which will overstate their impact in some cases (see 3.5.2.1).

ii. The electrons in the region about $\mathbf{r}$ have an equilibrium distribution appropriate to the local temperature (i.e. the Fermi distribution) and this is not altered by collisions. This ensures that collisions maintain the thermodynamic equilibrium.

In its most general form, the relaxation time may be a function of position, wavevector and band in which the scattering occurs – i.e. $\tau = \tau_n(\mathbf{r}, \mathbf{k})$ where the subscript refers to the band in question.

3.4 Calculating Conductivities

3.4.1 Thermal Conductivity

The Boltzmann equation provides a method to calculate the distribution function under certain conditions of applied field and temperature gradient. If the distribution function is known, it is then possible to calculate the electronic heat flux (per unit volume) according to:

$$\dot{q} = \frac{2}{8\pi^3} \int \epsilon_{\mathbf{k}} \mathbf{v}_{\mathbf{k}} f_{\mathbf{k}} \, \boldsymbol{d}\mathbf{k}. \tag{3.53}$$

Equation (3.53) is just an expression of the fact that the heat current is the sum of all the electrons (in a unit volume) multiplied by the energy they are carrying and their velocities. The numerical factor before the integral arises from the fact that there are $1/8\pi^3$ states in a unit volume of k-space, since in any given direction (k_x, k_y, k_z) the allowable states are spaced at intervals of $2\pi/L$ and there is therefore exactly one in a volume of $(2\pi/L)^3 = 8\pi^3/V$. This follows directly from the Schrödinger equation of an electron in a fixed volume (i.e. the sample) for which solutions must be multiples of $2\pi/L$ (see 3.2). The factor of 2 appearing on top of the fraction accounts for the electron spin degeneracy – i.e. for every k-state in the distribution there will be two possible electron states: one spin-up and one spin-down. Multiplying by the distribution function and integrating over all of k-space then gives the total number of electrons.

In fact, equation (3.53) is not entirely correct. This can be seen by considering the arrival at the end of a sample of an electron whose energy is far below the Fermi energy. As there will be no available states at this energy, all of the thermally excited electrons must donate a proportion of their energy to lift the new arrival into an unoccupied state [163]. Although this electron has a non-zero energy, it actually transports "cold" rather than heat. Therefore, to calculate the heat current properly, the electrons' energies must be related to some reference value. This is equivalent to recognising that heat is internal energy minus free energy [160]. The free energy in this case is the electron's chemical potential, μ, giving:

$$\dot{q} = \frac{1}{4\pi^3}\int (\epsilon_{\mathbf{k}} - \mu)\mathbf{v}_{\mathbf{k}} f_{\mathbf{k}}\, \mathbf{dk}. \tag{3.54}$$

3.4.2 Electrical Conductivity

There is a corresponding expression for the electrical conductivity

$$j = \frac{1}{4\pi^3}\int e\mathbf{v}_{\mathbf{k}} f_{\mathbf{k}} \mathbf{dk}. \tag{3.55}$$

As described in 3.2, one can think of the electric current in terms of the displacement of the Fermi surface caused by the electric field. The change of electron wavevector resulting from an applied electric field is given by (3.39). This displaces the whole electron distribution in k-space and the amount of the displacement ($\delta\mathbf{k}$) in time δt is given by

$$\delta\mathbf{k} = e\boldsymbol{E}\delta t/\hbar. \tag{3.56}$$

The rate of displacement due to the field is then

$$\left.\frac{d\mathbf{k}}{dt}\right|_{field} = \frac{e\boldsymbol{E}}{\hbar}. \tag{3.57}$$

The fact that the displacement does not continue indefinitely is due to the restoring effect of collisions, whose impact on the distribution is found from the relaxation time (i.e. by

assuming exponential decay towards the equilibrium distribution on removal of the applied field) [164]:

$$\delta\mathbf{k} = \delta\mathbf{k}_\infty(1 - \mathrm{e}^{-t/\tau}). \tag{3.58}$$

Therefore, the initial rate of decay (at $t = 0$) is given by:

$$\left.\frac{d\mathbf{k}}{dt}\right|_{scatt} = -\frac{\delta\mathbf{k}_\infty}{\tau}. \tag{3.59}$$

Equilibrium is reached when the two rates balance:

$$\frac{e\boldsymbol{E}}{\hbar} - \frac{\delta\mathbf{k}_\infty}{\tau} = 0. \tag{3.60}$$

The amount that the distribution shifts in k-space is then found to be

$$\delta\mathbf{k}_\infty = \frac{e\boldsymbol{E}\tau}{\hbar}. \tag{3.61}$$

Now, the current that results from this displacement (i.e. the effect of additional electrons with velocities in the direction of the field and the reduction of electrons with velocities opposite to the field) integrated over the entire Fermi surface is:

$$j = \frac{1}{4\pi^3}\int e\mathbf{v}_\mathbf{k}\delta\mathbf{k}_\infty dS_F. \tag{3.62}$$

Substituting (3.61) into (3.62) gives:

$$j = \frac{e^2\tau}{4\pi^3\hbar}\int \mathbf{v}_\mathbf{k} dS_F \cdot \boldsymbol{E}, \tag{3.63}$$

so that, using Ohm's law, the conductivity is given by:

$$\sigma = \frac{e^2\tau}{4\pi^3\hbar}\int \mathbf{v}_\mathbf{k} dS_F. \tag{3.64}$$

3.4.3 Matthiessen's Rule

Matthiessen's rule [154] states that the contributions of all scattering processes are additive – i.e.

$$\rho = \rho_1 + \rho_2 + \cdots \tag{3.65}$$

or, equivalently:

$$\frac{1}{\tau} = \frac{1}{\tau_1} + \frac{1}{\tau_2} + \cdots \tag{3.66}$$

The subscripts refer to contributions to the resistivity (or relaxation time) arising from different sources, typically factors such as impurities, phonon scattering, etc. The implicit assumption is that these will be independent, although this is not always true for all types of scattering. The rule is sometimes phrased as the existence of a temperature independent resistance term (due to impurities) which is combined with a temperature dependent term (ascribed to phonon scattering) to give the total resistance [129].

The rule allows different scattering processes to be subsumed into a single relaxation time, which can then be employed in formulae such as (3.52) and (3.64). A useful corollary is that where multiple scattering processes are present, the one with the shortest relaxation time will dominate. This can be useful when interpreting the variation of conductivity with temperature since different scattering mechanisms will dominate at different temperatures (see 3.5.2.1).

Although of great utility (as demonstrated below), it is a fairly crude way of viewing the interaction of scattering processes and is highly likely to be inaccurate when one scattering process influences another, or when one or more of the relaxation times are functions of **k**. To account for the latter, it would be necessary to calculate a total relaxation time due to all processes averaged over all **k** values – i.e.

$$\frac{1}{k}\sum_{k}\left(\frac{1}{\tau_1}+\frac{1}{\tau_2}+\cdots\right)_k. \tag{3.67}$$

In contrast, Mathiessen's rule can only account for averaging over different **k** in the individual relaxation times, the reciprocals of which are then summed – i.e.

$$\frac{1}{k}\sum_{k}\frac{1}{\tau_{1_k}}+\frac{1}{k}\sum_{k}\frac{1}{\tau_{2_k}}+\ldots \tag{3.68}$$

Deviations from Matthiessen's Rule continue to be a subject of research and this has been reviewed by van Vucht *et al* [165].

3.5 Scattering Mechanisms in Electronic Heat Transport

3.5.1 Impurity and Grain Boundary Scattering

Anything which disturbs the perfect periodicity of the crystal will be a source of scattering for Bloch electrons. There are several different features which may give rise to such disturbances and they may be categorised according to their dimensionality:

i. Point imperfections (e.g. vacancies, interstitials, impurities, isotopes);
ii. Line imperfections (e.g. dislocations);
iii. Surfaces of imperfection (e.g. grain boundaries, twin boundaries, stacking faults);
iv. Volume disorder, such as substitutional alloys.

Of these, point imperfections will generally have a greater effect on the scattering of electrons because of the electric charge associated with the defect.

Impurity scattering can almost always be considered an elastic process because the energy between the impurity's ground state and its lowest excited state is usually large compared with $k_B T$. This means that for an electron to give up its energy to excite an impurity it would need to drop into a low-lying energy state deep below the Fermi surface and the

Fermi distribution dictates that it is extremely unlikely to find such a state unoccupied. Energy exchange in the opposite direction – from impurity to electron – is unlikely to occur simply because the large energy gap makes it unlikely to find impurities in an excited state. An additional simplifying feature is that the electron-impurity interaction is independent of the other electrons and hence it does not depend on the form of the electron distribution function.

Impurity scattering is independent of temperature and therefore becomes increasingly dominant as the temperature drops and scattering of electrons by phonons (see 3.5.2) or other electrons (see 3.5.3) reduces.

3.5.2 Scattering of Electrons by Phonons

In addition to impurities and grain boundaries, the perfect periodicity of the lattice may be destroyed by thermal excitations of the ions (i.e. phonons) causing them to oscillate about their equilibrium positions. Such distortions in the periodicity of the lattice may scatter an electron either elastically or inelastically [16]: in elastic processes the phonon and electron both change wavevector in such a way that energy and momentum are conserved; in inelastic processes a phonon is either emitted or absorbed by the electron, causing the electron's wavevector and energy to change. An additional inelastic process results from the fact that the electron's charge will distort the lattice around it. This distortion is another way in which an electron can emit a phonon and lose energy.

In inelastic processes, both absorption and emission will follow a similar temperature dependence which results from the phonon energy. At temperature T, the characteristic phonon energy is $\sim k_B T$ (see 3.5.2.1) and this is therefore the energy absorbed by the electron; in the case of emission, the characteristic energy is limited by the available states which the electron can subsequently scatter into; this is also $\sim k_B T$ because emitting a higher energy phonon would scatter the electron to a low energy state in the depths of the Fermi sea and all such states will already be occupied.

3.5.2.1 The Breakdown of the Wiedemann-Franz Law

The Wiedemann-Franz law as formulated from quantum considerations (see 3.1.1) will hold for any situation where scattering is elastic. This will almost certainly be the case for scattering by lattice imperfections and the law is expected to be obeyed when these dominate (e.g. at low temperatures in impure crystals).

However, it cannot always be relied up when phonon scattering dominates. The reason for this is that while an electric current can only be degraded by changing the velocities of electrons (since their charge is always conserved), a thermal current can be degraded by changing either the velocity or energy of the electrons. If the energy of an electron is conserved – as it will be in elastic collisions – then the scattering process affects both thermal and electrical currents in the same way, and the Wiedemann-Franz law will be respected. Should an electron's energy not be conserved[12], however, this scattering process may degrade the thermal current without affecting the electrical current and the law can break down.

The influence of inelastic electron scattering is shown in Figure 3.5 for the idealised spherical (i.e. free-electron) Fermi surface. Electric current flow is illustrated on the left side; thermal current flow is shown on the right side. In bottom half of the figure are the distribution functions for each case: the solid line represents the equilibrium distribution, while the dashed line represents the steady state transport distribution. The top half of the figure shows the Fermi surfaces, with extra electrons indicated by black dots and electron deficiencies (i.e. empty states) indicated by white dots.

[12] Such as by emission of a phonon.

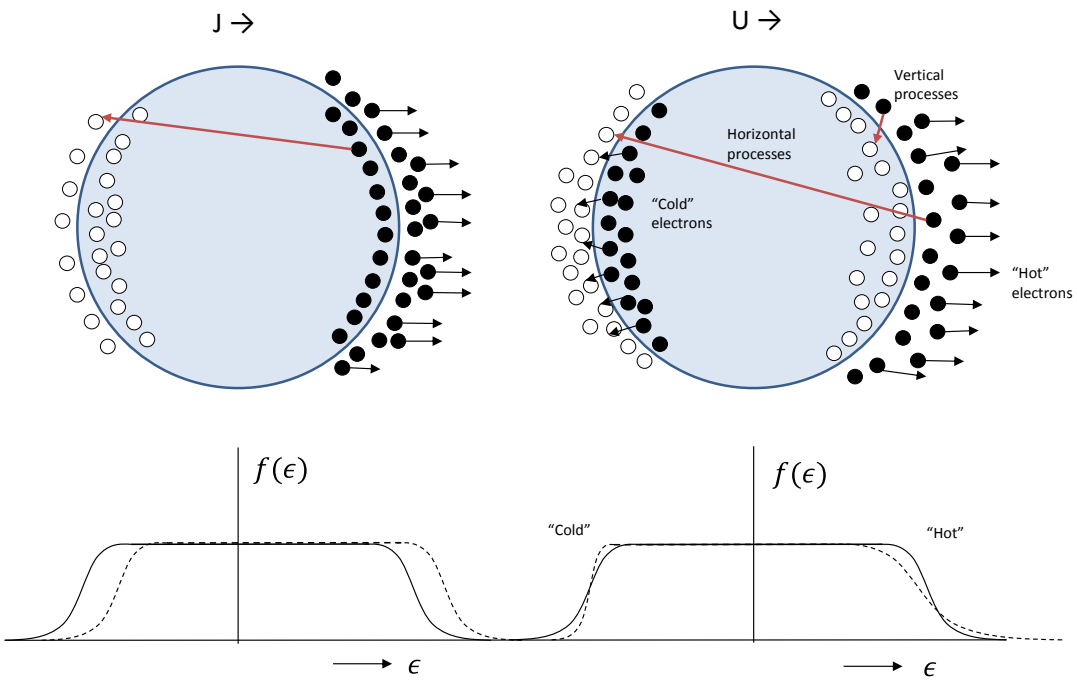

Figure 3.5: Fermi surface and distribution functions for electrical conduction (left) and thermal conduction (right).
Adapted from [154].

The left side of the figure shows that in electrical conduction, when the Fermi distribution is just shifted in the direction of current flow, the only available states into which an electron can be scattered are all the way on the other side of the Fermi surface. To within the "smearing" of the Fermi function these states will be at the same energy and the scattering is elastic.

In the thermal case (right side of Figure 3.5), the Fermi distribution takes different forms for the "hot" electrons travelling down the thermal gradient and the "cold" electrons travelling up it. This creates available states just below the Fermi energy, in addition to those on the opposite side of the Fermi surface. The current can now be degraded in one of two ways: electrons can be scattered all the way across the Fermi surface in the same way as in electric conduction (these are called "horizontal" processes), or it can be scattered into one of the vacant states just below the Fermi surface (a "vertical" process). In the latter case, the energy of the electron has clearly decreased and the scattering process in inelastic.

For these inelastic processes to occur, phonons of the appropriate energy must be available. Although there will be a distribution of phonon energies at any given temperature, the distribution will have a peak and the energy at which the peak occurs can be calculated from Debye theory. Since the Debye model of phonons (see sections 3.6.1 and Appendix C) is based on the same principles as Planck's radiation law, the spectral density of phonon energy has the same distribution [14] – c.f. Appendix C:

$$\frac{x^3}{\mathrm{e}^x - 1}, \tag{3.69}$$

where $x = h\omega/k_B T$. The value of x at which the spectrum peaks can therefore be found from

$$\frac{d}{dx}\frac{x^3}{\mathrm{e}^x - 1} = 0. \tag{3.70}$$

Using the quotient rule to evaluate the differential, this becomes:

$$3 - 3\mathrm{e}^{-x} = x, \tag{3.71}$$

which can be solved numerically [14] to give

$$x_{max} \approx 2.82 = h\omega_{max}/k_B T. \tag{3.72}$$

To within a factor of three, then, the phonon energy ($h\omega_{max}$) at temperature T is equal to $k_B T$ and this can be used to determine whether there are phonons present of the appropriate energy for a particular scattering process.

The different contributions to the electronic thermal conductivity in the different temperature ranges are summarised in Table 3.1. θ_D is the Debye temperature (see 3.6.1), τ_κ is the thermal relaxation time and L_0 is the Lorenz number.

Temperature	Dominant Scattering mechanism	Relaxation time	Temperature dependence of κ	Lorenz number
$T \ll \theta_D$	Impurities	$\tau_\kappa \sim const$	$\kappa \propto T$	L_0
$T \sim \theta_D/10$	Phonons	$\tau_\kappa \propto T^{-3}$	$\kappa \propto T^{-2}$	$< L_0$
$T > \sim\theta_D$	Phonons	$\tau_\kappa \propto T^{-1}$	$\kappa =$ const.	L_0

Table 3.1: Variations in thermal conductivity and its effect on Lorenz number at different temperatures
(reproduced from [16]).

At room temperature[13] and above ($T > \sim\theta_D$) the phonon energy is of the order of $k_B\theta_D$ whereas the thickness of the thermal layer at the Fermi level will be $\sim k_B T$. Phonons are therefore unlikely to have sufficient energy to scatter an electron across the thermal layer into a vacant state just below the Fermi level (a vertical process). However, since θ_D is the temperature at which the highest phonon modes are excited (see 3.6.1), phonons with energy $k_B\theta_D$ will be the most energetic phonons and will have wavevectors that are roughly half the width of the Brillouin[14] zone (see the dispersion relation in 3.6). These wavevectors are approximately equal to the Fermi wavevector – i.e. $\mathbf{q} \sim \mathbf{k}_F$**.** Thus electrons can be scattered elastically all the way across the Fermi surface. The scattering rate will be proportional to the number of phonons, which increases according to T. The relaxation time therefore goes as T^{-1}, but is balanced by heat capacity of the electrons which increases linearly with T (see 3.2).

At lower temperatures ($T < \theta_D$) the phonon wavevector $\mathbf{q}$ will be much less than $\mathbf{k}_F$ and so scattering processes that involve vacant states in the vicinity of the local Fermi surface will be more probable. Equally, the phonon energy will be of the same order of the thickness of the thermal layer and emission of a phonon of this energy will be consistent with such

[13] For most metals room temperature is close to θ_D; for tungsten $\theta_D \sim$ 400 K [14].
[14] The Wigner-Seitz cell in k-space. The Wigner-Seitz cell is constructed from planes which bisect vectors joining adjacent lattice points.

vertical process. It is at these temperatures where the Wiedemann-Franz law breaks down. The effect is an example of the weakness in assuming a single relaxation time.

At very low temperatures ($T \ll \theta_D$) all but the longest wavelength phonons will be absent. The small wavevectors of these phonons almost totally preclude phonon scattering at all.

If Matthiessen's rule (equation (3.66)) is assumed to apply, an expression can be constructed for the temperature dependence of thermal conductivity using the different scattering rates in Table 3.1. This leads to an equation of the following form for the thermal conductivity of metals below their Debye temperature, when the primary scattering mechanisms are due to impurities and phonons:

$$\frac{1}{\kappa} = \frac{A}{T} + BT^2. \tag{3.73}$$

The first term is the result of a temperature independent relaxation time for impurity scattering coupled to the linear temperature dependence of the electronic heat capacity (see 3.2); the second term results from a combination of the T^3 Debye phonon spectrum with the same linear dependence of heat capacity. A more rigorous mathematical derivation of the same result can be arrived at by application of the variational principle to solve the Boltzmann equation [154]. Figure 3.6 illustrates how the different effects dominate at different temperatures.

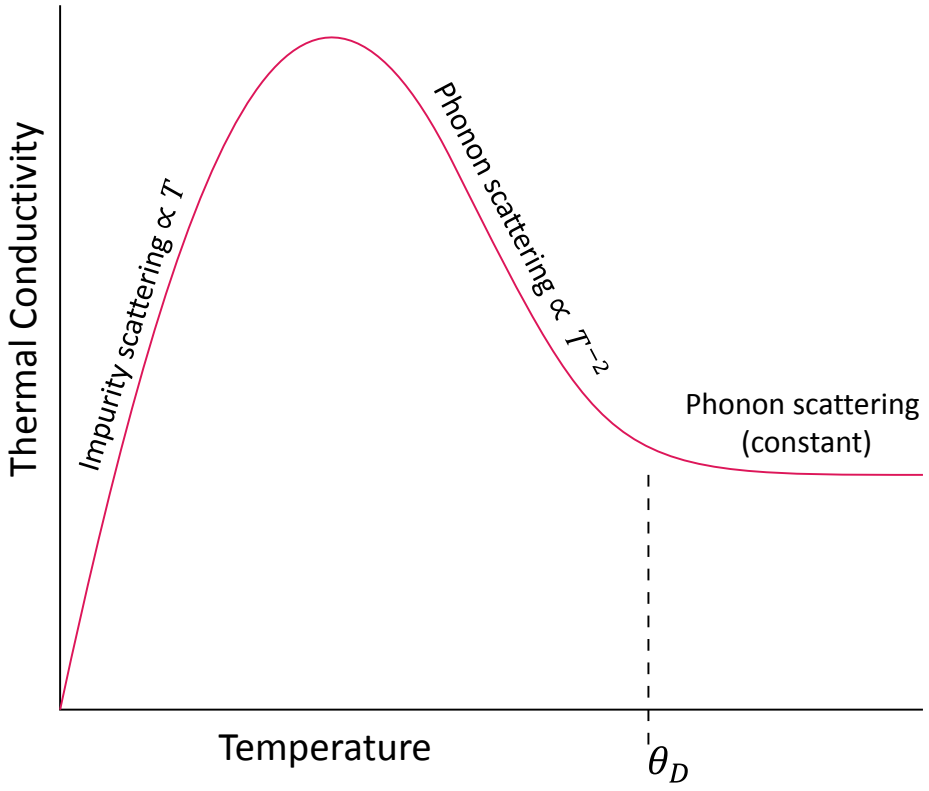

Figure 3.6: The different dominant contributions to thermal conductivity at different temperatures. θ_D is the Debye temperature.

The change from electron-phonon dominated scattering to impurity dominated scattering will naturally depend on the purity of the sample in question. Figure 3.7 shows this effect for copper samples with RRRs from 30 to 3000 (a high values is normally a good indicator of high purity – see 3.5.2.2). It can be seen that the transition occurs at around 30 K in the low purity samples, dropping to ~ 8 K in the higher purity ones. Some authors suggest the transition takes place even lower (between 1 and 4 K [166]), although this would presumably be in even purer samples.

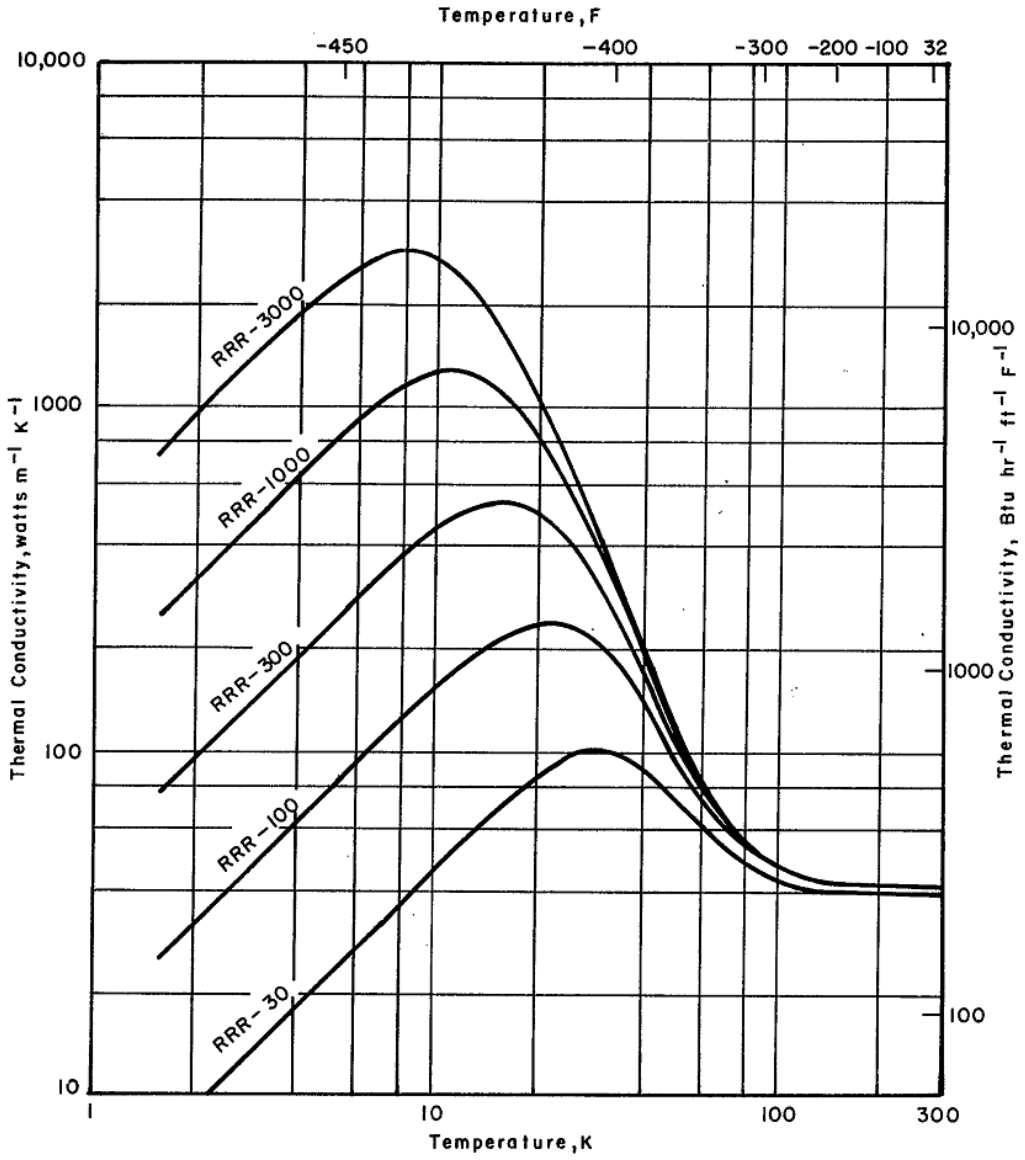

Figure 3.7: Thermal conductivity of oxygen free copper shown for different values of RRR [167].

For tungsten, published data for a polycrystalline sample of 99.99% purity [168,169] suggests the transition is around 30 K, as indicated by the location of the maximum in Figure 3.8. Most of the tungsten samples studied in this thesis have a higher purity than this. Probably more importantly, they are also single crystals and hence there will be no scattering from grain boundaries. It is therefore suggested that the transition to impurity dominated scattering happens well below 30 K for the samples described in the subsequent chapters.

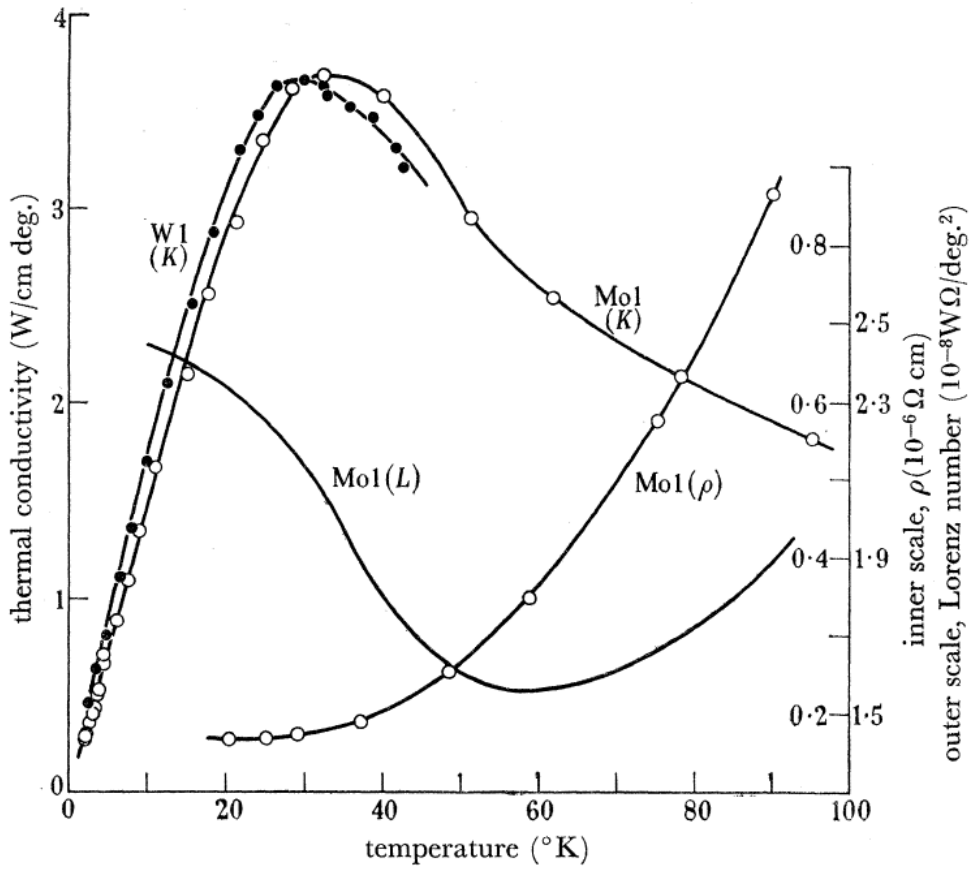

Figure 3.8: Thermal conductivity of tungsten and molybdenum between 0 and 100 K [168].

3.5.2.2 Relevance of RRR Measurements

The Residual Resistance Ratio (RRR) is the ratio of a sample's electrical resistance at room temperature to its resistance at liquid helium temperature (4 K). At around 4 K the contribution to the electrical resistance from electron-phonon scattering will usually be small because there are so few phonons capable of scattering an electron across the Fermi surface (see 3.5.2.1). Consequently, any resistance measured at this temperature can usually be attributed almost entirely to electron scattering by impurities. A high RRR is therefore usually taken as an indication that the sample has a high purity and it can be useful for comparing sample purities when detailed composition analysis is not available. The RRR is used in this way in Chapters 4 and 5.

Given that the majority of heat in metals is carried by electrons, it might be inferred that the ratio of the thermal conductivity at 4 K to its room temperature value is also of the order of the RRR. However, from the arguments in section 3.5.2.1 it can be seen that the RRR will not always be an accurate indicator of thermal conductivity at low temperatures. If the low temperature measurement is made at a temperature where the Wiedemann-Franz law breaks down (i.e. below the Debye temperature, but where some phonon contribution to the scattering remains) then the RRR is likely to be much greater than the ratio of thermal conductivities at the same temperatures.

3.5.2.3 Umklapp Scattering

In the preceding sections, electron scattering has been assumed to take place between k-states within a single Brillouin zone. However, scattering into states in adjacent zones is possible and this results in Umklapp[15] scattering.

Umklapp scattering (U-processes) of electrons by phonons is illustrated in Figure 3.9, which shows a section through two adjacent Brillouin zones. A normal electron-phonon collision (N-process) is shown in the bottom half of the left hand zone: an electron in state $\mathbf{k_2}$ is scattered to state $\mathbf{k_2}'$ by a phonon with wavevector $\mathbf{q}$. In the upper half of the figure a U-process is illustrated: here the same phonon wavevector scatters an electron across the zone boundary from state $\mathbf{k_1}$ to state $\mathbf{k_1}'$. This point in k-space is exactly equivalent to the state $\mathbf{k_1}'$ in the upper half of the left hand zone as they are connected by the reciprocal lattice vector $\boldsymbol{G}$. The result is a large angle scattering process, which will be much more effective in degrading an electronic thermal current.

[15] The name derives from the German word umklappen (to turn over). Its use implies the wavevector has been flipped or turned over (see Figure 3.9).

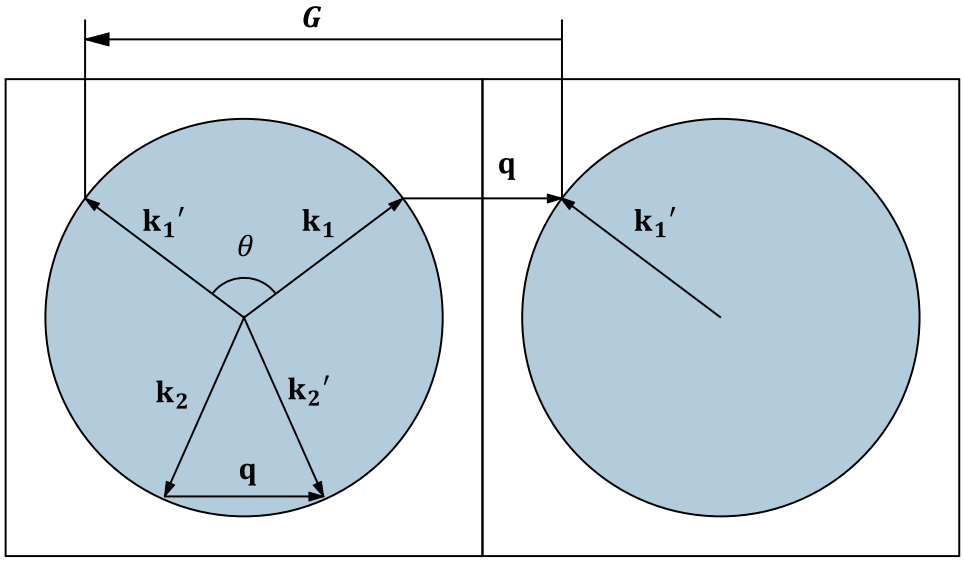

Figure 3.9: Umklapp scattering of an electron with wavevector k by a phonon with wavevector q. Adapted from [129].

When the Fermi surface does not intersect the zone boundaries, a minimum phonon wavevector is required for Umklapp scattering and at low enough temperatures the number of suitable phonons falls exponentially (see 3.6).

3.5.3 Electron-Electron Scattering

Electron transport is further complicated by the fact that the "free" electrons move within a background of the "bound" electrons and the negative charge from these acts to screen the effects of the positively charge ions. These bound electrons, along with other free electrons, are also possible scattering sources for any electron involved in transport processes. In constructing wavefunctions for Bloch electrons, no explicit account is made for the fact that the electron exists in the presence of many other electrons and that interactions must take place between them.[16] The term "independent electron approximation" is used to refer to this approach, which also assumes that separate Schrödinger equations can be written for

[16] The form taken for the lattice potential can account for the presence of other electrons implicitly, but choosing the correct form then becomes quite challenging [154,159]. The true electron wavefunction should combine both the features of a wavefunction for a tightly bound electron (sharply varying in the vicinity of the nucleus) with those of a free electron (a nearly perfect plane wave spread across many lattice cells) and the difficulty arises in reconciling these.

each electron [159]. Two important features of electron behaviour for which this approximation cannot account are:

i. Correlation – the electrons are point charges, not a uniform cloud of negative charge, and coulomb repulsion keeps them apart. Their true wavefunctions will dictate that the probability of finding two very close together will be much less than if they were completely independent particles.
ii. Exchange – It is impossible for two electrons of the same spin to be found at the same point (by the Exclusion Principle). There results a kind of "correlation repulsion" (as above) acting between electrons of the same spin.

These two features of electron-electron interaction tend to cancel the effects of strong coulomb forces which might otherwise make electron-electron scattering significant. As a result, the effects of electron-electron interactions on scattering processes are orders of magnitude smaller than the effects from interactions with phonons or lattice imperfections at room temperature [159]. However, in very pure metals at temperatures where most phonon processes are frozen out (as considered in this thesis) the effects of electron-electron scattering may become apparent. It will also be more important when: (i) the Fermi surface is complicated (as it is in tungsten), so that conservation of energy and momentum become easier for a wider variety of possible scattering processes; (ii) the density of states at the Fermi energy is very large (e.g. transition metals such as tungsten), bumping up the number of possible initial and final states. [16]

The presence of electron-electron scattering can be deduced from the appearance of a term proportional to T in the thermal resistivity and the argument for this is now outlined.

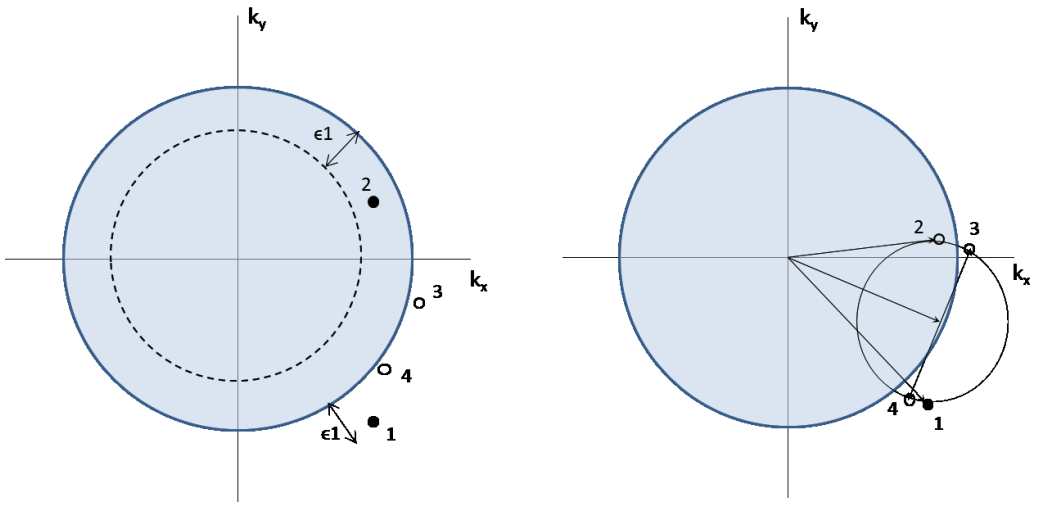

Figure 3.10: Electron states in k-space for an electron-electron scattering process (after [129]).

Consider a collision between two electrons with wavevectors $\mathbf{k}_1$ and $\mathbf{k}_2$:

$$\mathbf{k}_1 + \mathbf{k}_2 \rightarrow \mathbf{k}_3 + \mathbf{k}_4. \tag{3.74}$$

The Exclusion Principle will only allow this collision if states $\mathbf{k}_3$ and $\mathbf{k}_4$ are vacant before the collision. This situation is illustrated on the left of Figure 3.10, where vacant states are shown by white dots and occupied states by black dots. Referring energies to the Fermi energy, the following must be true:

i. ϵ_3 and ϵ_4 must be positive because they must lie outside the Fermi surface

ii. Assuming electron 2 lies within the Fermi sea, $|\epsilon_2| < \epsilon_1$ to keep $\epsilon_3 + \epsilon_4$ positive (i.e. electron 2 must lie in a band that is within ϵ_1 of the Fermi surface)

This reduces the candidate electrons for a collision by a factor ϵ_1/ϵ_F. To satisfy conservation of energy $\epsilon_1 - |\epsilon_2| = \epsilon_3 + \epsilon_4$, which defines the total energy of the states after the collision. A circle (sphere in three dimensions) can be drawn on which all pairs of states 3 and 4 that satisfy this requirement lie (this is shown on the right of Figure 3.10). Any given pair of states will be on opposite sides of the circle's (sphere's) diameter. States 3 and 4 must also lie outside the Fermi sea. It can be seen from Figure 3.10 that this reduces the

candidate states for a collision by a *further* factor $\sim\epsilon_1/\epsilon_F$. The collision frequency is thus reduced by a factor $(\epsilon_1/\epsilon_F)^2$.

For a thermal distribution of electrons at "low" temperature ($k_BT \ll \epsilon_F$), ϵ_1 can be replaced in the argument above with the thermal energy (k_BT). This recognises the fact that at finite temperature, available states exist over the width of the thermal boundary which is approximately equal to k_BT. The scattering rate is thus written:

$$\frac{1}{\tau} \propto \left(\frac{k_BT}{\epsilon_F}\right)^2. \tag{3.75}$$

Using the equation (3.9) for thermal conductivity, and noting that the electronic heat capacity is proportional to temperature, it can be seen that electron-electron scattering should show up as a term proportional to T in the thermal resistance. Adding this term into equation (3.73) above produces:

$$\frac{1}{\kappa} = \frac{A}{T} + BT^2 + CT. \tag{3.76}$$

This expression applies for thermal conductivity in a metal below its Debye temperature.

Electron-electron scattering can only affect electrical resistivity as a U-process, but N-processes may limit thermal conductivity since the interaction may reduce the electron's thermal energy without drastically changing its velocity vector (see the arguments in section 3.5.2.1). Electron-electron scattering would therefore be expected to be more important in thermal conductivity measurements as opposed to electrical ones and this too must be borne in mind if inferring thermal conductivities from RRR measurements (which rely on the Wiedemann-Franz law).

3.6 Phonons and Phonon Transport

Visualising the lattice of a crystal as an array of atoms or molecules constrained to their positions by the strength of their electrostatic interactions leads to the idea of connection by some kind of elastic spring force. From this picture it follows that such a structure will be capable of transmitting energy in the form of elastic waves, where the crystal as whole will vibrate. In electrical insulators, this is the dominant method of heat transfer. In metals such as tungsten, this contribution will be small; however, these waves are still of concern for heat transport because of the effect their interactions with electrons have on the more dominant electronic heat conduction.

The energy of elastic waves in solids is quantised just as electromagnetic waves in cavities are and the quanta of these lattice vibrations are phonons. Phonons can be subjected to a quantum treatment equally as well as electrons. In many cases, however, the model of them as classical waves with a minimum wavelength determined by the lattice spacing is sufficient.

Unlike electrons, phonons are not constrained by the Pauli Exclusion Principle: a single mode may be occupied by many phonons of the same wavevector. As such, they obey Bose-Einstein statistics and average number of phonons in a mode is given by [14]:

$$\langle s \rangle = \frac{1}{\mathrm{e}^{h\omega_q/k_B T} - 1}, \tag{3.77}$$

where ω_q is the frequency of the mode.

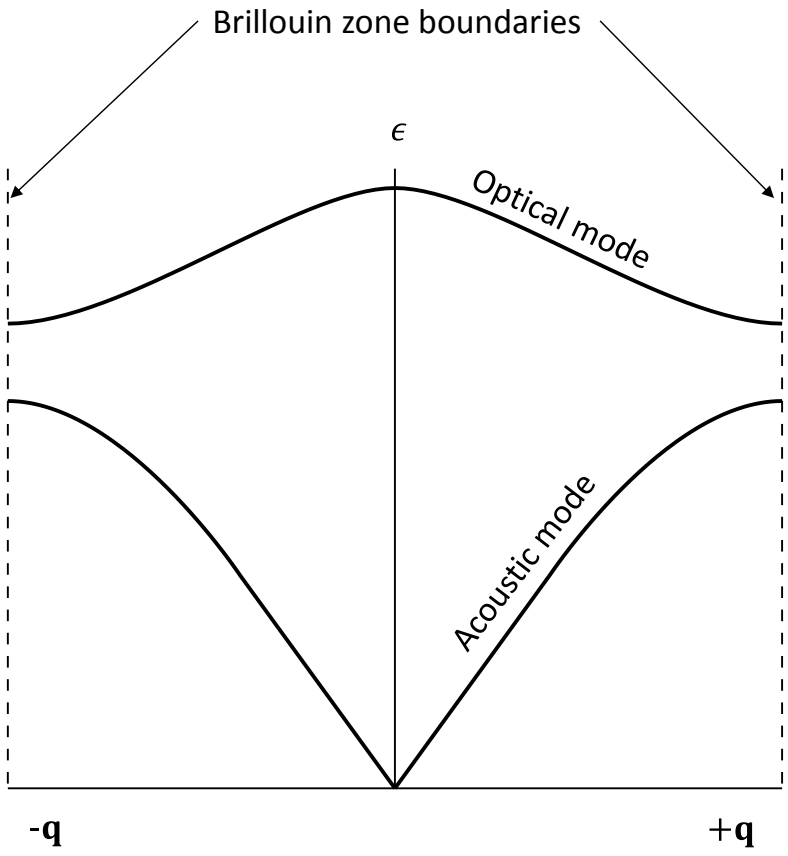

Figure 3.11: Phonon dispersion relationship for a diatomic lattice with both acoustic and optical modes (after [154]).

An important consideration for lattice waves is the relationship between their frequency (≡ energy) and wavevector – the "dispersion relationship"[17] (shown in Figure 3.11). For small wavevectors, the frequency (i.e. energy) will be proportional to wavevector, but the linearity is lost at higher wavevectors and this fact has important implications for phonon scattering (see 3.7). The phonon dispersion relationship is different for different polarisations. It is also different for so-called "optical modes" compared to "acoustic modes". In the former, atoms within a repeating lattice cell (e.g. a molecule) are vibrating in opposition to each other; these atoms are actually ions of opposite charge and their motion generates electric moments corresponding to electromagnetic radiation of a particular frequency which leads to the term "optical". In acoustic modes, by contrast, all atoms in the cell are moving in the same direction at any given instant. Figure 3.11 illustrates the different dispersion

[17] This dispersion relationship is equivalent to that for electron described in 3.2.1

relationships for these two modes: while the energy in the acoustic mode drops linearly to zero at $\mathbf{q} = 0$, the energy in the optical mode rises to a fixed value. This initially counterintuitive result is due to the atoms moving in opposition, so that when the resultant wavevector is zero they are precisely out-of-phase and the associated electric moment is maximum.

3.6.1 Debye Theory

Debye's theory was developed by applying the same approach that Planck had used to describe electromagnetic radiation in a box [14] to analyse lattice vibrations in a solid. It is based on classic elasticity theory where the potential energy is a quadratic function of local strain; this is a simplification for real lattices [154], but not one that significantly affects the central predictions of the theory.

Unlike photons, phonons are vibrations in a discontinuous medium and therefore have a maximum number of modes in a finite solid given by $3N$, where N is the number of atoms. Furthermore, there will be three possible polarisations of elastic waves: two perpendicular to the direction of wave propagation (transverse polarisations) and one in the direction of propagation (longitudinal polarisation). Debye theory assumes that propagation speeds will be equal for all three polarisations.

These assumptions lead to the Debye T^3 law (see Appendix C) which can be expressed as follows:

$$C = \frac{12\pi^4 N k_B}{5}\left(\frac{T}{\theta_D}\right)^3. \tag{3.78}$$

It implies that the heat capacity, C, of an insulator is proportional to T^3. This result is useful for estimating the temperature dependence of the phonon contribution to a heat current. It is also used in determining the temperature dependence of phonon scattering of electrons as in 3.5.

The Debye temperature, θ_D, is found to be (see Appendix C):

$$\theta_D = \left(\frac{hv}{k_B}\right)\left(\frac{6\pi^2 N}{V}\right)^{1/3}. \tag{3.79}$$

Here N is the number of atoms in the lattice and $V = L^3$, where L is the lattice side length. It is the temperature at which all possible modes in the lattice will be excited. Consequently, a high Debye temperature is an indication that only a small fraction of the available modes will be excited at low temperatures – i.e. phonon conduction will be low at low temperatures.

3.6.2 Variations from the Debye Law

The assumptions made in deriving the Debye T^3 law represent just one way of modelling the dynamics of a lattice. Several other alternatives are possible which relax one, or more, of Debye's assumptions. Examples include: introducing different frequency cut-offs for the different polarisations ("Isotropic continuum model"); introducing a dispersion factor for each polarisation so that the variation of propagation speeds with wavevector is different for different polarisations ("Born-von Kármán model"); and more complete theories that use the elastic moduli of the material in various directions to directly link energy and strain [154]. A true lattice spectrum is a complex function which is highly likely to differ from the Debye approximation; the comparison for lithium is shown in Figure 3.12.

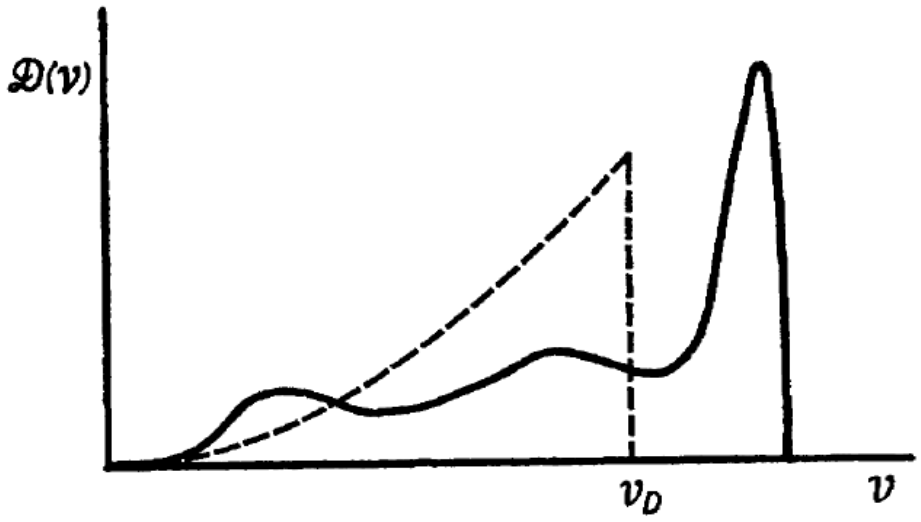

Figure 3.12: Comparison of the Debye spectrum (dashed line) with the true lattice spectrum of lithium (solid line) [154].

Debye temperatures can be found by measuring the specific heat of a substance at a certain temperature and then determining the value of T/θ_D that must be inserted into equation (3.78) to obtain this value. Of course the specific heat will not always follow an exact T^3 dependence and so estimates of θ_D made by this method will usually show considerable variation with temperature. This is a consequence of the difference between the Debye spectrum and the true frequency spectrum [154] and it should be borne in mind when making inferences from a single quoted value for a material's Debye temperature.

3.6.3 Lattice Conduction

The heat current due to phonons is given by [157]:

$$\dot{q}_l = \sum_{\mathbf{q}} \mathbf{v}\hbar\omega_{\mathbf{q}} N_{\mathbf{q}}, \tag{3.80}$$

where $\mathbf{v}$ is velocity, $N_{\mathbf{q}}$ is the number of phonons in mode $\mathbf{q}$ and $\hbar\omega_{\mathbf{q}}$ is the phonon energy. In equilibrium, the sum vanishes because modes of equal energy but opposite velocity cancel. To find the steady-state heat current, it is therefore necessary to know the deviation from the equilibrium distribution. Deviations from equilibrium will be caused by a

temperature gradient and scattering processes, and steady-state is reached when these two balance

$$\left.\frac{dN_{\mathbf{q}}}{dt}\right|_{\nabla T} = \left.\frac{dN_{\mathbf{q}}}{dt}\right|_{scatt}. \tag{3.81}$$

The temperature gradient causes the equilibrium distribution, N^0, to vary with position and hence:

$$\left.\frac{dN_{\mathbf{q}}}{dt}\right|_{\nabla T} = -\mathbf{v}\cdot\nabla N^0 = -(\mathbf{v}\cdot\nabla T)\frac{dN^0}{dT}. \tag{3.82}$$

To handle scattering process, the relaxation time concept introduced in 3.1 can be employed. It is assumed that the deviation from the equilibrium distribution is $n_{\mathbf{q}}$, where $N = N^0 + n_{\mathbf{q}}$, and scattering processes cause this to decrease according to:

$$\left.\frac{dN_{\mathbf{q}}}{dt}\right|_{\text{scatt}} = -\frac{n_{\mathbf{q}}}{\tau_{\mathbf{q}}}, \tag{3.83}$$

which defines the phonon relaxation time $\tau_{\mathbf{q}}$. Substituting (3.82) and (3.83) into (3.81) gives:

$$n_{\mathbf{q}} = -(\mathbf{v}\cdot\nabla T)\tau_{\mathbf{q}}\frac{dN^0}{dT}. \tag{3.84}$$

Using this non-equilibrium distribution in (3.80) then leads to:

$$\dot{\boldsymbol{q}}_l = \sum_{\mathbf{q}} \mathbf{v}\tau_{\mathbf{q}}(-\mathbf{v}\cdot\nabla T)\hbar\omega_{\mathbf{q}}\frac{dN^0}{dT}. \tag{3.85}$$

Writing $\hbar\omega_{\mathbf{q}}\, dN^0/dT = c_{\mathbf{q}}$, the contribution of mode $\mathbf{q}$ to the specific heat capacity, and dividing by the temperature gradient, the lattice thermal conductivity is seen to be:

$$\kappa_l = -\frac{\dot{\boldsymbol{q}}_l}{\nabla T} = \sum_{\mathbf{q}} c_{\mathbf{q}}(\mathbf{v}\cdot\mathbf{t})^2\tau_{\mathbf{q}}, \tag{3.86}$$

where $\mathbf{t}$ is a unit vector in the direction of the temperature gradient. Recognising that $\mathbf{v}\tau_{\mathbf{q}} = \Lambda$ is the mean free path and noting that averaging the velocity over the three orthogonal directions will introduce a factor of 1/3, it can be seen that this is equivalent to equation (3.9).

It is thus possible to calculate the heat conduction due to phonons using the kinetic formula. The Debye law (equation (3.78)) can be utilised to find the material's heat capacity and the phonon velocity can be assumed to be equal to the average velocity of sound in the medium. All that is then missing is the mean free path of the phonons; an estimate of which can be made from the relevant scattering mechanisms. These scattering mechanisms are discussed in more detail below (see 3.7). Whatever the precise mechanism, it will usually result in the mean free path having some temperature dependence [157] and this can be combined with the T^3 dependence for the Debye heat capacity so that:

$$\kappa_l \propto T^{3+n_l}, \tag{3.87}$$

where n_l is the temperature dependence of the mean free path.

3.7 Scattering Mechanisms in Phonon Heat Transport

Since phonon conduction plays a relatively small part in the thermal conductivity measurements described in the following chapters, details of the scattering mechanisms are not considered extensively. However, the effects of impurities and phonon-phonon interactions are briefly noted because they illustrate the behaviour of phonon heat transport at the low temperatures relevant to ADRs.

The uniformity of the lattice may be disrupted in a number of ways (see 3.5.1) and these can act to change a phonon's wavevector. In the case of point imperfections, the scattering effect depends on the wavelength of the phonons; typically this will be long in comparison to the lattice spacing and the imperfection can usually be treated as a region in which the

properties of the lattice are different from their normal values. The scattering rate will depend on the volume over which the imperfection disrupts the lattice. The central point for the purposes of this work, however, is that it will be independent of temperature and hence when lattice imperfections are the dominant scattering source a T^3 dependence is expected for phonon thermal conductivity.

In the case of phonon-phonon scattering, the following condition must be satisfied [154]:

$$\mathbf{q} + \mathbf{q}' = \mathbf{q}'' + \mathbf{G}, \tag{3.88}$$

where $\mathbf{q}, \mathbf{q}', \mathbf{q}''$ are the phonon wavevectors and $\mathbf{G}$ is a reciprocal lattice vector. If $\mathbf{G} = 0$, the processes is referred to as a normal (or N) process; if $\mathbf{G} \neq 0$, the process is an Umklapp (or U) process. It might be assumed that the likelihood of phonon $\mathbf{q}$ – which is transporting heat – being scattered (i.e. its mean free path) just depends on the number of phonons of wavevector $\mathbf{q}'$ which are present. This is not the case. For N-processes ($\mathbf{G} = 0$) wavevector, and therefore phonon momentum $\hbar\mathbf{q}$, are conserved. If dispersion is ignored, the total energy on both sides of equation (3.88) is the same and the change in wavevector does not affect the flux of energy; it just distributes it into different modes [154]. In other words, N-process cannot affect the thermal conductivity of the lattice. The same is not true for U-processes which can change the sign of the lattice wavevector – i.e. reverse the direction of the lattice wave. This is the only phonon-phonon scattering mechanism which reduces the lattice conductivity.

At low temperatures, however, U-processes are "frozen out"; in other words, there are simply no phonons of the appropriate wavevector to cause scattering. This occurs because energy conservation still applies to equation (3.88) even when $\mathbf{G} \neq 0$ and so $\mathbf{q}''$ must be large enough for its energy to equal the sum of the energies of $\mathbf{q}$ and $\mathbf{q}'$. As a minimum, one of $\mathbf{q}$ or $\mathbf{q}'$ must be comparable to $\mathbf{G}/2$ in order for the sum of the wavevectors to extend into

the neighbouring zone.[18] Thus, $\mathbf{q}''$ must also be of this order, making the frequency of this phonon comparable with the highest frequencies in the lattice spectrum. At low temperatures, these high frequency phonons will not be present and U-processes will not be possible.

3.8 Surface Scattering

3.8.1 Electrons

Effects relating to the surface of a conductor become important when the mean free path of the carrier exceeds (or is at least of the same order of) the dimensions of the sample. As has been mentioned above, electron mean free paths at low temperature can be of the order of millimetres and so surface effects must be considered when dealing with conductors that have cross-sections of this order of magnitude.

It is possible to apply the full Boltzmann equation to this situation with an additional boundary condition [154]. It is supposed that $\mathbf{n}$ is a vector normal to the surface and directed into the sample. All carriers incident on the surface (i.e. with negative component of velocity in the direction $\mathbf{n}$, so that $\mathbf{v_n} < 0$ at the location of the surface $\mathbf{r}_S$) will be scattered into new states that have positive components of velocity in the $\mathbf{n}$ direction ($\mathbf{v_n} > 0$). This is written:

$$f_{\mathbf{k}}(\mathbf{r}_S, \mathbf{v}_n > 0) = \int f_{\mathbf{k}'}(\mathbf{r}, \mathbf{v}'_n < 0) R(\mathbf{k}', \mathbf{k}) d\mathbf{k}', \tag{3.89}$$

where $R(\mathbf{k}', \mathbf{k})$ is the probability that a carrier is scattered from state $\mathbf{k}'$ to state $\mathbf{k}$. Much like the transition probability $Q(\mathbf{k}, \mathbf{k}')$ in (3.45), $R(\mathbf{k}', \mathbf{k})$ will be difficult to define; to do so properly would require detailed knowledge of microscopic features of the particular surface. Even if it could be defined appropriately, this still leaves the difficult problem of solving the

[18] This can be seen from Figure 3.9, if one imagines the electron wavevectors $\mathbf{k}$ and $\mathbf{k}'$ refer to phonon wavevectors.

Boltzmann equation in its full integro-differential form. As with general conduction problems, the relaxation time is of more practical use:

$$\dot{f}_{\boldsymbol{k}}\big|_{scatt} = -\frac{1}{\tau} g(\mathbf{k}, \mathbf{r}). \tag{3.90}$$

This leads to the same form of equation as above (see equation (3.52)). When the effects of surface scattering are considered, the solution is modified as follows [154,170]:

$$g_{\mathbf{k}} = \left(-\frac{\partial f_{\mathbf{k}}^0}{\partial \epsilon}\right) \tau \mathbf{v}_{\mathbf{k}} \cdot \boldsymbol{A}\left(1 + G(\mathbf{v}, \mathbf{r}_{\mathrm{S}}) \mathrm{e}^{-(\mathbf{r}-\mathbf{r}_{\mathrm{S}})/\tau \mathbf{v}}\right), \tag{3.91}$$

where

$$\boldsymbol{A} = \left(-\left(\frac{\epsilon - \mu}{T}\right) \nabla T - e(\boldsymbol{E} + \mathbf{v}_{\mathbf{k}} \times \boldsymbol{B})\right) \tag{3.92}$$

and $G(\mathbf{v}, \mathbf{r}_{\mathrm{S}})$ is a function which is adjusted to suit the particular boundary conditions of the situation (e.g. thin wire, thin film, etc.). When equation (3.91) is inserted into an equation such as (3.54) or (3.55) it leads to integrals which are generally difficult to evaluate and this has only been performed for the specific examples of thin films [171] and wires [172].

Another approach is to define a reflecting function that represents the effect of the surface on an incident carrier [154]. A phenomenological description is employed where a fraction p of the carriers are specularly reflected such that:

$$g(\mathbf{k}, \mathbf{r}_{\mathrm{S}})_{\mathrm{v_n}} = p g(\mathbf{k}', \mathbf{r}_{\mathrm{S}})_{-\mathrm{v_n}}. \tag{3.93}$$

As above, $\mathbf{r}_{\mathrm{S}}$ is the position of the point where the carrier hits the surface with velocity $\mathrm{v_n}$. This condition defines "specular" reflection as maintaining all components of electron velocity except that directed towards the surface, which has its sign reversed, but its magnitude unchanged (i.e. scattering is elastic). It may be difficult to specify p exactly, but by making calculations with a few different values the general impact of the surface condition can be evaluated.

One approach to derive an expression for p is by using diffraction theory [154]:

$$p(\lambda) = \exp\left(-\frac{16\pi^3\eta^2}{\lambda^2}\right), \tag{3.94}$$

where the "asperity parameter" η is the root mean square deviation of the height of the surface from an appropriate reference plane. In simple terms, if the wavelength is much less than the asperity parameter, p will be small; if the wavelength is much larger than η, most of the waves will be specularly reflected and p will approach unity. The result is intuitively understood by considering that height differences on the surface greater than the incident wavelength will cause the reflected waves to gain or lose phase at random. Conversely, if the asperity height is just a small fraction of the wavelength, any phase changes will be minimal and whatever coherence is present in the incident waves will be nearly perfectly preserved.

Equation (3.94) treats incident waves as normal to the surface and does not allow for glancing incidence which would reduce any phase change by a factor of the cosine of the angle of incidence. This cosine term would appear squared in the exponential of (3.94) and would thus increase p. For the case of electrons, this type of analysis suggests that it will be extremely difficult to prepare a surface with a level of polish sufficient to specularly reflect any significant proportion of electrons incident upon it. However, there is some evidence that specular reflection can be achieved with sufficient care in surface preparation (see 3.8.3)

A simpler approach than direct solution of the Boltzmann equation, credited to Nordheim [173], has been shown to lead to very similar results [170,172]. It treats the surface as a source of scattering that can be added to other scattering mechanisms using Matthiessen's rule:

$$\rho = \rho_0 + \rho_s, \tag{3.95}$$

where ρ_0 is the bulk resistivity and ρ_s is the resistivity due to the surface. The second term is then expressed as a correction to the bulk resistivity based on the mean free path, Λ, and the diameter of the sample[19], d, which leads to a formula for the ratio of the total resistivity (incorporating surface effects) to the bulk value:

$$\rho/\rho_0 = 1 + \frac{8}{3\pi}\left(\frac{\Lambda}{d}\right). \tag{3.96}$$

Expressed in terms of conductivities:

$$\frac{\sigma}{\sigma_0} = 1/\left(1 + \frac{8}{3\pi}\left(\frac{\Lambda}{d}\right)\right). \tag{3.97}$$

This ratio is plotted against $k = d/\Lambda$ in Figure 3.13. The values calculated by Dingle [172] from direct integration of Boltzmann equation are also shown for comparison. It is clear that this approximation is very good if it is assumed that $p = 0$ – i.e. if all electrons are diffusely scattered at the surface.

[19] The expressions in this section have generally been developed to describe the effects seen in thin wires [170,172]. In this context, d should be interpreted as the diameter of such a wire sample. However, it could be interpreted with equal validitiy as the representative cross-section dimension in any sample where the cross-section dimensions are significantly smaller than the length dimension (along which the electrical – or thermal – potential is applied).

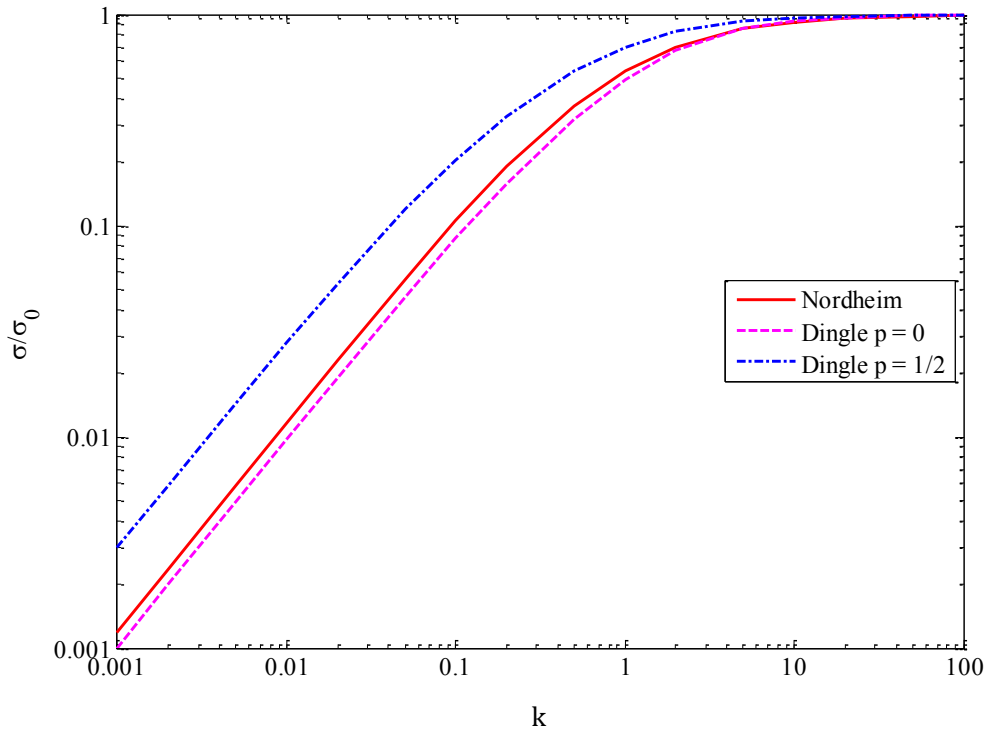

Figure 3.13: Variation of conductivity as a fraction of bulk conductivity plotted against $k = d/\Lambda$. d is the sample diameter and Λ is the mean free path. The different curves are for the models of Nordheim [173] and Dingle [172] and p is the fraction of electrons specularly reflected at the surface.

An approximate solution, incorporating the reflection parameter, for thin films was derived by Fuchs [171]. He calculated the change in conductivity of thin films as a function of the proportion of electrons specularly scattered from the surface and the ratio of the sample thickness to the electron mean free path:

$$\frac{\sigma}{\sigma_0} \sim \frac{3}{4}(1-p)\frac{d}{\Lambda} ln\left(\frac{\Lambda}{d}\right), \tag{3.98}$$

where d is the film thickness. For thick samples, it simplifies further [172]:

$$\frac{\sigma}{\sigma_0} \sim 1 - \frac{3}{8}(1-p)\frac{\Lambda}{d}. \tag{3.99}$$

Dingle [172] suggested that this could be modified to wires of arbitrary cross section using the following argument. If the sample cross-section is sufficiently large, the current will only be affected by surface scattering in a region of the sample near the surface. Inside this

region the sample has its usual bulk conductivity. When looking to find the mean conductivity resulting from both contributions, it can be assumed that the reduction from the bulk value will be proportional to ratio of the surface region to the bulk region. The size of the surface region depends on area of the surface and the electron mean free path, since longer mean free paths increase the distance from within the sample that electrons can interact with the surface before being scattered by other sources. Meanwhile, the proportion of the sample occupied by this region depends inversely on the overall sample volume. Dingle expressed this as follows:

$$\frac{\sigma}{\sigma_0} = 1 - \frac{C\Lambda P}{A}, \tag{3.100}$$

where C is a constant, P is the sample perimeter and A is its cross sectional area. Recognising that for a film of thickness d and width w, $P/A \cong 2/d$, equations (3.99) and (3.100) can be compared to determine C. This gives:

$$\frac{\sigma}{\sigma_0} \sim 1 - \frac{3}{16}(1-p)\frac{\Lambda P}{A}. \tag{3.101}$$

3.8.2 Phonons

The approach outlined above for electron scattering at a surface can be applied equally well to phonons. The Boltzmann equation is used with the distribution $g(\mathbf{q}, \mathbf{r})$ which is now a function of phonon wavevector and position. The additional boundary conditions from equations (3.89) and (3.93) are applied to find the distribution and this then allows the total heat current to be computed. The resulting equation can be compared with the kinetic equation for conduction (3.9) to define a mean free path for the phonons.

This was originally performed by Casimir [174] who assumed that scattering was entirely due to the surface and that all phonons incident on the sides of the specimen were diffusely reflected. This is equivalent to assuming that all phonons are absorbed and re-emitted at rate appropriate to the temperature of the wall of the specimen. The result is that the mean free

path will be equal to the diameter of the specimen in circular rods and equal to 1.1 × the side length in a sample of square cross-section [154,174].

This argument can be extended to include the case where some phonons are reflected from the walls of the sample [175] by making use of the parameter p as defined in 3.8.1; the mean free path is modified as follows [154]:

$$\Lambda_B = \frac{1+p}{1-p}\Lambda_{0B}, \tag{3.102}$$

where $\Lambda_{0B}$is the mean free path for a perfectly rough surface.

Equation (3.94) applies to phonons as well and this can give an indication of the surface finish required to achieve specular reflection of phonons. As with electrons, to achieve a significant proportion of specular reflection would require the phonon wavelength to be greater than the asperity height.

3.8.3 Surface Scattering in Tungsten

In spite of what might be expected from the analysis in section 3.8.1, a number of experiments [176,177] have been performed on tungsten which suggest that, with sufficiently careful preparation of the surfaces, there will be some specular reflection of electrons. Furthermore, the proportion of specular reflection has been shown to depend on the orientation of the reflecting surfaces with respect to the crystal axes. In samples which have been ground after cutting and then electro-polished in a sodium-hydroxide (NaOH) solution, faces in the (110) plane are found to be the most specularly reflecting ($p = 0.5$–0.8 [176,177]). However, the degree of specular reflection is significantly less for the (100) faces ($p \cong 0.1$ [177]). One explanation for this behaviour is that the proportion of specularly reflected electrons depends on the angle of incidence on the surface and this may change for different crystal planes due the Fermi surface geometry.

A further finding is that the temperature dependence of such scattering appears to follow an approximately quadratic relationship ($\propto T^{2.1}$ [177]). Although Startsev *et al.* [177] discuss a number of possible explanations for this temperature dependence, it remains an open question.

3.9 Boundary Scattering

The dominant cause of thermal resistance at a boundary between two solids will almost always be surface imperfections in the contacting materials; these will limit contact to a finite number of points, rather than occurring over the whole surface, and effectively reduce the actual area of the surfaces in contact. The simplest way to reduce this type of resistance is to obtain a high quality finish for the mating surfaces and ensure sufficient pressure is used to make the joint.

Over and above the type of boundary resistance described above, there exists the "interfacial thermal resistance" which is present even for atomically perfect surfaces and results from differences in the lattice and electronic properties of the two materials. If either one of the materials which make up the boundary is an electrical insulator, conductance across the boundary will only be by phonons, whereas if both materials are metals, electrons may carry heat across the boundary and the thermal resistance may not play a limiting role. It is therefore the former which is the focus of the remainder of this section.

To develop a quantitative argument, the flow of heat due to phonons across a boundary between two sides labelled 1 and 2 is considered. The general approach, following [178], is to take phonons of a given frequency and angle of incidence impinging on an area A and multiply by the phonon energy ($\hbar\omega$) and the transmission probability between the two sides ($\alpha_{1\rightarrow 2}$). The total heat flow is then the sum over all frequencies and angles of incidence. First, the phonon velocity on side 1 is labelled $v_{1,j}$, where j is the phonon mode, and the angles of incidence are labelled θ (angle to the boundary normal) and φ (azimuthal angle).

The component of phonon velocity normal to the boundary is then $v_{1,j}\ cos\theta$. If $N_{1,j}(\omega, T)$ is the number of phonons with given angles θ and φ, the number of such phonons incident on area A per unit time is:

$$\frac{N_{1,j}(\omega,T)}{4\pi} d\Omega\, v_{1,j} \cos\theta, \tag{3.103}$$

where $d\Omega = \sin\theta\, d\theta\, d\varphi$ is an element of solid angle. As described above, the gross heat current per unit area is found by integrating over all angles and frequencies and summing over the modes j:

$$\frac{\dot{Q}_{1\to2}}{A} = \frac{1}{2}\sum_j \int_0^{\pi/2} \int_0^{\omega_{max}} N_{1,j}(\omega,T)\hbar\omega v_{1,j}\, \alpha_{1\to2}\, \cos\theta \sin\theta\, d\theta\, d\omega, \tag{3.104}$$

where the integral over the azimuthal angles contributed a factor 2π which combined with the $1/4\pi$ in equation (3.103) to give the factor of $1/2$. The number of phonons can be found from the Debye model. The transmission probability, however, will be a function of incidence angle, phonon mode and frequency and is less easy to determine. For solid-solid interfaces there are two theoretical approaches to this problem [178]: the acoustic mismatch model (AMM) and the diffuse mismatch model (DMM). The former assumes a geometrically perfect interface, across which phonon transport is elastic; the latter assumes the other extreme: all phonons will be scattered diffusively. Boundary resistance predictions using the two theoretical limits usually differ by < 30% and, within this margin, both agree well with experiment [178].

3.9.1 The Acoustic Mismatch Model

The central assumption of the AMM is that diffuse scattering at the boundary is ignored, but elastic interactions with it are allowed. Phonons are treated as acoustic waves in a continuous medium so that at an interface one of four possible changes can take place: reflection, reflection and mode conversion, refraction, or refraction and mode conversion.

This will be valid only as long as the phonon wavelengths are longer than the interatomic distances. The following additional assumptions are made:

i. Phonons treated as plane waves;

ii. Materials are isotropic Debye solids. Different longitudinal and transverse speeds of sound are, however, permitted.

On this basis, each material is assigned an impedance, Z, which is a product of its density and phonon velocity, v:

$$Z_i = \rho_i v_i. \tag{3.105}$$

The transmission probability can then be defined as [178]:

$$\alpha_{1\to 2} = \frac{4Z_1 Z_2}{(Z_1 + Z_2)^2}. \tag{3.106}$$

The resistance at the boundary then follows [178]:

$$R_{Bd} = \left\{ \frac{\pi^2 {k_B}^4}{15\hbar^3} \left(\sum_j {v_{1,j}}^{-2} \Gamma_{1,j} \right) \right\}^{-1} T^{-3}, \tag{3.107}$$

where the sum is over all j phonon modes and

$$\Gamma_{1,j} = \int_0^{\pi/2} \alpha_{1\to 2}(\theta, j) \cos\theta \sin\theta \, d\theta. \tag{3.108}$$

The T^{-3} factor is the result of the assumption that the materials are Debye solids and it indicates that the boundary conductance is proportional to the number of phonons. The form of equation (3.106) dictates that the transmission probability will be highest when the impedances of the materials are similar.

3.9.2 The Diffuse Mismatch Model

In the DMM, the assumption of complete specularity is removed and *all* phonons are diffusely scattered at the interface. The only determinants of transmission probabilities are the densities of phonon states either side of the boundary and the principle of detailed balance (see 3.3).

The main features of the DMM can be developed in a qualitative way directly from the assumption of complete diffuse scattering. Consider a phonon incident on the boundary. It will certainly be scattered from the aforementioned assumption; what is unknown is whether it will be scattered forward across the boundary, or backwards away from the boundary. It is then the proportion of phonons which backscatter that will determine the boundary resistance. The probability of the phonon crossing the boundary depends on the number of available states for phonons of that mode on each side of the boundary.

The expression for the resistance at the boundary is very similar to the AMM. The only difference is that the transmission probability depends on the phonon velocities on both sides of the boundary:

$$\alpha_i = \frac{\sum_j {v_{3-i.j}}^{-2}}{\sum_j {v_{i,j}}^{-2}}, \tag{3.109}$$

which, upon substitution into the equations above, yields [178]:

$$R_{Bd} = \left(\frac{\pi^2 {k_B}^4}{15\hbar^3} \frac{\left[\sum_j {v_{i,j}}^{-2}\right]\left[\sum_j {v_{3-i.j}}^{-2}\right]}{\sum_j {v_{i,j}}^{-2}}\right)^{-1} T^{-3}. \tag{3.110}$$

Again, the same T^{-3} factor is evident.

3.9.3 The Phonon Radiation Limit

A natural question is: "what is the maximum possible (phonon) thermal boundary conductivity that can be achieved at an interface?" An answer is provided by the phonon radiation limit in which all phonons from the side with lower phonon density of states are

transmitted to the side with a higher phonon density of states. Precisely the correct number of phonons passes in the opposite direction to satisfy the principle of detailed balance and the second law of thermodynamics. Snyder [179] has calculated a theoretical value for this and it has the same T^{-3} dependence as the expressions above.

3.9.4 The Importance of Boundary Resistance in ADRs

The effects of boundary resistance are most apparent in ADRs at the interface between the pill and thermal bus. Here, heat must be conducted into – or away from – the pill by phonons crossing the boundary between the electrically insulating salt and the electrically conducting thermal bus. Below 1 K, such an interface will give rise to a thermal resistance which dominates others within the ADR [100,180,181].

Mendoza [180] proposed a simple model of the boundary effect by suggesting that the thermal conductivity for a unit thickness of the boundary layer will go as $\beta A T^2$, where β is an empirical constant and A is the area of the boundary. The heat flow across the boundary then follows upon integration:

$$\dot{Q} = \int_{T_1}^{T_2} \beta A T^2 dT = \frac{\beta A}{3}(T_2^3 - T_1^3). \qquad (3.111)$$

It is worth noting that the T^3 dependence in this expression is consistent with both the AMM and DMM interpretations of phonon scattering at the boundary. Mendoza found this expression to be a good fit to experimental data on a copper-CPA boundary using $\beta \sim 0.3$ $Wm^{-2}K^{-3}$. Using the same equation and boundary materials, Goodman [181] found a higher value of $\beta \sim 6.7$ $Wm^{-2}K^{-3}$. There is clearly a significant difference between the two, but this is not of great concern for the work that follows as a different value is used which was found from fitting data collected on a representative pill-thermal bus interface.

3.10 Thermal Conductivity in a Magnetic Field

When a magnetic field of sufficient strength is imposed on a metal, it can have a significant effect on its thermal conductivity. The effect is closely related to the change in electrical conductivity that occurs in a magnetic field. This phenomenon has been studied for many years [154] and, even before the detailed theory had been worked out, it was found that many measurements obeyed the following rule due to Kohler [182]:

$$\frac{\Delta\rho}{\rho_0} = f\left(\frac{B}{\rho_0}\right), \tag{3.112}$$

where B is the magnetic field, $\Delta\rho$ is the change in electrical resistivity and ρ_0 is the electrical resistance in zero-field. This rule shows immediately that the effects of magnetoresistance are most noticeable at low temperatures and in metals of high purity since, aside from increasing the applied field, the proportional change in resistance is increased by reducing the zero-field resistance; reducing phonon scattering (by lowering the temperature) and impurity scattering (by using pure samples) will both achieve this. Hence, magnetoresistance offers a way to change the electrical conductivity of a high purity metal link at low temperature. Figure 3.14 illustrates that the change can be several orders of magnitude.

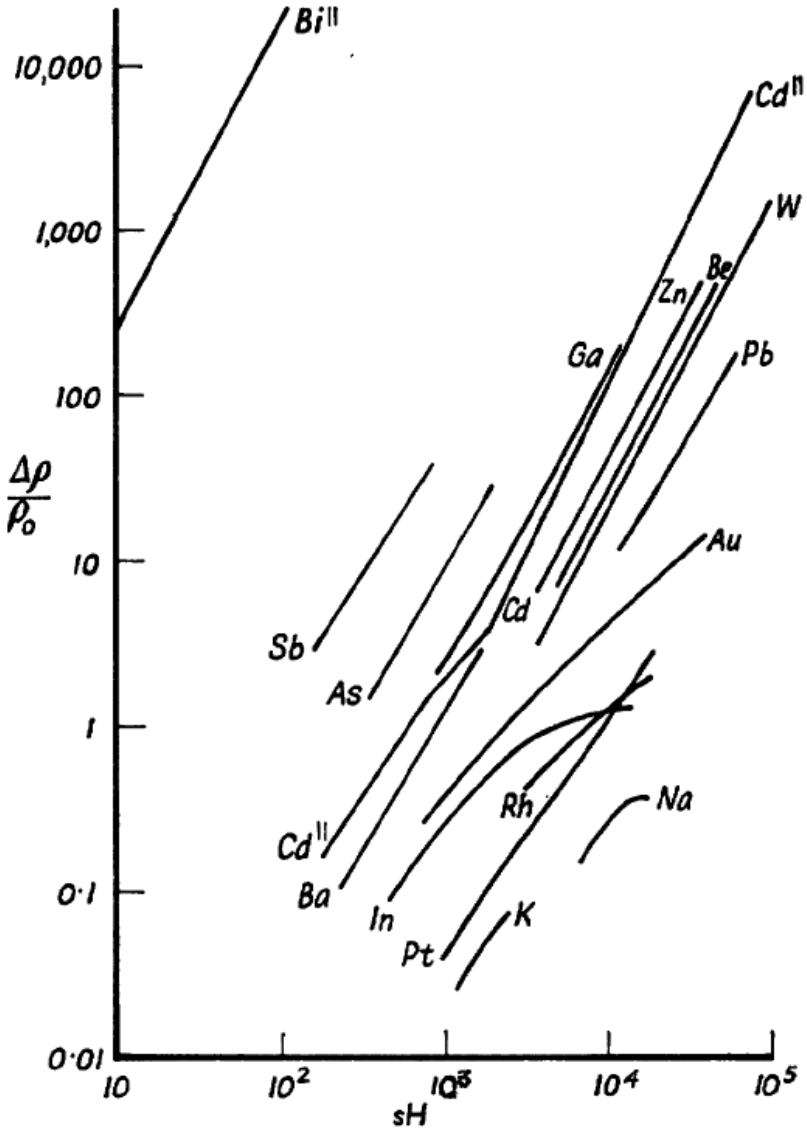

Figure 3.14: Reduced Kohler plot from [154].
Change in resistance as a fraction of zero-field resistance (ρ_0) plotted against sH, where, in this plot, H is magnetic field and s = $\rho_0/\rho(T_0)$ where $\rho(T_0)$ is the lattice component of resistivity of resistivity at a standard temperature.

The large change in electrical conductivity is associated with a large change in thermal conductivity provided that the contribution to the thermal current from phonons is comparatively small. At the usual operating temperatures of ADRs (< 4 K) very few phonon modes are excited in a metal, as explained in 3.6. This is particularly true when the metal has a high Debye temperature. Heat is carried almost entirely by electrons in this situation and consequently any phenomenon which inhibits the motion of electrons in the material

will also inhibit the flow of heat. It is for this reason that magnetoresistive effects are of such interest for ADR heat switches.

The current magnetoresistive heat switches under investigation at MSSL are manufactured from tungsten. As Figure 3.14 indicates, its magnetoresistance spans a large range of conductivities. Although it is not the only metal for which this is true, it is more appropriate as a thermal switch than others shown in the plot for the reasons discussed in Chapter 2 (2.4.2.4). From the arguments above, it is clear that very pure samples are required and it has been found that a difference in purity in the third decimal place can measurably affect the magnetoresistive effect [130]. Tungsten has several inherent properties which make it suitable for use in a magnetoresistive heat switch: it has a high Debye temperature (400 K [14]); it is compensated (equal number of electrons and holes); and it has a highly non-spherical, closed Fermi surface. The importance of these features will be elucidated in the following sections.

3.10.1 Summary of Basic Principles

A magnetic field introduces an additional effect on electrons in the form of the Lorentz force, defined by the vector product of an electron's velocity and the applied magnetic field. Consequently, it acts in a direction which is mutually perpendicular to these vectors. The effect on an electron's k-state is [160]:

$$\dot{\mathbf{k}} = \frac{e}{\hbar}\mathbf{v} \times \boldsymbol{B}. \tag{3.113}$$

Therefore the change in vector **k** is:

(i) normal to the direction of $\boldsymbol{B}$;
(ii) normal to **v**, which is itself normal to the constant energy surface.

Hence, **k** is confined to the orbit defined by the intersection of the constant energy surface with a plane normal to $\boldsymbol{B}$ (see Figure 3.15). The field drives the representative point around this orbit *without changing its energy*. The effect in real space is to curve electron

trajectories into helices, which will only be regular for spherical (free-electron) energy surfaces.

The resultant angular velocity of an electron around its axis is called the cyclotron frequency, defined by [183]:

$$\omega_c = \frac{eB}{m_c^*}. \tag{3.114}$$

This can be applied in general, providing it is noted that the cyclotron mass (m_c^*) will be an effective mass and dependent on the shape of the orbit (in other words, the shape of the Fermi surface).

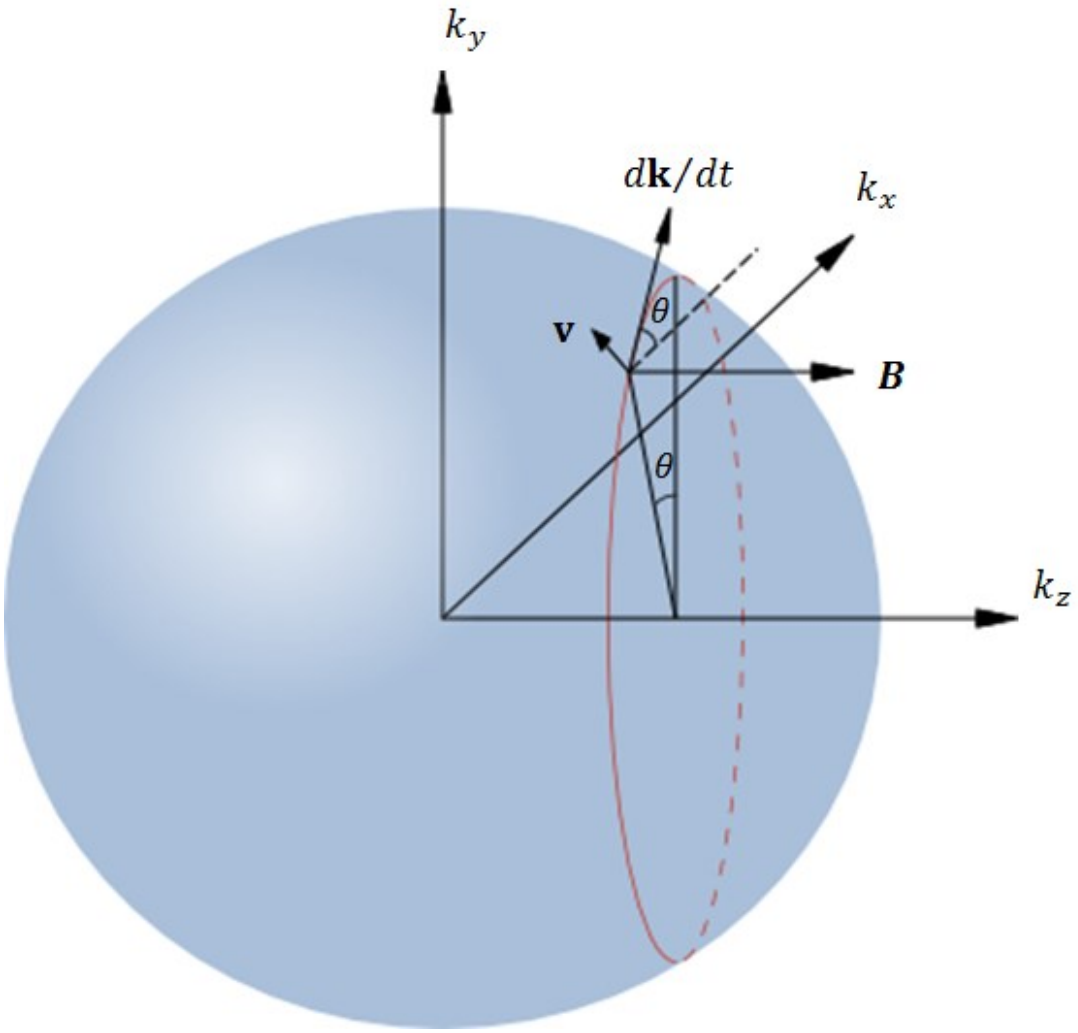

Figure 3.15: Electron orbit on a spherical Fermi surface under the influence of magnetic field in the z-axis.

A result of the effects described above is that the conductivity (either electrical or the electronic part of the thermal) will be anisotropic; it will become a tensor instead of just a scalar. For the case of thermal conductivity (see equation (3.1)), this can be written as

$$\begin{pmatrix} \dot{Q}_x \\ \dot{Q}_y \\ \dot{Q}_z \end{pmatrix} = A \begin{pmatrix} \kappa_{xx} & \kappa_{xy} & \kappa_{xz} \\ \kappa_{yx} & \kappa_{yy} & \kappa_{yz} \\ \kappa_{zx} & \kappa_{zy} & \kappa_{zz} \end{pmatrix} \begin{pmatrix} dT/dx \\ dT/dy \\ dT/dz \end{pmatrix}, \tag{3.115}$$

or, more concisely,

$$\dot{Q}_i = A\kappa_{ij}(\nabla T)_j. \tag{3.116}$$

Once the heat flow has been expressed in this form, calculating it becomes a question of knowing the relevant elements of the conductivity tensor. The remainder of this section summarises the most relevant parts of the extensive theories developed for this purpose.

3.10.2 Low-Field Magnetoresistance

The scenario of electrons moving through a lattice in the presence of a magnetic field may be tackled using the Boltzmann equation (see equation (3.44)). As noted in 3.3.1, the magnetic field has no effect on the equilibrium distribution. However, the magnetic field term on right hand side of the equation involving the out-of-balance part of the distribution $g_{\mathbf{k}}$ remains. This leads to the grouping of the magnetic field terms with the scattering terms, which oppose the "drift" terms on the other side of the equation.[20]

Using the relaxation time approximation and the properties of the Fermi function (see equation (3.52)), equation (3.44) can be re-written as follows:

$$\left(-\frac{\partial f_{\mathbf{k}}^0}{\partial \epsilon}\right)\mathbf{v}_{\mathbf{k}} \cdot \left(-\left(\frac{\epsilon-\mu}{T}\right)\nabla T + e\boldsymbol{E} - \nabla\mu\right) = \frac{g_{\mathbf{k}}}{\tau} + \frac{e}{\hbar}(\mathbf{v}_{\mathbf{k}} \times \boldsymbol{B}) \cdot \frac{\partial g_{\mathbf{k}}}{\partial \mathbf{k}}. \tag{3.117}$$

In the analysis of electrons in magnetic fields, it is their velocity (i.e. the group velocity of the wave-packet) not their wavevector that is the important property. Recognising this, and

[20] This interpretation of the magnetic field as a type of scattering device will be returned to in Chapter 4.

considering the case of thermal gradients without an electric field or any variation of the chemical potential:

$$\left(-\frac{\partial f_{\mathbf{k}}^{0}}{\partial \epsilon}\right)\mathbf{v}_{\mathbf{k}}\cdot\left(-\left(\frac{\epsilon-\mu}{T}\right)\nabla T\right)=\left(\frac{1}{\tau}+\frac{e}{\hbar}(\mathbf{v}_{\mathbf{k}}\times\boldsymbol{B})\cdot\frac{\partial\mathbf{v}}{\partial\mathbf{k}}\cdot\frac{\partial}{\partial\mathbf{v}}\right)g(\mathbf{v}), \tag{3.118}$$

which leads to the following solution for $g(\mathbf{v})$

$$g(\mathbf{v})=\left(1+\frac{e\tau}{\hbar}(\mathbf{v}_{\mathbf{k}}\times\boldsymbol{B})\cdot\frac{\partial\mathbf{v}}{\partial\mathbf{k}}\cdot\frac{\partial}{\partial\mathbf{v}}\right)^{-1}\left(-\frac{\partial f_{\mathbf{k}}^{0}}{\partial \epsilon}\right)\tau\mathbf{v}_{\mathbf{k}}\cdot\left(-\left(\frac{\epsilon-\mu}{T}\right)\nabla T\right), \tag{3.119}$$

or, more concisely,

$$g(\mathbf{v})=(1+\boldsymbol{\Omega})^{-1}\left(-\frac{\partial f_{\mathbf{k}}^{0}}{\partial \epsilon}\right)\tau\mathbf{v}_{\mathbf{k}}\cdot\left(-\left(\frac{\epsilon-\mu}{T}\right)\nabla T\right), \tag{3.120}$$

where the operator $\boldsymbol{\Omega}$ is defined as

$$\boldsymbol{\Omega}=\frac{e\tau}{\hbar}(\mathbf{v}_{\mathbf{k}}\times\boldsymbol{B})\cdot\frac{\partial}{\partial\mathbf{k}}. \tag{3.121}$$

If $\boldsymbol{\Omega}$ is small compared with unity (i.e. the magnetic field is small), then it can be expanded using a MacLaurin series, giving:

$$g(\mathbf{v})=(1-\boldsymbol{\Omega}+\boldsymbol{\Omega}^{2}-\boldsymbol{\Omega}^{3}+\cdots)\left(-\frac{\partial f_{\mathbf{k}}^{0}}{\partial \epsilon}\right)\tau\mathbf{v}_{\mathbf{k}}\cdot\left(-\left(\frac{\epsilon-\mu}{T}\right)\nabla T\right). \tag{3.122}$$

This is effectively an expansion in powers of $\boldsymbol{B}$. Having thus obtained an expression for the out-of-balance part of the distribution, it is inserted into an equation of the form of (3.54) to find the thermal current:

$$\dot{q}=\frac{1}{4\pi^{3}}\int(\epsilon-\mu)\mathbf{v}_{\mathbf{k}}g(\mathbf{v})\,d\mathbf{k}. \tag{3.123}$$

In general, this will lead to a lengthy expression, but it can be simplified greatly when the crystal has cubic symmetry[21]. By drawing a direct analogy with the case of electrical magnetoresistance [183,184], the form of the thermal current when equation (3.122) is inserted into (3.123) will be as follows:

$$\dot{q} = \kappa_0 \nabla T + \kappa_1 \boldsymbol{B} \times \nabla T + \kappa_2^{(1)} B^2 \nabla T + \kappa_2^{(2)} \boldsymbol{B}(\boldsymbol{B} \cdot \nabla \mathrm{T}) + \cdots \qquad (3.124)$$

The zeroth power of $\boldsymbol{B}$ is merely the conductivity in the absence of magnetic field; the first power is the thermal analogue of the Hall coefficient; the first term in B^2 ($\kappa_2^{(1)}$) determines the transverse thermal magnetoresistance and the second term in B^2 ($\kappa_2^{(2)}$) determines the longitudinal thermal magnetoresistance. In anisotropic materials, there will be an additional term in B^2 relating to an anisotropy of the transverse effect, which is apparent under different crystal orientations [183]. Terms above B^2 in the power series are neglected [154]. Davis [185] cites the fact that the magnetic force is very much larger for electrons than the electric force (for which a linear dependency – i.e. Ohm's Law – is taken as given) as the reason for this. This point can be illustrated by considering the effect of electric and magnetic fields on an electron's wavevector [159]. Taking typical values for electric field strength (10^{-2} V/cm) and relaxation time (10^{-14} s) the change in wavevector (found from equation (3.39) – i.e. $d\mathrm{k} = eE\tau/\hbar$) is of the order of 10^{-1} cm^{-1} whereas typical zone dimensions are of the order of $1/a \sim 10^8$ cm^{-1}. In contrast, the change of wavevector caused be a magnetic field of 1 T over the same relaxation time on an electron with a Fermi velocity of 10^7 cm^{-1}s^{-1} ($= e\tau \mathrm{v}B/\hbar$) is of the order of the zone dimensions (i.e. 10^8 cm^{-1}).

On the basis of equation (3.124), it is found that changes in conductivity in cases where the temperature gradient and thermal current are measured in the same direction (κ_2) should be proportional to $1/B^2$; where they are measured in perpendicular directions (and still perpendicular to the field - i.e. κ_1) a $1/B$ factor is expected. This is the thermal analogue of the Hall effect and is referred to as the Righi-Leduc effect.

[21] This will usually be the case and is true for tungsten.

3.10.3 High-Field Magnetoresistance

The high field regime is normally defined by $\omega_c\tau \gg 1$, indicating that the cyclotron frequency is sufficiently large that electrons involved in the conduction process are able to traverse several complete orbits before being scattered. In this case, the representation of electron states by Cartesian components of $\mathbf{k}$ is no longer appropriate and it is more sensible to use coordinates that recognise the periodic motion in k-space: these are $\epsilon, \mathrm{k}_{\boldsymbol{B}}$ and ϕ [160], where ϵ is the energy (not affected by the magnetic field), $\mathrm{k}_{\boldsymbol{B}}$ is the component of $\mathbf{k}$ along the direction of the magnetic field (this also stays constant regardless of field), and ϕ is a "phase variable", defined by:

$$\phi = \omega_c \frac{\hbar}{eB} \int^{\mathbf{k}} \frac{d\mathrm{k}}{\mathrm{v}_\perp}, \tag{3.125}$$

where $\mathrm{v}_\perp$ is the component of $\mathbf{v}$ in the plane normal to $\boldsymbol{B}$ at point $\mathbf{k}$. ϕ increases at a constant rate under the influence of a magnetic field – i.e. $\dot{\phi} = \omega_c$. For a complete orbit $\phi = 2\pi$ and the period is:

$$\frac{2\pi}{\omega_c} = \frac{\hbar}{eB} \int^{\mathbf{k}} \frac{d\mathrm{k}}{\mathrm{v}_\perp}. \tag{3.126}$$

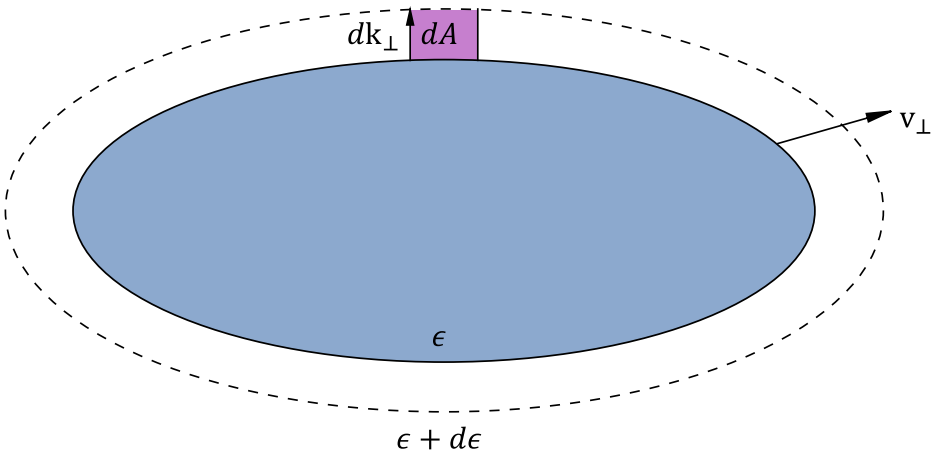

Figure 3.16: Area enclosed by an electron's k-space orbit in the plane perpendicular to the magnetic field
(adapted from [160]).

As the electron completes an orbit, it encloses an area (A_k) of k-space as shown in Figure 3.16. Equation (3.114) can be used with (3.126) and the definition of velocity (equation (3.38)) to define the effective cyclotron mass in terms of this area:

$$\begin{aligned} m_c^* &= \frac{eB}{\omega_c} \\ &= \frac{eB}{2\pi}\frac{\hbar}{eB}\int^{\mathbf{k}}\frac{d\mathrm{k}}{\mathrm{v}_\perp} \\ &= \frac{\hbar^2}{2\pi}\oint\frac{d\mathrm{k}_\perp}{d\epsilon}d\mathrm{k} \\ &= \frac{\hbar^2}{2\pi}\frac{\partial A_\mathrm{k}}{\partial\epsilon}. \end{aligned} \tag{3.127}$$

Expressed using the new high-field variables described above, the Boltzmann equation becomes [160]:

$$\left(\frac{\epsilon-\mu}{T}\nabla T\right)\cdot\mathbf{v}\left(-\frac{\partial f^0}{\partial\epsilon}\right) = \frac{g}{\tau} + \omega_c\frac{\partial g}{\partial\phi}. \tag{3.128}$$

Here, the term on the left hand side gives the effect of the temperature gradient, the first term on the right hand side is the scattering term and the final term incorporates the effects of the magnetic field; $g(\epsilon, k_{\boldsymbol{B}}, \phi)$ is again the change from the equilibrium distribution function as defined in equation (3.48), but is now a function of the high field variables. Equation (3.128) has the following solution [160]:

$$g = \frac{1}{\omega_c}\left(-\frac{\partial f^0}{\partial\epsilon}\right)\int_{-\infty}^{\phi}\mathbf{v}\,\mathrm{e}^{(\phi''-\phi)/\omega_c\tau}d\phi''\cdot\left(\frac{\epsilon-\mu}{T}\nabla T\right). \tag{3.129}$$

Following similar lines to the argument in 3.4.1, the heat flow (per unit area) is defined as:

$$\dot{q} = \frac{1}{4\pi^3}\int(\epsilon-\mu)\mathbf{v}g\,d\mathbf{k}. \tag{3.130}$$

The k-space integral can be expressed as an element of the area on the plane $\mathrm{k}_{\boldsymbol{B}}$ = constant (see Figure 3.16), which is then integrated along $\mathrm{k}_{\boldsymbol{B}}$. By making use of (3.127) this allows (3.130) to be written in terms of the new high-field variables:

$$\dot{q} = \frac{1}{4\pi^3}\iiint (\epsilon - \mu)\mathbf{v}\, g \frac{m_c^*}{\hbar^2} d\epsilon d\mathrm{k}_{\boldsymbol{B}} d\phi. \tag{3.131}$$

Substituting (3.129) into (3.131) and using (3.116) the conductivity tensor can be defined:

$$\kappa_{ij} = \frac{{k_B}^2 T}{12\pi\hbar^2}\int \frac{m_c^*}{\omega_c}\left\{\int_0^{2\pi}\int_0^{\infty} \mathrm{v}_i \mathrm{v}_j \mathrm{e}^{-\phi'/\omega_c\tau} d\phi d\phi'\right\} d\mathrm{k}_{\boldsymbol{B}} \tag{3.132}$$

where use is made of the fact that [163]:

$$\int_{-\infty}^{\infty} (\epsilon - \mu)^2 \left(-\frac{\partial f^0}{\partial \epsilon}\right) d\epsilon = \frac{(\pi k_B T)^2}{3}. \tag{3.133}$$

Equation (3.132) is the Shockley tube integral formula [186], so-called because the integrals describe a series of tubes in k-space. It can be evaluated by expanding the exponential (as shown in equation (3.134)) and using the first non-vanishing term for each component of the conductivity tensor:

$$\mathrm{e}^{-\phi'/\omega_c\tau} = 1 - \frac{\phi'}{\omega_c\tau} + \frac{1}{2}\left(\frac{\phi'}{\omega_c\tau}\right)^2 - \cdots \tag{3.134}$$

The full details are given in Appendix E. To find the form of each component of the conductivity tensor, the procedure is to find the first term in the exponential series which does not cause the integral to vanish [154]. The general argument below follows that given by Ziman [154,160], but has been adapted for the thermal conductivity. κ_{xx} and κ_{zz} are considered specifically as these have application for the results discussed in Chapters 4 and 5.

In the case of κ_{xx}, the linear term in the expansion leads to the following integral.

$$\int \mathrm{v}_x(\phi')d\phi'. \tag{3.135}$$

Equations (3.125) and (3.114) can be used to show that:

$$\phi = \omega_c \frac{\hbar}{eB}\int \frac{d\mathrm{k}}{\mathrm{v}_\perp} = \frac{eB}{m_c^*}\frac{\hbar}{eB}\int \frac{d\mathrm{k}}{\mathrm{v}_\perp} = \frac{\hbar}{m_c^*}\int \frac{d\mathrm{k}}{\mathrm{v}_\perp} \tag{3.136}$$

so that,

$$d\phi = \frac{\hbar}{m_c^*}\frac{d\mathrm{k}}{\mathrm{v}_\perp}. \tag{3.137}$$

Using this and the geometry of the orbit (see Figure 3.15), (3.135) can be written as:

$$\int \mathrm{v}_\perp cos\theta \frac{\hbar}{m_c^*}\frac{d\mathrm{k}}{\mathrm{v}_\perp} = -\frac{\hbar}{m_c^*}\int d\mathrm{k}_y. \tag{3.138}$$

It can be seen from Figure 3.15 that the integral around a closed orbit must vanish and so this term can be neglected.

Turning attention to the second term in the expansion, one finds the integral:

$$\int_0^{2\pi} \phi' \mathrm{v}_x(\phi - \phi')d\phi', \tag{3.139}$$

which can be integrated by parts, using (3.137) as above, to give

$$\frac{2\pi\hbar}{m_c^*}\mathrm{k}_y(\phi) - \frac{\hbar}{m_c^*}\int_0^{2\pi} \mathrm{k}_y(\phi - \phi')d\phi'. \tag{3.140}$$

The second part of this expression vanishes due to the symmetry of the orbit. The first part can be substituted back into (3.132) to give:

$$\begin{aligned}\kappa_{ij} &= \frac{{k_B}^2 T}{12\pi\hbar^2}\int \frac{m_c^*\tau}{2\pi}\frac{1}{\omega_c\tau}\int \mathrm{v}_x \frac{2\pi\hbar}{m_c^*}\mathrm{k}_y d\phi d\mathrm{k}_{\boldsymbol{B}} \\ &= \frac{{k_B}^2 T}{12\pi\hbar}\int \frac{1}{\omega_c}\int \mathrm{v}_x \mathrm{k}_y d\phi d\mathrm{k}_{\boldsymbol{B}} \\ &= \frac{{k_B}^2 T}{12\pi\hbar}\int \frac{1}{\omega_c}\int \mathrm{v}_\perp cos\theta\ \mathrm{k}_y \frac{\hbar}{m_c^*}\frac{d\mathrm{k}}{\mathrm{v}_\perp} d\mathrm{k}_{\boldsymbol{B}} \\ &= \frac{{k_B}^2 T}{12\pi}\int \frac{1}{\omega_c m_c^*}\oint \mathrm{k}_y d\mathrm{k}_y d\mathrm{k}_{\boldsymbol{B}}.\end{aligned} \tag{3.141}$$

The inner integral:

$$\oint \mathrm{k}_y d\mathrm{k}_y \tag{3.142}$$

will also vanish around the orbit. Consequently, the third term in the expansion of the exponential must be used. This does not vanish and leads to a factor of $1/{\omega_c}^2$ in the expression for κ_{xx}. From equation (3.114) it can be seen that this will result in a $1/B^2$ dependence for the conductivity.

In the case of κ_{zz}, the first term is:

$$\int \mathrm{v}_z d\phi. \tag{3.143}$$

Except for particular orbits (see Figure 3.19, for example), v_z will not vanish when integrated around the orbit and, even if this should be the case, it is extremely unlikely to vanish for all values of k_z. Hence this term is expected to saturate at a field-independent value once the high-field regime has been reached.

Evaluating all components using the method above, the complete thermal conductivity tensor [187] can be written and has the following form:

$$\kappa_{ij} = \begin{pmatrix} \frac{k_{xx}}{B^2} & \frac{k_{xy}}{B} & \frac{k_{xz}}{B} \\ \frac{k_{yx}}{B} & \frac{k_{yy}}{B^2} & \frac{k_{yz}}{B} \\ \frac{k_{zx}}{B} & \frac{k_{zy}}{B} & k_{zz} \end{pmatrix}. \tag{3.144}$$

In experimental situations such as those described in Chapters 4 and 5, the thermal current is forced to flow along a known direction (the direction of the sample) and the resulting temperature difference is measured. In terms of equation (3.116), all but one of the elements of $\dot{Q}_i$ are forced to be zero and one of the three (all potentially non-zero) components of $\nabla_j T$ is measured. It is therefore appropriate to re-cast equation (3.116) as:

$$\nabla_i T = \frac{1}{A}\gamma_{ij}\dot{Q}_j. \tag{3.145}$$

and work instead with the resistivity tensor γ_{ij}. This can be found from inversion of (3.144) using standard methods. Working on the assumption of high fields, and therefore only retaining terms of the lowest order in $1/B$, the determinant of κ_{ij} is approximated as:

$$|\kappa_{ij}| \approx c/B^2 \tag{3.146}$$

where c is a constant. The terms relating to transverse thermal resistivity are then found to be:

$$\begin{aligned} \gamma_{xx} &= \left(k_{zz}k_{yy}/B^2 - k_{zy}k_{yz}/B^2\right)/|\kappa_{ij}| \approx \left(k_{zz}k_{yy} - k_{zy}k_{yz}\right)/c \\ \gamma_{yy} &= \left(k_{zz}k_{xx}/B^2 - k_{zx}k_{xz}/B^2\right)/|\kappa_{ij}| \approx \left(k_{zz}k_{xx} - k_{zx}k_{xz}\right)/c, \end{aligned} \tag{3.147}$$

i.e. the transverse resistivity saturates to a constant value in high fields.

It can be shown [188] that the terms in $1/B$ calculated for κ_{xy} and κ_{yx} depend on the number of electrons relative to the number of holes, and that they will vanish in a compensated metal. In this case – which is applicable to tungsten – the next term in the exponential expansion is used to give a $1/B^2$ dependence for both κ_{xy} and κ_{yx}. When the

conductivity tensor containing these elements is inverted, the determinant only contains terms in $1/B^4$:

$$\left|\kappa_{ij}\right| = c/B^4. \tag{3.148}$$

The transverse resistivity terms now become:

$$\begin{aligned}\gamma_{xx} &= \left(k_{zz}k_{yy}/B^2 - k_{zy}k_{yz}/B^2\right)/\left|\kappa_{ij}\right| = B^2\left(k_{zz}k_{yy} - k_{zy}k_{yz}\right)/c \\ \gamma_{yy} &= \left(k_{zz}k_{xx}/B^2 - k_{zx}k_{xz}/B^2\right)/\left|\kappa_{ij}\right| = B^2\left(k_{zz}k_{xx} - k_{zx}k_{xz}\right)/c\end{aligned} \tag{3.149}$$

and are both $\propto B^2$. This indicates that the transverse thermal magnetoresistivity of compensated metals such as tungsten would not be expected to saturate in high fields. It can also be noted that the transverse resistivity terms behave as the reciprocal of the conductivity terms and this makes it equally valid to plot γ_{xx} against B^2 or κ_{xx} against $1/B^2$. This is made use of in Chapters 4 and 5.

The above solutions only apply for closed orbits. If open orbits are present, the first term in the expansion may not vanish in the general case and the conductivity will no longer tend to $1/B^2$ as B tends to infinity, but may saturate [188]. That this will be the case is best illustrated by considering a diagram of a typical open orbit (Figure 3.17). If the open orbit is in the y-direction, the electron velocity – which is directed normal to the Fermi surface by (3.38) – will have constant component in the x-direction, but no net velocity in y-direction as $\mathbf{v}(\mathbf{k})$ rocks back and forth in a periodic fashion causing the y-components to sum to zero. A component of velocity in the x-direction remains, however, and leads to saturation of conductivity in this direction.

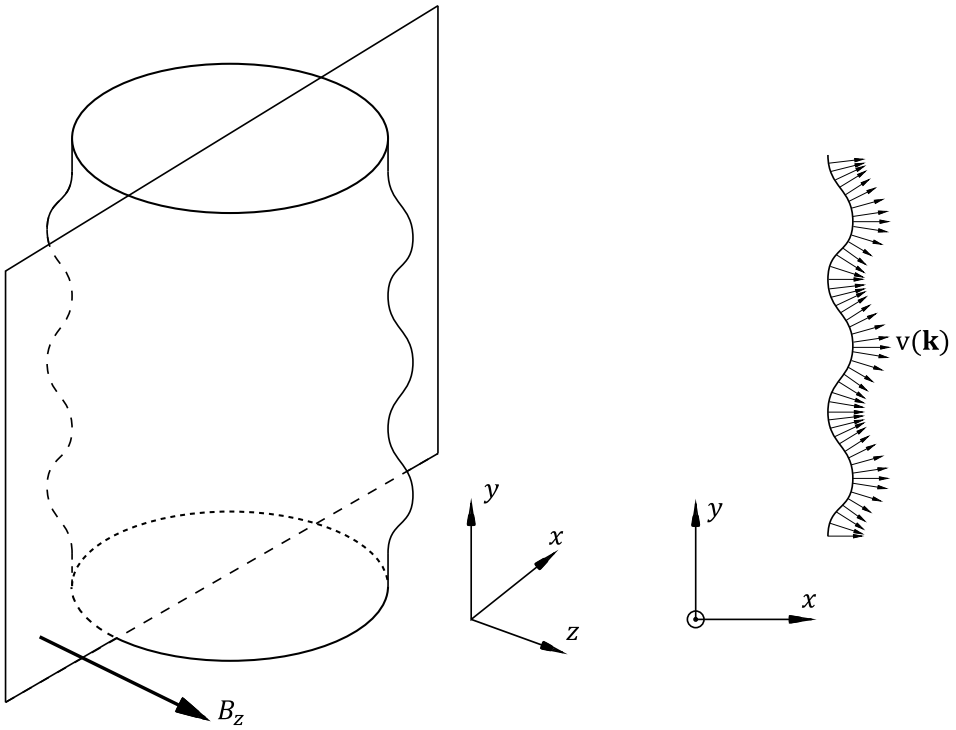

Figure 3.17: Illustration of a multiply connected Fermi surface
cut by a plane normal to the magnetic field (left) and the resulting electron velocity as it moves along an orbit created by the intersection of the plane and the Fermi surface (right) (adapted from [16]).

Open orbits can only be present in connected Fermi surfaces. This scenario usually need not be considered for tungsten as all the sheets of its Fermi surface are closed (see Figure 3.18, below). However, despite its closed Fermi surface, there is a scenario where open orbits may arise: that is when intersheet scattering takes place. This has been studied by Marchenkov *et al.* [189], who observed differences in the magnetic field exponent when the current is directed along different crystal axes. They suggested that at certain temperatures, there will be phonons of an appropriate wavevector to scatter electrons from one Fermi surface sheet to a nearby point on an adjacent one. The sizes of the gaps between sheets in k-space depend on the plane in which the electrons are moving. For certain crystal orientations, this intersheet scattering then permits some electron orbits to become open, or extended, even though the energy surfaces themselves are closed. This is discussed in more detail in Chapter 4 in relation to the results presented there.

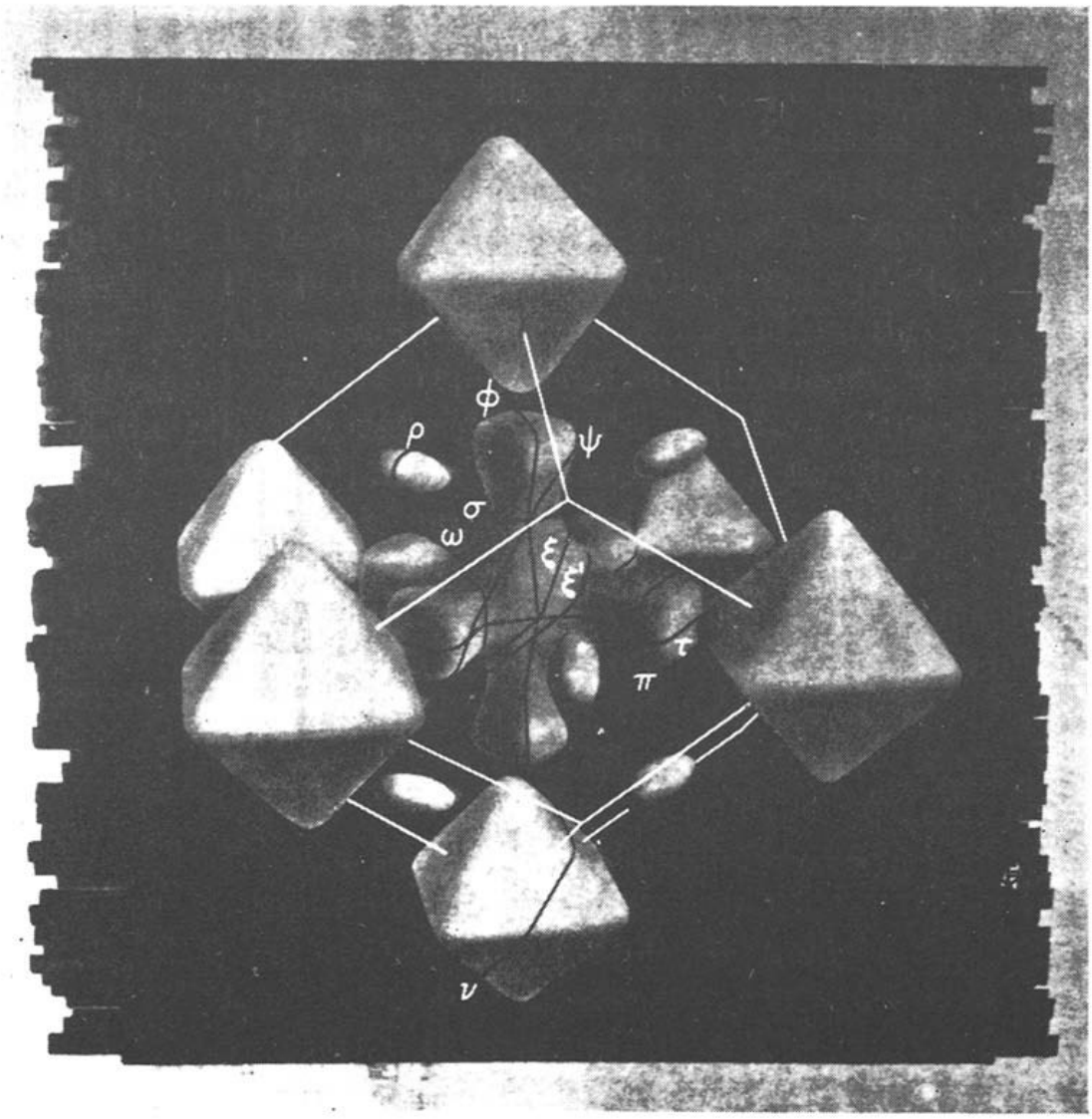

Figure 3.18: Fermi surface of tungsten sketched from de Haas–van Alphen measurements [190].

3.10.4 Longitudinal Magnetoresistance

The κ_{zz} term in the conductivity tensor determines the conductivity when the magnetic field and temperature gradient are aligned. As shown above, it becomes independent of B at high fields. However, the value at which it saturates depends on the properties of the metal's Fermi surface.

For any effect to be seen at all, the shape of the energy surface must be such that the electron velocity (normal to the surface) can change direction as it moves around the surface under the influence of a magnetic field. An example of such a section of Fermi surface is shown in

Figure 3.19. It is seen that the component of velocity in the z-direction ($= \mathrm{v}\cos\theta$) reverses as a complete orbit is traversed.

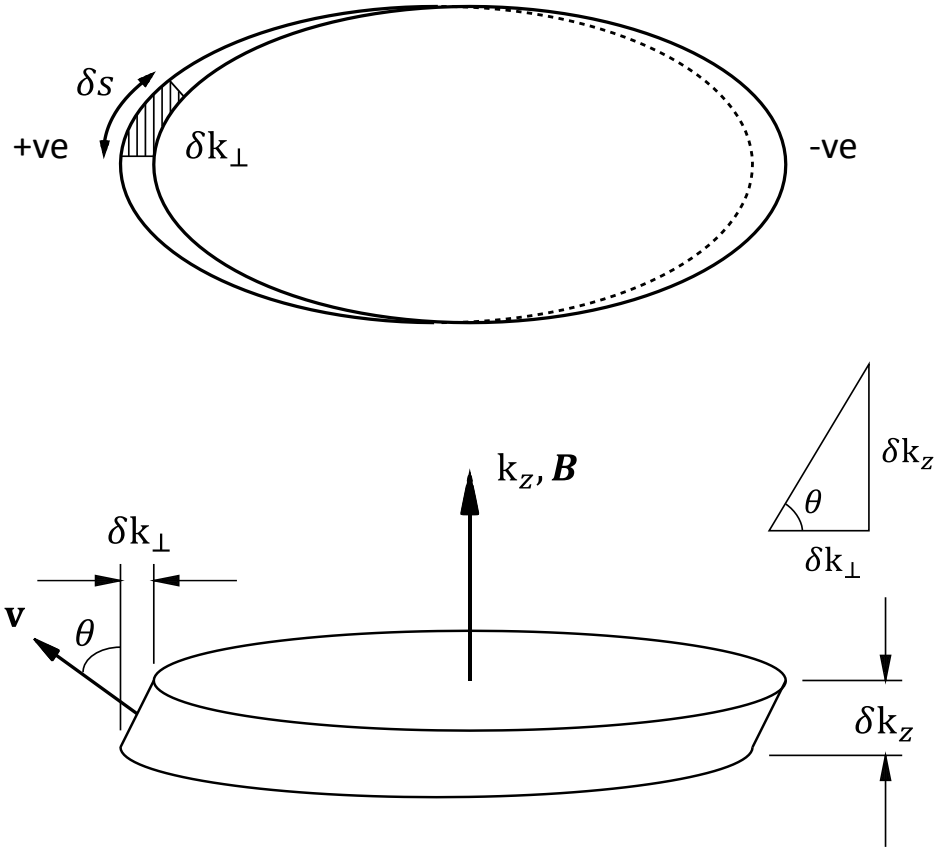

Figure 3.19: Example slice of Fermi surface in k_z (after [183])
where the z-component of velocity is reversed around the orbit (bottom) and projection of the slice onto a plane normal to $\boldsymbol{B}$ (top).

An expression for the electrical conductivity term σ_{zz} can be a found in terms of the parameters of the Fermi surface and the electron orbits [183], which leads to an alternative form of equation (3.64):

$$\sigma_{ij} = \frac{e^2}{4\pi^3\hbar}\int L_i dS_{F_j}. \tag{3.150}$$

The full derivation is given in Appendix F. L_i represents the mean vector distance travelled by each electron in the bunch from the moment of creation until scattering brings the

centroid of the bunch to rest; it is a function of the position on the Fermi surface, the applied magnetic field and scattering mechanisms. $\int dS_{F_j}$ is the integral over the Fermi surface.

To find the longitudinal conductivity, σ_{zz}, one must find L_z and then integrate over dS_{F_z}. L_z depends on the distance travelled in the z-direction in each orbit and the probability of being scattered in any given orbit. A complete derivation is given in Appendix G and leads to equation (3.151) for the saturation value of the longitudinal conductivity.

$$\sigma_{zz}(\infty) = \frac{e^2}{4\pi^3\hbar}\int \bar{l}C^2 dS_F, \tag{3.151}$$

where

$$C = \left(\frac{\partial A_k}{\partial S_F}\right)_E. \tag{3.152}$$

The argument can be understood in a qualitative sense with reference to Figure 3.19. The z-component of velocity summed over the full orbit is proportional to the projected area of the Fermi surface slice $\delta \mathrm{k}_z$ onto the plane normal to the field, $\boldsymbol{B}$. The sign of the area depends on the direction of the z-component of velocity, as indicated in the bottom half of the figure. If the positively and negatively signed parts of the area are equal, v_z will vanish when integrated around a full orbit. To minimise the total conductivity, the integrated contribution from all the slices of the Fermi surface must be a minimum. Equivalently, the parameter C – determined by the geometry of the Fermi surface – must be minimized to minimize the saturation value of the longitudinal conductivity. For a given Fermi surface, there will be certain combinations of magnetic field direction and crystal orientation for which this minimisation can be achieved; and they will occur where the magnetic field is directed on an axis about which the Fermi surface does not have axial symmetry (as in Figure 3.19).

3.10.5 Galvanomagnetomorphic Effect

The application of a magnetic field will not always act to increase the thermal or electrical resistance of a metal. The galvanomagnetomorphic effect is an example of this. If the field

is applied parallel to the direction of the current (i.e. electron motion), the electron trajectories will be curved into helices[22] (see Figure 3.20). When the mean free path in the bulk material is long compared to the sample dimensions (as it will be in very pure, single crystal samples) and the dominant cause of scattering is electron interactions with the sample surface, this can act to reduce the resistivity.

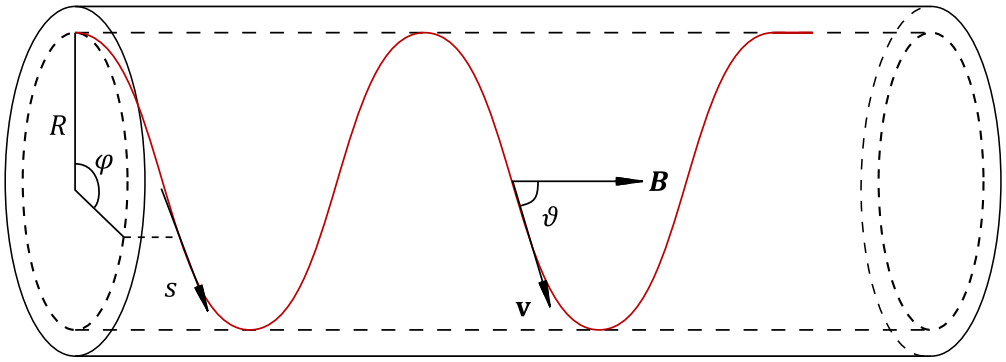

Figure 3.20: Motion of an electron down a wire with an axial magnetic field applied (after [154]).

In the following description, a circular cross-section wire is considered, but the same arguments could apply to rectangular cross-sections. For an electron of velocity v travelling at angle ϑ to the magnetic field, the projection of its helical path on the normal plane will have a radius:

$$R = \frac{m_e \mathrm{v}}{eB} \sin\vartheta = r_B \sin\vartheta. \tag{3.153}$$

$r_B = m_e \mathrm{v}/eB$ is the Larmor radius and is the radius of the real-space orbit of an electron with velocity v in the plane perpendicular to a magnetic field B. When the projection traverses an angle φ round the circle between leaving the wall and reaching the cross-section where it is counted in the current, the length of the arc of the circle is $R\varphi$. The length of the helix is then:

[22] Assuming a spherical "free-electron" Fermi surface; the trajectories will not be regular helices for metals with different Fermi surfaces, but the principles of the argument still apply.

$$s = \frac{R\varphi}{\sin\vartheta} = r_B\varphi. \tag{3.154}$$

Using kinetic arguments similar to those employed in 3.1, the probability of an electron travelling a distance greater than x is $\mathrm{e}^{-x/\Lambda}$ where Λ is the mean free path. Therefore, if Λ_0 is the mean free path in a bulk sample (i.e. one where surface scattering is not a limiting factor) that is not in a magnetic field, the twisting of a trajectory by the field will introduce the following factor into the conductivity [170] (c.f. equation (3.58)):

$$1 - \mathrm{e}^{-(r_B\,\varphi)/\Lambda_0}. \tag{3.155}$$

The change in mean free path of the electron distribution can be calculated by integrating over the cross-section of the sample and all angles of initial velocity [154]:

$$\frac{\Lambda}{\Lambda_0} = \frac{3}{4\pi S_c}\iint\left\{1 - \mathrm{e}^{-(r_B\,\varphi)/\Lambda_0}\right\}\cos^2\vartheta\; d\Omega dS_c, \tag{3.156}$$

where $d\Omega$ is an element of solid angle giving the direction of electron trajectory and S_c is the cross-sectional area of the sample. This integral has be evaluated by Chambers who also made measurements on lengths of 30 micro-inch diameter sodium wire at different temperatures [170]. The results are shown in Figure 3.21. In Chambers' notation, κ is the ratio of the sample diameter to the mean free path. The points show the measured values and the dashed lines show the theoretical curves adjusted to provide best fit by tuning the electron velocity and mean free path.

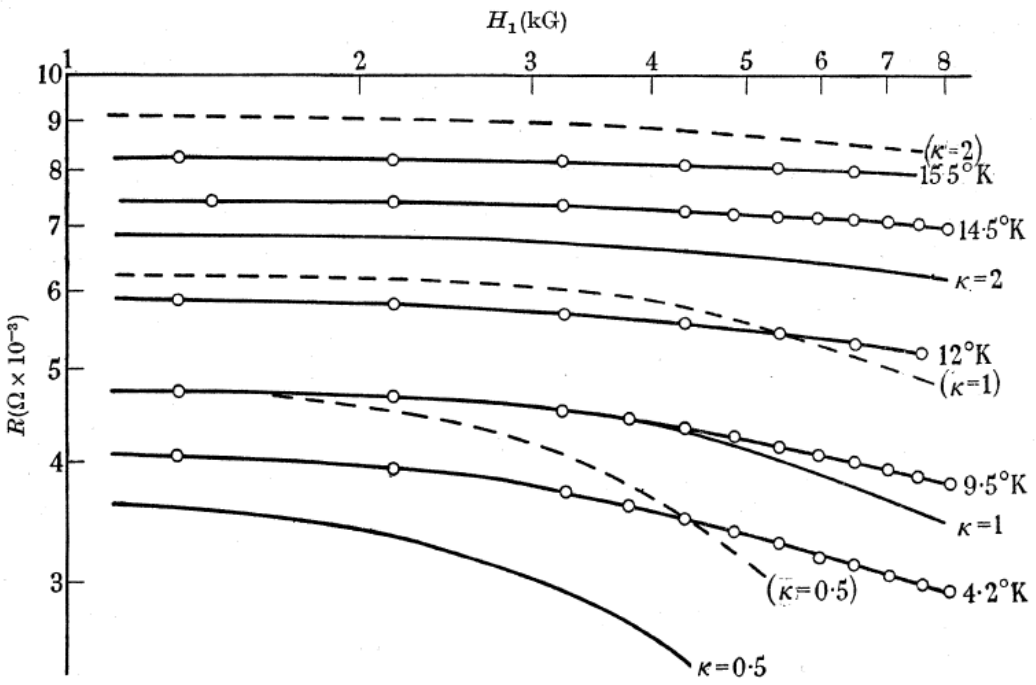

Figure 3.21: Experimental results on 30μ-inch sodium wire, with theoretical curves [170].

The general trend of a resistance reduction as the field increases can clearly be seen. The effect is not as great as the theoretical predictions and Chambers attributed this to bulk magnetoresistance.

For materials with non-spherical Fermi surfaces, such as tungsten, the electron trajectories will not be regular helices. However, the field will still act to constrain the motion within with radius R and as long as this is less than the sample's cross-sectional dimensions the resistance will be reduced. Baer and Wagner [191] found evidence that this does occur in tungsten. Their results are summarised in Figure 3.22 with the pertinent sample details given in Table 3.2. They identify two type of behaviour: the first (shown in the upper half of Figure 3.22 and labelled I) is a very small rise in resistance (negligible in some cases) followed by a substantial decrease; the second (shown in the lower half of Figure 3.22 and labelled II) is a small rise followed by a small decrease. The results do not present an entirely consistent picture, but the first type of behaviour is broadly associated with samples that have either very small diameters and/or very high purity – i.e. samples for which the mean free path might be expected to exceed the sample dimensions. In these cases curving

electron trajectories in helices can be expected to decrease the resistance and the greater the mean free path in comparison to the sample size, the higher the fields for which a benefit can be expected to be seen. Conversely, in the samples with large diameters and/or lower purities (i.e. the mean free path would be expected to be less than the sample dimensions) the effects of bulk magnetoresistance appear to dominate with curves showing an initial rise which is overcome when the field reaches a sufficient level to keep a majority of the electrons from interacting with the surface, before an upward trend reappears. Comparing samples W-7 and W-16, for example, one can see that in the much smaller diameter sample (W-16), the decrease in resistivity continues to grow with field, whereas in the larger sample (W-7) this benefit is short-lived and is overcome by bulk magnetoresistance at relatively low fields. It can also be noted that reducing interactions between the electrons and the surface might be expected to have greater benefit in samples with a poorer surface finish. This appears to be consistent with the results for sample W-4 which was electro-etched rather than electro-polished as the other samples were: its resistance is reduced at almost all fields measured. Perhaps all that can be concluded for certain is that the data shows clear evidence of two competing effects and these are presumably the galvanomagnetomorphic effect and the bulk magnetoresistance.

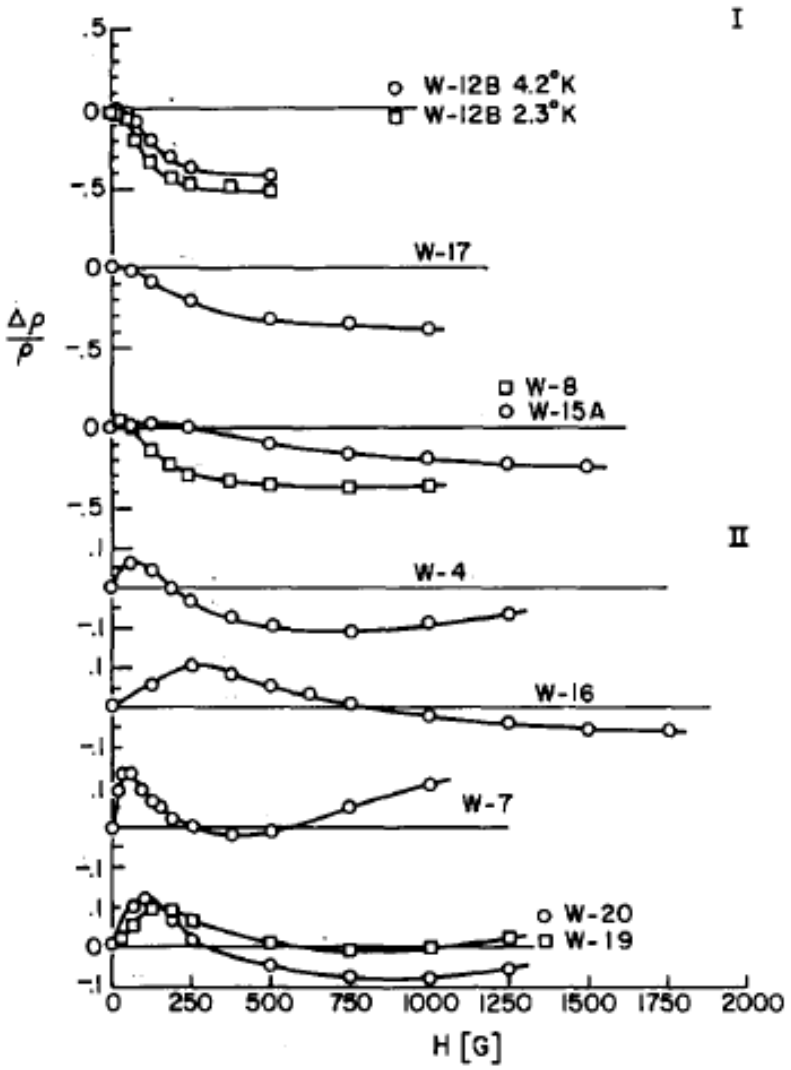

Figure 3.22: Longitudinal magnetoresistance of single crystal tungsten at 4.2K [191].

Sample	Diameter (mm)	RRR	Surface treatment	Surface condition
W-4	1	30000	Electro–etched	Matt
W-7	3	96000	Electro–polished	Mirror
W-8	1.5	75000	Electro–polished	Mirror
W-12B	0.9	52000	Electro–polished	Mirror
W-15A	0.28	15000	Electro–polished	Mirror
W-16	0.23	23000	Electro–polished	Mirror
W-17	0.6	18000	Electro–polished	Mirror
W-19	0.6	~28000	Electro–polished	Mirror
W-20	1	~40000	Electro–polished	Mirror

Table 3.2: Summary of properties of tungsten samples used to obtain the results in Figure 3.22 (adapted from [191]).

3.10.6 Small Angle Scattering

It has already been discussed (3.5.2.1) how small angle scattering ("vertical processes" in the terminology of 3.5.2.1) can have a greater effect on thermal transport than electrical transport (and therefore cause deviations from the Wiedemann-Franz law). At low temperatures they are likely to be the main scattering process attributable to the lattice, since the only phonon modes excited are those with short wavevectors; phonons with wavevectors large enough to scatter an electron to the opposite side of the Fermi surface simply do not exist. When a magnetic field is present the effect becomes more complex.

In general, small angle scattering will delay the onset of the high-field regime, since an electron is more likely to be scattered to another state before it can complete a full orbit. The true scattering situation then lies somewhere between full catastrophic scattering and diffusive motion of the electrons over the Fermi surface. It might not change the overall magnetoresistive trend because each scattering event only causes a small shift in state and the resulting "random walk" across the Fermi surface will eventually lead to the electron traversing a full orbit of the surface, but in a correspondingly longer time. Although $\omega_c\tau$ as calculated from (3.114) might be much greater than 1, its effective value is actually reduced. In the case of longitudinal magnetoresistance this will mean a delay in the onset of high-field saturation.

There may be a further effect relating particularly to longitudinal magnetoresistance. If the field is aligned in certain crystal directions, a small angle scattering event may move an electron into a portion of the Fermi surface where its velocity will experience many reversals and its contribution to the overall current is lost. Pipppard has made calculations for a Fermi surface like that of copper (where the velocity reversals occur in the "neck" regions) and finds that this effect may result in nearly an order of magnitude change in the longitudinal conductivity at saturation [183]. In another calculation [192], he suggests that exponent of B in the transverse terms of the conductivity tensor (e.g. σ_{xx}) may be modified by the same effects.

3.10.7 Orbit Quantisation

In sufficiently high magnetic fields, the wavefunctions of the electrons are modified so drastically that their states are condensed onto a series of discrete energy levels (*Landau levels*). In this situation, $\mathrm{k}_x, \mathrm{k}_y, \mathrm{k}_z$ are no longer good quantum numbers and the problem must be described in terms of the electron's energy, and its position in an orbit. The condensation of states onto discrete energy levels causes oscillations in conduction phenomena as the field is increased (the *Shubnikov-de Haas effect*) because higher fields force successive energy levels upwards; conduction peaks when a particular level coincide with the Fermi level and drops when there is no coincidence.

This effect will not be considered further as it is assumed that the fields employed in the experiments described in the following chapters are not sufficient to cause this in tungsten. As will be seen from the results, the lack of oscillatory behaviour in conduction seems to confirm this.

3.10.8 Static Skin Effect

The Static Skin Effect is a surface effect arising in pure metals in a magnetic field. The purity must be such that the mean free path in the absence of a magnetic field exceeds the Larmor radius when the field is applied. Its impact on electron transport is felt most keenly when the magnetic field is perpendicular to the current flow. In the bulk material, the electron dynamics described in section 3.10.1 apply and the magnetic field causes the electrons to traverse orbits about an axis parallel to the field, thus hindering their ability to progress through the sample and contribute to the current. However, things are slightly different at distances less than the Larmor radius from the sample surface. Here, electrons will interact with the surface before completing a complete orbit. If this interaction results in a specular reflection they will progress a distance equal to another Larmor radius down the sample (see Figure 3.23). As a result, the majority of the current will be carried in a thin layer of thickness r_B just below the surface.

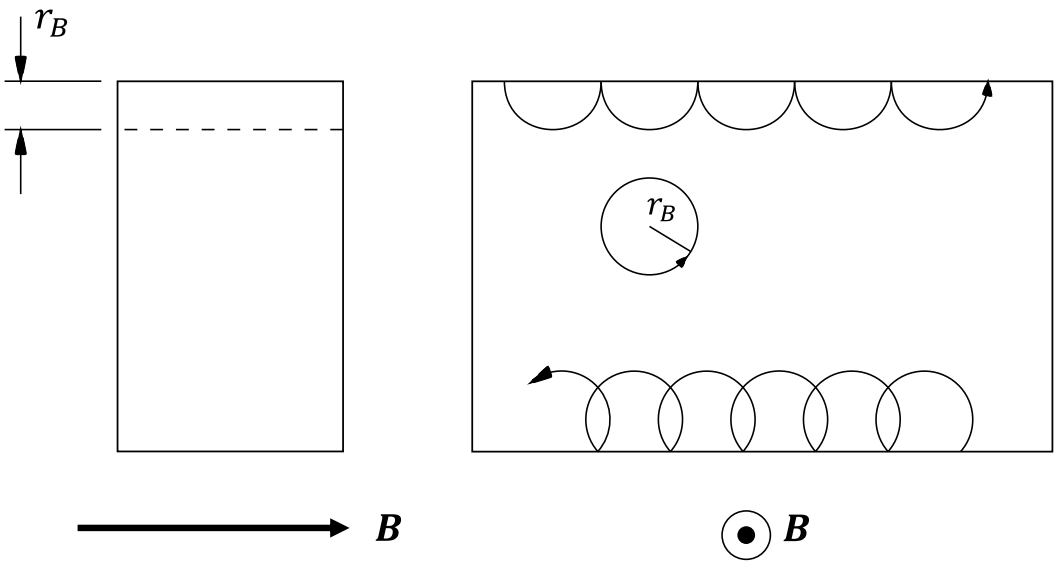

Figure 3.23: Examples of electron trajectories in a magnetic field showing the effects of interaction with the sample surface.
The right hand image shows a plan view of the sample with the magnetic field directed out of the page; the left hand image shows the corresponding end view.

In samples where the Static Skin Effect plays a role, the cross-sectional dimension perpendicular to the magnetic field is less important for the overall conductivity; it is the dimension parallel to the field that is more crucial since the majority of the current flow occurs in a thin layer below this surface (as illustrated in the left hand side of Figure 3.23).

If scattering is diffuse, each collision with the surface randomises the electron's motion in the same way as a scattering event in the bulk. The mean free path near the surface then becomes of the same order as the mean free path in the bulk ($\sim r_B$). The dependence of the conductivity on magnetic field is therefore the same as for bulky samples, but the current flows differently in different parts of the conductor cross-section [193].

If, on the other hand, scattering is specular, the components of the electron momentum parallel to the surface are conserved and only the component perpendicular to the surface is affected; its magnitude will be the same, but its direction reversed (c.f. equation (3.93)). In this way, it is possible for electrons to move on open trajectories even when the Fermi surface is closed; they are continuously reflected onto a different portion of the Fermi

surface before they are able to complete a full cyclotron orbit. When this occurs, the conductivity near the surface will play a key role in the sample's overall conductivity and can cause the dependence on magnetic field to differ from what would be expected in a larger sample. It will be seen that this is important for interpreting the results presented in Chapter 4.

Chapter 4 – Thermal Magnetoconductivity of Tungsten over a Range of Magnetic Fields

This chapter and the following one investigate in detail the performance of tungsten as a material for magnetoresistive heat switches in ADRs. In the current chapter, attention is restricted to thermal magnetoconductivity in the transverse case – i.e. when the direction of heat flow is perpendicular to the magnetic field. In the first part, the relevant theory from Chapter 3 is applied to this scenario and then results are presented which confirm the theoretical approach.

4.1 Introduction

For miniaturisation of a tandem CADR it is crucial to be able to rapidly transfer heat between the cold stage, the pills and the bath. This permits the side of the CADR that is not providing cooling to be recycled quickly and thus reduces the required hold time for the "active" side. Shorter hold times translate to smaller pills and magnets, which lead to a smaller ADR. The required pill size can also be reduced by minimising the parasitic heat loads on it. As described in Chapter 2, the heat switch plays the central role in achieving both these aims: a high conductivity when it is "on" will ensure the heat of magnetisation is dumped to the bath as quickly as possible and a low conductivity when it is "off" will minimise parasitic loads. The latter point becomes even more important when heat leak through the "off" switch is the dominant parasitic load. The two requirements can be combined to one by requiring the heat switch to have a large switching ratio.

As shown in Chapter 3, tungsten has the potential to offer this performance through the large reduction in thermal conductivity achieved by applying a magnetic field. It is also worth noting at this point that because high purity, single crystal tungsten has such a high thermal conductivity in the zero-field state, even when reduced by several orders of magnitude it can still be comparable to materials traditionally used for their low conductivity (e.g. G-10

[194]). This necessitates large (length)/(cross-sectional area) ratios, which hampers miniaturisation. The absolute "off" conductivity is therefore also an important parameter and should be used in conjunction with the switching ratio to assess heat switch performance.

To evaluate the extent to which tungsten heat switches enable ADR miniaturisation, it is important to understand how its conductivity changes in a magnetic field and to be able to accurately model this. Developing such a model and verifying it experimentally are the subjects of this chapter.

4.2 Modelling the Thermal Conductivity

The details of the semi-classical theory of thermal conductivity were given in Chapter 3. Here, this theory is used to develop an expression which is capable of modelling the thermal conductivity in zero magnetic field, high magnetic field and all fields in between. At the temperatures of concern (< 6 K), the phonon contribution to the heat current is at least 4 orders of magnitude smaller than the electronic contribution [195]. Furthermore, it is not affected by the presence of the magnetic field. For these reasons the approach taken focuses primarily on the electronic part of the thermal conductivity and exploits the similarities of its behaviour in a magnetic field to its electrical counterpart.

As noted in Chapter 3, the distinction between "low" and "high" fields is made using the quantity $\omega_c\tau$, where ω_c is the cyclotron frequency and τ is the relaxation time. A metal is normally said to be in the "high-field" condition when $\omega_c\tau \gg 1$. However, this statement leaves some ambiguity as to the point at which $\omega_c\tau$ is considered to be much greater than 1. A more precise definition can be made by interpreting $\omega_c\tau$ as the mean angle turned by an electron between collisions [183]. The transition between low and high fields can then be deemed to occur when $\omega_c\tau \geq 2\pi$ – i.e. when the applied field is such that an electron can complete one or more orbits about the axis of the magnetic field before being scattered. An additional assumption in what follows is that the field is not sufficient to cause orbit

quantisation, such as is associated with the *Shubnikov-de Haas* effect and other oscillatory phenomena.

As noted above, this chapter will only be concerned with tungsten's transverse magnetoconductivity[23] – i.e. where the thermal current and the measured thermal gradient are in the same direction, which is perpendicular to the magnetic field. As described in Chapter 3, both the low and high field theories predict a conductivity which varies as $1/B^2$ for this arrangement.

Calculating the thermal conductivity requires knowledge of the distribution function of the heat carriers, which are primarily electrons in this case (see 3.5). This can be determined by solution of the Boltzmann equation. It was shown in 3.3.1 that the most direct (and sometimes only) route to a solution is to make the relaxation time approximation; when this is done the relaxation time τ appears as a factor in the distribution function and therefore also the conductivity. Furthermore, Mathiessen's rule (see 3.4.3) can be used to combine different relaxation times (from different scattering sources) and these combinations will also appear as a factor in the conductivity. This is used below when looking to combine the low and high-field conditions.

Although the relaxation time approximation is a simplified phenomenological description of the real processes at work, it is generally considered to be reasonably accurate when scattering is catastrophic and there is evidence that it produces realistic results for tungsten [196]. It is likely to be a good assumption at low temperatures when impurities and electron-electron interactions are the dominant scattering mechanisms. Measurements of the temperature dependence of tungsten's conductivity made at MSSL appear to back up this assumption [Hepburn *et al.* in preparation], which is further reinforced by the findings of others [195,197].

[23] The conductivity when the applied field and thermal current are not perpendicular is the subject of Chapter 5.

The implicit assumption in using the relaxation time approach is that the scattering probability per unit time, P, is proportional to the reciprocal of the relaxation time [159]:

$$\frac{1}{\tau} \propto P. \tag{4.1}$$

Now, as an equation is sought which covers the zero-field to high-field conditions and everything in between, the following postulate is made: an electron will be scattered either by mechanisms which limit the zero-field conductivity (with probability P_0) *or* by the mechanisms that modulate the field dependent conductivity (with probability P_B) and that these two mechanisms are independent. Since it is known that the low-field conductivity has the same magnetic field dependence as the high-field conductivity, these two effects can be subsumed into a single term. To find the total probability of an electron being scattered the zero-field and field-dependent probabilities are simply summed:

$$P_{tot} = P_0 + P_B. \tag{4.2}$$

This could equivalently be formulated in terms of Matthiessen's rule:

$$\frac{1}{\tau} = \frac{1}{\tau_0} + \frac{1}{\tau_B}. \tag{4.3}$$

Here a relaxation time has been associated with the part of the conductivity which varies in a magnetic field. This idea has been used before [198], where it was argued that one could equate the reversal of an electron's motion due to the Lorentz force with a scattering event. No claim is made here that such a direct physical interpretation is valid, but it is merely used as a phenomenological mechanism to deal with conductivities over a wide range of fields.

If a k independent relaxation time is assumed for each mechanism, each reciprocal of relaxation time, $1/\tau$, can be associated with a resistivity due to that mechanism [159], giving

$$\rho = \rho_0 + \rho_B, \tag{4.4}$$

i.e.

$$\frac{1}{\kappa_e} = \frac{1}{\kappa_0} + \frac{1}{\kappa_B}. \tag{4.5}$$

In equation (4.5) the resistivities have been converted to conductivities and κ_e is the electronic part of the thermal conductivity. For the purposes of comparison with the more rigorous approach of solving the Boltzmann equation using the variational principle, it can be noted that this method leads to $\rho \geq \rho_0 + \rho_B$ [154].

The thermal conductivity of a metal in zero-field can be found using equation (3.73). Given that tungsten has a high Debye temperature and the present concern is with temperatures below 6 K, it is reasonable to neglect the effects of electron scattering by phonons. Taking this approach has been found to model the zero-field thermal conductivity of tungsten well below 6K [195] and leads to the following equation:

$$\frac{1}{\kappa_0(T)} = \frac{a_1 + a_2 T^2}{T}. \tag{4.6}$$

where a_1 and a_2 are fitting parameters. If they are interpreted according to the theory described in Chapter 3, then they represent contributions from impurity and electron-electron scattering, respectively (c.f. equation (3.76)).

Although studies have been made on the field-dependent conductivity as a function of temperature and magnetic field [199], it does not have such a simple theoretical form as the zero-field conductivity. Consequently, it is necessary to turn to an empirical expression. High-field measurements on tungsten [199] have shown that, below 6 K, κ_B, can be fitted to:

$$\kappa_B(T) = \frac{a_3 T + a_4 T^4}{B^n}, \tag{4.7}$$

where B is the magnetic field and a_3, a_4 and n are fitting parameters. Semi-classical magnetoresistance theory predicts a value of 2 for n [187,188], although deviations from this have been observed for tungsten [189,200,201].

Substituting (4.6) and (4.7) in to equation (4.5) and re-arranging gives:

$$\kappa_e(T) = \frac{1}{\frac{a_1 + a_2T^2}{T} + \frac{B^n}{a_3T + a_4T^4}}. \tag{4.8}$$

At this point a term for the lattice conductivity is included, which is assumed to be acting in parallel to the electronic thermal conductivity. Although the scattering effects of phonons were neglected in equation (4.6), above, this does not mean that the transport of heat by them should also be neglected. As described in 3.5.2.1, phonons present at low temperatures will have long wavelengths and short wavevectors, which will not significantly affect the wavevectors of any electrons with which they interact. Nevertheless, such phonons are still capable of transporting heat. It is found below that the phonon contribution to the conductivity is indeed small, but inclusion of a phonon term allows for its effect to be incorporated in the modelled thermal conductivity.

The lattice conductivity in tungsten at low temperatures has been measured by a number of researchers and is found to be proportional to T^2 [156,195,199]. A quadratic dependence suggests that electrons are the dominant source of scattering for phonons. This is explained by noting that the scattering rate $(1/\tau)$ for phonons in electron-phonon interactions can be shown to be proportional to phonon frequency [157] and, from equation (3.72), this is proportional to T. This means that the phonon mean free path will be proportional to $1/T$ and when this is combined with the T^3 Debye specific heat capacity in the kinetic formula for thermal conductivity (see equation (3.9)), the result is proportional to T^2. Thus, the equation for the combined conductivity becomes

$$\kappa(T) = b_0T^2 + \frac{1}{\frac{a_1 + a_2T^2}{T} + \frac{B^n}{a_3T + a_4T^4}}, \tag{4.9}$$

where b_0 is the phonon conductivity coefficient. This expression was initially proposed by Canavan *et al.* [131] for predicting the performance of tungsten heat switches. Those authors arrived at the expression as the result of an argument based on adding resistances

and made no experimental verification. The aim of this chapter is to show that equation (4.9) is a reliable predictor of thermal conductivity over a range of magnetic fields. In the experiments described below, equation (4.9) is tested at constant temperature. For this case, all terms which are functions of T become constant and it may be simplified to:

$$\kappa = b_l + \frac{1}{\frac{1}{\kappa_0} + \frac{B^n}{a}}, \tag{4.10}$$

where κ_0 is the zero-field conductivity and both a and b_l are fitting parameters. This is the expression used to fit the data presented below.

4.2.1 Estimate of Mean Free Path

It is useful to estimate the mean free path in the samples studied. For this purpose, equation (3.63) can be re-written [160]:

$$\boldsymbol{j} = \frac{e^2\tau}{4\pi^3\hbar}\int \frac{\mathbf{v_k}\mathbf{v_k}dS_F}{\mathrm{v_k}} \cdot \boldsymbol{E}. \tag{4.11}$$

For a crystal with cubic symmetry such as tungsten the conductivity is a scalar in the absence of magnetic field. If $\boldsymbol{E}$ and $\boldsymbol{j}$ were in the x-direction, the denominator in the integrand would be $(\mathbf{v_k}\mathbf{v_k} \cdot \boldsymbol{E}) = \mathrm{v}_{\boldsymbol{x}}^{\boldsymbol{2}}E$. This will be 1/3 of the contribution from the square of the total velocity v^2E. Therefore,

$$\boldsymbol{j} = \frac{e^2\tau}{4\pi^3\hbar}\frac{1}{3}\int \mathrm{v}dS_F \cdot \boldsymbol{E} \tag{4.12}$$

and

$$\sigma = \frac{e^2\tau}{12\pi^3\hbar}\int \mathrm{v}dS_F. \tag{4.13}$$

If the velocity is then averaged over the whole Fermi surface – i.e.

$$\bar{\mathrm{v}} = \frac{1}{S}\int \mathrm{v} dS_F, \tag{4.14}$$

the conductivity (or resistivity) can be written in terms of the mean free path:

$$\sigma = \frac{1}{\rho} = \frac{e^2 \Lambda S_F}{12\pi^3 \hbar} \tag{4.15}$$

using $\Lambda = \bar{\mathrm{v}}\tau$, which will be an average value over the whole Fermi surface.

The mean free path in a sample can then be estimated from its RRR and the Fermi surface area of the material using the following expression [154,202]:

$$\Lambda = \frac{RRR}{\rho_{300K}} \frac{12\pi^3 \hbar}{e^2 S_F}, \tag{4.16}$$

where ρ_{300K} is the sample resistivity at 300 K and S_F is the Fermi surface area; this has been estimated for tungsten by Girvan *et al.* [190] from de Haas–van Alphen measurements and by Fawcett and Griffiths [203] from cyclotron resonance measurements. Girvan *et al*.'s value is over twice that found by Fawcett and Griffiths, which is significant even when account is taken of the 30% error that Fawcett and Griffiths estimate for their measurement. The technique used by these authors (the anomalous skin effect) required a correction to account for scattering and this correction was determined from a method of approximations. Girvan *et al.*'s value of 1.45×10^{21} m^{-2} is therefore used here. It can be seen from equation (4.16) that halving the Fermi surface area (as using Fawcett and Griffiths' value would do) will double the mean free path and this should be borne in mind when considering the values calculated below.

The room temperature resistivity of a similar tungsten sample[24] was found to be ~ 58×10^{-9} Ωm; using this, the mean free path (in mm) as a function of RRR will be given by

$$\Lambda \approx (1.82 \times 10^{-5})\mathrm{RRR}. \tag{4.17}$$

[24] MaTecK Sample 1 (see Chapter 5)

This expression is used below to compute the electron mean free paths in the two samples investigated.

4.3 Experimental Details

To test the validity of equation (4.10), thermal magnetoconductivity measurements were made on two very different single crystal tungsten samples. The samples had significantly different purities (see Table 4.1) and were chosen to demonstrate that equation (4.10) would apply for different levels of impurity scattering. The details of both samples are given below.

Sample	Supplier	Dimensions	RRR	Crystal orientation
C-3b	Metal Crystals and Oxides Ltd[a] (Cambridge, UK)	1.55 mm × 1.37 mm × 5.9 mm long	> 100 000	[100] direction along sample length ($\parallel \dot{Q}$) (see Figure 4.3)
M-2.2	MaTecK[b] (Juelich, Germany)	2.22 mm × 2.12 mm × 82 mm long	580	[111] $\perp$ to plane containing the sample length (see Figure 4.3)

[a]www.metal-crystals.com
[b]www.mateck.com

Table 4.1: Sample details.

The first sample (Figure 4.1) was cut from a zone-refined rod such that the length of interest for the measurements was in the [100] direction (see Figure 4.3). It is referred to hereafter as sample C-3b. The short length of the sample, combined with its high purity, meant that it was not possible to measure its electrical resistance at 4 K and therefore the Residual Resistance Ratio (RRR = resistance at 300 K/resistance at 4.2 K) could not be determined. However, other samples from the same supplier with similar thermal conductivities had RRR values of over 100 000. Using this value in equation (4.17) suggests $\Lambda \approx 1.82$ mm.

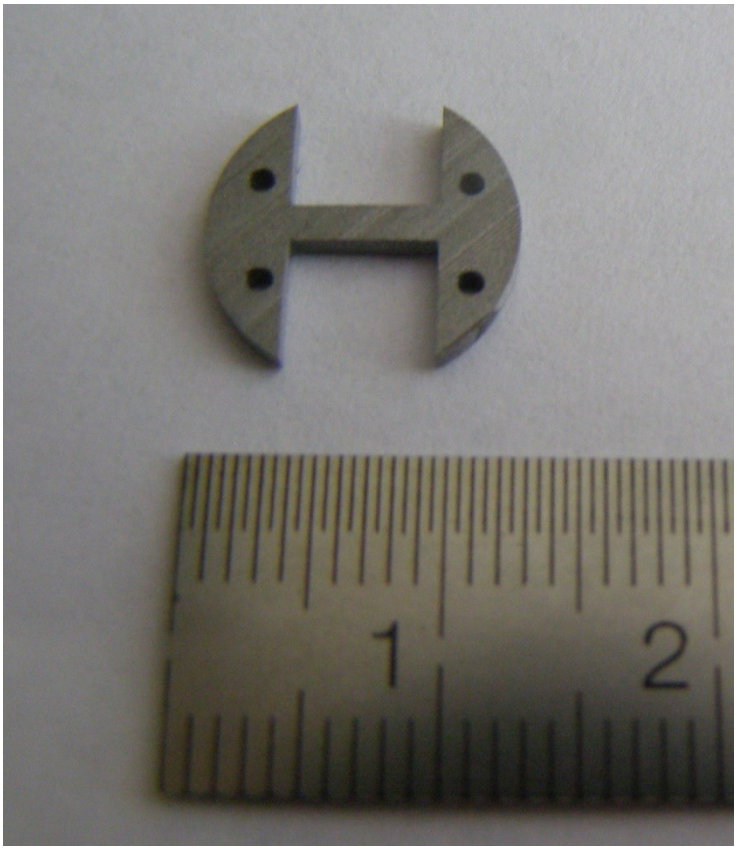

Figure 4.1: The high purity tungsten sample (C-3b).

The second sample was cut – from a less pure single crystal – into a more complex shape to maximise the free length for heat switch applications (see Figure 4.2). It is referred to as sample M-2.2. The crystal was grown in the [111] direction and then cut so that the free length was in the plane perpendicular to this direction (see Figure 4.3). The sample's RRR was measured as 580±65, suggesting $\Lambda \approx 0.01$ mm – significantly less than in sample C-3b. Thermometers were placed such that the temperature difference was measured over a length of 82 mm.

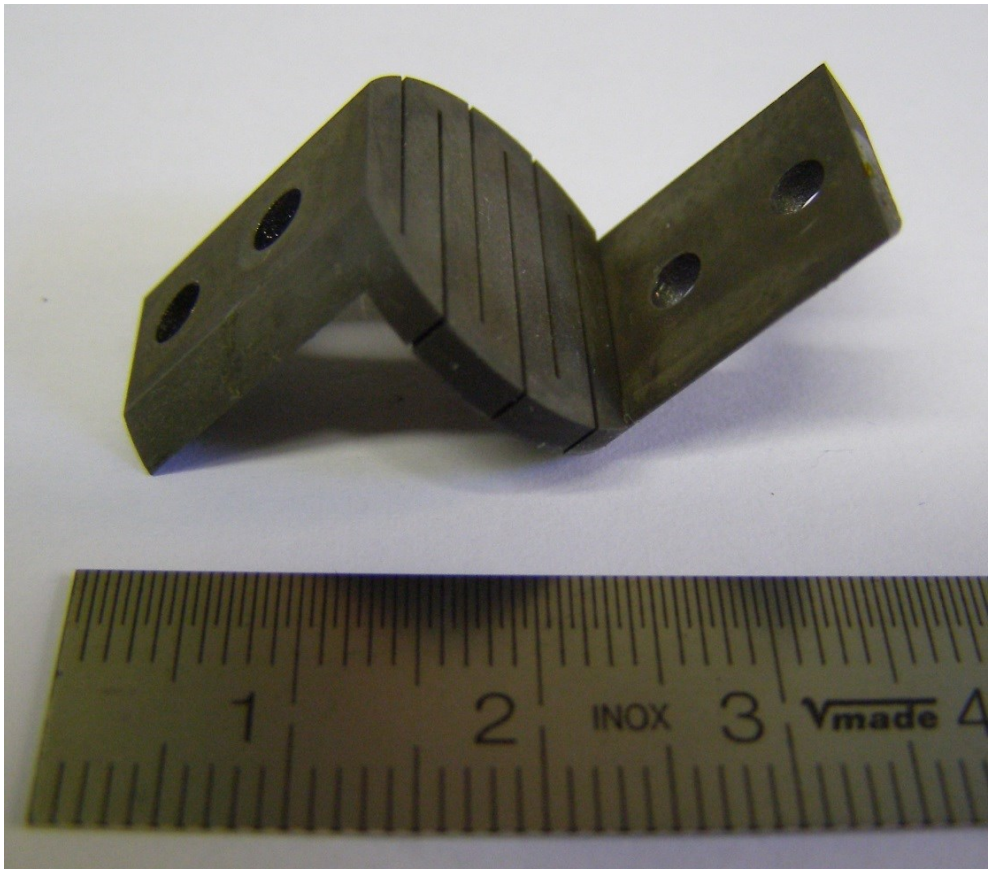

Figure 4.2: The lower purity tungsten sample (M-2.2).

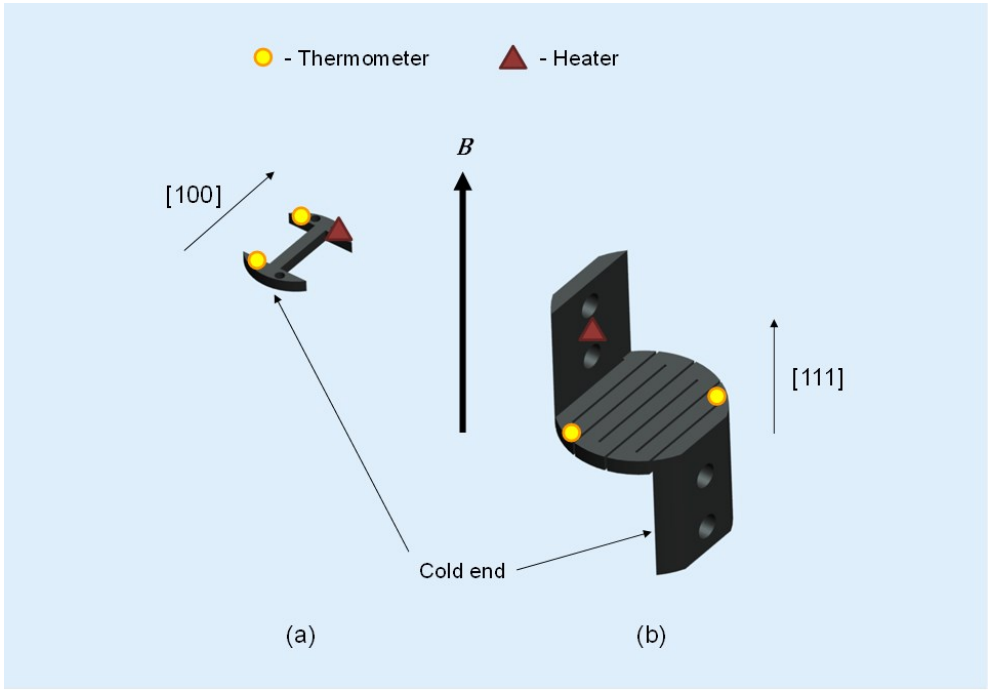

Figure 4.3: Measurement set-up showing relative orientations of the sample, the applied magnetic field and known crystal axes (a) sample C-3b (b) sample M-2.2.

The samples were mounted in a cryogen-free cryostat, cooled by a Cryomech Pulse Tube Refrigerator (PTR), and oriented such that the direction of heat flow between the thermometers would be perpendicular to the magnetic field, which was provided by a 2 T, 2 A superconducting magnet (see Figure 4.4). For the low-field measurements, this was powered from a Cryogenic power supply that permitted current control to ±1 mA, whereas for fields of > 0.1 T current was provided by a Thurlby Thandar power supply with a precision of ±10 mA. The true current flowing in the magnet was measured separately on a Fluke ammeter.

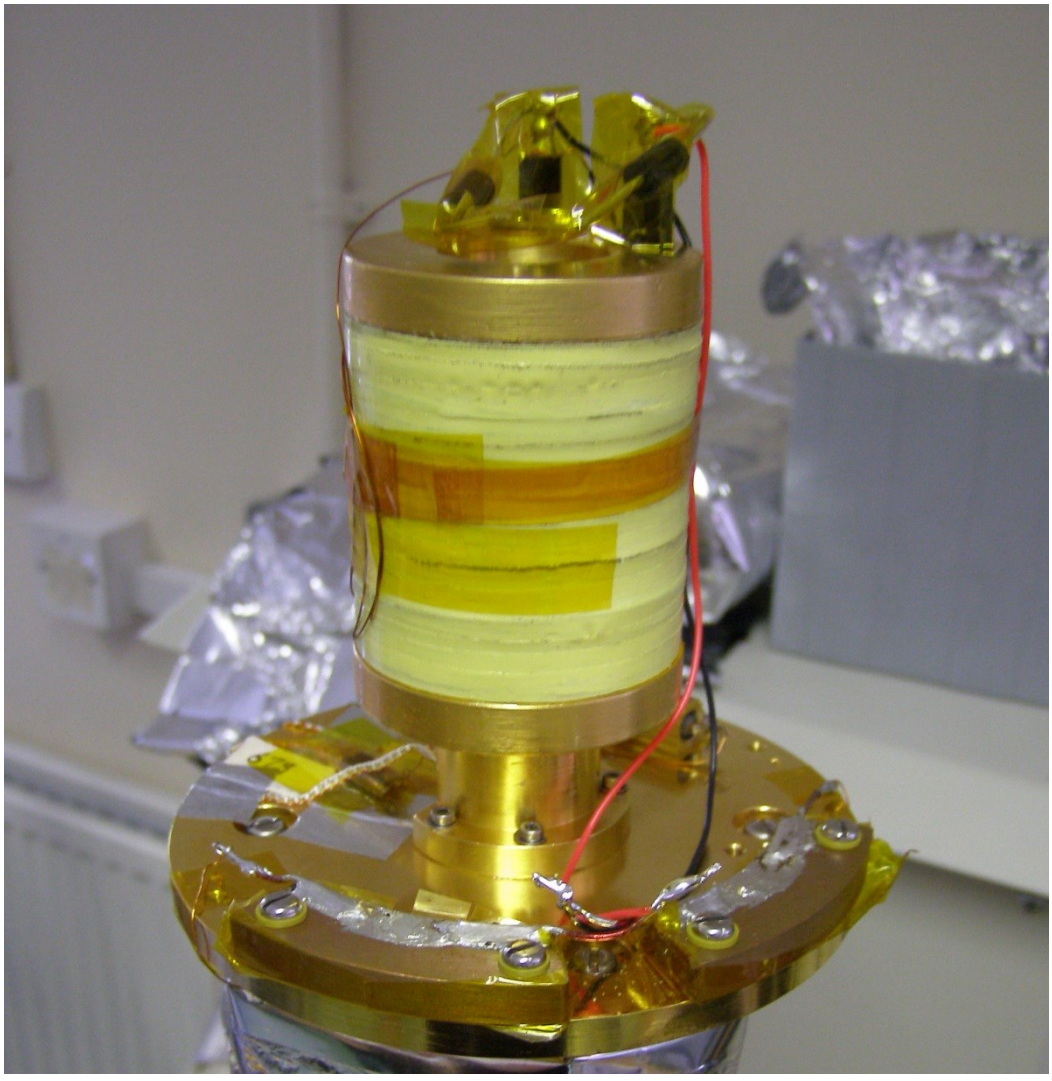

Figure 4.4: The 2 T, 2 A superconducting magnet mounted to the second stage of the PTR.

In order to measure the thermal conductivity one end of the sample was fixed to the cold stage of the PTR (see Figure 4.5 and Figure 4.6). Cernox thermometers were mounted at each end of the length of interest of the sample, as shown in Figure 4.3, and these were used to measure the temperature difference (ΔT) created by passing current through a heater (10 kΩ resistor) mounted to the free end. The thermal conductivity was measured by recording the steady-state temperature difference between the thermometers for a given heater power. To improve measurement statistics, the thermometers were read by taking the output from an AVS- 47 resistance bridge into an Agilent nano-voltmeter and using this to average a 30 second sample (with readings taken at approximately 2.5 Hz ≈ 75 readings). Two separate measurements were made for each heater power and magnetic field combination, and the temperature differences averaged. The thermal conductivity was then calculated according to:

$$\kappa = \frac{\dot{Q}}{\Delta T}\frac{L}{A}, \tag{4.18}$$

with $\dot{Q}$ being the supplied power, L the sample length and A the area.

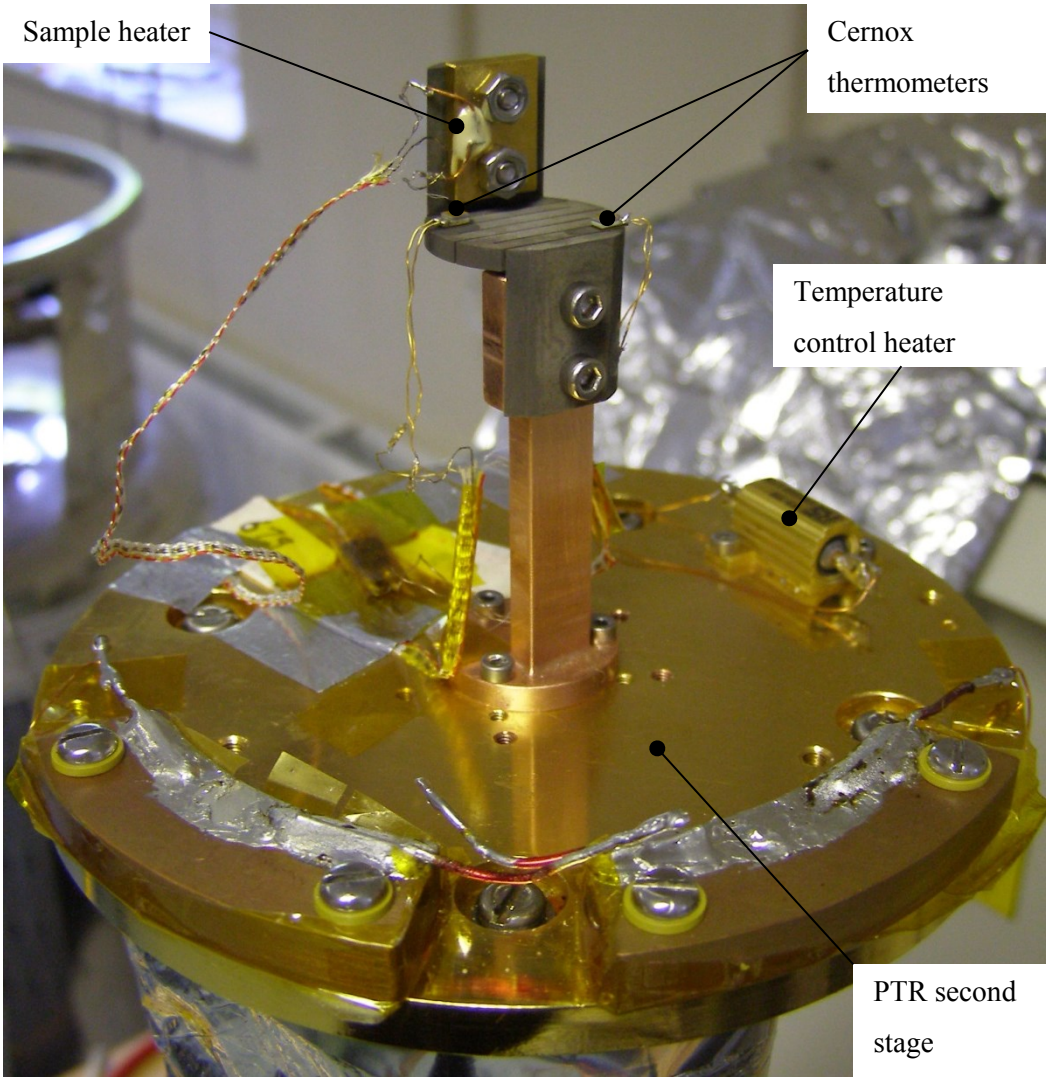

Figure 4.5: Measurement set-up for sample M-2.2.

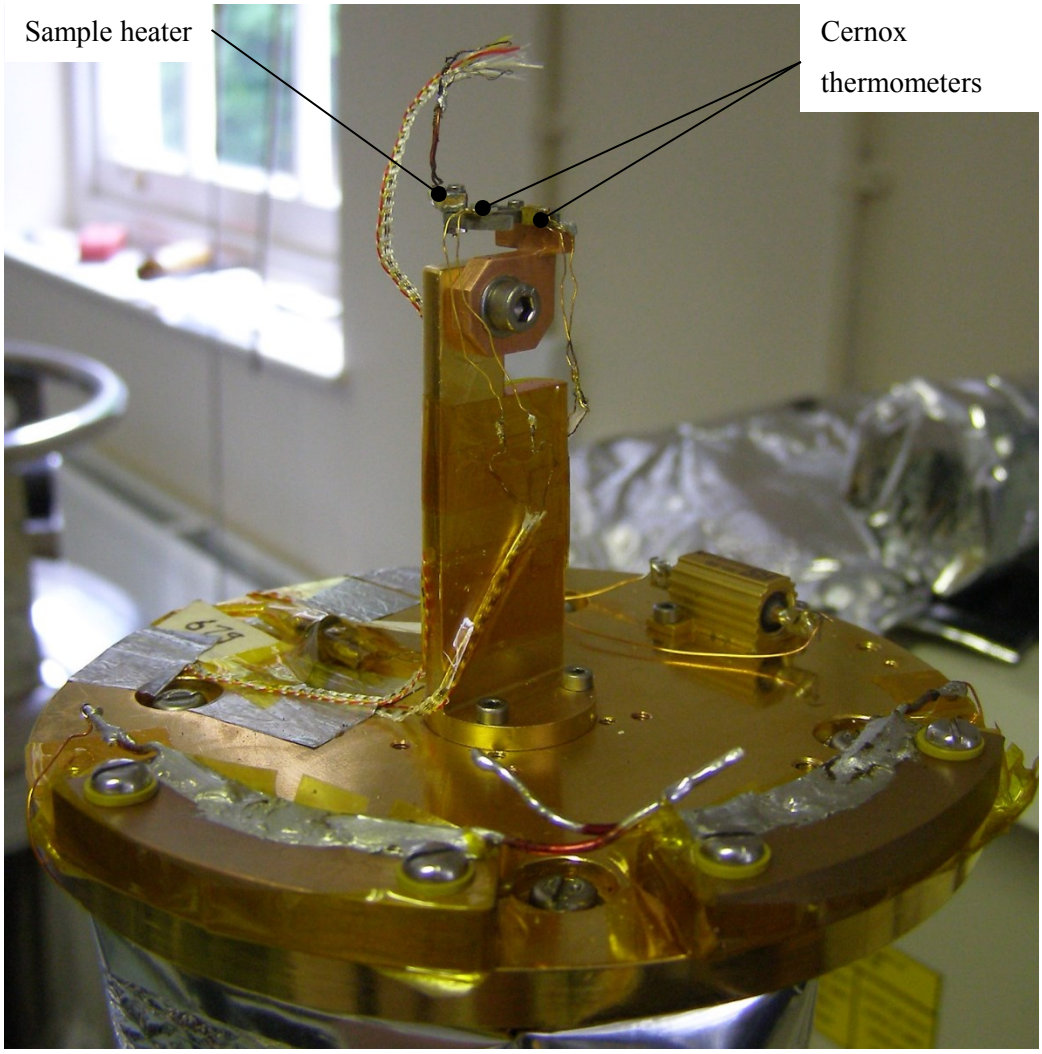

Figure 4.6: Measurement set-up for sample C-3b.

Temperature stability of the sample mount was achieved through a 100 Ω resistor fixed to the PTR second stage (see Figure 4.5) and a Cernox thermometer on the sample mount. These were connected to a Picowatt PID (Proportional Integral Derivative) controller, which was used to regulate the power to the 100 Ω resistor such that the average temperature of the sample was constant. This was necessary because of the wide range of heater powers required to achieve a measureable ΔT depending on the applied magnetic field. All measurements were performed at 5.5 K. At this temperature the PTR had sufficient cooling power to absorb the heat input required to achieve a measureable ΔT of ~250 mK. As the field was increased – and hence the sample conductivity reduced – the temperature control heater was used to provide additional heat input to the stage and maintain the sample at

5.5 K. The PID controller was fine-tuned such that the average temperature between the two ends of the sample was always 5.5±0.05 K.

4.3.1 Errors

The following sources of error were considered when calculating the vertical error bars in the figures: errors in the thermometer readings, errors in the measured voltage and current in the heater, and errors in the measured sample dimensions. Errors in the temperature readings were the averaged standard deviations of the 30 second samples read out by the nano-voltmeter. Each temperature measurement has a standard deviation (s) calculated by the nanovoltmeter from the statistics collected in the ~ 30 second sampling time. Since the temperature difference (ΔT) is found from two temperature measurements, the variances (s^2) must be added. The standard deviation of ΔT was then calculated as the square root of the sum of the two variances. The resulting standard deviations were of the order of 5–10 mK and these were much larger than errors due to the thermometer calibration fits (1–2 mK) and self-heating effects (~ 20 pW), which were consequently both neglected. No account was made for magnetoresistive effects in the thermometers, although previous research suggests this will be less than 1% for the temperatures and fields in this study [204,205]. Current and voltage errors were assumed to be of the same order as the resolutions of the respective meters. The sample dimensions were measured at room temperature, but any change in size due to thermal contraction would only be a small fraction of ±20 micron errors assumed for the cross section dimensions and the ±50 micron error assumed for the sample lengths.

Of the sources of error mentioned above, by far the most dominant were errors in the measured ΔT – these ranging from approximately 5% to more than 25% for the lowest field measurements on sample C-3b. The same errors in sample M-2.2 were always below 5% because the longer sample length enabled larger ΔTs and proportionally smaller errors. Errors in measured heater power ranged from less than 0.5% to around 5%; however, the largest errors were at the highest fields (when the smallest powers were used), so that there

was no coincidence of large power errors and large ΔT errors. By comparison, the errors in the measured samples dimensions were small, being less than 1% in length and less than 3% in area. The percentage errors from all sources have been combined to give the maximum possible percentage error in the conductivity. This is likely to be a conservative estimate of the true error, but is considered appropriate given that, aside from the temperature, the error values were based on fairly arbitrary estimates.

As is evident from the figures, total errors are larger in the lower field measurements, where the temperature differences are smaller. All errors are reduced by averaging more than one measurement. According to the rules for error propagation [206] the fractional errors are added in quadrature. By taking advantage of averaging at least two readings for each data point, errors are reduced to less than 15% in all but the lowest fields.

Horizontal error bars in the figures indicate the error in the measured field, taken to be either 0.001 T or 0.01 T depending on the power supply being used.

4.4 Results and Discussion

The results for sample C-3b are shown in Figure 4.7 and Figure 4.8; those for sample M-2.2 are shown in Figure 4.9 and Figure 4.10. The fits were made using chi-square minimisation[25] to equation (4.10).

[25] The graphing software used (OriginPro 9.0) employs a Levenberg-Marquardt (L-M) algorithm [207] for this procedure.

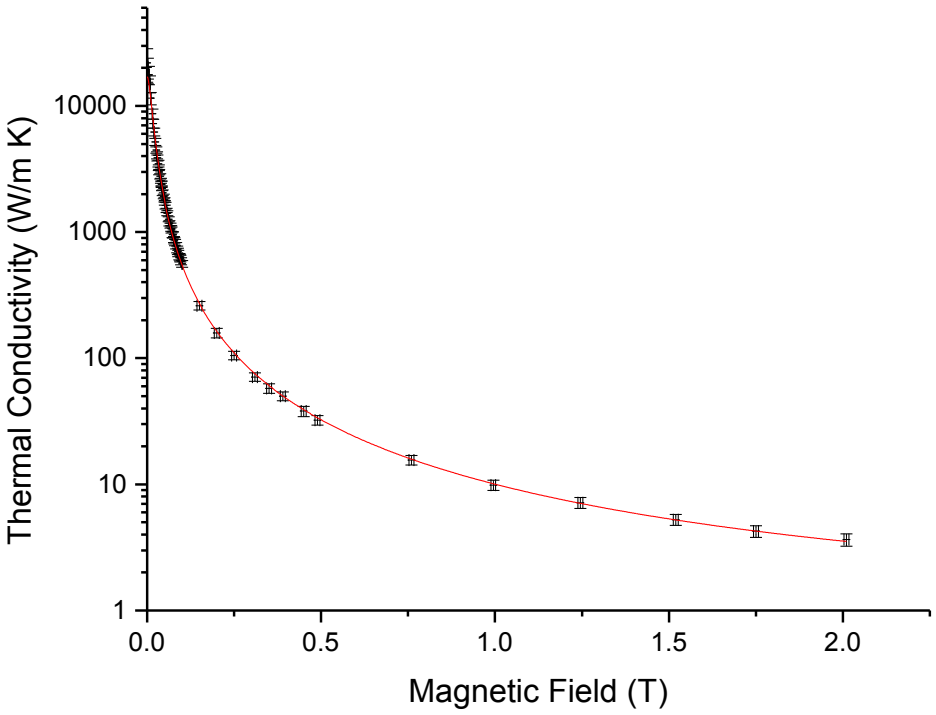

Figure 4.7: Magnetoconductivity of sample C-3b from 0 to 2 Tesla.
The fitted curve is to equation (4.10).

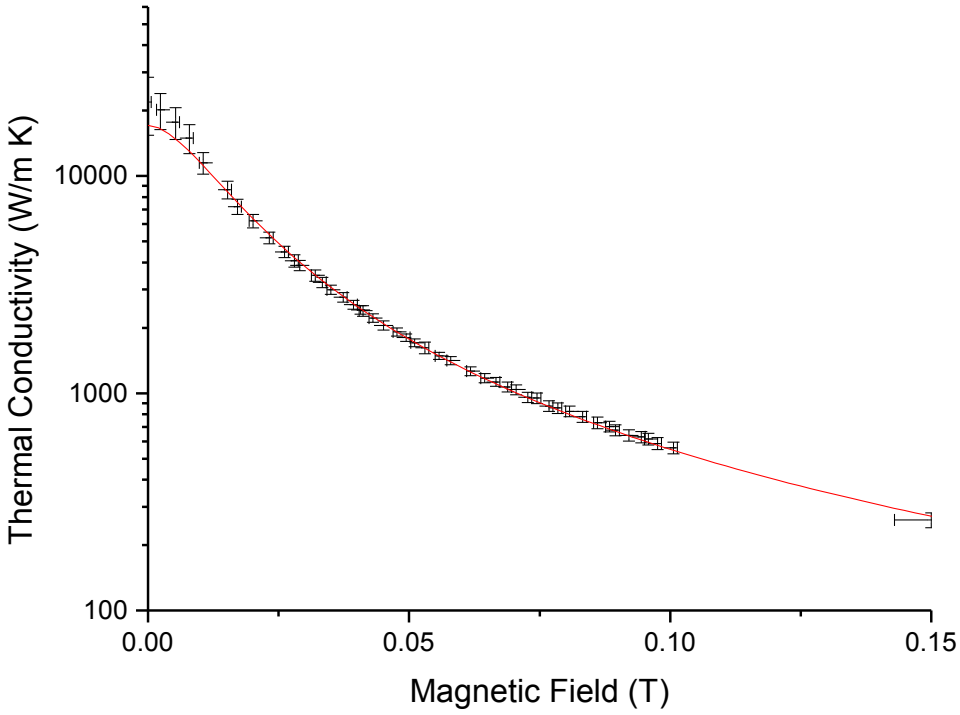

Figure 4.8: Low-field (0–0.15 Tesla) magnetoconductivity of sample C-3b.
The fitted curve is to equation (4.10).

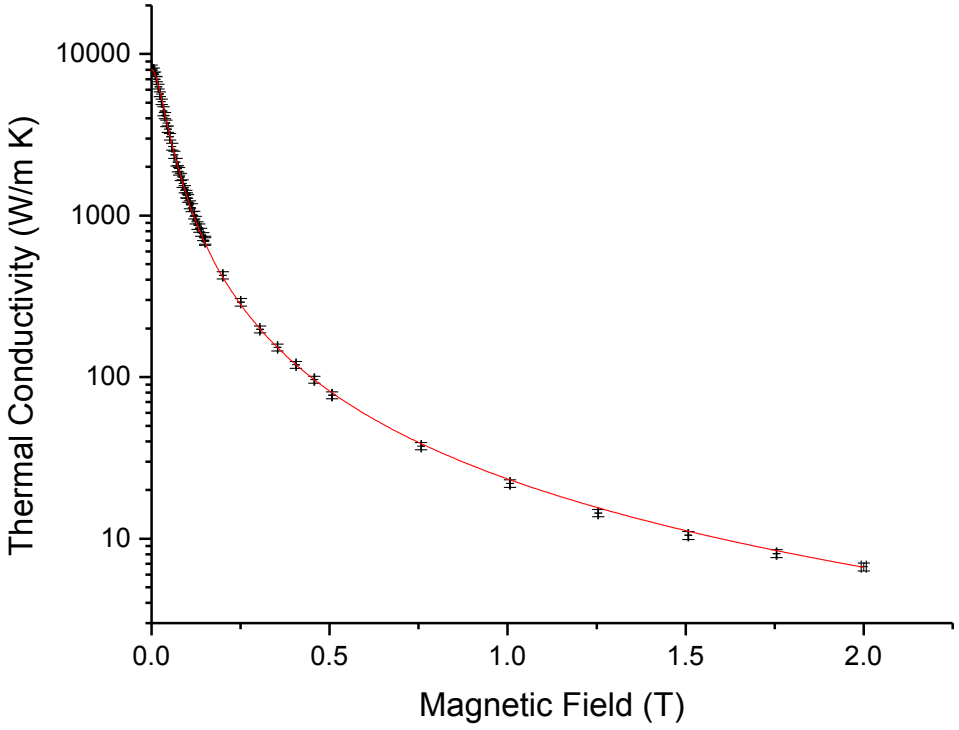

Figure 4.9: Magnetoconductivity of sample M-2.2 from 0 to 2 Tesla.
The fitted curve is to equation (4.10).

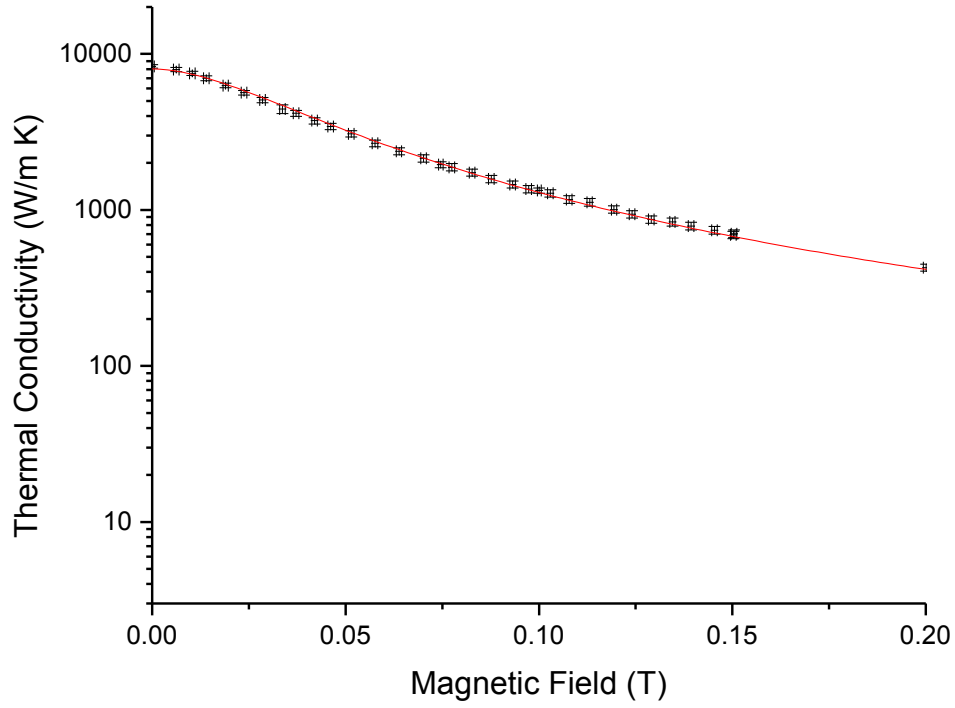

Figure 4.10: Low-field (0–0.2 Tesla) magnetoconductivity of sample M-2.2.
The fitted curve is to equation (4.10).

The parameter values for the fits are summarised in Table 4.2.

Sample	b_l	κ_0 (measured)	κ_0 (fitted)	n	a	Adjusted R-Square[a]
C-3b	0.93±0.16	21920±6530	17085±642	1.80±0.01	9.11±0.19	0.99923
M-2.2	0±0.30	8333±223	8032±84	1.82±0.01	23.48±0.48	0.99895

[a]Used as a measure of the goodness of fit; the closer this value to 1, the better the fit. It is calculated as $\bar{R}^2 = 1 - \frac{RSS/df_{Error}}{TSS/df_{Total}}$ where RSS is the residual sum of squares, TSS is the total sum of squares about the mean, df_{Total} is the total number of degrees of freedom ($= (n-1)$ where n is the sample size) and $df_{Error} = (n-p-1)$ where p is the number of parameters in the fitting expression.

Table 4.2: Comparison of fitting parameters for the two samples.

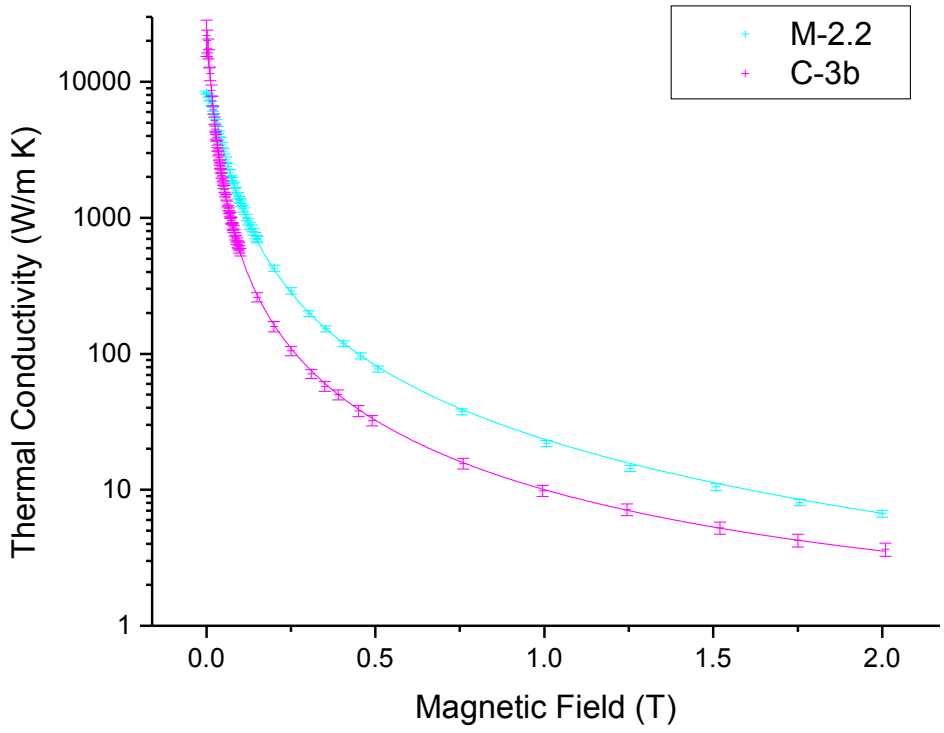

Figure 4.11: Comparison of the thermal conductivity fits for the samples M-2.2 and C-3b.

The figures illustrate that equation (4.10) is an excellent fit to the thermal magnetoconductivity of both samples. Figure 4.11 provides a comparison between the behaviour of the two and illustrates the two main differences: (i) sample M-2.2 displays a

smaller change in thermal conductivity than C-3b over same range of magnetic fields; (ii) the curve for C-3b is much steeper at lower fields indicating a greater rate of change of conductivity in this region. Both of these features are believed to be reflections of sample C-3b's higher purity and are explored in more detail below. Of course it is clear from Table 4.1, along with Figure 4.1 and Figure 4.2, that purity is not the only difference between these samples: they have different sizes, shapes, crystal orientations and possibly surface finishes (although this was not measured). How these differences may have contributed to the different fitting parameter values for the two samples is discussed in the following paragraphs. It would be extremely worthwhile to confirm the conclusions presented below by performing measurements on samples which differ in only one of the variables mentioned above. Unfortunately, such crystals were not available for this study.

As described in 4.2, equation (4.10) combines both a zero-field and a high-field thermal conductivity. The relative contributions of these elements of the fit are plotted in Figure 4.12 and Figure 4.14, which illustrate how they vary with magnetic field. The relative percentage contributions to the electronic thermal resistivity (the second term in equation (4.10)) are shown in Figure 4.13 and Figure 4.15. For sample C-3b, the high field term is already dominating at 0.005 T, whilst in sample M-2.2 the high field term does not become dominant until 0.05 T. This can be interpreted as a consequence of the differing purities of the samples: the higher purity sample (C-3b) has a much lower zero-field resistivity which means its contribution to the fit is overtaken much more quickly by the high-field term. There is also a more rapid rise in the high-field contribution for sample C-3b because of the smaller a term; this is discussed in more detail below.

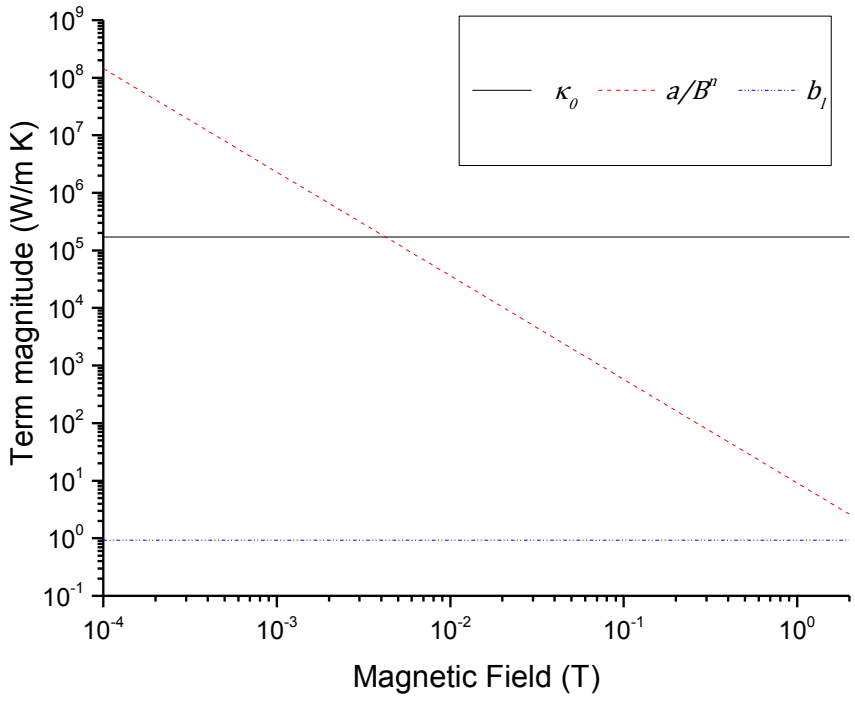

Figure 4.12: Relative contributions of the lattice, zero-field electrical and field dependent parts of equation (4.10) for sample C-3b plotted as absolute magnitudes.

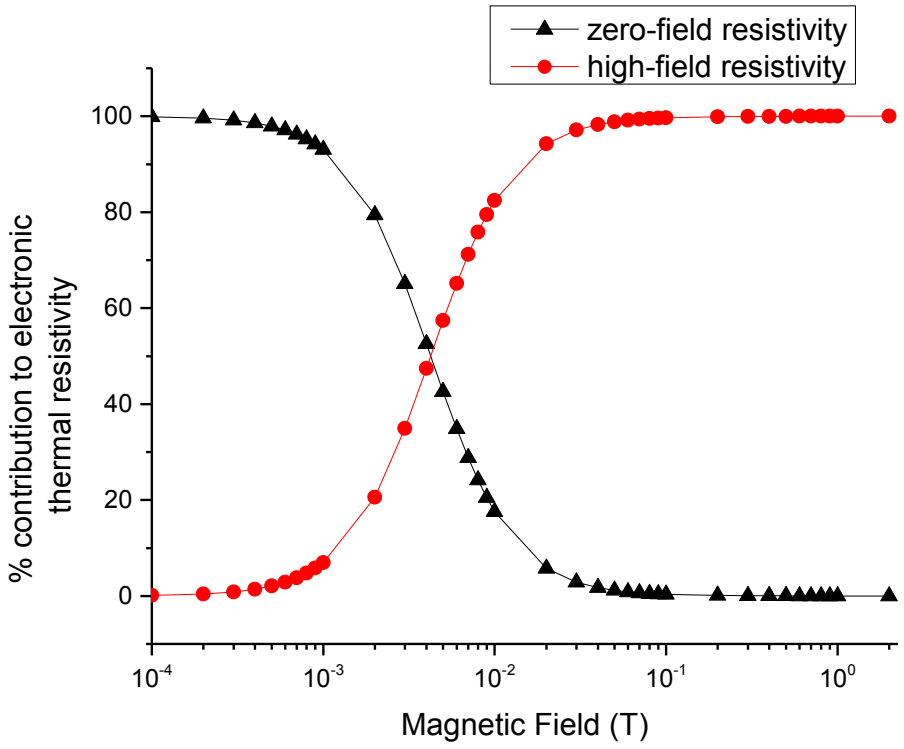

Figure 4.13: Relative percentage contributions of the zero-field electrical and field dependent resistivities for sample C-3b.

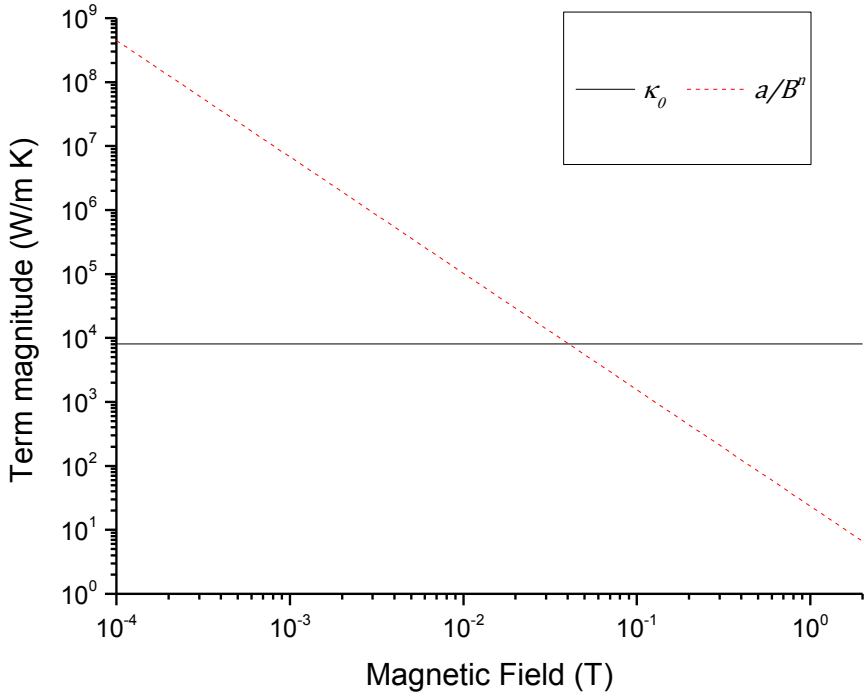

Figure 4.14: Relative contributions of the zero-field electrical and field dependent parts of equation (4.10) for sample M-2.2 plotted as absolute magnitudes.
No lattice term is plotted since $b_l = 0$ for this sample.

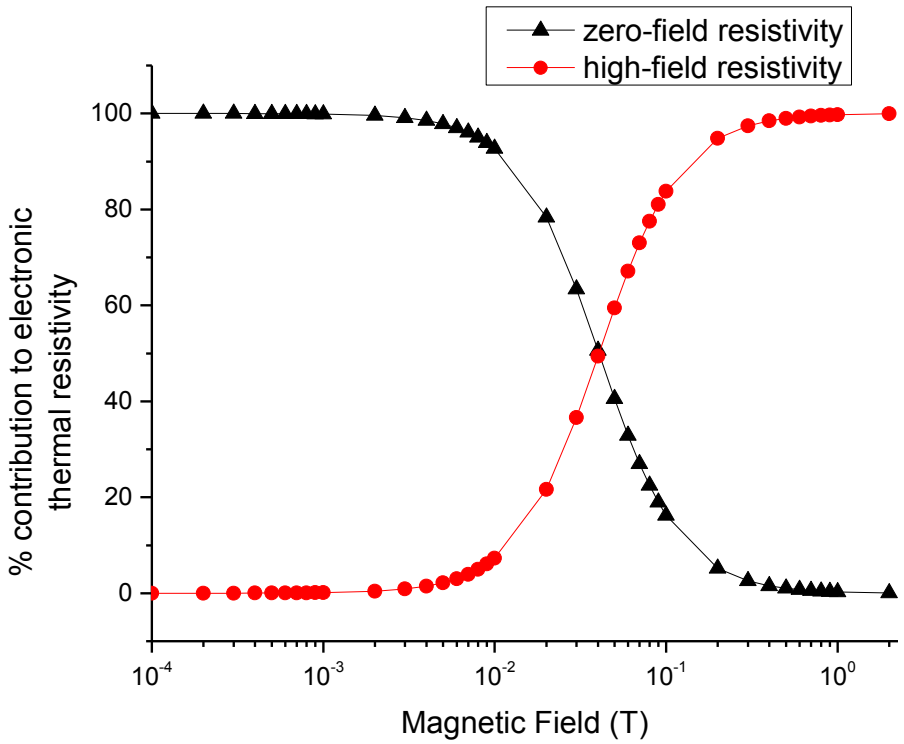

Figure 4.15: Relative percentage contributions of the zero-field electrical and field dependent resistivities for sample M-2.2.

The chi-square minimisation produces different fitting parameters for each sample and these will be discussed in turn.

4.4.1 Lattice Conductivity

The lattice conductivity in sample M-2.2 is found to be zero with the fitting error of ±0.30, compared to 0.93±0.16 for sample C-3b. The results of others [195,199] suggest that b_l can be approximated by $0.05T^2$ W/m K. Using this with $T = 5.5$ K yields a value of 1.51, which is greater than the b_l value in both of the fits above. It is unlikely that there is no phonon contribution at all. However, it may be that the phonon current is restricted by the geometry of the samples. Scattering from the sample surface could act to destroy the phonon current, particularly in the case of sample M-2.2 because the convoluted geometry forces a phonon that travels the whole sample length to interact with the surface. As described in Chapter 3, scattering will be diffuse when the phonon wavelength is significantly smaller than the typical asperity height on the surfaces. It can be shown that this is likely to be the case in the samples studied here by calculating the wavelength corresponding to the peak in the phonon energy spectrum. Assuming a Debye distribution, the frequency at which the peak occurs is given by equation (3.72):

$$\omega_{max} \approx \frac{2.82 k_B T}{h}, \tag{4.19}$$

where k_B is the Boltzmann constant and h is Planck's constant. Calculating this for $T = 5.5$ K, yields $\omega_{max} = 3.23\times10^{11}$ s^{-1}, which can then be converted to a wavelength using the speed of sound in tungsten, v_W:

$$\lambda_{\omega_{max}} = \frac{2\pi v_W}{\omega_{max}}. \tag{4.20}$$

If the speed of sound in tungsten is taken – from high frequency mechanical resonance measurements [208] – as approximately 2900 m/s, one finds $\lambda_{\omega_{max}} \cong 0.06$ μm. Surface asperities this small would be difficult to achieve in a carefully polished sample and these

crystals were not subject to such preparation. On this basis, it is entirely possible that surface scattering plays an important role in limiting the phonon current and may explain why it is smaller in the case of M-2.2.

A second way to assess the importance of surface scattering of phonons is to estimate the mean free path and confirm that it is of the same order as the sample dimensions. This can be done using the kinetic formula for thermal conductivity (equation (3.9)) rewritten as follows:

$$\kappa_l = \frac{1}{3}\frac{C_{mol}}{V_{mol}}\bar{v}\Lambda, \tag{4.21}$$

where C_{mol} is the molar specific heat capacity and V_{mol} is the molar volume. The specific heat of tungsten at 5.5 K is 0.0114 J/mol K [209]; combining this with a molar volume of 9.5×10^{-6} m^3/mol [210] and using the lattice conductivity and speed of sound quoted above, gives a mean free path of ≈1.3 μm. At first sight, this might seem inconsistent with the conclusion that surface scattering plays a role in phonon conduction, given a sample size that is of the order of millimetres. However, even if the phonon mean free path is much smaller than the sample dimensions, where the geometry of the sample forces the phonon current to change direction (as in M-2.2), phonons must interact with the surfaces. This is illustrated in Figure 4.16 below.

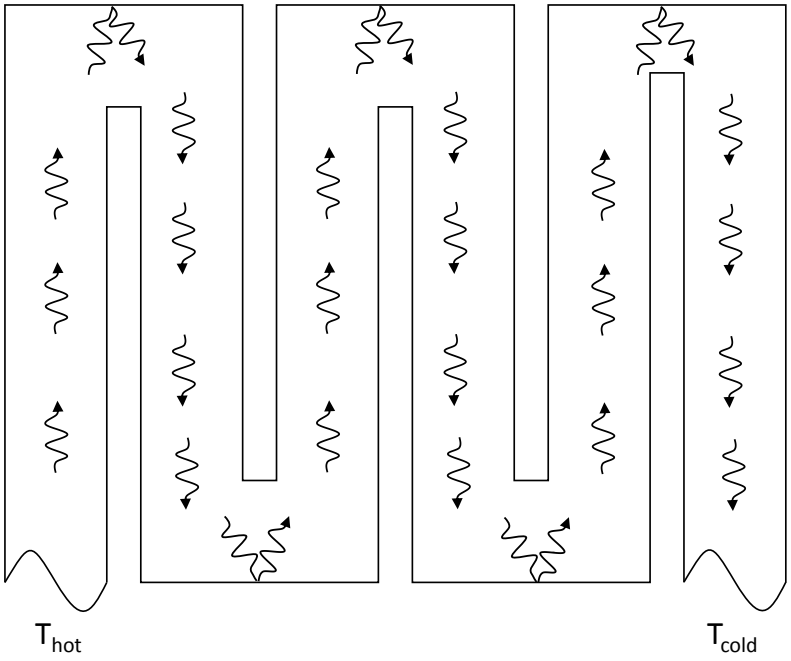

Figure 4.16: Illustration of phonons with short mean free paths interacting with sample surfaces in the case of a "meander" sample geometry.

Since C-3b does not force the phonon current to change direction, it might be expected that any effects from surface scattering do not show up as clearly in this sample.

4.4.2 Electronic Conductivity

The difference in the zero-field conductivities (κ_0) is as might be expected for two samples of such differing purities. The values from both fits agree with the measured zero-field conductivities of the samples within the measurement errors: 21920±6530 W/m K for sample C-3b and 8333±223 W/m K for sample M-2.2. The larger error on the measured zero-field conductivity of sample C-3b is the result of only being able to generate a small ΔT without raising the base temperature of the apparatus (a consequence of the sample's short length and high conductivity).

The different values of a can be interpreted as a reflection of the different levels of impurity scattering in the two samples. Wagner [199] shows that an expression for a, derived according to semi-classical high-field transport theory, is of the same form as the theoretical

expression for the zero-field thermal resistivity found by solving the Boltzmann equation using the variational method [211]. The zero-field resistivity so derived depends on choosing a particularly simple trial function for the variational solution. Nevertheless, Wagner suggests that because of the similarity of the expressions, it may be reasonable to expect them to have similar temperature dependences. As illustrated by equation (4.6), the zero-field resistivity is expected – and has been confirmed experimentally [195] – to contain a $1/T$ term, which can be associated with the impurity scattering. One would expect this term to increase with greater impurity scattering (i.e. lower sample purity and RRR) and the a value in our fits seems to follow this general trend, being significantly larger for the lower purity sample M-2.2.

There is good agreement between fits for the magnetic field exponent (n). As detailed in Chapter 3, semi-classical magnetoresistance theory leads one to expect a value of 2. However, deviations from this that are of the same order as found in these fits have been seen by Long [200], Canavan *et al.* [131], Marchenkov *et al*. [189] and Cherepanov *et al.* [212]. Long attributes his value to an appreciable (field independent) lattice conductivity, but this would be at odds with the minimal lattice contribution found here. It also seems inconsistent with tungsten's relatively high Debye temperature (400K [14]). Canavan *et al.* merely note that the deviation from $n = 2$ is surprising without offering further explanation. Marchenkov *et al.* [189], on the other hand, present a physical mechanism related to the difference they observe in the exponent when the current is directed along different crystal axes. They suggest that at certain temperatures, there will be phonons of an appropriate wavevector to scatter electrons from one Fermi surface sheet to a nearby point on an adjacent one. The sizes of the gaps between sheets in k-space depend on the plane in which the electrons are moving (see Figure 4.17). For certain crystal orientations, this intersheet scattering then permits some electron orbits to become open, or extended, even though the energy surfaces themselves are closed. As described in Chapter 3, the presence of some open orbits changes the predictions of semi-classical magnetoconductivity theory: for

orientations in which these orbits play a role in conduction, the electrical part of the thermal conductivity is expected to saturate at a constant value as B approaches infinity [183]. In other words, the conductivity becomes independent of B at high fields and n tends towards zero.

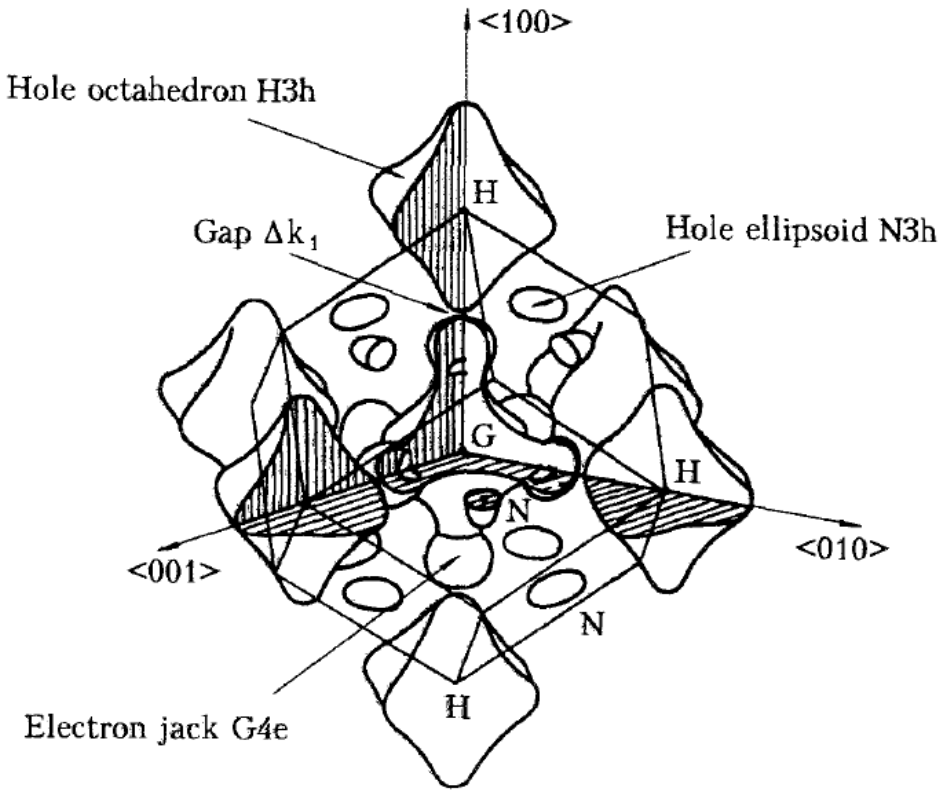

(a)

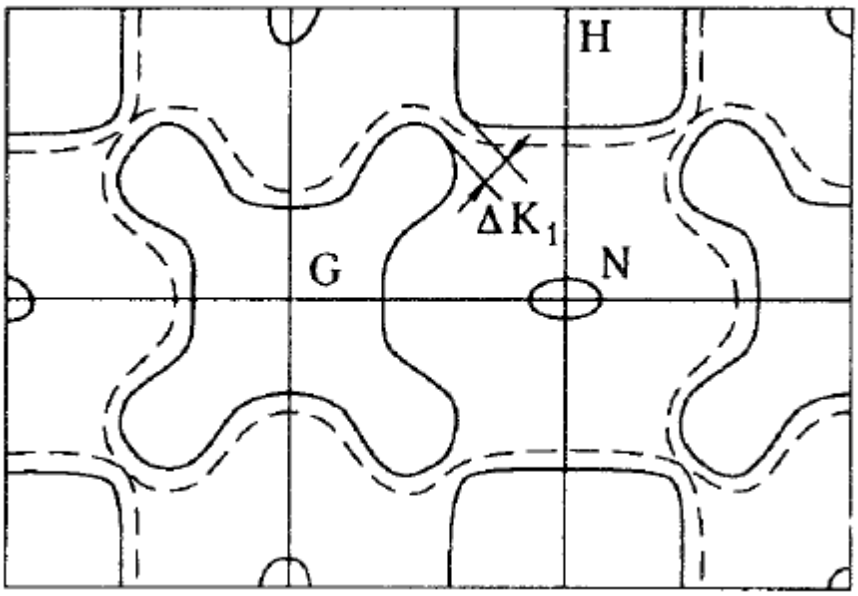

(b)

Figure 4.17: (a) Fermi surface of tungsten with shading showing slices though the (100), (010) and (001) planes. (b) Section through the (100) plane illustrating how closed orbits may become quasi-open when intersheet scattering occurs. [189]

Figure 4.17(b) illustrates intersheet scattering for the (100) plane, which, due to the cubic symmetry of tungsten, will be the plane of the electron orbits in sample C-3b. At their closest, the electron jack surface and the hole octahedron surface are separated by a distance Δk_1 in this plane. Marchenkov *et al.* quote the size of this gap, as measured by the radio-frequency size effect, to be 1.5±0.2 nm^{-1}. In order for intersheet scattering to take place across this gap, there must be phonons of this wavevector present. Using the result from Chapter 3 (equation (3.72)) that typical phonon energy will be of the order of $k_B T$ and that this is $h\omega_q = \hbar v \mathbf{q}$ where v is the speed of sound and $\mathbf{q}$ is the phonon wavevector, it is possible to calculate the temperature at which phonons of wavevector $q = \Delta k_1$ will be the dominant presence the spectrum. Thus, using $T \approx \hbar v \Delta k_1 / k_B$ and the speed of sound quoted above for tungsten, the appropriate temperature is found to be ~ 30 K. Other intersheet scattering process may also be possible in our samples (and these may differ between samples due to the different crystal orientations). However, the nature of tungsten's Fermi surface dictates that these would involve larger jumps in k-space and therefore larger wavevector phonons (i.e. higher temperatures). It is consequently assumed that 30 K is representative of the lowest typical temperature at which such effects might occur. In their experiments, Marchenkov *et al*. only see evidence for the effect at temperatures above 30 K [189]. Nevertheless, given a Debye phonon distribution, there is no reason why phonons of the appropriate wavevector should not also be present (albeit not in the same quantity) at lower temperatures. It may therefore be possible that this process occurs to some small degree in the measurements described here.

Quasi-open orbits may arise from another source: namely the Static Skin Effect [193]. This effect was described in Chapter 3 and it was shown that when the Larmor radius (r_B) of electrons (i.e. the radius of the electron orbits) is significantly smaller than the sample dimension perpendicular to the magnetic field, the majority of the electron transport takes place in a layer of approximately the same thickness as the Larmor radius next to the surface. This is because electrons interacting with the surface (either specularly or diffusely)

are much more likely to progress along the sample than those in the bulk, which make multiple orbits before scattering and are hence constrained to travel no further than the Larmor radius. Cherepanov *et al.* found that this effect was so pronounced in electrical measurements of their high purity samples that removing the central portion of a bar sample actually increased the conductivity since it created more surface area over which the Static Skin Effect could take place [213].

The Larmor radius can be calculated using the following equation (see 3.10.5).

$$r_B = \frac{m_c^* \mathrm{v}}{eB}. \qquad (4.22)$$

Here m_c^*, e and v are the electron's cyclotron mass, charge and velocity respectively; B is the magnetic field. Using standard values for the mass and charge of a free electron, and a typical value for the Fermi velocity of an electron in tungsten (~ 5×10^5 ms^{-1} [214])[26], r_B in our samples is found to vary between approximately 6×10^{-2} mm at B = 0.05 T and 1.4×10^{-3} mm at B = 2 T – i.e. several orders of magnitude smaller than the sample dimensions. This, taken together with the fact the electron mean free paths for our samples in the absence of magnetic field are likely to be much greater than these values, satisfies the conditions for the Static Skin Effect [215]. It should be noted that although the electron's cyclotron mass will differ from the free electron value, Girvan *et al*. have found cyclotron masses of between $0.25m_e$ and $0.93m_e$ from their de Haas-van Alphen measurements on tungsten [190]. Differences of this order would not affect the conclusion that the Larmor radius will be orders of magnitude smaller than our sample dimensions.

When incident and reflected electrons at a surface are correlated, with just the component of momentum perpendicular to the sample surface being reversed, they can be said to be specularly reflected. Electrons interacting in this way are able to move to a different Fermi surface sheet, creating an open trajectory. These open orbits may then contribute to a

[26] As described in [214], the Fermi velocity in tungsten is highly anisotropic and depends on the electron's location on the Fermi surface. However, for an order of magnitude calculation like that performed above the quoted value is adequate.

change in *n* on the same basis as described above for intersheet scattering. On as-cut tungsten crystals, the surface imperfections are presumably mush greater is size than the electron wavelength. One would therefore not expect as significant amount of specular reflection of electrons. However, electron focussing experiments [176,216] have demonstrated that specular reflection does indeed occur. Although in one case the crystal was carefully prepared by grinding and electro-polishing in sodium hydroxide solution [176], in the other measurements [216] a measureable degree of electron reflection was still apparent even after the surface had been etched. This indicates that electron reflection cannot be ruled out, even in tungsten crystals whose surfaces have not been polished.

Some initial results from a study by Volkenshtein *et al*. [217] suggested that when sample faces specularly reflect a high proportion of electrons (approximately 60%) the magnetoresistance contains an additional linear component. However, in a fuller report on their findings [215], they conclude that a magnetic field exponent of 1.96±0.05 fits their data for samples with both specularly and diffusely reflecting surfaces.

A separate, but connected, surface effect that may also be present in the samples measured here is the influence of lattice defects just below the surface [212]. The crystals were spark-eroded to their final geometry and were not subject to any polishing or other surface treatment. As a result, some level of damage to the crystal structure in the vicinity of the sample surface might well be expected. Lattice defects arising in this way can penetrate hundreds of microns into the sample [212] and thus encompass the region of the sample where most of the electron current is present under the Static Skin Effect. Cherepanov *et al*. [212] studied the impact of this on the magnetoresistance through high-field measurements on spark-eroded crystals which satisfied the conditions for the Static Skin Effect: they measured the transverse magnetoresistance for samples after spark eroding and again after they had been electro-polished to remove the defect layer. Polishing caused the magnetic field exponent to increase from 1.34 to 1.98, indicating that sub-surface defects were responsible for a reduction in the magnetic field exponent. It is considered that this is the

most likely cause of the fact that a magnetic field exponent of < 2 occurs in the fits above. The mechanism for the change is discussed in more detail by Kolesnichenko [218]; it is related to the fact that the increased scattering in the defect layer causes the magnetoresistance to depend not just on the applied field, but on the electron mean free path in the layer and the layer's thickness. Kolesnichenko derives an expression for the change in transverse conductivity on the basis of introducing an additional relaxation time for electrons that are scattered in the defect layer and adding it to the bulk relaxation time using Mathiessen's rule. The resulting expression for the conductivity then contains two terms: the first includes the Larmor radius squared (and is hence proportional to $1/B^2$, by equation (4.19)), while the second is a function of the product of the thickness of the defect layer and the mean free path of the electrons in this layer [218]. The implication is that the change in conductivity can no longer be expected to be a simple function of $1/B^2$.

4.5 Conclusions

This chapter has developed an equation to describe the thermal magnetoconductivity of tungsten from zero to high-field conditions drawing on the principles of semi-classical transport theory. The equation has been tested against results from two very different single crystals of tungsten and has been shown to be an extremely good fit to the data in both cases. The measurements cover a range of fields, which is sufficient to include regions where the high-field conductivity contribution dominates and ones where the low-field contribution dominates. The magnetic fields associated with these regions differ between the samples due to their differing purities. It is thus concluded that the fit works well in both low-field and high-field regions and that it handles differing sample impurities well through appropriate adjustment of the κ_0 and a parameters. The phonon contribution to the thermal conductivity is found to be minimal in the fits and it is suggested that this may be the result of surface scattering.

The data presented confirm the applicability of equation (4.9) at 5.5 K and between 0 and 2 T. Nevertheless, it is also expected to work equally well at any temperature below 6 K (down to tungsten's superconducting transition at approximately 10 mK [219]) and at any magnetic field below that at which electron orbit quantisation occurs.

Chapter 5 – Thermal Magnetoconductivity of Tungsten at a Range of Angles

To obtain the small A/L ratios required in tungsten heat switches for ADRs demands complex geometries (see Figure 2.13 for example). In such geometries it is unlikely – and may even be undesirable – that all sections of the switch will be perpendicular to the applied magnetic field. This chapter takes the equation developed and tested in Chapter 4 and generalises it to cases where the length of the sample – and therefore the direction of heat flow – is rotated so that it is no longer perpendicular to the magnetic field. This includes the case where the sample length is parallel to the magnetic field. The generalised equation is compared to measurements performed at a range of angles between the perpendicular and parallel directions. A global fit is then applied to determine a single set of parameters that are able to model the thermal conductivity as a function of angle.

5.1 Theory

It was shown in Chapter 3 that for a compensated metal, such as tungsten, the conductivity tensor takes the following form in a high magnetic field aligned along the z-axis[27] [183,187]:

$$\kappa_{ij}(T,B) = \begin{pmatrix} \frac{k_{xx}(T)}{B^2} & \frac{k_{xy}(T)}{B^2} & \frac{k_{xz}(T)}{B} \\ \frac{k_{yx}(T)}{B^2} & \frac{k_{yy}(T)}{B^2} & \frac{k_{yz}(T)}{B} \\ \frac{k_{zx}(T)}{B} & \frac{k_{zy}(T)}{B} & k_{zz}(T) \end{pmatrix}. \qquad (5.1)$$

The dependence of κ_{ij} on magnetic field and temperature is shown explicitly in this expression. In the experiments described here, $\dot{Q}$ is forced to flow along a known direction (the sample direction, labelled $\dot{Q}_z$) and the element of $(\nabla T)_j$ in this direction is measured.

[27] If the heat flow is along a symmetry axis of the crystal the terms k_{xz}, k_{yz}, k_{zx} and k_{zy} will vanish. The more general case is assumed here as the crystal orientation is not precisely known in the sample used for the majority of the measurements described below.

As this is the only term in $(\nabla T)_j$ that *is* measured, the temperature gradient must be set as the independent variable and equation (3.115) must be re-cast using the resistivity tensor:

$$\begin{pmatrix} dT/dx \\ dT/dy \\ dT/dz \end{pmatrix} = \frac{1}{A}\begin{pmatrix} \gamma_{xx} & \gamma_{xy} & \gamma_{xz} \\ \gamma_{yx} & \gamma_{yy} & \gamma_{yz} \\ \gamma_{zx} & \gamma_{zy} & \gamma_{zz} \end{pmatrix}\begin{pmatrix} \dot{Q}_x \\ \dot{Q}_y \\ \dot{Q}_z \end{pmatrix}, \tag{5.2}$$

or, more concisely:

$$(\nabla T)_i = \frac{1}{A}\gamma_{ij}\dot{Q}_j. \tag{5.3}$$

The resistivity tensor is found by inverting the conductivity tensor using the standard method for tensor inversion and has the following form (see 3.10.3):

$$\gamma_{ij}(T,B) = \begin{pmatrix} c_{xx}(T)B^2 & c_{xy}(T)B^2 & c_{xz}(T)B \\ c_{yx}(T)B^2 & c_{yy}(T)B^2 & c_{yz}(T)B \\ c_{zx}(T)B & c_{zy}(T)B & c_{zz}(T) \end{pmatrix}. \tag{5.4}$$

As in equation (5.1), the notation indicates explicitly the dependence on magnetic field and temperature. The γ_{xx} and γ_{zz} terms are the relevant ones for the results discussed below. When the heat flow is aligned with the magnetic field (i.e. longitudinal magnetoresistance, corresponding to term γ_{zz}), there is no dependence on magnetic field according to equation (5.4); that is not to say that the field has no effect on the resistivity at all, but just that it should saturate in the high-field condition. As discussed in Chapter 4, a metal is usually said to be in the high-field condition when the relaxation time (τ) exceeds the period of the cyclotron orbit ($2\pi/\omega_c$) – i.e. $\omega_c\tau > 2\pi$ [160,183,187]. When the heat current is perpendicular to the magnetic field (γ_{xx} and γ_{yy}), the thermal magnetoresistivity has a B^2 dependence.

5.1.1 The Conductivity Tensor under Rotational Transformations

In the test set-up used for the measurements of this chapter, the sample was rotated about the y-axis by an angle, θ, from the vertical as illustrated in Figure 5.1.

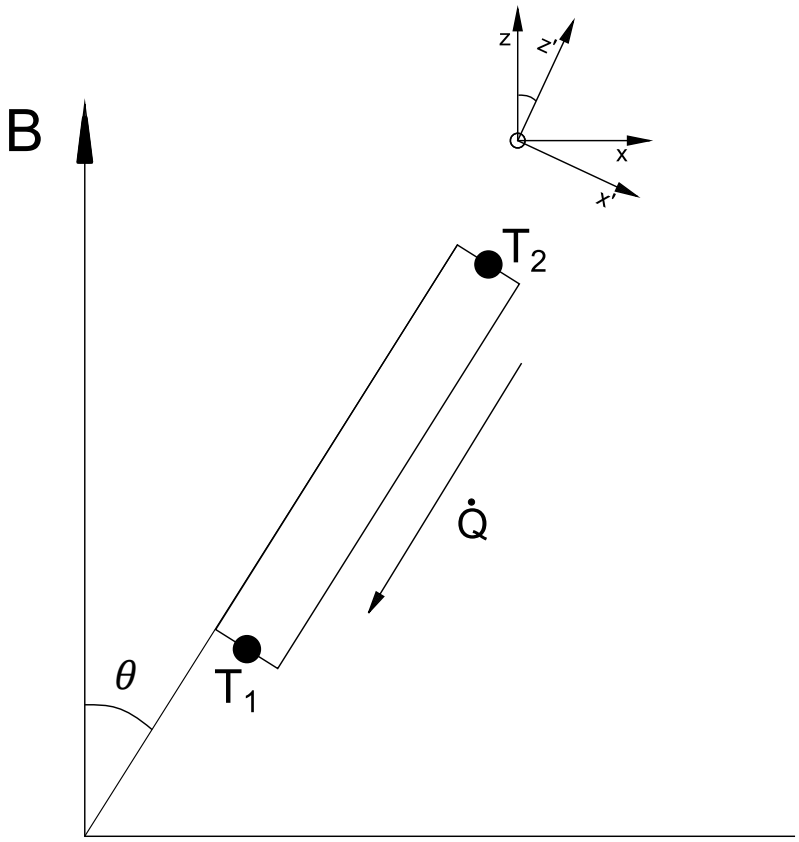

Figure 5.1: Schematic of experimental set-up.

The transformation matrix for this type of orthogonal rotation is:

$$\boldsymbol{R} = \begin{pmatrix} \cos\theta & 0 & -\sin\theta \\ 0 & 1 & 0 \\ \sin\theta & 0 & \cos\theta \end{pmatrix}. \tag{5.5}$$

The resistivity tensor in the primed coordinate system can then be found as follows:

$$\boldsymbol{\gamma'} = \boldsymbol{R\gamma R}^T, \tag{5.6}$$

since $\boldsymbol{R}$ is an orthogonal tensor [220]. Noting that the resistivity tensor is symmetric (i.e. $c_{ij} = -c_{ji}$), this leads to:

$$\gamma'_{ij} =$$

$$\begin{pmatrix} c_{xx}c^2\theta B^2 + c_{zz}s^2\theta & c_{xy}c\theta B^2 - c_{yz}s\theta B & (c_{zz-}c_{xx}B^2)c\theta s\theta + c_{xz}B \\ c_{yz}s\theta B - c_{xy}c\theta B^2 & c_{yy}B^2 & c_{yz}c\theta B + c_{xy}s\theta B^2 \\ (c_{zz-}c_{xx}B^2)c\theta s\theta - c_{xz}B & -c_{xy}B^2 s\theta - c_{yz}Bc\theta & c_{xx}s^2\theta B^2 + c_{zz}c^2\theta \end{pmatrix} \quad (5.7)$$

where the contractions $s\theta = \sin\theta$ and $c\theta = \cos\theta$ have been made.

As the geometry of the sample forces heat to flow in the z-direction of the rotated coordinate system and the temperature difference is measured in this direction, γ'_{zz} is the tensor element of interest:

$$\gamma'_{zz} = c_{xx}(T)\sin^2\theta\, B^2 + c_{zz}(T)\cos^2\theta. \quad (5.8)$$

Terms can now be added for the zero-field resistivity and the lattice conductivity. Using the arguments of the Chapter 4, the electronic part of the resistivity, γ_e, can be expressed as:

$$\gamma_e = \gamma_0 + \gamma_B, \quad (5.9)$$

where γ_0 is the zero-field resistivity and γ_B ($\equiv \gamma'_{zz}$) is the field dependent part of the thermal resistivity, given by equation (5.8).

The lattice conductivity, κ_l, can be incorporated by assuming it runs in parallel with the electronic conductivity:

$$\kappa = \kappa_l + \kappa_e, \quad (5.10)$$

or,

$$\frac{1}{\gamma} = b_l + \frac{1}{\gamma_e}, \quad (5.11)$$

where, as in Chapter 4, b_l is the lattice conductivity term . It is left as a free parameter in the fits below. Inserting equations (5.8) and (5.9) into (5.11), gives:

$$\gamma = \frac{1}{b_l + \dfrac{1}{\gamma_0 + c_{xx}\sin^2\theta\, B^2 + c_{zz}\cos^2\theta}}. \tag{5.12}$$

Equation (5.12) can be compared with the thermal conductivity equation developed in Chapter 4:

$$\kappa = b_l + \frac{1}{\dfrac{1}{\kappa_0} + \dfrac{B^n}{a}}, \tag{5.13}$$

where the parameters have the same meanings as in that chapter. For the reasons noted above, the results reported in this chapter should be fitted to the thermal resistivity rather than the conductivity. The equivalent expression to equation (5.13) for resistivity is as follows.

$$\gamma = \frac{1}{b_l + \dfrac{1}{\gamma_0 + \dfrac{B^n}{a}}}. \tag{5.14}$$

In equation (5.14), the zero-field resistivity, γ_0, has been used in place of the zero-field conductivity, κ_0.

It can be seen that equation (5.14) is in fact a special case of equation (5.12) for $\theta = 90°$ and where the exponent of magnetic field has been allowed to vary from 2 (for the reasons discussed in Chapter 4). The c_{xx} term in equation (5.12) is the equivalent of the $1/a$ term in equations (5.13) and (5.14). In section 5.3, below, it is shown that equation (5.12) can be used to produce a global fit to results over a range of angles.

5.2 Experimental Details

The tungsten sample (see Figure 5.3) used for the majority of the measurements was a high purity single crystal with a RRR of > 100 000 and will be referred to hereafter as M-1. This RRR is a lower limit since the resistance at 4 K was below the noise limits of the measuring equipment. The sample was grown and spark eroded to the dimensions indicated in Figure

5.2 by MaTecK GmbH. The central bar section was measured using a micrometer and found to have a length of 9mm (rather than the 8.5 mm specified) and a cross-section of 1.5 mm by 1.5 mm. The sample details are summarised in Table 5.1 along with those for sample C-3b (see Chapter 4), which is used for comparison purposes.

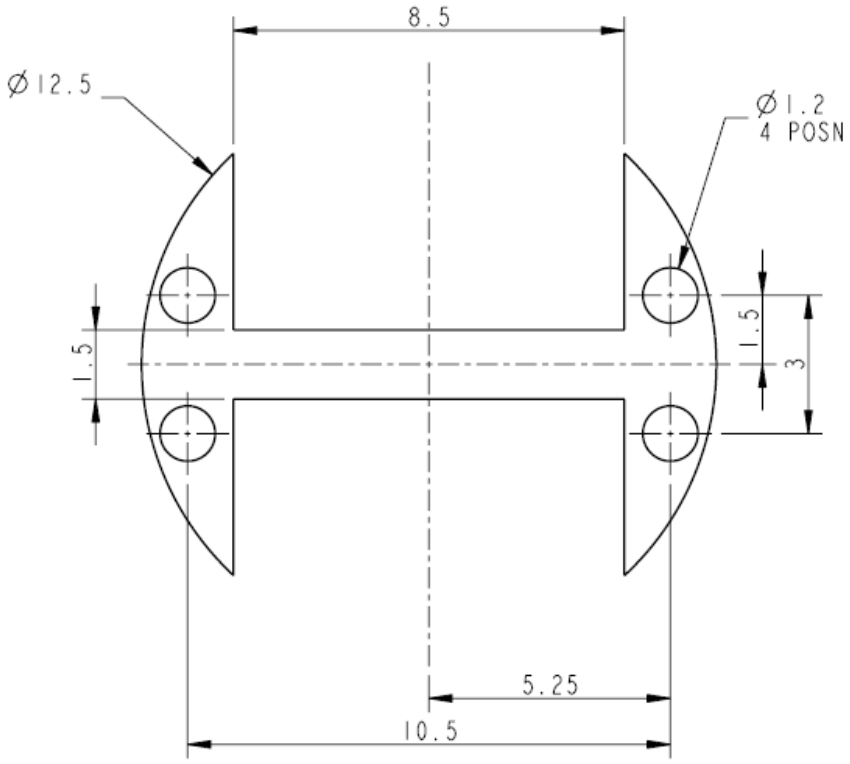

Figure 5.2: Dimensions of tungsten sample.

Sample	Supplier	Dimensions	RRR	Crystal orientation
M-1	MaTecK (Juelich, Germany)	1.5mm x 1.5mm x 9mm long	>100 000	Heat flow in plane perpendicular to [111]
C-3b[a]	Metal Crystals and Oxides Ltd (Cambridge, UK)	1.55mm x 1.37mm x 5.9mm long	>100 000	[100] direction along sample length ($\parallel \dot{Q}$)

[a]Sample C-3b was only measured in two orientations: with its length parallel and perpendicular to the magnetic field

Table 5.1: Sample details.

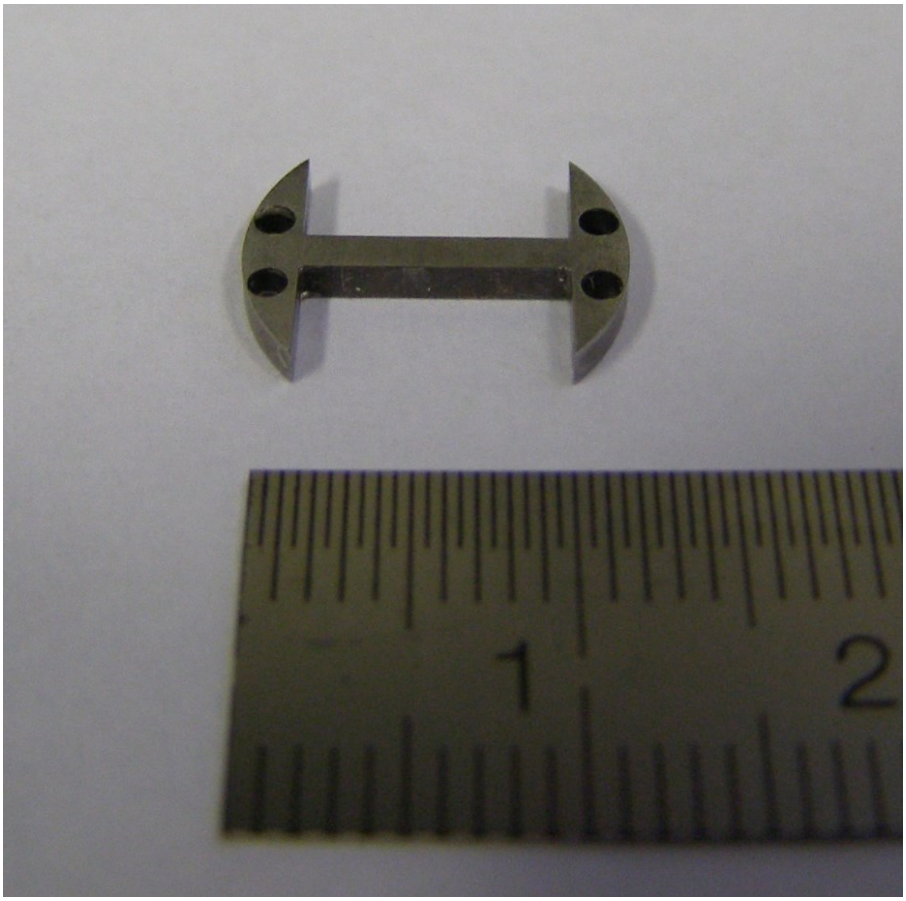

Figure 5.3: Sample M-1.

The experiments were performed in the same PTR cooled cryostat described in Chapter 4. With one end of the sample attached to the cooled mount, heat was applied to the other end using a 10 kΩ resistor and the resulting steady-state temperature difference (ΔT) recorded using thermometers mounted to either end. Measurements were again performed in magnetic fields from 0 to 2 Tesla and at 5.5 K, with a temperature stability of ±0.05 K achieved by PID control of the PTR.

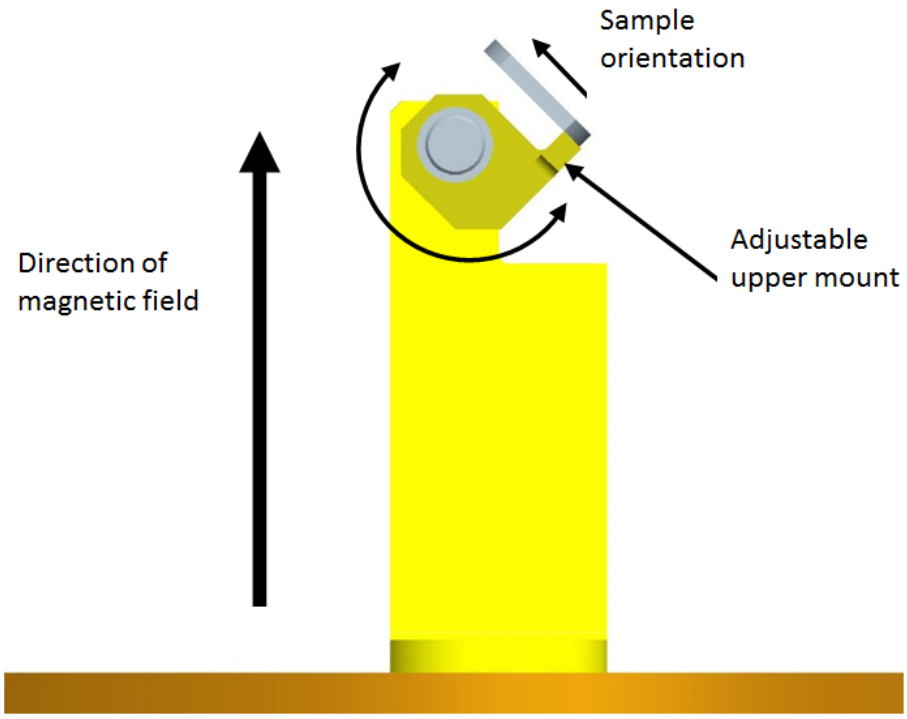

Figure 5.4: Illustration of the adjustable sample mount.

For this study, an adjustable sample mount was used to permit the direction of the sample to be altered with respect to the magnetic field (see Figure 5.4). Data were taken with the sample at angles of 0°, 15°, 30°, 45°, 60° and 90° to the magnetic field. As noted above, the thermal resistivity was the more appropriate measure for interpreting these results and this was calculated as follows.

$$\gamma = \frac{\Delta T}{\dot{Q}} \frac{A}{L}, \tag{5.15}$$

with ΔT being the temperature difference measured between the two thermometers, $\dot{Q}$ the supplied power, L the sample length and A the area.

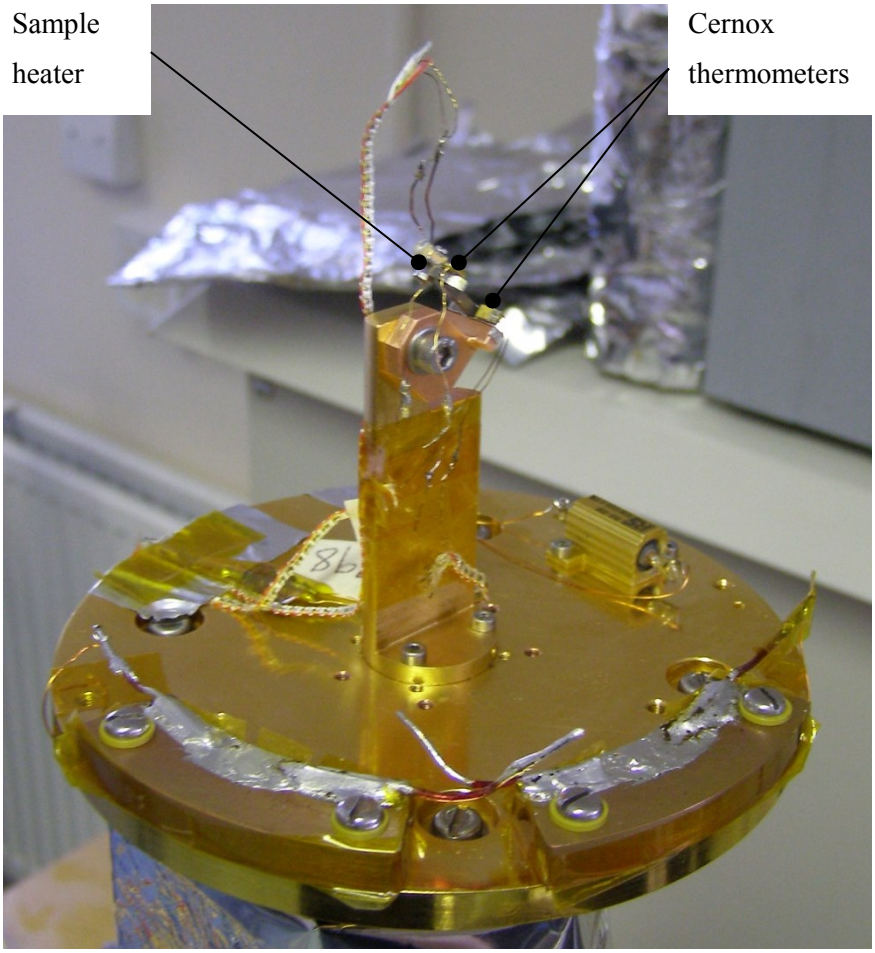

Figure 5.5: Measurement set-up (the 45° angle is shown).

5.2.1 Errors

A full discussion of the sources of error in the set-up is given in Chapter 4. In common with the plots of that chapter, the error bars in the figures below contain contributions from uncertainties in the thermometer readings, the voltage and current in the heater, and in the measured sample dimensions. As before, by far the greatest contribution to the errors came from the thermometer readings. However, by collecting temperature statistics over 30 second intervals for each reading and averaging at least two readings for every data point, total 1-sigma errors are reduced to below 10% in all but the zero-field cases. The errors in

these measurements were up to 25% in some cases and this is likely to be a contributory factor in some of the fitting difficulties described below.

The angle of the sample relative to the axis of the solenoid was measured using angle blocks (see Figure 5.6, below). The blocks were positioned on the PTR's 2nd stage interface plate such that they indicated the angle between the sample length and the normal to this plate. Since the solenoid was mounted with its axis perpendicular to the plate (see Figure 4.4), it is considered that this normal is an accurate enough proxy for the magnetic field direction. Although the final alignment of the sample was done be eye, the true angle is expected to be within ±1° of the nominal figure.

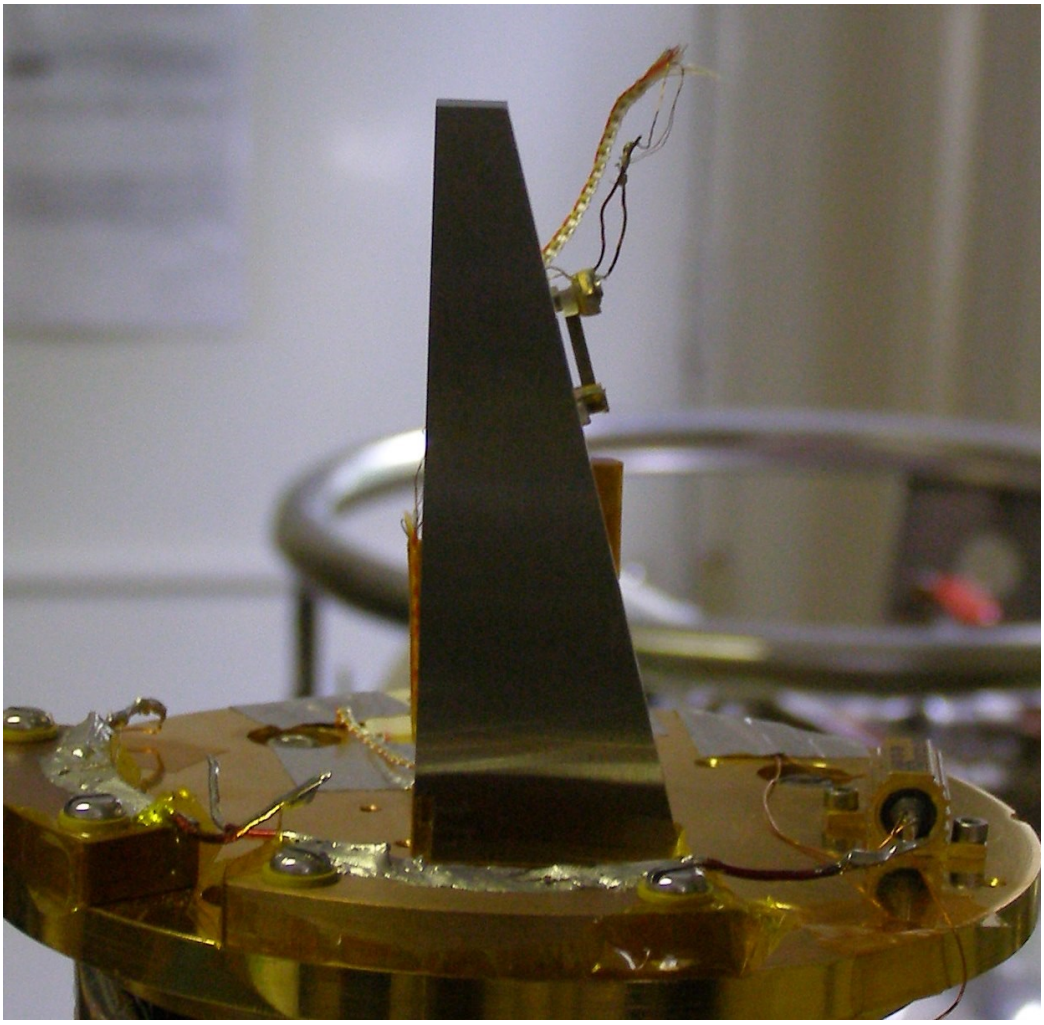

Figure 5.6: Example of sample set-up using angle blocks (the 15° set-up is shown).

5.3 Results and Discussion

In analysing the data, the two extreme cases are considered first: the sample perpendicular to the magnetic field (measuring the transverse thermal magnetoresistance – see 5.3.1) and the sample parallel to the field (measuring the longitudinal thermal magnetoresistance – see 5.3.2). These cases correspond to $\theta = 90°$ and $\theta = 0°$ respectively, which eliminate the c_{zz} ($\theta = 90°$) or the c_{xx} ($\theta = 0°$) term from equation (5.12). This permits use of the simplified form of the expression (equation (5.14)) to analyse these results. The $\theta = 90°$ case is equivalent to the configuration used for the measurements in Chapter 4 and it is therefore possible to make comparison with these results. Using this form for the $\theta = 0°$ case recognises the fact that, whilst the high-field longitudinal magnetoresistance is expected to saturate at a constant value, it may well show a dependence on B before saturation occurs (i.e. $n \neq 0$).

5.3.1 Heat Current Perpendicular to Magnetic Field

A thermal conductivity plot of the format used in Chapter 4 is shown for sample M-1 in Figure 5.7. The data in this plot is fitted using equation (5.13).

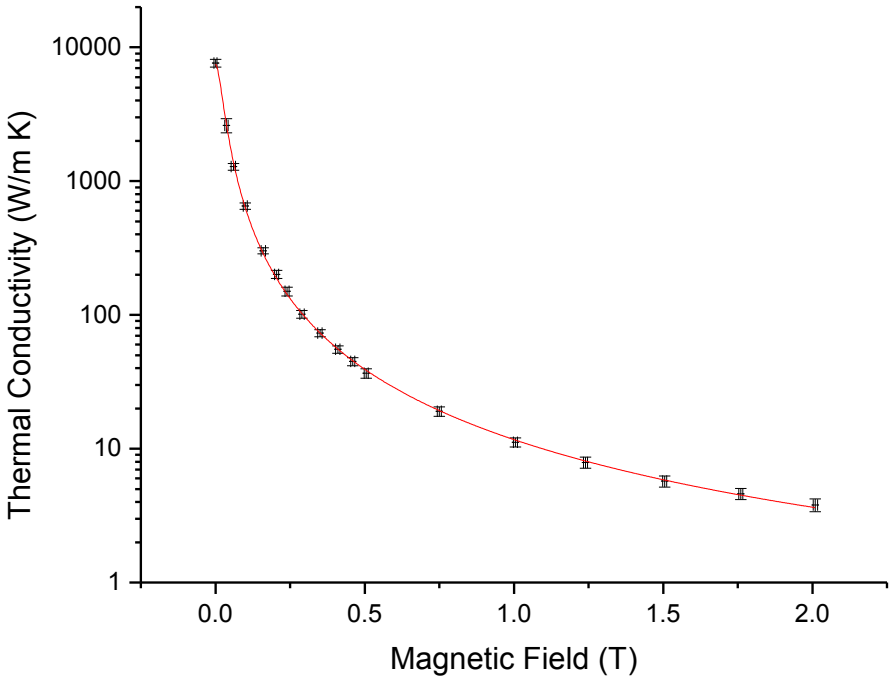

Figure 5.7: Thermal magnetoconductivity of sample M-1 perpendicular to the applied field.

For the reasons noted above, a fit to the thermal resistivity will be appropriate for analysing data over a range of angles and this is plotted in Figure 5.8. The fitted line in this figure uses equation (5.14).

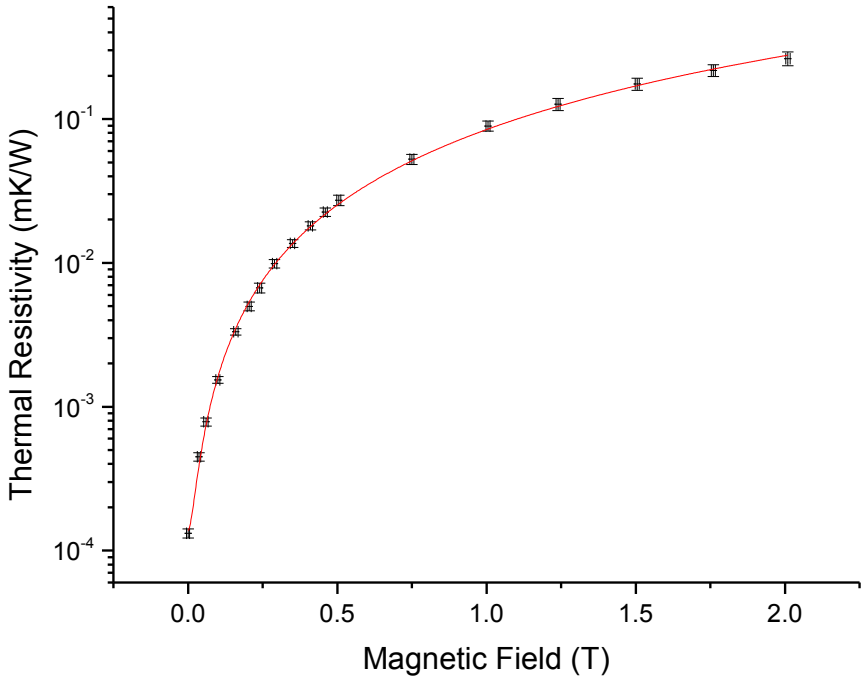

Figure 5.8: Thermal magnetoresistance of sample M-1 perpendicular to the applied field.

A comparison between the thermal conductivity and resistivity fits is made in Table 5.2. This provides a useful consistency check and, as expected, it can be seen that all parameters agree to within the estimated fitting errors.

Fit	b_l	γ_0 (m K/W)	κ_0 (W/m K)	n	a	Adjusted R-Square
Thermal Conductivity	0.35±0.28	1.332×10^{-4} $\pm5.89\times10^{-6}$ (equivalent)	7505±332	1.78±0.02	11.4±0.4	0.99722
Thermal Resistivity	0.20±0.38	1.380×10^{-4} $\pm8.26\times10^{-6}$	7246±434 (equivalent)	1.77±0.03	11.7±0.6	0.99552

Table 5.2: Comparison of fitting parameters for the conductivity and resistivity equations with sample M-1 perpendicular to the magnetic field.

Plotting the data in terms of thermal conductivity (Figure 5.7) makes a comparison with the results of Chapter 4 particularly straightforward. Of the two samples investigated in that chapter, sample C-3b is the more appropriate one for comparison with sample M-1 since they both have similar geometries and purities. Given the similar purities, it is slightly

surprising that there is more than a factor of two difference in the fitted zero-field conductivities. However, it should be noted that although the fitted value of 7505 W/mK agrees well with the measured value for this orientation (7492 W/mK), there was considerable variation in the values of zero-field conductivity measured for each orientation (7492 W/m K – 16957 W/m K). This is most likely to be a reflection of the inherent difficulty in measuring the zero-field conductivity of such small, high purity samples: even when applying the maximum power that was possible without overwhelming the PTR, the temperature difference developed along the short length of the sample was only a few tens of milli-Kelvin. In Figure 5.9, below, the resistivity data is re-fitted using the values from Table 5.2, with the exception that the γ_0 value is equivalent to the highest of the measured zero-field conductivity values (i.e. $\kappa_0 = 16957$ W/m K $\equiv \gamma_0 = 5.89\times10^{-5}$ m K/W). As can be seen from the figure, this still produces a good fit to the data with only a small deviation at low field. It is therefore concluded that the other fitting values in Table 5.2 can be relied upon regardless of the exact value taken by the zero-field conductivity within the range of measured values.

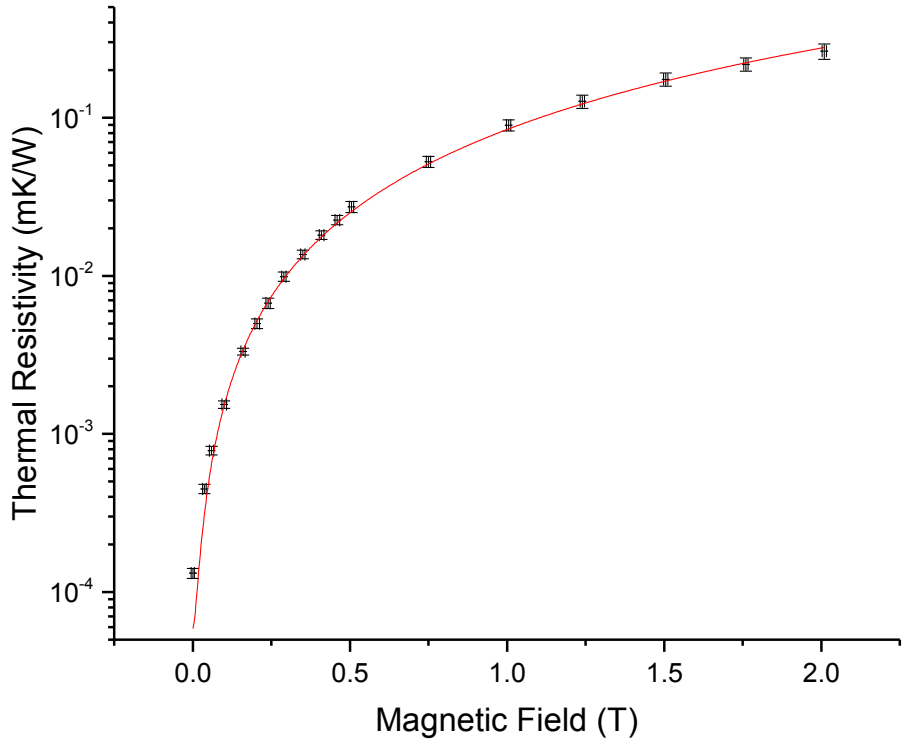

Figure 5.9: Thermal magnetoresistance of sample M-1 perpendicular to the applied field. The fit uses the maximum measured value of κ_0.

There is over a factor of two difference between the lattice conductivity of sample M-1 (0.35±0.28) compared to sample C-3b (0.93±0.16) and both are below the previously reported values of 0.05T^2 W/m K (= 1.51 at 5.5 K) found by Wagner and Batdalov & Red'ko [195,199] (see Chapter 4). The reasons discussed in Chapter 4 for the low lattice conductivity may well apply equally to sample M-1 and the even lower value in this sample may be a reflection of a poorer surface condition than sample C-3b.

The agreement of the magnetic field exponents (n) between the samples is excellent: both fits produce values of n = 1.8 to within the fitting errors. The a values also agree very well. The value for sample C-3b (9.11±0.19) is slightly lower than the figure for M-1 (11.4±0.4). As discussed in Chapter 4, it is expected that this parameter will show some dependence on the impurity scattering and its larger value in M-1 may reflect slightly higher impurity levels in this sample.

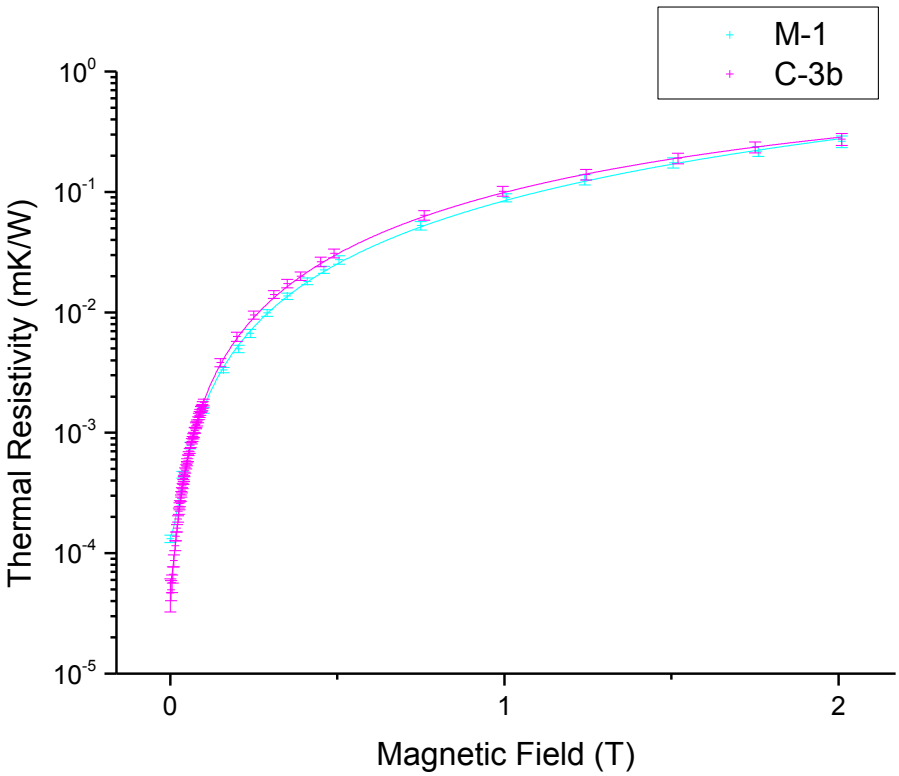

Figure 5.10: Comparison of the thermal resistivity fits for sample M-1 and C-3b when perpendicular to the applied field.

Sample	b_l	γ_0 (m K/W)	κ_0 equivalent (W/m K)	n	a	Adjusted R-Square
M-1	0.20±0.38	1.380×10^{-4} $\pm8.26\times10^{-6}$	7246±434	1.77±0.03	11.7±0.6	0.99552
C-3b	0.84±0.16	5.568×10^{-5} $\pm1.93\times10^{-6}$	17960±623	1.79±0.01	9.27±0.21	0.99859

Table 5.3: Comparison of fitting parameters for the resistivity equation between samples M-1 and C-3b (samples perpendicular to the magnetic field).

Figure 5.10 and Table 5.3 show the comparison between the thermal magnetoresistivity of sample M-1 and that of sample C-3b (plotted using the data from Chapter 4). It is clear that despite a difference in the zero-field resistivities, all the parameters agree very closely. This is further evidence that equation (5.14) works well with different samples. In addition, it suggests that apart from differences in purity (reflected in both γ_0 and a) the magnetoresistive behaviour of the samples is similar.

It was noted above that there was considerable variation in the zero-field conductivity values measured for sample M-1 at the different orientations. To enable a global fit to be made to equation (5.12), a single value of γ_0 is required and it was therefore decided to take an average of the measured values ($7.61 \times 10^{-5} \pm 2.52 \times 10^{-5}$ m K/W) and to make this a fixed parameter in the fits. The result of this is shown in Figure 5.11 and the fitting parameters are given in Table 5.4.

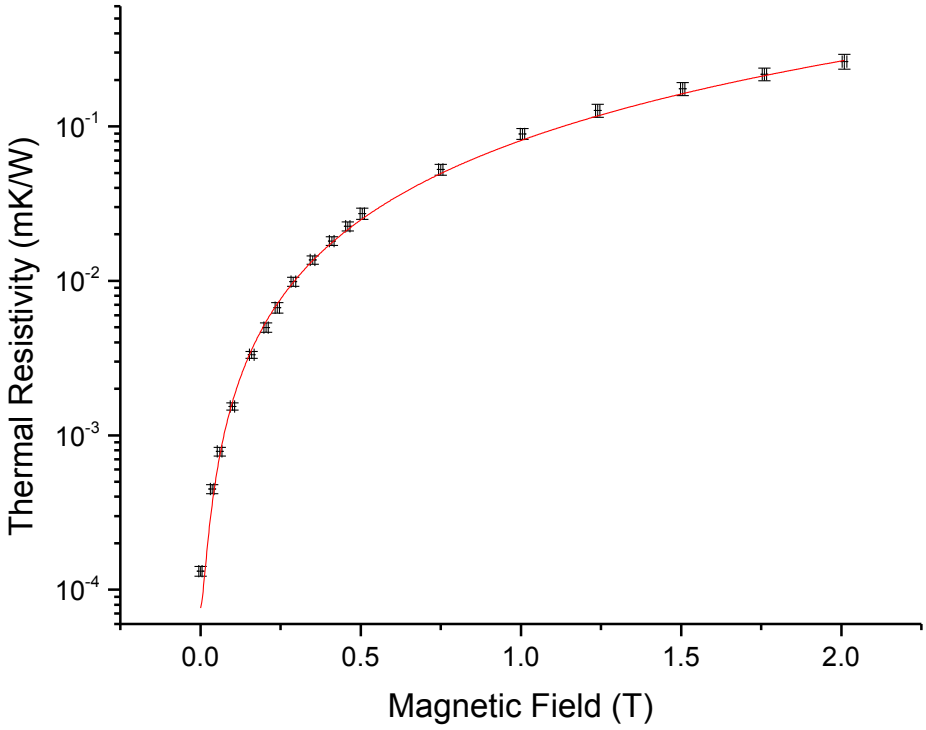

Figure 5.11: Thermal magnetoresistance of sample M-1 perpendicular to the applied field. In this fit the zero-field resistivity (γ_0) has been fixed at the average value given in the text.

It is clear from the figure that the fit is still good. The lattice conductivity has now dropped to zero, albeit with a larger error (±0.88). The magnetic field exponent has dropped to 1.71±0.06 and the a value of has increased slightly (12.36±1.27), but the percentage change in both is not excessive given the sizes of the errors in in the data. This fit is summarised in Table 5.4 alongside that for the case where the sample length was parallel to the field, which is explored in the following section.

Fit (sample M-1)	b_l	γ_0 (m K/W)	κ_0 equivalent (W/m K)	n	a	Adjusted R-Square
Perpendicular	0.00 ±0.88	7.61×10^{-5} (fixed)	13141 (fixed)	1.71±0.06	12.36±1.27	0.97883
Parallel	0 (fixed)	7.61×10^{-5} (fixed)	13141 (fixed)	1.17±0.03	499.67±17.30	0.98582

Table 5.4: Fitting parameters for the parallel and perpendicular cases.

5.3.2 Heat Current Parallel to Magnetic Field

For these measurements, the sample was rotated so that its length (and therefore the direction of heat flow) was aligned to the magnetic field, thus probing the longitudinal magnetoresistance. Again, results are plotted in terms of both thermal conductivity and resistivity (see below). In fitting this data, the average value of the zero-field resistivity calculated above was used. The lattice conductivity was also fixed at zero from the parallel fits since this should not show any variation with angle.

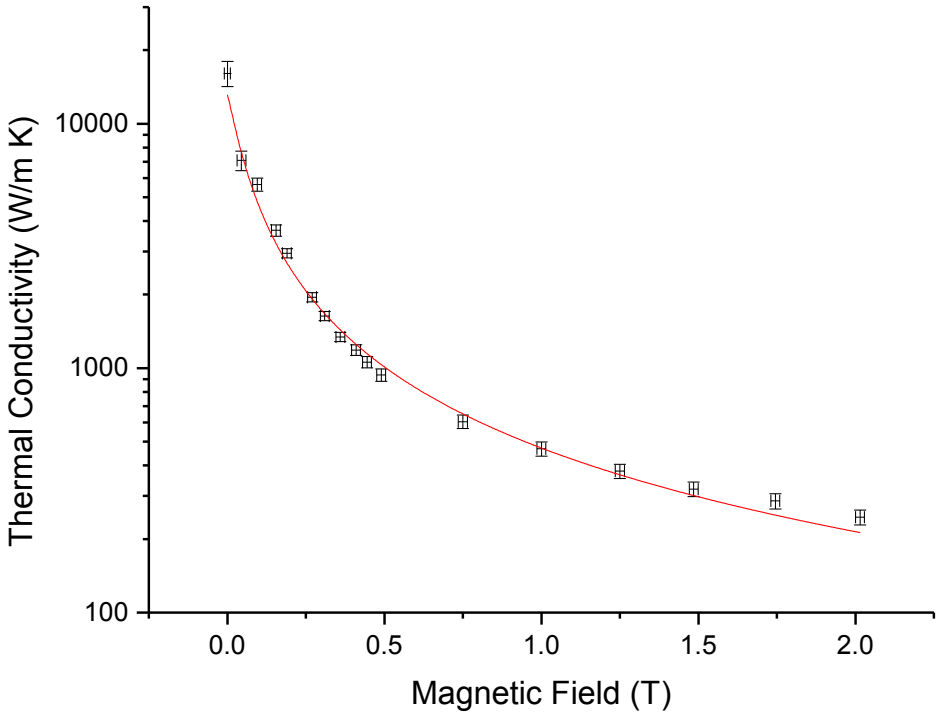

Figure 5.12: Thermal magnetoconductivity of sample M-1 parallel to the applied field.
The lattice conductivity (b_l) and the zero-field conductivity (κ_0) have been fixed at the values given in the text.

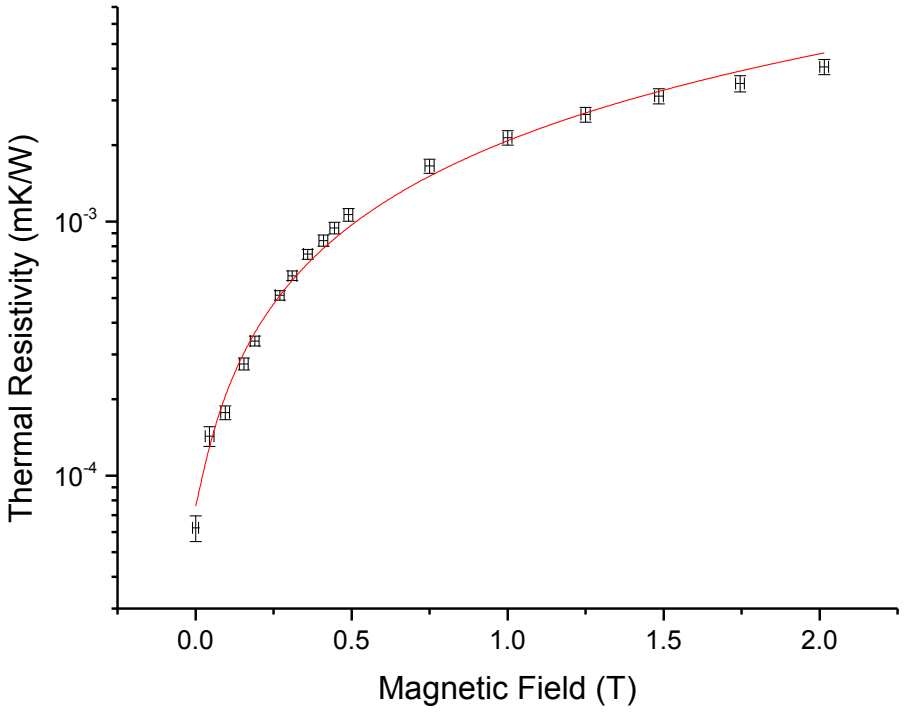

Figure 5.13: Thermal magnetoresistance of sample M-1 parallel to the applied field.
The lattice conductivity (b_l) and the zero-field resistivity (γ_0) have been fixed at the values given in the text.

Longitudinal magnetoresistance measurements were also performed on sample C-3b which can be used for comparison. A thermal resistivity plot of this data is shown below (Figure 5.14) along with a comparison of the thermal resistivity curves for the two samples (Figure 5.15) and the fitting parameters (Table 5.5). In making these fits, the algorithm was initially found to converge on a solution that gave an unreasonably high lattice conductivity ($b_l \approx 100$). Such a high value clearly cannot represent the real physical situation, given that almost no lattice conductivity is observed when the sample was measured parallel to the field (see Chapter 4). In the fits shown, therefore, the lattice conductivity is fixed at the value found in Chapter 4. The zero-field resistivity is also fixed, but at the measured value (4.49×10^{-5} m K/W).

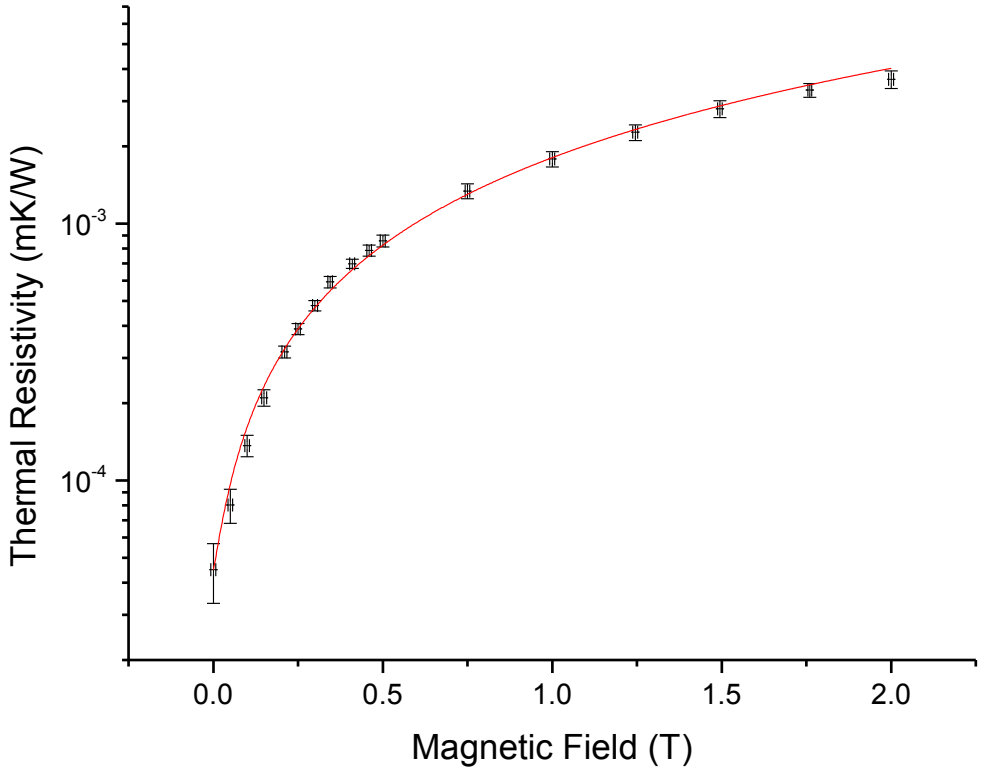

Figure 5.14: Thermal magnetoresistance of sample C-3b parallel to the applied field.
In this fit, the lattice conductivity (b_l) and the zero-field resistivity (γ_0) have been fixed at the values given in the text.

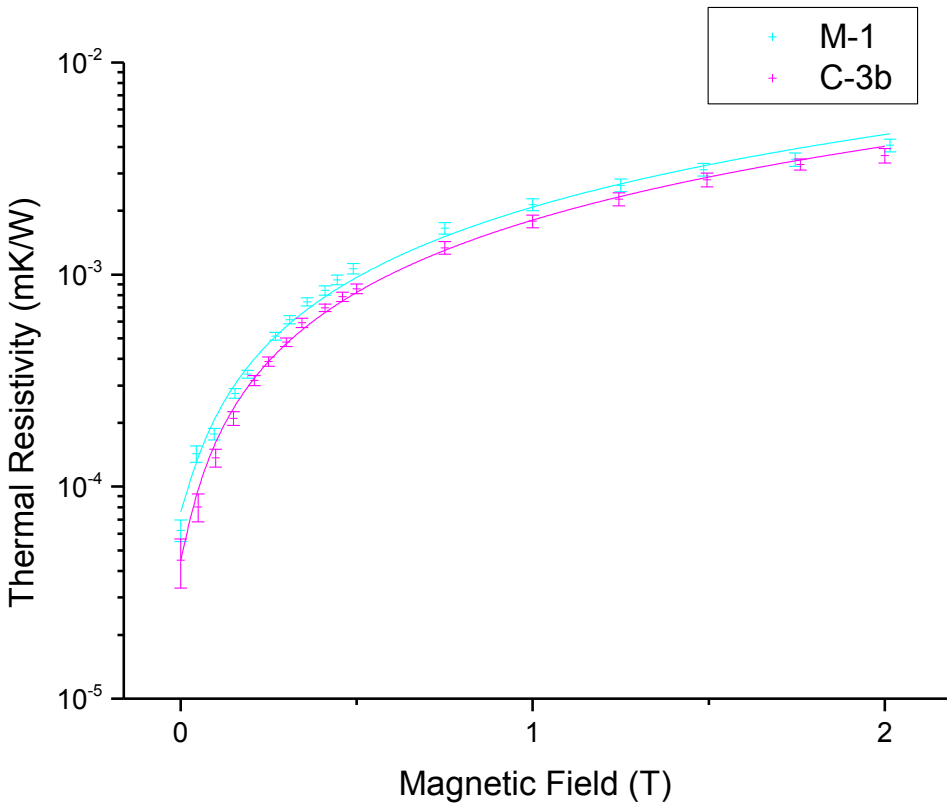

Figure 5.15: Comparison of the thermal resistivity fits for sample M-1 and C-3b when parallel to the applied field.

Sample	b_l	γ_0 (m K/W)	κ_0 equivalent (W/m K)	n	a	Adjusted R-Square
M-1	0 (fixed)	7.61×10^{-5} (fixed)	13141 (fixed)	1.17±0.03	499.7±17.3	0.98582
C-3b	0.93 (fixed)	4.49×10^{-5} (fixed)	22260 (measured)	1.18±0.02	566.7±12.7	0.99303

Table 5.5: Comparison of fitting parameters for the resistivity equation between samples M-1 and C-3b (samples parallel to the magnetic field).

The plots above illustrate that equations (5.13) and (5.14) work as well for the longitudinal magnetoresistivity as they do in the transverse case. Figure 5.15 and Table 5.5 confirm that there is good agreement between the parameters for samples M-1 and C-3b, with differences in their zero-field resistivity able to be accommodated in the use of different γ_0 values. The lower value of this parameter in sample C-3b can be tentatively interpreted as an indication of higher purity, although it must be borne in mind that – as noted above – there was

considerable variation in zero-field resistivities measured for sample M-1. The a values also add some doubt to this assumption. In Chapter 4, it was found that the lower purity sample had a lower a value and a possible explanation for this based on impurity scattering was put forward; in contrast, Table 5.5 shows a higher a value for the sample with the lower zero-field resistivity (sample C-3b), which presumably reflects lower impurity content. This is perhaps an indicator that this parameter in longitudinal magnetoresistance fits is in fact influenced by some other feature of the sample. Chapter 3 (3.10.4) described how the longitudinal magnetoresistance of a metal with a highly non-spherical Fermi surface like tungsten depends strongly on the orientation of the current with respect to the crystal axes. Although the crystal orientation along the sample length is not known exactly for M-1, it will be in a plane perpendicular to the [111] direction and therefore must be different from sample C-3b in which the length of the sample is along the [100] direction (see Table 5.1).

The magnetic field exponent for both samples measured in the parallel direction agrees within the limits of the fitting errors. While this is encouraging, its value (~1.2) does not match up neatly to any existing longitudinal magnetoresistance theory. As remarked above, the constant term for the tensor component γ_{zz} in equation (5.4) is to be interpreted not as the absence of magnetoresistance, but as the saturation of its effect at a sufficiently high field. As there is no indication of saturation in the presented data, it is of interest to determine whether the sample used is in the high-field condition at the fields applied. To do this $\omega_c\tau$ is calculated and compared it the criterion in section 5.1 ($\omega_c\tau > 2\pi$).

From Chapter 3, the cyclotron frequency is defined as:

$$\omega_c = \frac{eB}{m_c^*}. \tag{5.16}$$

Equation (5.16) illustrates that to calculate $\omega_c\tau$ accurately requires knowledge of the effective cyclotron mass (m_c^*) as well as the relaxation time (τ), both of which may vary

considerably depending on position on the Fermi surface. However, an estimate can be made using the free-electron approximation for the electrical conductivity [16]:

$$\sigma_0 = \frac{n_e e^2 \tau}{m_c^*}, \tag{5.17}$$

where n_e is the number of carriers and e (= 1.602×10^{-19} C) is the electron charge. By combining equations (5.16) and (5.17), the effective mass is eliminated and an expression for $\omega_c\tau$ is obtained [183]:

$$\omega_c\tau = \frac{B\sigma_0}{n_e e}. \tag{5.18}$$

Through de Haas–van Alphen measurements of tungsten's Fermi surface, Sparlin and Marcus found the number of carriers per atom to be 0.25 [221]. Assuming an atomic concentration for tungsten of 6.3×10^{28} atoms per cubic metre [129], this gives n_e = 1.58×10^{28} m^{-3}. The electrical resistivity of sample M-1 was measured at room temperature as ~58 nΩm. Using a RRR value of 100 000, the conductivity at 5.5 K can be estimated as $\sigma_0 = 1/(\rho_0 \times RRR)$ = 1.72×10^{12} Ω^{-1}m^{-1}. Inserting these values into equation (5.18) then yields:

$$\omega_c\tau = \frac{1.72\times10^{12}}{(1.58\times10^{28})\times(1.602\times10^{-19})}B \approx 680\times B. \tag{5.19}$$

The high-field condition is thus realised when $B > \sim 0.01$ T. By this estimate, sample M-1 was in the high field condition for all measurements where field was applied.

The preceding calculation makes the absence of any evidence of saturation in the longitudinal thermal resistivity somewhat surprising. Measurements on copper and silver [222] show some evidence for a significant delay in the onset of saturation and the explanation of these results [192] may apply in this case. The basis of the argument is that "small angle" scattering events play an equally – if not more – important role in dissipative processes as the catastrophic scattering events, which completely randomise an electron's

motion. While samples M-1 and C-3b may have been in the high field condition in the sense that an electron could make multiple orbits of the Fermi surface without experiencing a scattering event that would send it directly across the Femi surface – potentially reversing its velocity – it could have experienced many "small angle" scattering events which would move it into a nearby k-state. In the case of the thermal resistivity of tungsten, this could dissipate a heat current in two ways:

(i) Due to the smearing of the Fermi surface above 0 K, a small angle scattering event could move an electron from a state just above the Fermi surface to a vacant state just below it, reducing its thermal energy in the process (see Figure 3.5). Effectively a "hot" electron just above the Fermi-level becomes a "cold" electron just below it [16,154]. In the terminology of section 3.5.2.1 this would be a vertical process.

(ii) In regions of Fermi surface with rapid changes of gradient (and so velocity[28]), such as the central ("electron jack") surface in tungsten (see Figure 3.18) [190,223] a relatively small movement across the Fermi surface may be accompanied by a large change in velocity. Note that the velocity change may equally well be from negative to positive as vice versa.

Small angle scattering events of the first type are attributed to phonons [16,154]. As described in Chapter 3 (3.5.2.1), for an electron to move across the thermal layer around the Fermi energy, it will need to emit a phonon of energy $\sim k_B T$ and the probability of this occurring will depend on the density of available final phonon states. At very low temperatures, there will be so few phonons present that the probability will diminish. Given the temperature of the measurements above, this effect may well be small. Nonetheless, there is no reason why impurities and lattice defects might not also play a role at temperatures where phonon effects are virtually frozen out [192]. The elastic scattering associated with these scattering sources would be consistent with the second type of small

[28] $\mathbf{v} = \frac{1}{\hbar}\nabla_{\mathbf{k}}\epsilon$

angle scattering mentioned above. Regardless of the source, while an electron experiences small angle scattering events before completing multiple orbits, saturation will not be complete and, if impurities or lattice defects are responsible, it may never be achieved.

In addition to not observing saturation, there is a clear field dependence of the longitudinal magnetoresistivity. This can be related to the relatively complex nature of tungsten's Fermi surface. Referring to the "electron jack" section in Figure 3.18 it can be seen that for an orbit such as that labelled ψ, the velocity vector will experience several changes of direction around the orbit. Moreover, the component of velocity in the direction normal to the plane of the orbit will be reversed as the orbit is traversed. It is orbits such as these which lead to a high longitudinal magnetoresistance. Since the exact orientation of our sample is not known it isn't possible to determine the direction of the magnetic field with respect to the crystal axes and therefore the sort of orbits which may be involved in the longitudinal measurements described here.

5.3.3 Angle Sweep

From the results of the previous sections, it has been found that both the longitudinal magnetoresistance ($\propto B^{1.2}$) and the transverse magnetoresistance ($\propto B^{1.7}$) are dependent on B. In seeking a global fit to the data over all angles, these results are incorporated in equation (5.12) by making both the c_{xx} and c_{zz} terms functions of B, with the exponents left as fitting parameters:

$$\gamma = \frac{1}{b_l + \dfrac{1}{\gamma_0 + c_{xx} sin^2\theta B^{n_x} + c_{zz} cos^2\theta B^{n_z}}}. \qquad (5.20)$$

Equation (5.20) is used to fit the data presented in Figure 5.16; b_l and γ_0 are fixed at the values from the 90° data and the average from all measurements, respectively, while c_{xx}, c_{zz}, n_x and n_z are allowed to vary (but constrained to have the same value for all data sets).

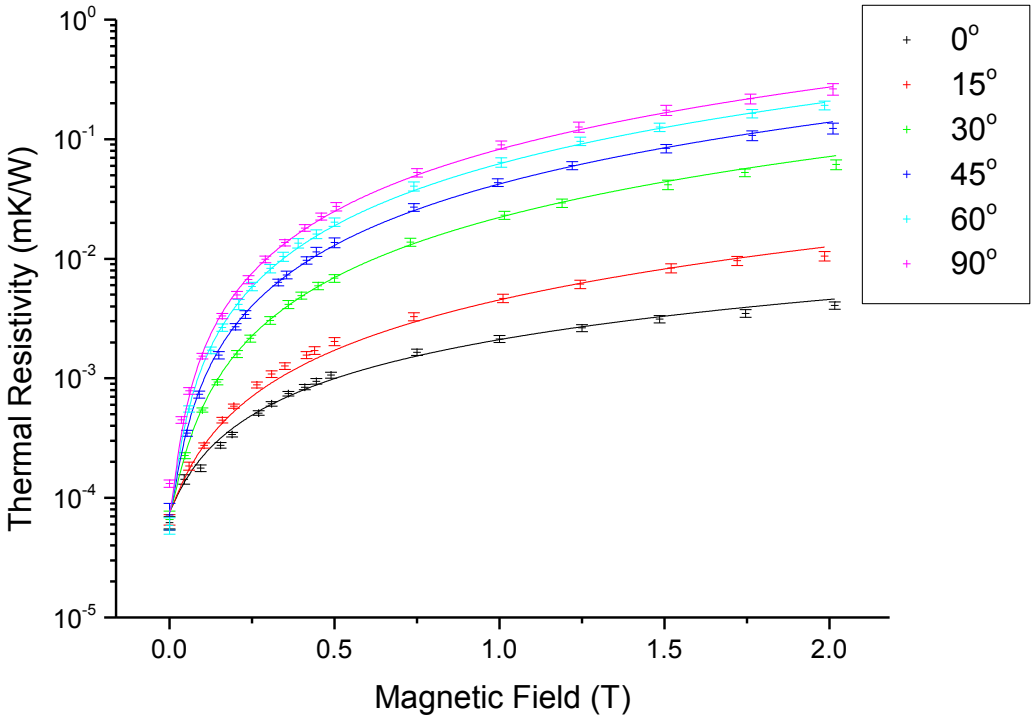

Figure 5.16: Thermal magnetoresistivity of sample M-1 at a range of angles with respect to the applied field (0° ≡ sample parallel to field, 90° ≡ sample perpendicular to field). Fitted curves are to equation (5.20).

Fit	b_l	γ_0 (m K/W)	κ_0 equivalent (W/m K)	n_x	n_z	c_{xx}	c_{zz}	Adjusted R-Square
All data	0 (fixed)	7.61×10^{-5} (fixed)	13141 (fixed)	1.66 ±0.02	1.15 ±0.04	0.071 ±0.002 (≡ a~14.1 ±0.4)	0.0018 ±0.0001 (≡ a~556 ±30)	0.96752
Excluding 15° data	0 (fixed)	7.61×10^{-5} (fixed)	13141 (fixed)	1.73 ±0.01	1.17 ±0.02	0.082 ±0.001 (≡ a~12.2 ±0.2)	0.0020 ±0.0001 (≡ a~500 ±24)	0.9908

Table 5.6: Fitting parameters for the full angle sweep

It can be seen from Figure 5.16 and Table 5.6 that a reasonable global fit is arrived at with values for the free parameters (c_{xx}, c_{zz}, n_x and n_z) that are not dissimilar to those obtained in fitting the perpendicular and parallel data on their own. The equivalent a values are given in Table 5.6 to aid this comparison.

This global fit, however, does not always lie within the error bars of the data – particularly for the measurements performed with the sample at 15°. The fact that the general trend (of a reduced change in magnetoresistivity for a given change in angle as the sample approaches 90°) is well modelled by the fit suggests that the data (especially the 15° set) contains an error source that has not been properly quantified. It is also noteworthy that values of the zero-field resistivity ranged from 5.89×10^{-5} m K/W to 1.32×10^{-4} m K/W and using an average of these in the fitting will limit the ability of a global fit to accurately model the data. The range in these results is thought to be purely due to the difficulty in accurately measuring the very small ΔTs that arise from the combination of using short, high conductivity samples.

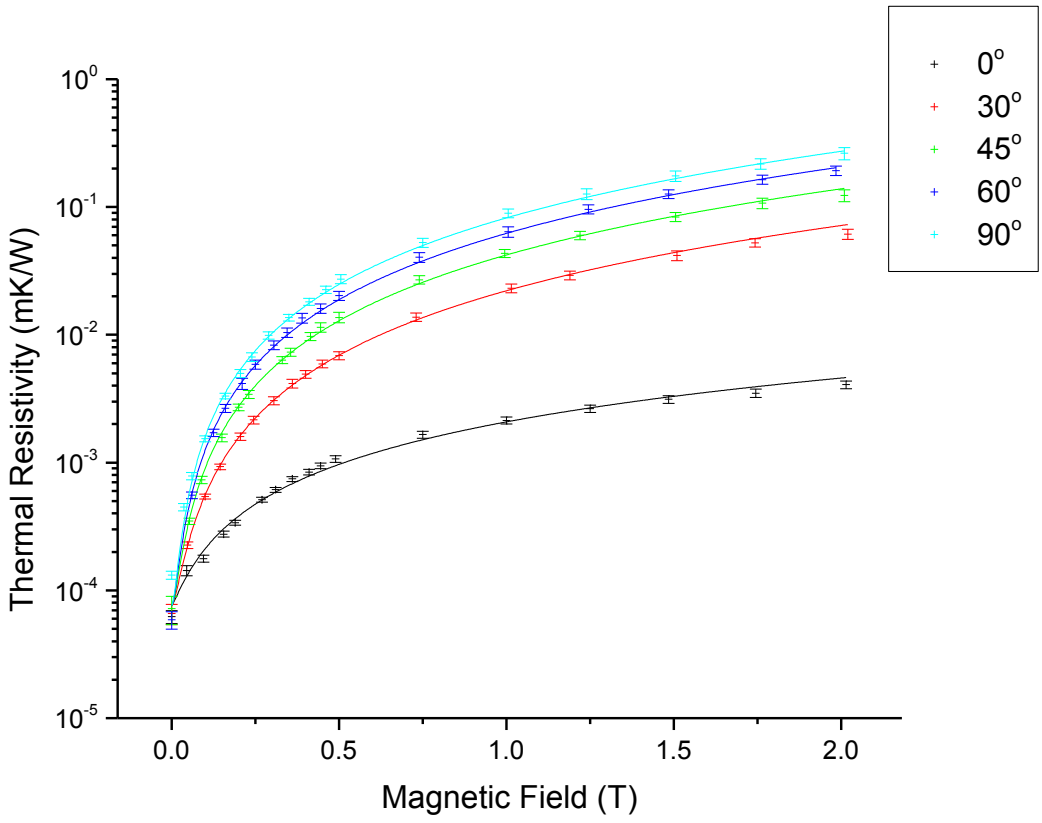

Figure 5.17: Thermal magnetoresistivity of sample M-1 at a range of angles with respect to the applied field (0° ≡ sample parallel to field, 90° ≡ sample perpendicular to field). The 15° data has been excluded.
Fitted curves are to equation (5.20).

Re-plotting the data without the 15° set shows that equation (5.20) is an even better fit when these points are excluded (Figure 5.17). This is confirmed by the higher R-square value in Table 5.6. In fact, with the help of the equivalent a values and comparison to Table 5.4, it can be seen that excluding the 15° data makes all the fitting parameters equal – within the errors – to the appropriate values from the perpendicular and parallel data. This provides further reinforcement that the form of equation (5.20) is correct and the method of combining longitudinal and transverse effects in this way is a valid approach.

5.4 Summary

The data presented in this chapter show how the magnetoresistance of tungsten is affected when the sample geometry is such that the direction of heat flow is not perpendicular to the applied magnetic field. It has been found that the longitudinal magnetoresistance, although not as great as the transverse effect, is significant. Furthermore, in contrast to the expectations of semi-classical magnetoresistance theory, it does not saturate and this may be due to small angle scattering effects.

The equation used in Chapter 4 to cover magnetoconductivity over a full range of fields has been employed to fit the data for the transverse and longitudinal magnetoresistance; in both cases the fits are extremely good. By generalising the resistivity tensor for rotations about the y-axis, the equation has then been adapted to fit the thermal magnetoresistance at arbitrary angles between the direction of the thermal current and the applied field. The global fit from this equation matches the general trends of the data well, although it falls outside the limits of the estimated errors when the angle between the field and the direction of heat flow is less than 30°. It is concluded that the fit is good enough to act as a reliable guide when making calculations about a sample's magnetoresistivity at arbitrary angles to the field. As such, it can be a useful tool in the design of low temperature heat switches and this is utilised in Chapter 6.

Chapter 6 – Mathematical Model of a Mini-ADR

This chapter describes the results of thermal modelling of a miniaturised ADR. The ADR architecture is based around the tandem CADR configuration described in Chapter 2. It consists of two pills; each one linked to the pre-cooling bath by one MR heat switch and linked the cold stage by another. The modelling makes use of the results of Chapters 4 and 5 to predict the performance of tungsten MR heat switches. The magnetic cooling of the pills is modelled using existing methods developed at MSSL and is described in detail below. The model is used to find initial design parameters for a miniaturised ADR and to test an alternative design that promises the potential of further size reductions. The impact of reducing an MR heat switch's dimensions on its switching ratio is also discussed.

6.1 Introduction

To determine the extent to which the use of tungsten heat switches allows a continuous ADR to be miniaturised, a Thermal Mathematical Model (TMM) of a tandem CADR has been produced using MATLAB[29]. The objective of this modelling is to understand the level of size reduction that can be achieved with tungsten heat switches and to arrive at a first-pass design for such an ADR which includes key parameters such as heat switch dimensions, pill sizes and requirements for the support structure.

[29] www.mathworks.co.uk/products/matlab

6.2 Conceptual Design

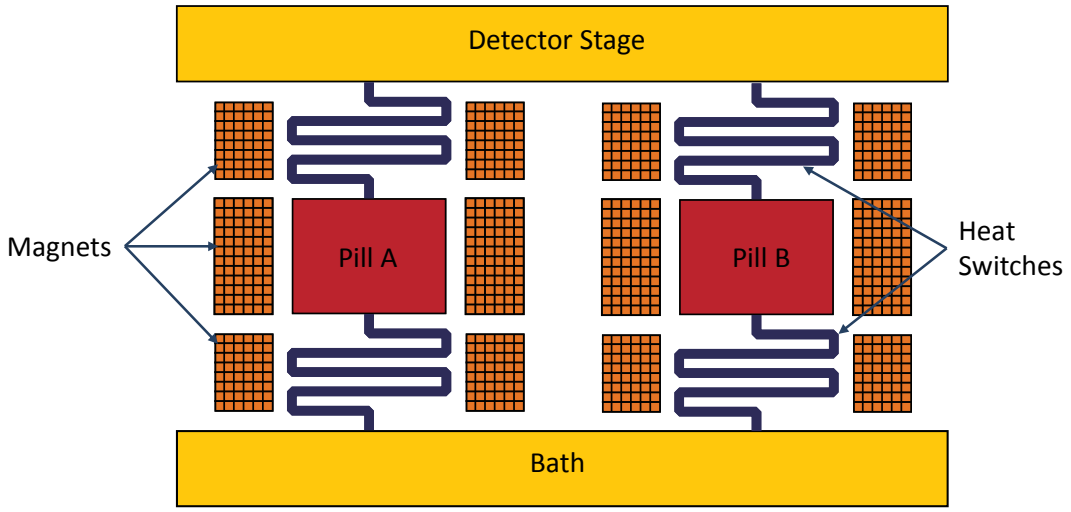

Figure 6.1: Schematic of the mini-ADR.

The cooler architecture is based on the schematic in Figure 6.1 and the thermal model layout is given in Figure 6.2. It is a tandem CADR layout, with one pill in each "leg", which cools a cold (detector) stage from a pre-cooling bath. The bath temperature is taken to be 2 K and the required detector temperature 100 mK. The pills are thermally linked to both the continuous cold stage and the bath with MR heat switches. The paramagnetic salt used in the pills is chosen to be CPA, both for its suitability in the temperature range of the model (0.1–2 K) and for the practical reasons discussed in Chapter 2. A support structure (not shown in Figure 6.1) is assumed for the cold stage which will be mounted from the bath; the form of the structure is left free with only the A/L ratio defined for the purposes of calculating the heat load due to conduction through it. It is also assumed that the design incorporates a radiation shield (not shown in Figure 6.1) which is thermally linked to the bath and surrounds the pills and the cold stage. In this way, the radiation loads on the pills and cold stage are only from surfaces at the temperature of the bath.

The Thermal Model contains nodes for both pills (labelled T_A and T_B), the detector stage (T_D) and the bath, in addition to which there are nodes at the pill ends of each heat switch.

These are to allow calculation of the temperature gradient resulting from thermal boundary resistances of the type described in Chapter 3 (3.9.4) (labelled $R_{B\text{-}XX}$ in Figure 6.2) between the heat switch at the pill (see 6.3.4). The complete list is given in Table 6.1.

Node	Description
T_A	Pill A
T_B	Pill B
T_D	Detector Plate
T_{Bath}	Pre-cooling stage
$T_{HSA1\text{-}P}$	Heat Switch A1 – Pill End
$T_{HSA2\text{-}P}$	Heat Switch A2 – Pill End
$T_{HSB1\text{-}P}$	Heat Switch B1 – Pill End
$T_{HSB2\text{-}P}$	Heat Switch B2 – Pill End

Table 6.1: mini-ADR Thermal Model nodes

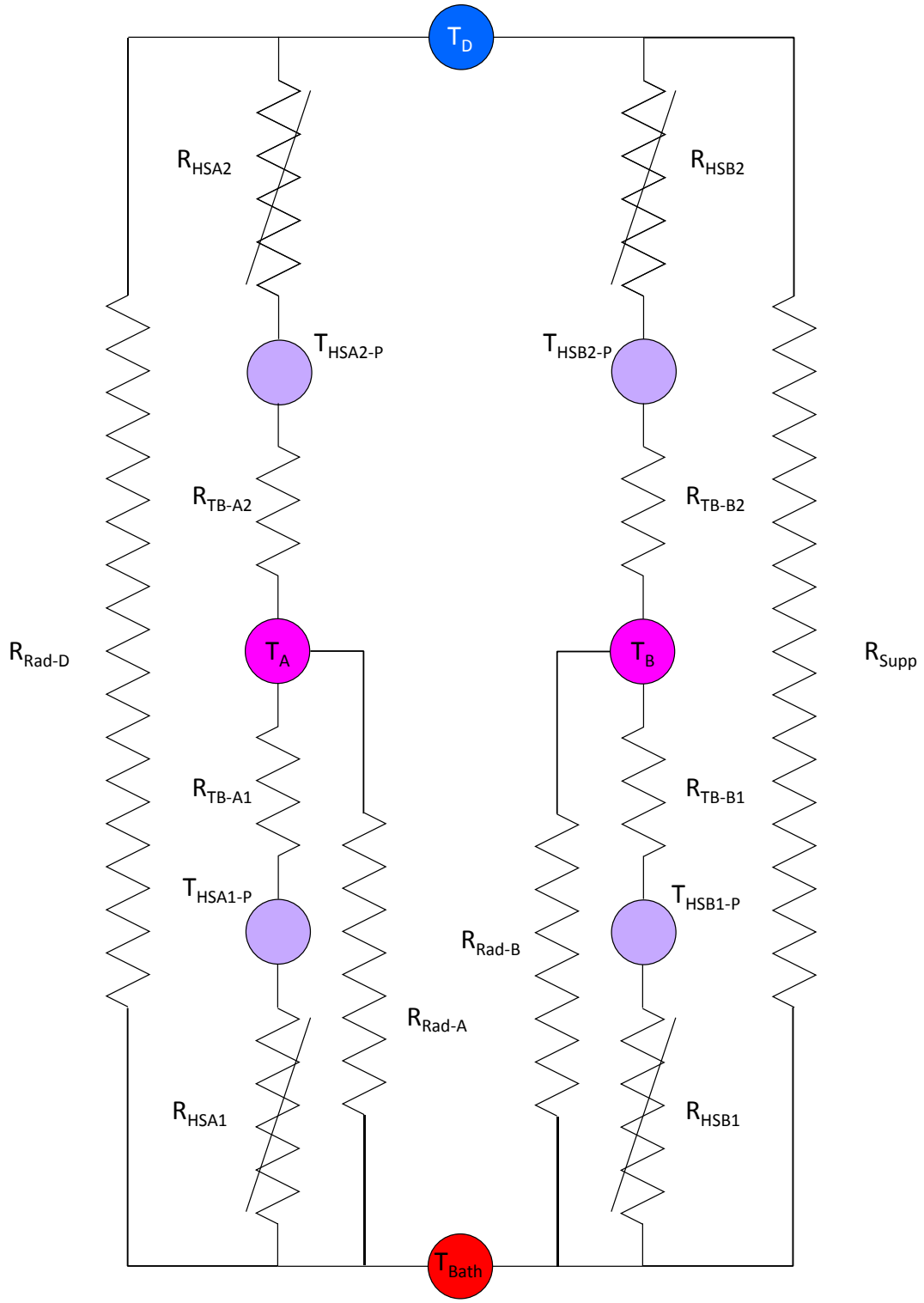

Figure 6.2: Thermal Model architecture.

The heat switches are labelled according to their "leg" (i.e. A or B) and whether they are between the bath and the pill, or the pill and the detector stage; for example the heat switch between the bath and Pill A is labelled HSA1.

6.3 Modelling Approach

The thermal model predicts the performance of the mini-ADR over an arbitrary number of cycles using a time-step approach. The pill temperatures are changed in discrete steps as the applied magnetic field changes, thus creating temperature gradients within the model. Heat flows through the thermal resistances shown in Figure 6.2 are calculated for each time step and these are then used to calculate the cold stage temperature for the subsequent time step using specific heat data. The following assumptions are made, most of which are discussed in more detail in the subsequent sections:

i. The bath temperature is assumed constant, regardless of the heat load on it;
ii. The variation of the entropy of CPA with magnetic field is assumed to be well represented by the free-ion approximation (see 6.3.1);
iii. The pill temperature changes linearly with magnetic field;
iv. Data for the zero-field entropy and heat capacity of CPA is taken from [152] (see 6.3.1.1 below);
v. The entire cooler is assumed to be sufficiently shielded that the only radiation loads are from the bath temperature;
vi. The performance of the heat switches will be as predicted by the equations developed in Chapters 4 and 5;
vii. The detector stage is assumed to be a copper plate of mass 75 g (≅ 80 mm × 50 mm × 2 mm). The heat capacity of copper as a function of temperature is calculated using a fit from [224];
viii. A heat load from the detector is 500 nW;
ix. No heat load from instrument wiring is included (this should not be significant if the wiring is sufficiently well heat sunk at the pre-cooling stage).

The 500 nW of detector cooling in viii – which is effectively the cooling power of the mini-ADR – was based on the requirements of currently proposed space missions (e.g. SPICA and Athena+) employing superconducting cryogenic detectors, such as Transition Edge Sensors or Microwave Kinetic Inductance Detectors. Being superconducting, the dissipation of the detector arrays themselves – which would contain of the order of 1000 pixels – is only a few nW [225]. However, there will usually be other loads on the cold stage (e.g. conduction down supports, conduction down wiring, radiation) and the cooling power available must be capable of dealing with these. Cryogenic chains for SPICA and Athena+ target cooling powers of around 0.5–1 μW at 50–100 mK [26,150,226] and the cooling power and temperature figures chosen for the model match the less stringent end of this range. As will be seen below, 500 nW is several times lower than parasitic loads from the ADR itself and it is therefore these that drive the size of the cooler rather than the detector cooling. Hence the cooler design could be adapted to deal with higher cooling powers without impacting greatly on the overall size.

6.3.1 Modelling the Magnetocaloric Effect

The magnetocaloric effect is modelled using the "Step Method" which has been developed at MSSL and validated through comparison with the results of tests on a manufactured ADR [152]. This technique seeks to replicate the cooling process in a real ADR, where magnetisation is not perfectly isothermal and demagnetisation is not perfectly adiabatic. As discussed in Chapter 2, magnetisation cannot be perfectly isothermally because the thermal link between the paramagnetic material and the bath does not have infinite conductivity; the temperature of the paramagnetic salt must therefore rise sufficiently that a temperature difference is developed across the thermal link and heat can flow to the bath. The size of this temperature difference will depend on the thermal conductivity of the link. Similarly, during demagnetisation of a paramagnetic material in a real ADR, parasitic heat loads (e.g. conduction from the support structure, radiation, etc.) cause its temperature to rise. The Step

Method allows the entropy and temperature of the pills to be calculated at each stage of magnetisation and demagnetisation, as is necessary for this type of time-step model.

The Step Method splits each stage of the magnetisation – or demagnetisation – process into two-part steps. The first part of the step is an isentropic temperature change and the second part is an isothermal entropy change. The temperature change is found from the following equation:

$$\Delta T = \left(\frac{\dot{Q}_{Pill}}{S}\right)\Delta t + \left(\frac{dT}{dt}\right)_{mag/demag}\Delta t. \qquad (6.1)$$

The first term is the temperature change due to parasitic heat loads onto the pill and the second term is temperature change resulting from the magnetocaloric effect. The second term is set by the (de)magnetisation rate $(dT/dt)_{mag/demag}$ in K/s, which is an input to the model. It is adjusted so that the magnetisation and demagnetisation rates match the ramp rates of the magnets. Using (6.1) the temperature at the (i+1)th step is found from the temperature at the (i)th step as follows:

$$T_{A_{i+1}} = T_{A_i} + \left(\frac{\dot{Q}_{A_i}}{S_{A_i}}\right)\Delta t + \left(\frac{dT}{dt}\right)_{mag/demag}\Delta t, \qquad (6.2)$$

where the subscripts refer to Pill A. An equivalent equation is used for Pill B. This equation cannot be considered a strict representation of the physics since $T \neq \int dQ/S$. It can, however, be thought of as a phenomenological approximation of the process.

The entropy change between the (i)th and the (i+1)th step is then found from the definition of entropy ($\delta S = \delta Q/T$):

$$S_{A_{i+1}} = S_{A_i} + \left(\frac{\dot{Q}_{A_i}}{T_{A_i}}\right)\Delta t. \qquad (6.3)$$

Again, the subscripts are in reference to Pill A and an equivalent expression is used for Pill B.

During the hold time, the magnetic field of the pill is adjusted to maintain constant temperature. In a real ADR this would be performed by a PID control loop adjusting the current in the magnet based on the difference between the cold stage's temperature and its target temperature. Replicating this in the TMM would add unnecessary complexity to the model, so a simpler algorithm is used: a tolerance is applied to the detector stage's target temperature (T_f); if the actual temperature of the detector stage (T_D) drops below $T_f -$ (tolerance), the magnetic field is increased according to the predefined magnetisation rate ($(dT/dt)_{mag}$) and the pill temperature rises according to equation (6.2); if T_D rises above $T_f +$ (tolerance), the magnetic field is decreased according to the demagnetisation rate ($(dT/dt)_{demag}$) and the pill temperature drops – again, according to equation (6.2). If the detector stage temperature is within the limits, the pill temperature is simply held constant:

$$T_{A_{i+1}} = T_{A_i} \tag{6.4}$$

and the entropy rise due to parasitic heat loads calculated using equation (6.3).

The Step Method is illustrated graphically for both magnetisation and demagnetisation in Figure 6.3.

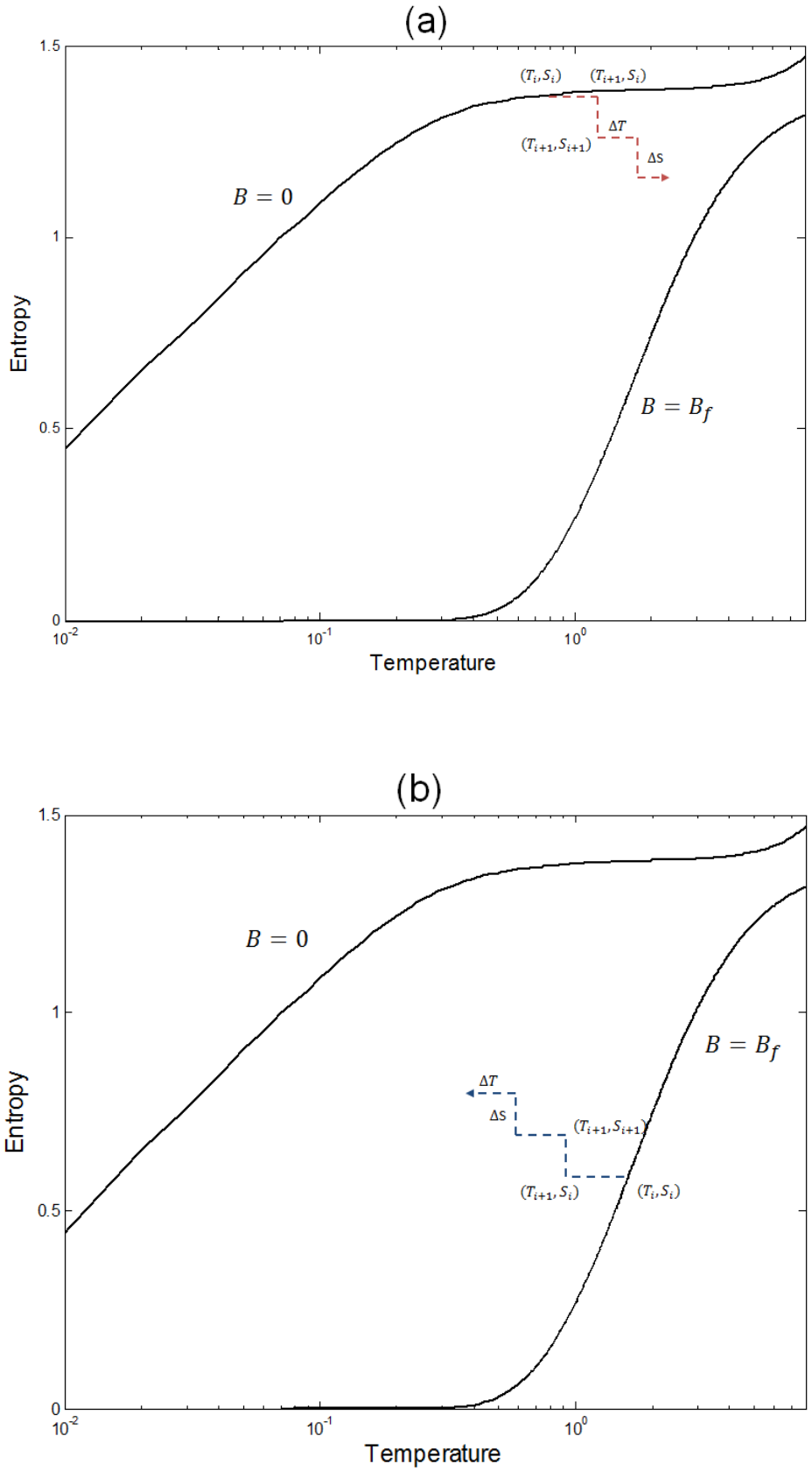

Figure 6.3: Graphical illustration of the Step Method for (a) magnetisation and (b) demagnetisation.

The underlying assumption of the above approach is that it is realistic to model the magnetisation and demagnetisation processes as a series of adiabatic temperature changes followed by isothermal entropy changes, whereas in reality both entropy and temperature will be changing simultaneously. The temperature change being calculated from an equation which cannot be justified by the physics of the process might lead to concerns about the validity of the approach. However, this modelling technique has been shown to be in very good agreement (< 5%) with measured results on a real ADR [152]. Furthermore, it will lead to an overestimation of final temperatures on both magnetisation and demagnetisation and therefore, where it is in error, it should be so conservatively.

A more accurate approximation would be to treat each magnetisation/demagnetisation step as a small increment in field, followed by small entropy increment along a line of constant magnetic field (see Figure 6.4). However, this would rely on having temperature-entropy curves for a very large number of magnetic fields and such data is not readily available. Using the free-ion approximation (as has be done when drawing Figure 6.4) would provide reasonable answers at higher fields, but it becomes progressively less accurate at lower fields and it is considered that this would introduce more errors into the modelling than arise from the Step Method itself.

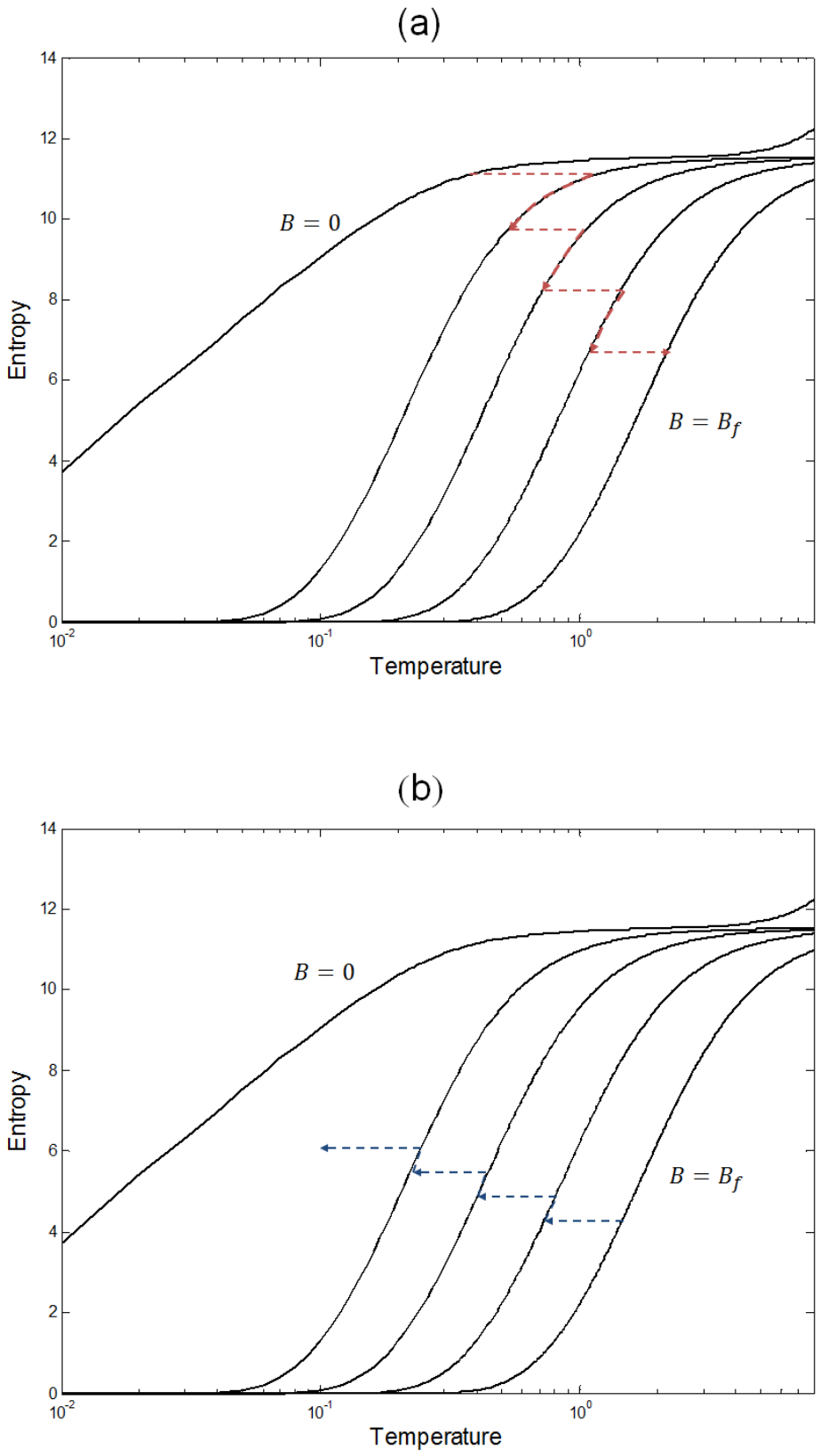

Figure 6.4: Graphical illustration of (a) the magnetisation process and (b) the demagnetisation process if entropy changes take place along lines of constant field.
The arrows indicate the direction of the process.

6.3.1.1 Pill Data

The paramagnetic refrigerant used in the model is Chromic Potassium Alum (CPA). As described in Chapter 2, this is a good low temperature refrigerant because it has a low ordering temperature and higher J value (3/2) than other salts suitable for low temperature use. FAA would offer an even higher J value, but it is highly corrosive to copper and this introduces practical difficulties for manufacturing the pill's thermal bus. It also has a limited life at room temperature, which further complicates pill construction.

The zero-field temperature-entropy data is the same as used in [152]. This an amalgamation of results from Vilches & Wheatley [227], Hudson [102] and, above 1 K, from Kapadnis [228]. The first two references provide entropy data and the third gives specific heat data; for this case, entropy has been obtained using the relation:

$$S = \int \frac{C}{T} dT. \tag{6.5}$$

Conversely, zero-field specific heat data below 1 K is found from rearranging equation (6.5):

$$C = T \frac{dS}{dT}. \tag{6.6}$$

Entropy and specific heat data in non-zero fields are calculated using the free-ion approximation (see Chapter 2 and Appendix H). The resulting data is summarised in Figure 6.5 and Figure 6.6 below.

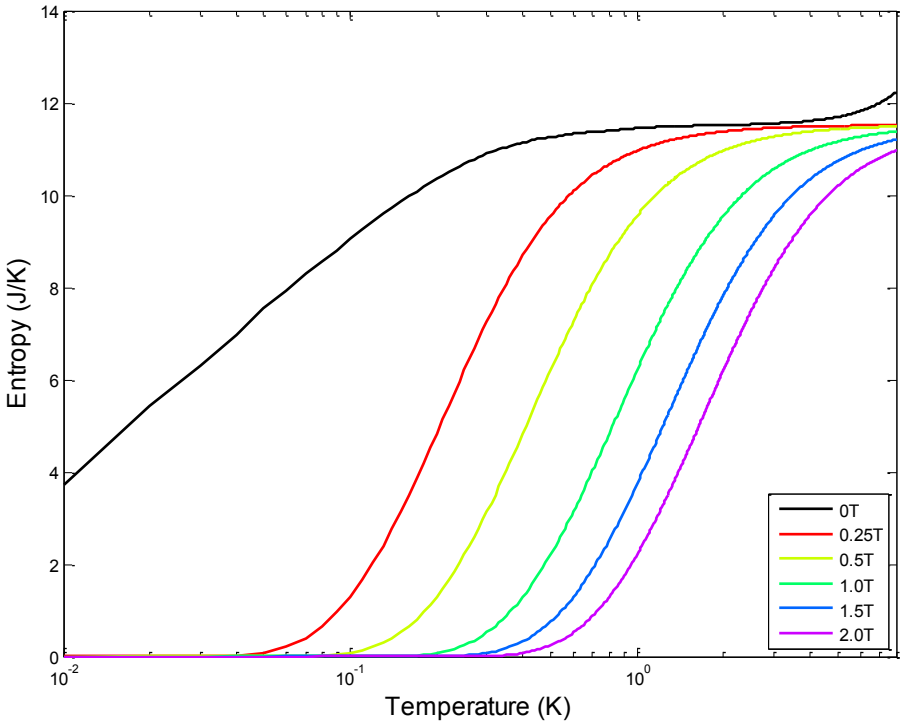

Figure 6.5: Temperature-entropy data for CPA (1 mole).
Above 0 T the free-ion approximation is used in the thermal model and curves produced from this calculation for a selection of fields are shown.

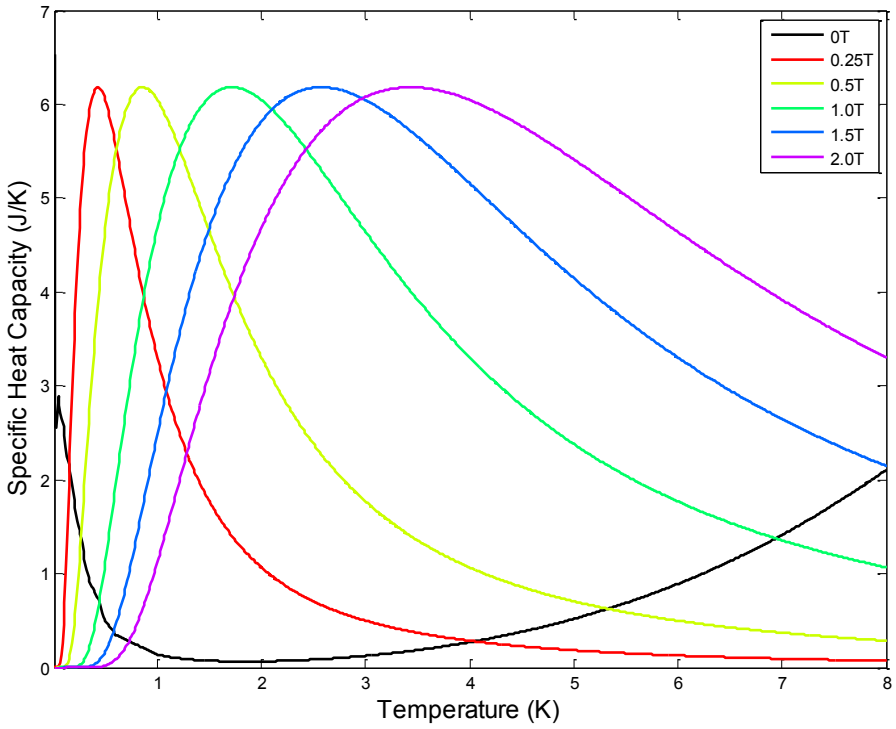

Figure 6.6: Temperature-specific heat data for CPA (1 mole).
Above 0 T the free-ion approximation is used in the thermal model and curves produced from this calculation for a selection of fields are shown.

This data has been used in the modelling of CPA in the MSSL ESA ADR and has been shown to be a reliable approximation [152].

It follows from the theory described in 2.3 that the energy which a paramagnetic refrigerant can absorb will be a function of: the temperatures of the hot and cold sinks between which it operates; the available magnetising field; and the number of moles of the refrigerant. For a CPA pill under the conditions relevant to the mini-ADR described here (i.e. operating between 0.1 and 2 K, and with a maximum available field of 2 T) the maximum energy that can be absorbed is calculated from the data presented in Figure 6.5 as 283 mJ/mol. The cooling power then just depends on the number of moles of CPA and the length of time for which cooling must be provided. For example, a pill containing 0.02 moles of CPA can provide 10 μW of cooling for 54 s and this will scale linearly with the amount of CPA.

6.3.2 Conduction

The model includes heat loads due to conduction through the cold stage support structure and the heat switches. The conductivity of the support structure is modelled using Fourier's law of conduction:

$$\dot{Q}_{C_{Bath-D}} = \frac{A_{Supp}}{L_{Supp}} \int_{T_D}^{T_{Bath}} \kappa_{Supp}(T) dT, \tag{6.7}$$

where A_{Supp} and L_{Supp} are the total cross-sectional area and length of the support structure, respectively; κ_{Supp} is the thermal conductivity of the support structure material and is a function of temperature. The support is assumed to be manufactured from Vespel® SP-22 due to its very low thermal conductivity at the operating temperatures of the mini-ADR. Its thermal conductivity is calculated according to the following equation:

$$\kappa_{Supp}(T) = \alpha T^{(\beta+\gamma T^n)}, \tag{6.8}$$

where $\alpha = 1.44\times10^{-3}$ W/m K, $\beta = 2.11$, $\gamma =$ -0.521 K^{-n} and $n =$ -0.0163. The expression and parameter values come from a fit to data collected by Runyan & Jones [229] from 0.3–

4 K. Although this does not cover entire temperature range of interest, comparison with others' results [230] suggests it will overestimate the conductivity at temperatures < 0.3 K and is therefore conservative for the purposes of this model (see Figure 6.7). Equation (6.8) is integrated numerically in MATLAB to obtain the heat load conducted down the support structure.

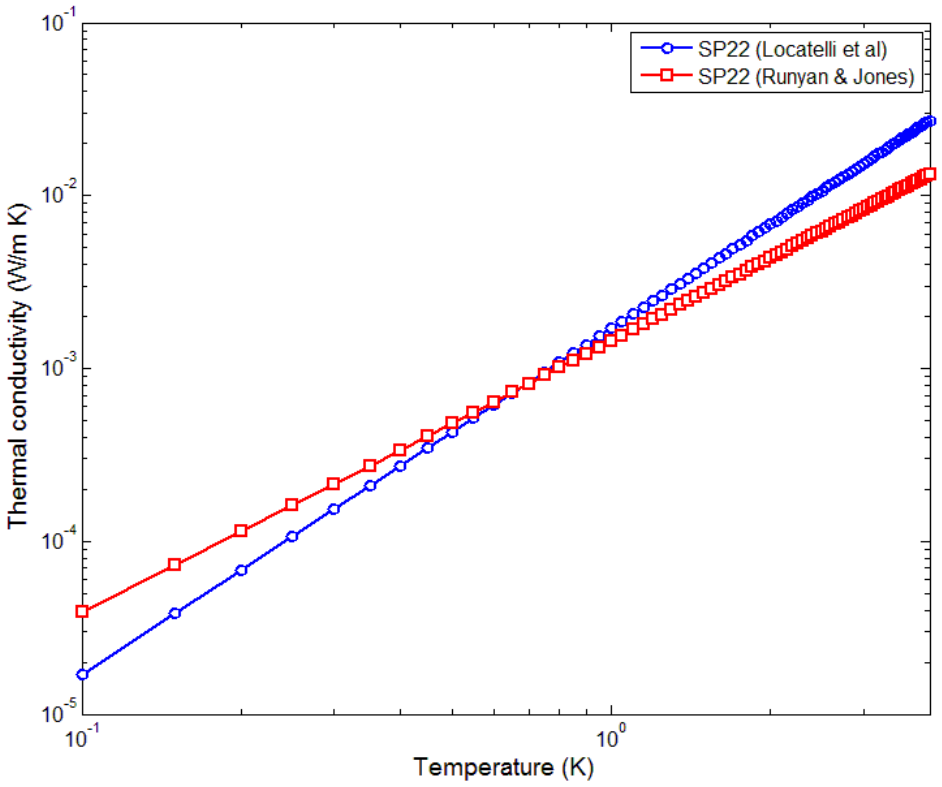

Figure 6.7: Thermal conductivity of Vespel® SP-22 as measured by different authors. The circles are a fit to data taken from 0.1–1 K by Locatelli *et al.* [230]; the squares are a fit to data taken from 0.3–4 K by Runyan & Jones [229].

The heat switches are modelled in a similar way, except that the thermal conductivity is also a function of magnetic field. The conductivity through heat switch HSA1 is written:

$$\dot{Q}_{C_{A-Bath}} = \frac{A_{HSA1}}{L_{HSA1}} \int_{T_{Bath}}^{T_A} \kappa_{HSA1}(T, B) dT \qquad (6.9)$$

and there are equivalent equations governing the conductivity in the other three heat switches. The thermal conductivity is calculated using the equation for tungsten derived and verified in Chapter 4:

$$\kappa(T,B) = b_0 T^2 + \frac{1}{\frac{a_1 + a_2 T^2}{T} + \frac{B^n}{a_3 T + a_4 T^4}}. \tag{6.10}$$

The following values are used for the constants:

Constant	Value
b_0	0.03
a_1	0.00025
a_2	0
a_3	1.1
a_4	0.006
n	1.8

Table 6.2: Values of constants used in the thermal conductivity equation for tungsten.

The phonon conductivity coefficient (b_0) and the magnetic field exponent (n) are those found from the measurements in Chapter 4 on the high-purity sample, C-3b. The other values are based on fits to measurements conducted at MSSL on similar samples over a range of temperatures. The zero-field conductivity was measured on a sample with similar RRR to C-3b and the results are shown in Figure 6.8. The values of a_1 and a_2 found from this fit are those given in Table 6.2. It can be seen from the plot that there are quite large error bars on the measurements and these are the result of the same problems encountered in measuring the zero-field conductivity in Chapters 4 and 5: with such high thermal conductivity, heat loads that do not raise the temperature of the entire sample only create small ΔTs and, with a fixed accuracy on the thermometer readings, the percentage uncertainty in measuring these is relatively large.

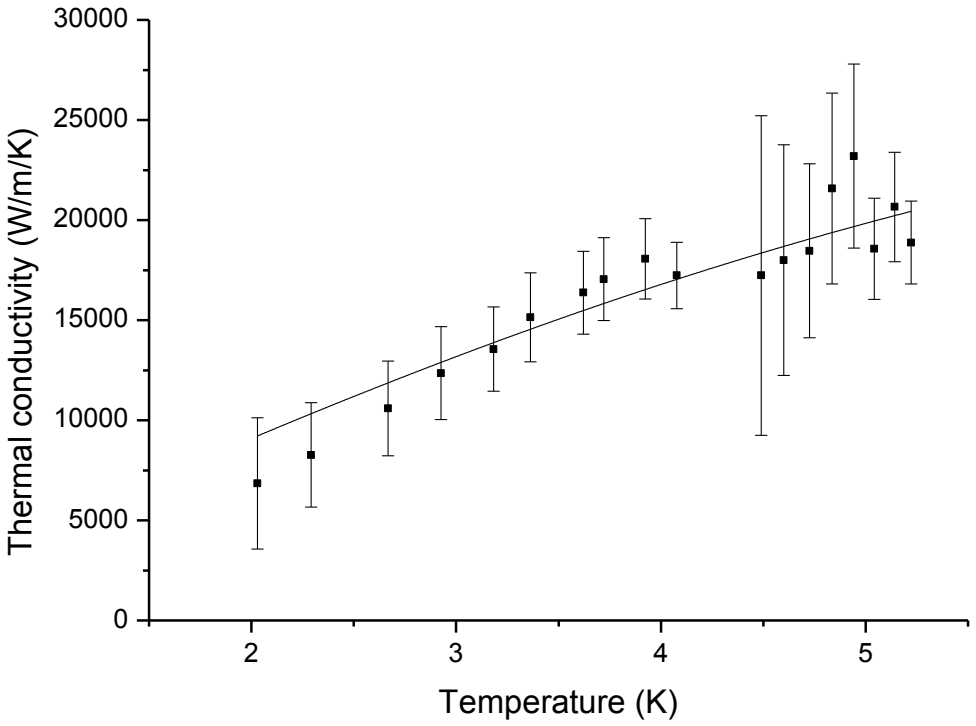

Figure 6.8: Thermal conductivity of a high purity tungsten sample in zero magnetic field between 2 and 5.5 K
(courtesy of Dr I. Hepburn).

The conductivity in a magnetic field at different temperatures has been measured on many samples at MSSL. The a_3 and a_4 values quoted above, were derived from a fit to data on a different sample to that used for a_1 and a_2, but still one with very similar purity to the high-purity samples measured in Chapters 4 and 5. The data and fit are shown in Figure 6.9 below.

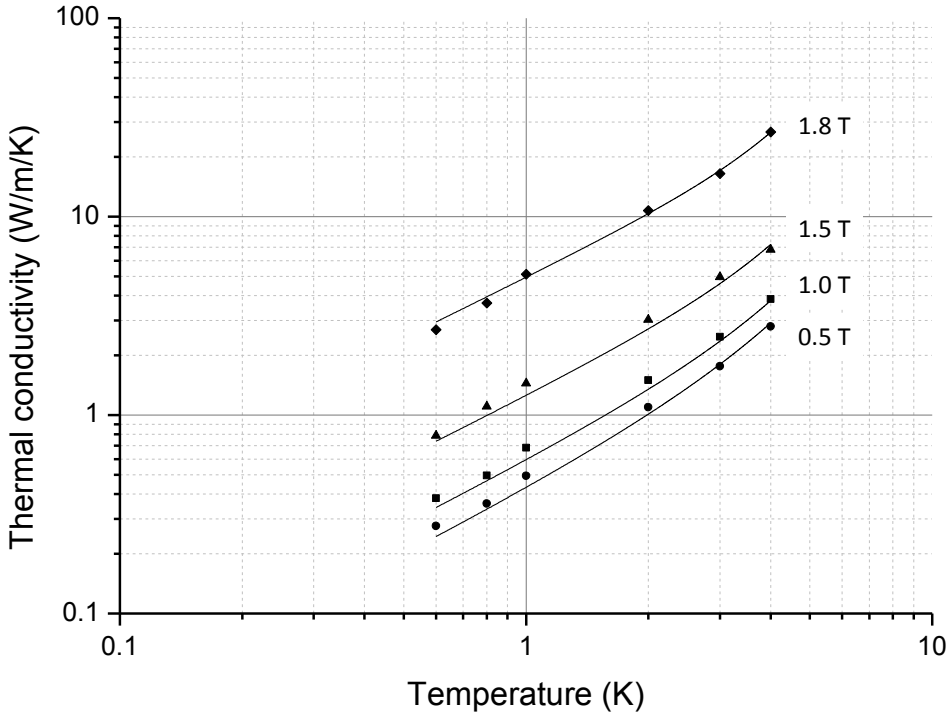

Figure 6.9: Thermal conductivity of a high purity tungsten sample measured at temperatures between 0.6 and 4 K in a selection of magnetic fields
(courtesy of Dr I. Hepburn).

As above, heat loads through the switches are determined by integrating equation (6.10) numerically in MATLAB.

6.3.3 Radiation

The cold stage (node T_D in Figure 6.2) and both pills (nodes T_A and T_B) are radiatively coupled to the bath. As noted above, it is assumed they are totally enclosed so that any radiation absorbed by these components has been emitted at the temperature of the bath. The heat loads resulting from this coupling are calculated from the Stefan–Boltzmann law. The application of this for the heat flow between the bath and the cold stage gives:

$$\dot{Q}_{R_{Bath-D}} = \frac{\sigma\left({T_{Bath}}^4 - {T_D}^4\right)}{R_{Rad-D}}, \tag{6.11}$$

where σ is the Stefan–Boltzmann constant. Equivalent equations are used for the radiative heat flow between the bath and pills A and B. The denominator is the thermal resistance associated with this heat flow. In black body radiation exchange the thermal resistance is

just the area of the first body and what proportion of the emitted radiation is absorbed by the second body (the view factor) – i.e.

$$R_{Rad\ 1-2} = \frac{1}{A_1 F_{1-2}}. \tag{6.12}$$

However, in grey body radiation exchange, the surface resistances must also be taken into account [46]. The surface resistances recognise the fact that the radiation leaving a surface is a combination of the emitted and reflected radiation. The "radiosity", $\dot{\mathrm{J}}$, is defined as the sum of these quantities:

$$\dot{\mathrm{J}} = \varepsilon\sigma T^4 + \rho\dot{\mathrm{G}}, \tag{6.13}$$

where ε is the emissivity, ρ is the reflectivity, $\dot{\mathrm{G}}$ is the irradiation and the radiosity is given per unit area. The net radiation flux leaving the surface – again, per unit area – is therefore given by $\dot{\mathrm{J}} - \dot{\mathrm{G}}$. Using equation (6.13) this can be expressed as:

$$\begin{aligned} \dot{\mathrm{J}} - \dot{\mathrm{G}} &= \dot{\mathrm{J}} - \frac{\dot{\mathrm{J}} - \varepsilon\sigma T^4}{\rho} \\ &= \frac{\dot{\mathrm{J}}(\rho - 1) + \varepsilon\sigma T^4}{\rho} \\ &= \frac{\varepsilon(\sigma T^4 - \dot{\mathrm{J}})}{\rho}, \end{aligned} \tag{6.14}$$

where use has been made of $\rho = 1 - \varepsilon$. This follows from the fact that the sum of a surface's absorptivity (α), transmission (τ) and reflectivity must be 1 – i.e.

$$\alpha + \tau + \rho = 1. \tag{6.15}$$

Then, using Kirchoff's law that the emissivity and absorptivity of a surface at a given temperature are equal ($\alpha = \varepsilon$) and the fact that for opaque surfaces there is no transmission of radiation ($\tau = 0$):

$$\varepsilon + \rho = 1 \Rightarrow \rho = 1 - \varepsilon. \tag{6.16}$$

Using (6.14), the net heat flow from an area A will be given by:

$$\frac{\varepsilon A(\sigma T^4 - \dot{\mathrm{J}})}{\rho} = \frac{\sigma T^4 - \dot{\mathrm{J}}}{\frac{\rho}{A\varepsilon}}. \tag{6.17}$$

This defines the surface resistance:

$$\frac{\rho}{A\varepsilon} = \frac{1 - \varepsilon}{A\varepsilon}. \tag{6.18}$$

These surface resistances must be added in series to the black body resistance and this is illustrated in Figure 6.10.

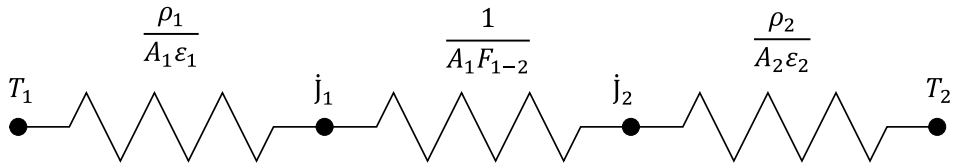

Figure 6.10: Resistance network for radiation exchange between two grey bodies.

Equation (6.19) shows how the total thermal resistance is calculated in the case of the heat flow between the cold stage (D) and the shield (S).

$$R_{Rad-D} = \frac{1 - \varepsilon_D}{A_D\varepsilon_D} + \frac{1}{A_D F_{D-S}} + \frac{1 - \varepsilon_S}{A_S\varepsilon_S}, \tag{6.19}$$

Similar equations to (6.19) are used for the radiation exchange between the bath and the pills. A full list of the relevant parameters is given in Table 6.3.

Label	Description	Value
ε_D	Emissivity of Detector stage	0.1
ε_S	Emissivity of Shield	0.1
ε_A	Emissivity of Pill A	0.1
ε_B	Emissivity of Pill B	0.1
ε_{Bath}	Emissivity of the Bath interface	0.1
A_D	Emitting area of Detector stage	4000 mm^2
A_S	Emitting area of Shield	30000 mm^2
A_A	Emitting area of Pill A	Calculated[a]
A_B	Emitting area of Pill B	Calculated[a]
A_{Bath}	Emitting are of the Bath interface	4000 mm^2
F_{D-S}	View factor from Detector plate to Shield	1
F_{A-Bath}	View factor from Pill A to Bath interface	1
F_{B-Bath}	View factor from Pill B to Bath interface	1

[a]The surface areas of the pills are calculated from the pill masses (see text)

Table 6.3: Parameters used in modelling radiation heat loads.

Emissivity values of 0.1 are used throughout; this is likely to be a conservative value for relatively clean copper surfaces. For simplicity it has been assumed that all view factors are equal to 1 – i.e. all the radiation leaving the emitting surface reaches the absorbing surface. This is likely to be fairly accurate for radiation exchange between the shield and the cold stage since the cold stage will be almost totally enclosed. It may not be such an accurate representation for radiation exchange between the bath and the pills, but using a value of 1 should give conservative answers. The emitting areas of the bath interface and the detector stage are based on assuming a surface of 80 mm by 50 mm. The emitting area of the shield is based on cylindrical shield of ~ 95 mm diameter and 100 mm high. The emitting area of the pill is calculated by assuming it will be cylindrical with a defined aspect ratio: the pill volume is computed from the mass of refrigerant used and its density; this is then converted to dimensions of a cylinder with a length/diameter ratio defined by the aspect ratio.

While a number of additional assumptions have been made in calculating the radiation loads, it should be noted that with the pills and detector stage not exposed to any surface at a higher temperature than the bath, these loads are several orders of magnitude lower than those due to conduction (see 6.5).

6.3.4 Boundary Resistance

As discussed in Chapter 3, the thermal boundary resistance can be significant for heat transfer at low temperatures, particularly < 1 K. It was noted in (3.9.4) that, by far the most significant boundary resistance in ADRs is the one occurring between the pill and thermal bus, since any other interfaces are generally metal-to-metal joints where electrons can carry heat across the boundary. Consequently, only the pill–thermal bus resistance is included in the TMM. It is modelled by creating a node at the pill end of each heat switch and applying equation (3.111) to the heat flow between this node and the pill node. Its application to the thermal boundary between the pill A and the heat switch connected to the detector stage is

$$\dot{Q}_{C_{A-D}} = \frac{\beta}{3} A_{TB} \left({T_A}^3 - {T_{HSA2-P}}^3 \right). \tag{6.20}$$

The thermal boundary area, A_{TB}, is calculated based on the pill dimensions. As described in 6.3.3, the mass of magnetic refrigerant is used together with a defined aspect ratio to determine the length and diameter of a cylindrical pill. To evaluate the area of the thermal boundary, it is then assumed that thermal contact will be made using an array of fine wires around which the pill is formed (see Chapter 2 and [145]). The diameter of the wires is an input to the model and they are assumed to run the full length of the pill. The number of wires that can be accommodated in the pill is calculated from its diameter; the algorithm used assumes that the wires are arranged in a series of concentric circles through the cross-section, with 1 mm between each circle and the wires spaced at intervals of 1 mm around the circumference of the circles (see Figure 6.11).

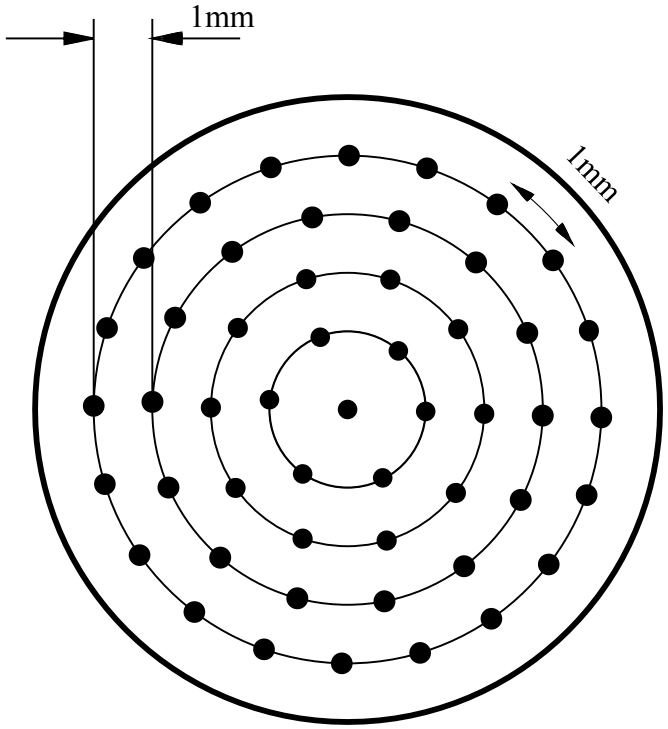

Figure 6.11: Circular array of wires for thermal bus through pill cross-section.

A β value of 4 W/m^{2}K^3 is used. This was found to model the boundary resistance of this type of copper–CPA interface most accurately in the MSSL ESA ADR [133].

The temperatures at nodes $T_{HSA1\text{-}P}$, $T_{HSA2\text{-}P}$, etc. used in equation (6.20) and the equivalent expressions for the other heat switches are unknowns to be found. Each unknown temperature appears in two equations: one for the heat flow through the heat switch and one for the heat flow through the thermal boundary. For case of node $T_{HSA1\text{-}P}$, these are:

$$\dot{Q}_{C_{A-Bath}} = \frac{A_{HSA1}}{L_{HSA1}} \int_{T_{Bath}}^{T_{HSA1-P}} \kappa_{HSA1} dT, \tag{6.21}$$

$$\dot{Q}_{C_{A-Bath}} = \frac{\beta}{3} A_{TB} \left({T_A}^3 - {T_{HSA1-P}}^3 \right). \tag{6.22}$$

Since the unknown temperature appears in one of these equations as the limit of an integral which is solved numerically, there is no straightforward analytical solution. Instead, an iterative approach is taken whereby the temperature is adjusted until both equations give

equal heat flows (as must be the case for conservation of energy). In practice, the model stops iterating once the two heat flows are within 10^{-9} W. The algorithm uses an initial guess which is halfway between the boundary temperatures (i.e. T_A and T_{Bath} in the equations shown above) and then adjusts this towards one limit or the other depending on which equation calculates the greater heat flow.

6.4 Operating Sequence

The flow diagram for the thermal model program is shown in Figure 6.13 with the nodes and heat switch labels (which are of the form HSXX) illustrated by Figure 6.12. A graphical description of the steps is given in Figure 6.14. The model starts with neither pill magnetised and begins the sequence by magnetising Pill A. After magnetisation, it is allowed to equilibrate with the bath before the heat switch to the bath is opened and demagnetisation can begin. Once Pill A is providing cooling, the main cycle of the cooler starts, recycling one pill while the other is providing cooling.

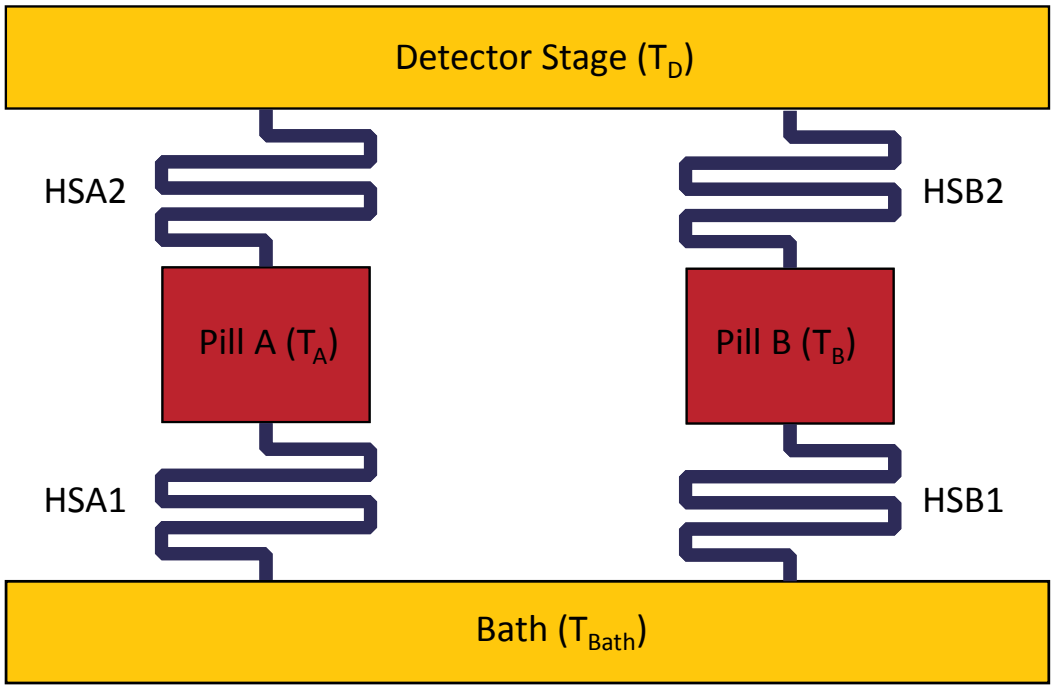

Figure 6.12: Schematic illustration of elements and their labelling in the mini-ADR TMM.

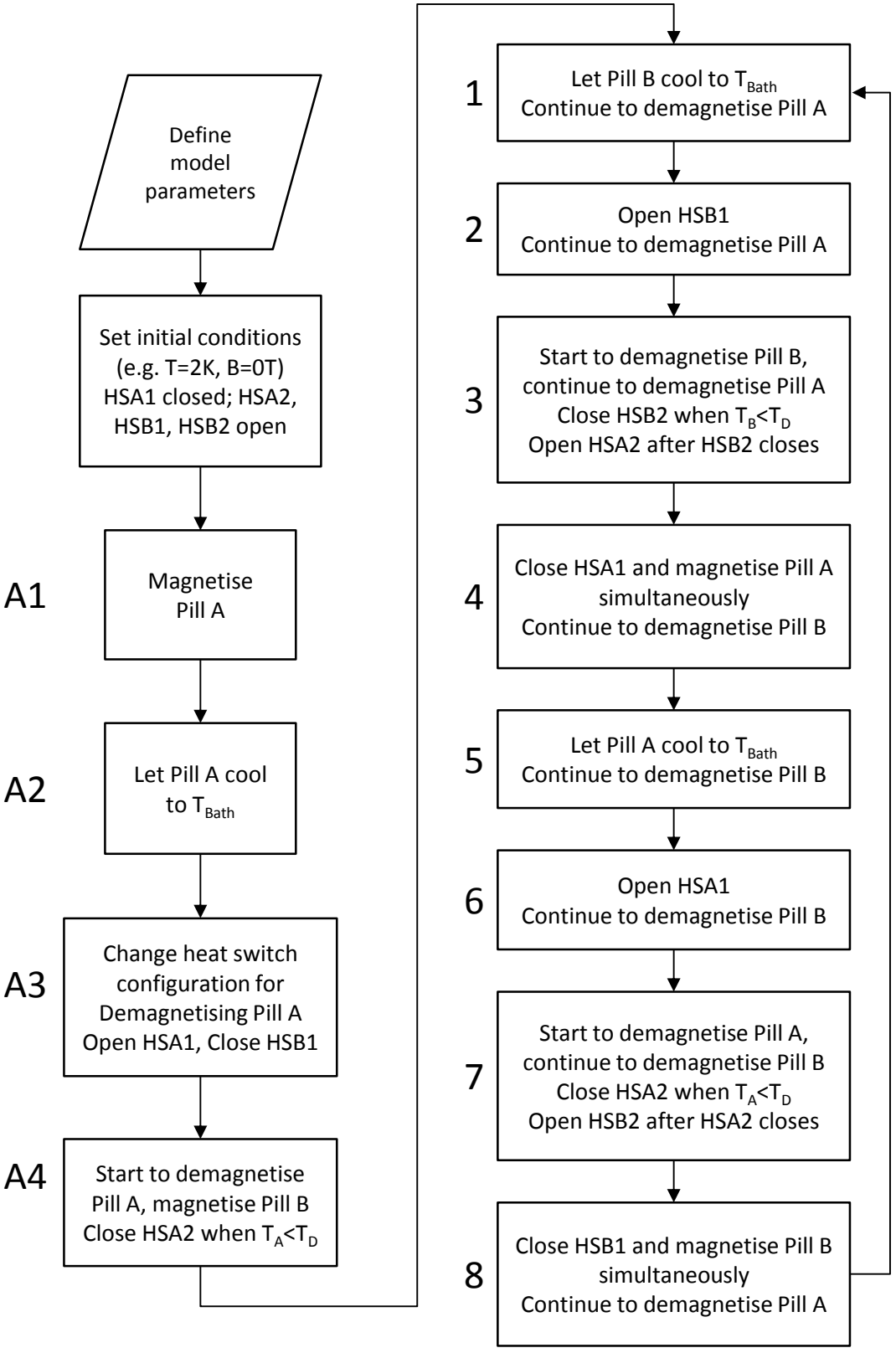

Figure 6.13: Flow diagram for the mini-ADR Thermal Model.

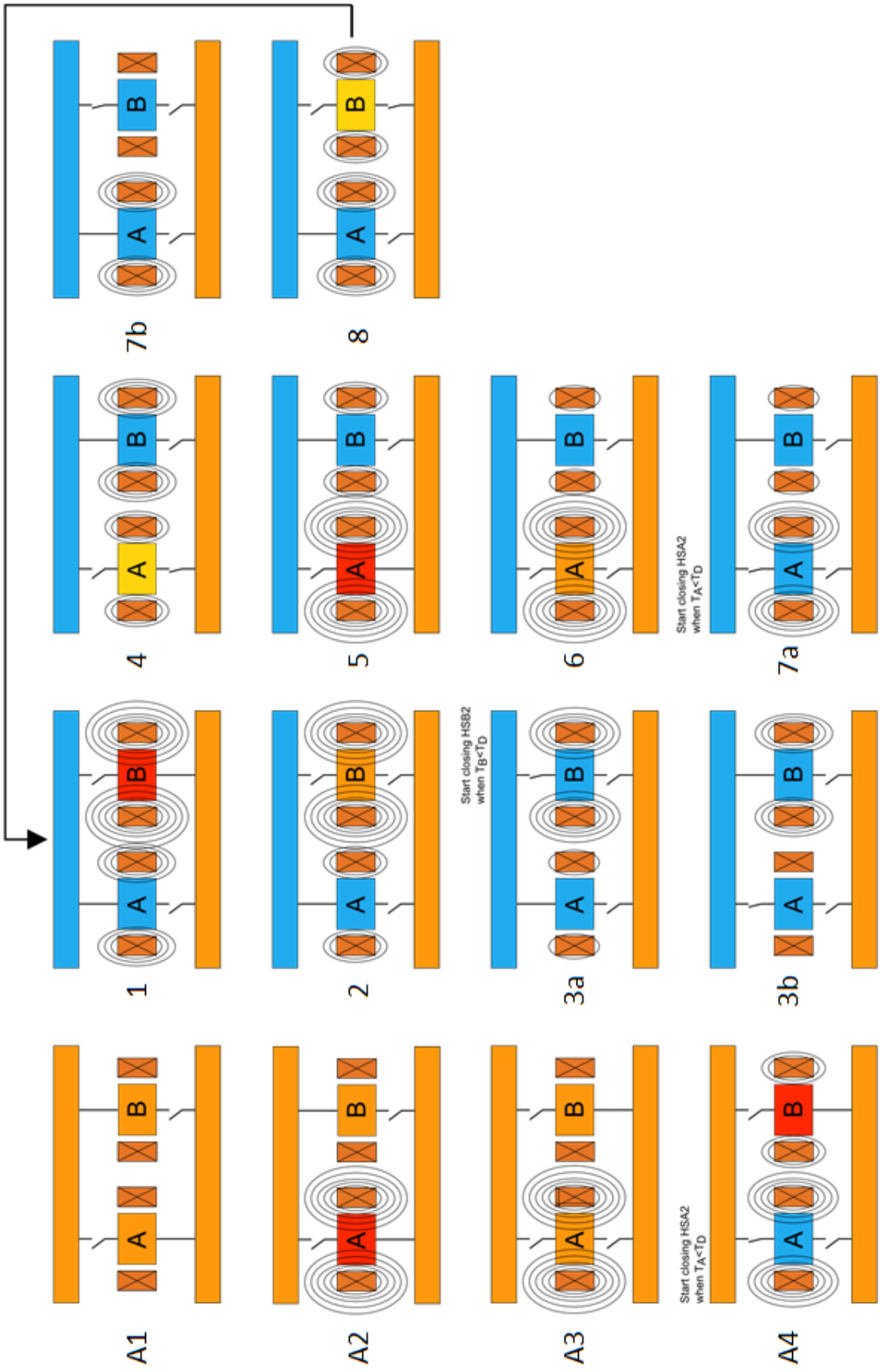

Figure 6.14: Illustration of cycle for mini-ADR Thermal Model.

The overall time to complete a magnetisation/demagnetisation cycle for each "leg" of the mini-ADR is driven by the achievable magnet ramp times. Based on results achieved with small superconducting magnets at MSSL [145], it has been assumed that it will be possible to ramp from 0 T to 2 T in approximately 30 seconds; this translates to a magnetisation rate of 0.07 T/s. This ramping time also applies to the magnets which operate the heat switches. As illustrated in Figure 6.13 and Figure 6.14, the following steps must be completed to recycle a pill:

i. The heat switch linking the pill to the cold stage is opened (~ 30 s);
ii. Once this heat switch is opened, magnetisation begins and the heat switch to the bath is simultaneously closed (~ 30 s);
iii. The heat of magnetisation is dumped to the bath (~ 10 s);
iv. The heat switch to bath is opened (~ 30 s);
v. Demagnetisation of the pill begins and the heat switch to the cold stage starts to close when $T_{pill} \leq T_D$ (~ 60 s).

This dictates that the active pill must be capable of at least a 160 second hold time to maintain constant temperature. The time of stage iii could potentially be reduced by a heat switch with better "on" conduction, but it is clear that the most effective way to reduce the overall hold time requirement would be to reduce the magnet ramp times[30]. This is discussed further in Chapter 7.

6.5 Modelling Results

Using the TMM it has been possible to arrive at preliminary sizes for a miniaturised ADR. These are summarised in Table 6.4 below. A major limitation was the thermal boundary area between the pill and the heat switch. This had to be large enough to ensure that the

[30] Recent results at MSSL [231] have shown that steps i and ii, and iv and v can be overlapped to achieve further reductions in recycle time. This is made possible because most of the reduction in conductivity of the MR heat switch occurs between 0 and 0.5 T (see Figure 4.7, for example) and magnetisation or demagnetisation of the pill can begin as soon as this field has been exceeded in the heat switch.

temperature difference across the boundary would not result in such a low pill temperature that no spare entropy capacity was left for cooling (see Figure 6.15). The thermal boundary area then constrained the minimum pill size because the pill had to be large enough to contain a sufficient number of wires. The heat switch geometry was subsequently optimised (i.e. the length for a 1 mm × 1 mm cross-section was minimised) so that the pill could just absorb the parasitic heat load. Other than the heat switch, the main source of parasitic loads is the support structure; a cross-sectional area of 5 mm^2 and a length of 100 mm were assumed for this. This cross-sectional area would be quite challenging to achieve in practice and suggests the use of thin rods. However, it is worth noting that if the mini-ADRs were used in groups to provide larger cooling powers, the load from conduction through the support structure could be shared between several "ADR units."

Parameter	Value
Heat Switch cross-sectional area	1 mm^2
Heat Switch length	200 mm
Moles of CPA	0.014
Pill aspect ratio (length/diameter)	1.5
Pill length	22.2 mm
Pill diameter	15.8 mm
Support Structure cross-sectional area	5 mm^2
Support Structure length	100 mm
Thermal bus wire diameter	0.4 mm

Table 6.4: Summary of mini-ADR design parameters.

The pill size and wire diameter in Table 6.4 equate to a contact area between the thermal bus and the pill of 4800 mm^2. The predicted performance of an ADR with these parameters is summarised in the figures below.

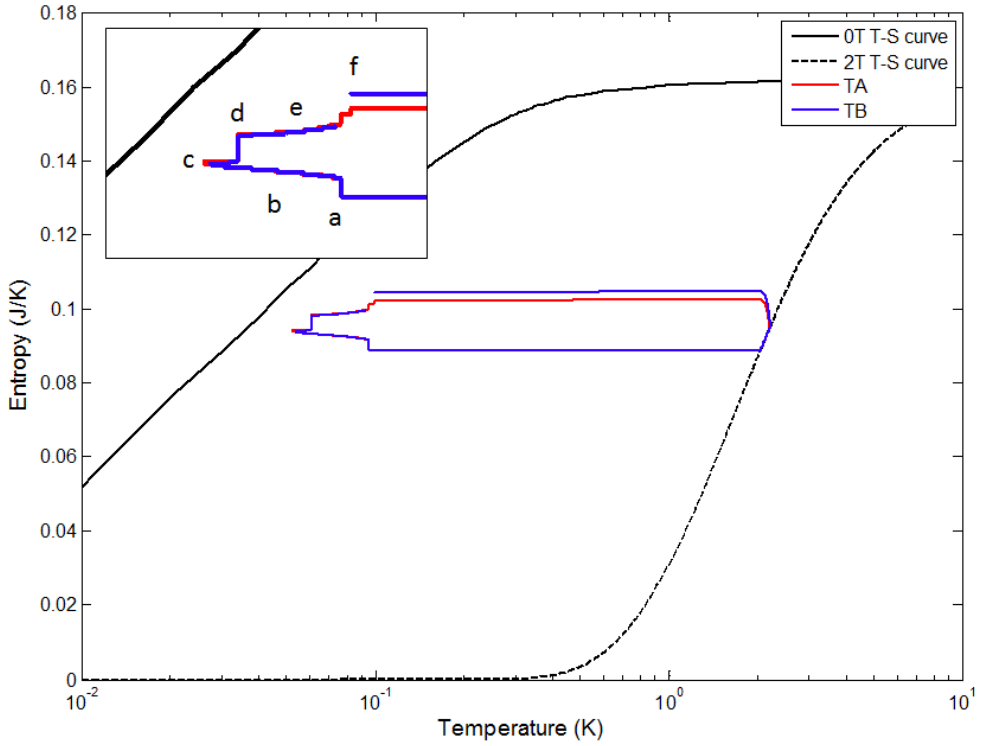

Figure 6.15: Temperature-entropy plot for the two pills (the second cycle is shown for each). Inset: detail of the stages during each pill's hold time. a – holding at cold stage temperature, b – further demagnetisation to balance additional heat load from magnetisation of the recycling pill, c – overshoot corrected by temperature control algorithm, d – holding whilst recycling pill is magnetised, e – re-magnetisation to maintain cold stage temperature as recycling pill cools to the bath temperature, f – holding during switchover to recycled pill.

Figure 6.15 shows the temperature-entropy curves of the two pills once instabilities caused by the initial cool-down have subsided. These curves (along with Figure 6.17 and Figure 6.18) illustrate the temperature control algorithm implemented in the model: the "inactive" pill is recycled and cooled to the same temperature as the "active" pill; the heat switch states are then changed to transfer cooling to the freshly recycled pill which becomes the active one; as the newly inactive pill is recycled it puts an increased heat load on the cold stage and this causes the active pill to be demagnetised at an increased rate to take up the additional heat load. After recycling of the inactive pill is complete, the field in the active pill is reduced to keep the cold stage temperature constant. A full PID control loop would be required for the real cooler, but implementing this in the model would cause excessive computational overheads.

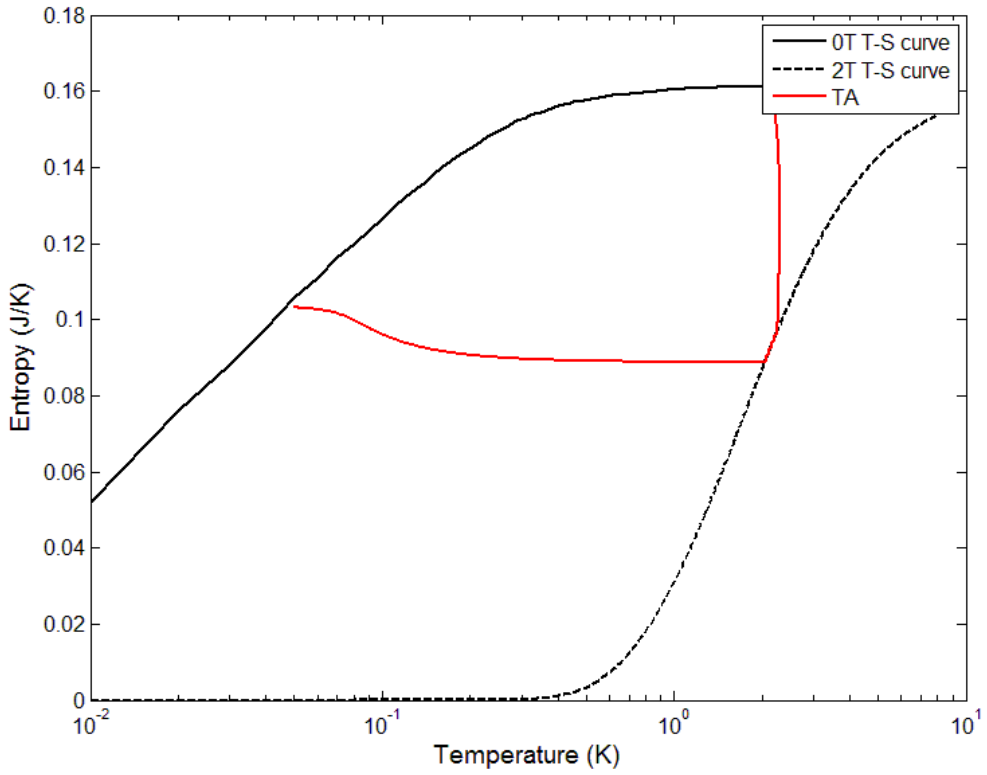

Figure 6.16: Temperature-entropy plot for Pill A in its first cycle.

The initial demagnetisation curve for Pill A is shown in Figure 6.16 to illustrate the difference with the first cycle. During this period, Pill A must extract the heat capacity of the detector stage. It is not able to achieve this and have enough entropy left over to hold at a stable temperature in a single demagnetisation (as confirmed by Figure 6.16). As it reaches a temperature sufficiently far below the starting temperature of the detector stage it begins to absorb heat across the thermal boundary and this causes its entropy to rapidly increase. Before it can hold the detector stage at a stable temperature, it reaches the zero-field line.

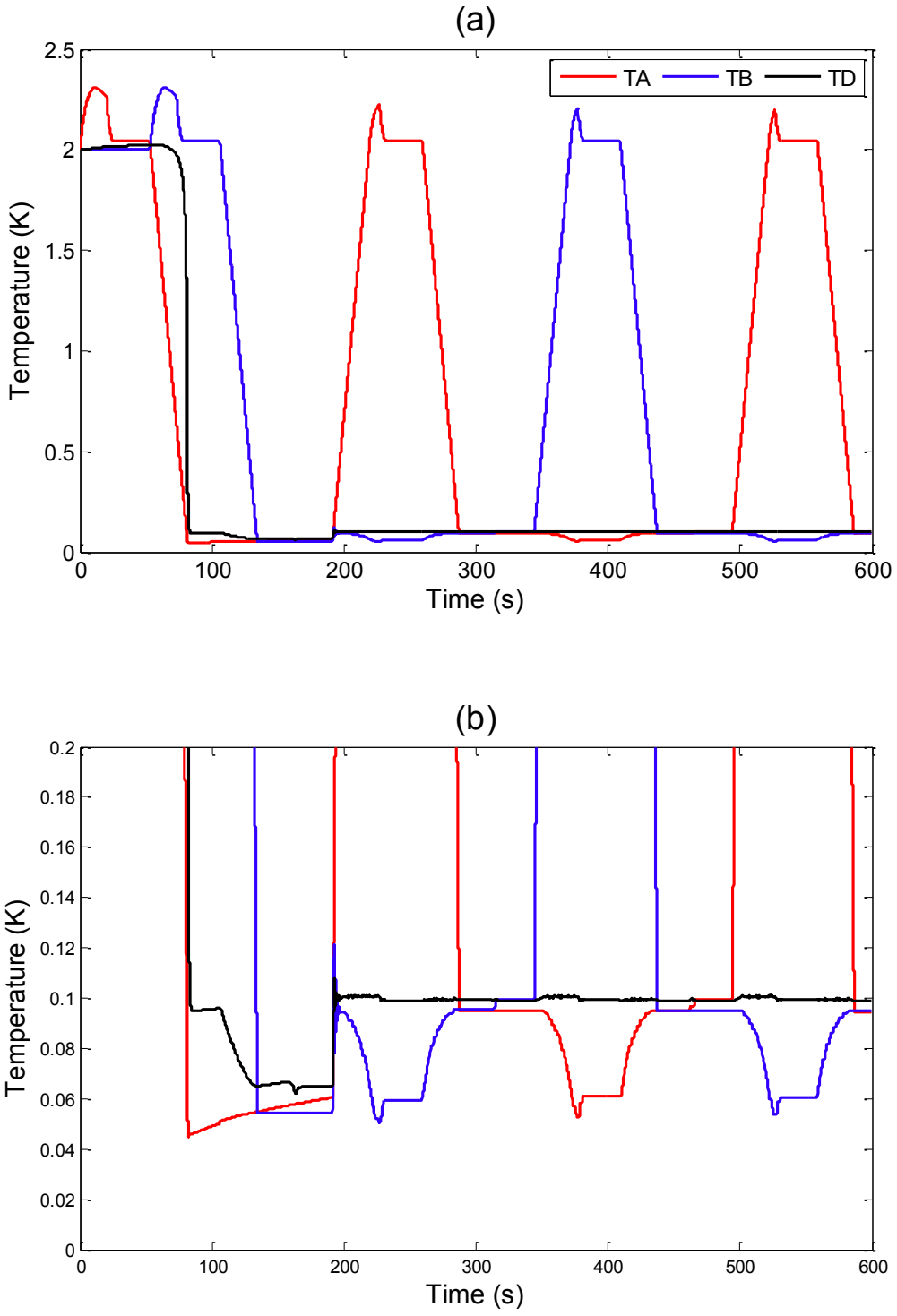

Figure 6.17: (a) Predicted pill and cold stage temperatures over first four cycles. (b) Detail of adjustments in pill temperature to maintain cold stage temperature during recycling of the "inactive" pill.

Figure 6.17(a) shows the temperature variations of the pills and detector stage over the first few cycles. After some initial instability – caused by the fact that Pill A reaches zero field before Pill B is ready to cool in the first cycle – the cold stage temperature is maintained consistently at 100 mK. Some minor fluctuations (of the order of mK) are evident on the detector stage temperature in Figure 6.17(b), but it is believed that these could be reduced still further if full PID control was implemented.

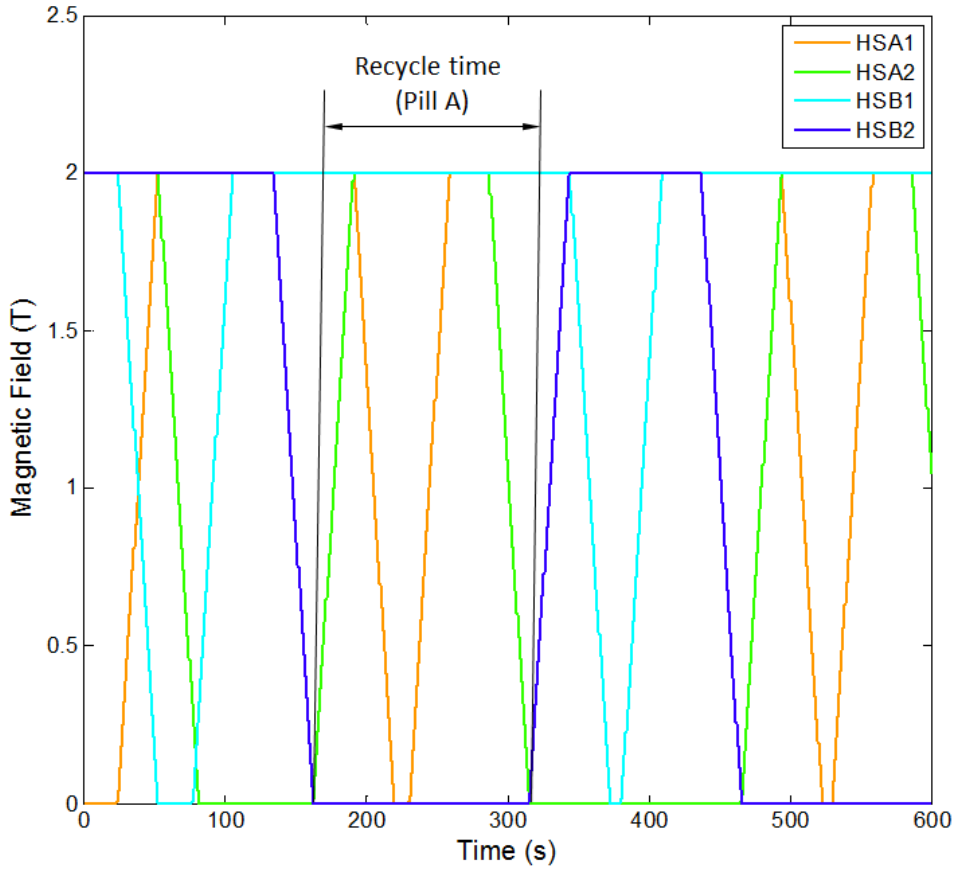

Figure 6.18: Heat switch fields over the first four cycles
(a total recycle time for Pill A is indicated).

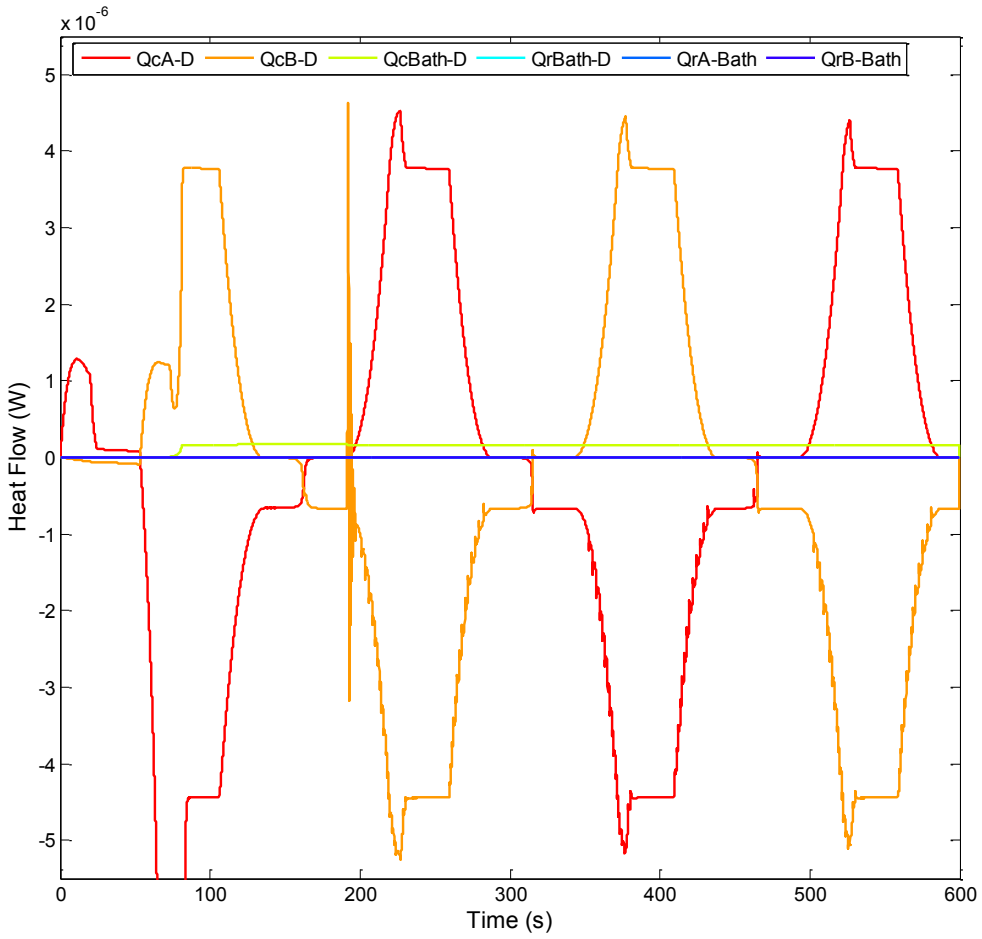

Figure 6.19: Heat loads on the cold stage during the first four cycles.
The first part of the line labels refer to the type of load – Qc = conduction, Qr = radiation; the second part refers to the nodes between which the heat flow occurs.

Figure 6.18 illustrates the opening and closing of the heat switches which facilitates the operating sequence described in 6.4. The recycle time for Pill A is indicated and matches the approximate timings given in 6.4. As noted above, there may be scope for reducing this recycle time, either from reducing the magnet ramp rates or overlapping the switching operations.

Figure 6.19 shows the heat loads on the cold stage. Lines with labels starting "Qc" are conduction loads and those with labels starting "Qr" are radiation loads. The remainder of the label indicates the nodes between which the heat flow is taking place. The radiation loads are more than an order of magnitude smaller than conduction loads and – with the geometry used (see Table 6.4) – the load from the open heat switch (~ 4 μW) is an order of

magnitude greater than that due to the support structure (< 0.5 μW). The large heat flow between the detector stage and Pill A in the first cycle results from the heat capacity of the detector stage as it is initially cooled from 2 K to 100 mK. The anomalous spike in heat flow between the detector stage and Pill B in the second cycle is caused by the temperature control algorithm: upon demagnetisation, Pill B is cooled so it matches the temperature of Pill A, which ensures a smooth switchover between the pills; however, on the first cycle Pill A is demagnetised to a much lower temperature to achieve the initial cool-down and the algorithm is then forced to rapidly adjusts the field on Pill B after switchover to maintain a constant detector stage temperature. Although the algorithm might potentially be refined, it was considered unnecessary as this spike and the associated instability only occur in the first cycles.

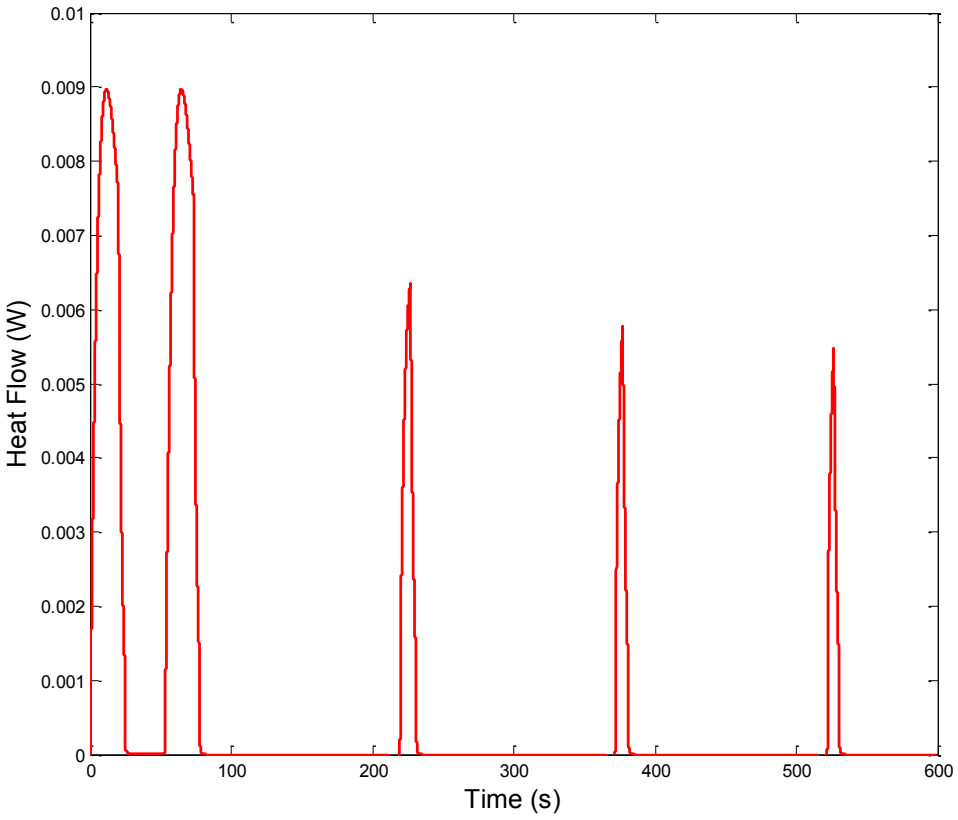

Figure 6.20: Heat loads from mini-ADR on to the pre-cooling bath

The total heat load on the pre-cooling bath from the mini-ADR is shown in Figure 6.20. This is important from a system perspective and will dictate the size and type of pre-cooler that would be used in a full cryogenic chain. As illustrated by the figure, the loads are only high when either side of the ADR is recycling. They peak at 9 mW during the initial cycles with the maximum load reducing to below 6 mW for latter ones. While a fluctuating load such as this is not particularly desirable, the magnitudes are not excessive and are well within those typically specified for next generation Joule-Thomson coolers operating at 2 K [52].

6.6 Heat Switch Miniaturisation

As the baseline results show, the dominant heat load on the active pill is from conduction through the tungsten heat switch linking the pill to the bath in its "off" state. One way to further reduce this – and therefore permit further miniaturisation – is to reduce the cross-sectional dimensions of the tungsten. This will clearly reduce the heat load in the "off" state, but will also decrease the "on" conductivity due to the combined effects of reduced area and increased surface scattering. Moreover, because of the Static Skin Effect (see Chapter 3), the reduction in "off" state conductivity will mainly come from decreasing the cross-sectional dimension parallel to the field. Methods of quantifying these changes are discussed below.

6.6.1 The Effect of Size Reduction on the Zero-Field Conductivity

The zero-field conductivity can be de-rated using equation (3.97) from Chapter 3:

$$\kappa = \frac{\kappa_0}{\left(1 + \frac{8}{3\pi}\left(\frac{\Lambda}{d}\right)\right)}, \tag{6.23}$$

where κ is the de-rated thermal conductivity, κ_0 is the thermal conductivity in zero magnetic field, Λ is the electron mean free path and d is the sample thickness. In order to use this equation it must be assumed that it is valid to replace the electrical conductivities with their

thermal counterparts. This may not be unreasonable for the case of diffuse scattering since any collision completely randomises the electron's momentum. It is not so likely to be acceptable in other cases because an electron reflected from the surface, while retaining its momentum in the direction of the current, may have lost some of its energy.

Using the value for the mean free path calculated in Chapter 4 for the sample C-3b (1.8 mm), the reduction in κ can be calculated for various values of d. The result of this calculation is plotted in Figure 6.21. Since the cross-section dimensions of sample C-3b are already smaller than its mean free path, the κ_0 value had to be calculated from the measured zero-field conductivity and the sample width; this led to a value of $\kappa_0 \approx 44500$ W/m K which was used in plotting Figure 6.21.

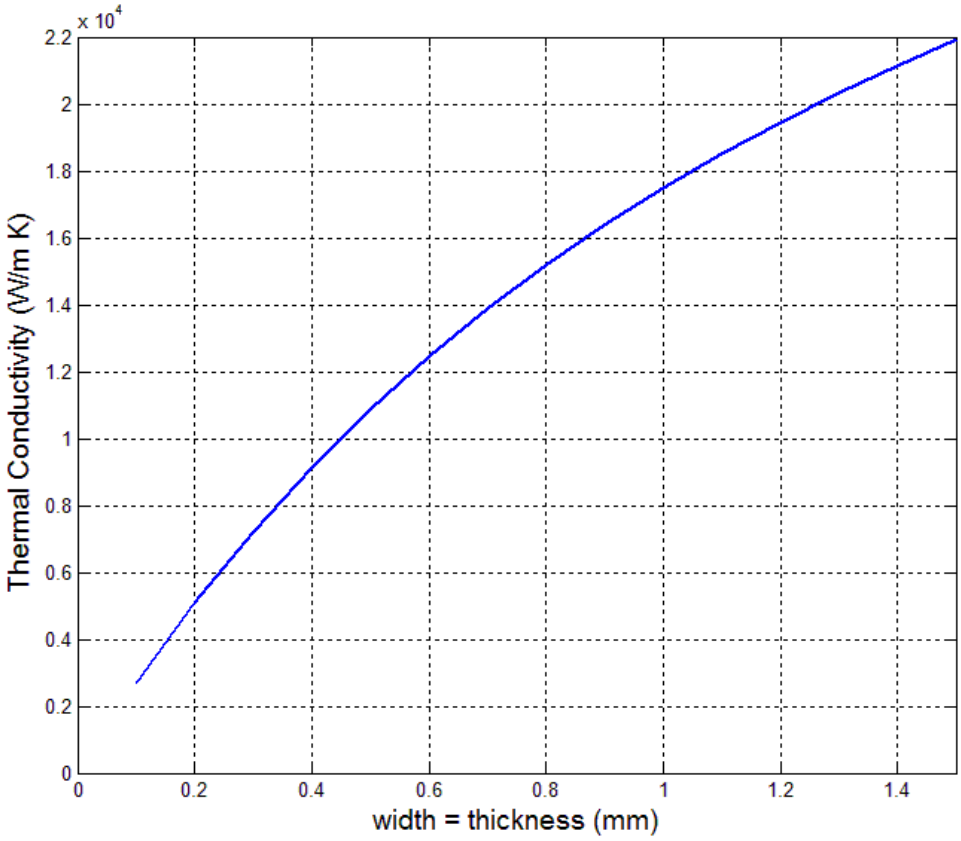

Figure 6.21: Predicted reduction in "on" conductivity with reduction in sample thickness (assumes a square cross-section of width = thickness).

The plot indicates a general trend of an increasingly rapid drop-off in thermal conductivity as the sample's cross-sectional dimensions decrease. Conductivities have been calculated

for a width (= thickness) of 1.5 mm (i.e. the width of sample C-3b) down to 0.1 mm. At a width of 0.5 mm the conductivity has approximately halved, although it remains in excess of 2000 W/m K even at 0.1 mm. Given the complications of calculating the effects of surface scattering described in Chapter 3 it is probably prudent to only consider these values as indicative.

6.6.2 The Effect of Size Reduction on the High-Field Conductivity

It was described in Chapter 3 that, under Static Skin Effect conditions, the majority of the current flows in a layer next to the surface which is parallel to magnetic field (see Figure 6.22). The layer's thickness is approximately equal to the Larmor radius. Volkenshtein *et al.* [215] show that a consequence of this is that changing the cross-section dimension that is perpendicular to the magnetic field barely affects the overall resistance of the sample at all. It is therefore of interest to estimate the extent to which this effect takes place in the tungsten samples investigated in this thesis.

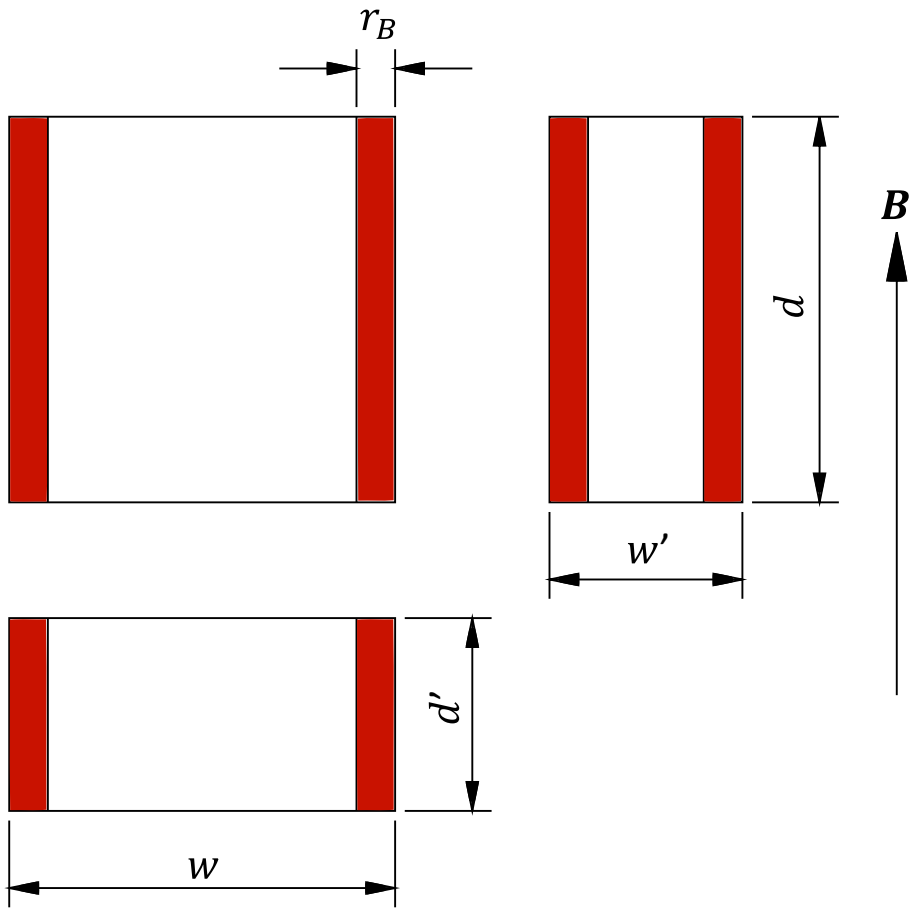

Figure 6.22: Different regions of current flow under the Static Skin Effect for different cross-sections. The direction of the magnetic field is indicated by the arrow on the right. The majority of the current flows in a layer of thickness r_B (highlighted) next to surfaces parallel to the magnetic field.

Assuming the boundary between bulk and surface currents to be sharp, one can model resistance in a magnetic field for a sample with cross-section dimensions $w \times d$ and length L using [215]:

$$\frac{1}{R} = \sigma_{xx}^{surf} \frac{2r_B d}{L} + \sigma_{xx}^{bulk} \frac{(w - 2r_B)d}{L}, \tag{6.24}$$

where σ_{xx}^{bulk} is the bulk electrical conductivity in a magnetic field. The surface conductivity (σ_{xx}^{surf}) can be estimated from [193]:

$$\sigma_{xx}^{surf} = \sigma_0 \left(\frac{r_B/\Lambda}{1 - p + r_B/\Lambda} \right), \tag{6.25}$$

where σ_0 is the conductivity in the absence of a magnetic field, r_B is the Larmor radius, Λ is the mean free path and p is the proportion of electrons that are specularly reflected at the surface.

If it is assumed that these relations hold equally well for thermal conductivity, equation (6.24) can be expressed as:

$$\kappa_{xx}\frac{A}{L} = \kappa_{xx}^{surf}\frac{2r_B d}{L} + \kappa_{xx}^{bulk}\frac{(w-2r_B)d}{L} \tag{6.26}$$

and the surface conductivity in the tungsten at 2 T can be estimated using:

$$\kappa_{xx}^{surf} = \kappa_0\left(\frac{r_B/\Lambda}{1+r_B/\Lambda}\right), \tag{6.27}$$

where $p = 0$ has been assumed (i.e. no specular reflection of electrons at the surface). Using the previously calculated Larmor radius, mean free path and the measured zero-field conductivity of sample C-3b (see Chapter 4), the surface contribution to the thermal conductivity is found to be $\kappa_{xx}^{surf} \approx 17$ W/m K.

Using the measured conductivity at 2 T of the same sample (3.6 W/m K - see Chapter 4), the bulk conductivity can then be estimated by rearranging equation (6.26):

$$\kappa_{xx}^{bulk} = \frac{w\kappa_{xx} - 2r_B\kappa_{xx}^{surf}}{w-2r_B}. \tag{6.28}$$

If the width of sample C-3b (1.5 mm) is taken with the values above, $\kappa_{xx}^{bulk} \approx 3.6$ W/m K. This suggests the surface conductivity is nearly five times greater than the bulk conductivity. These results are used to plot the effect of reducing both w and d on the switch conductivity in Figure 6.23[31]. The plot illustrates that reducing the width will cause a small increase in

[31] Note that it is the thermal conductivity which is plotted, not the thermal conductance, which would obviously decrease with decreasing area. The dimensionally independent parameter is the relevant one because the area of the switch cancels in calculating the switching ratio – i.e. one could easily reduce the "off" conductance by reducing the area, but it would result in a proportional reduction in the "on" conductance and leave the switching ratio unaffected.

overall conductivity as the surface conductivity becomes a bigger proportion of the total, whereas reducing the thickness has virtually no effect on the overall conductivity. Even in the former case, however, the change is relatively small (< 10% increase from 1 mm width to 0.1 mm width) and this can be attributed to the small region of the sample affected (Larmor radius ~ 1.4 μm). The combined effect of reducing both sample width and thickness together is shown in Figure 6.24.

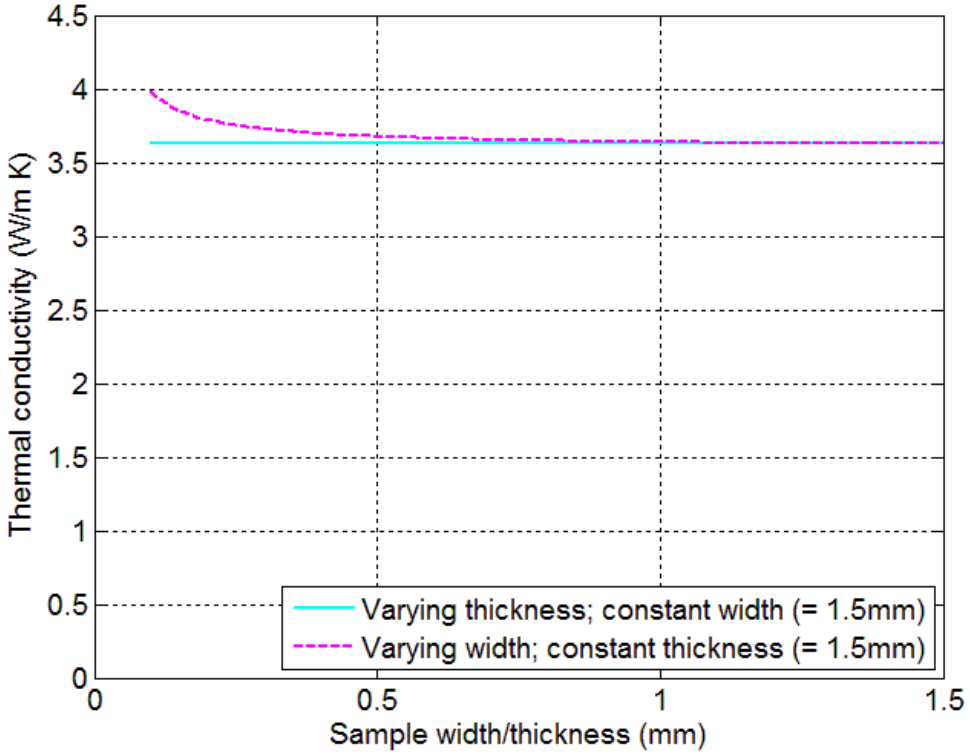

Figure 6.23: Predicted change in "off" conductivity for variation of sample width/thickness.

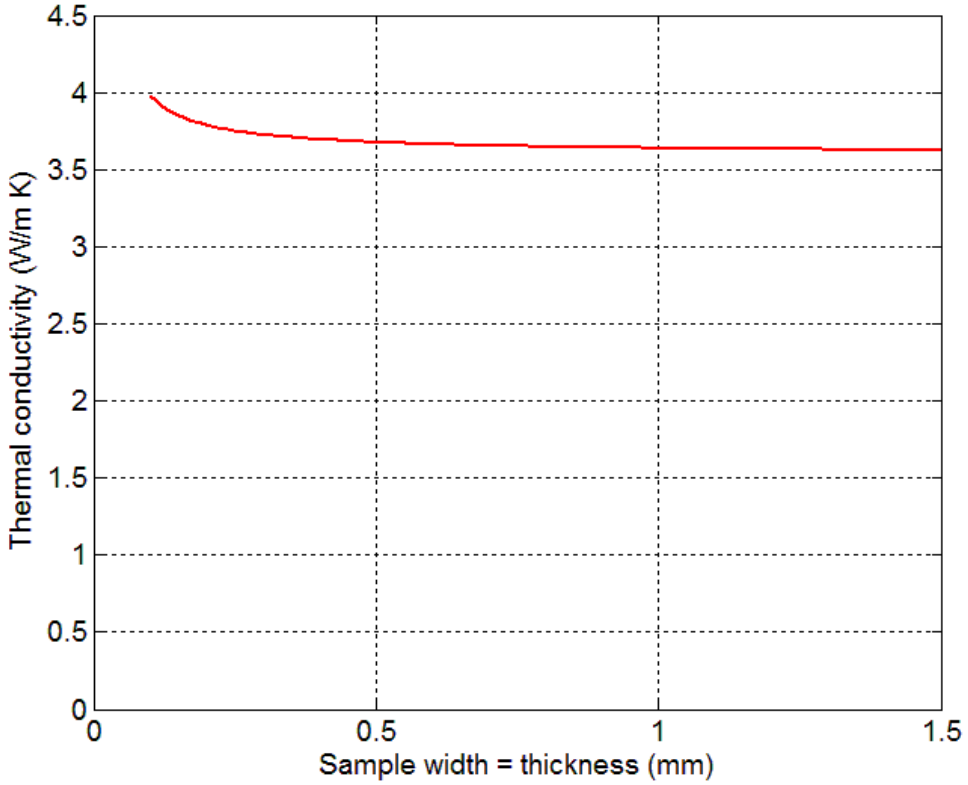

Figure 6.24: Predicted change in "off" conductivity for variation of width and thickness together (square cross-section assumed).

It is worth noting that differences of the order of 1000 were observed in the surface and bulk electrical conductivities by Volkenshtein *et al.* [215]. This is considerably larger than the factor of five calculated above and suggests that it would be worthwhile to confirm the thermal conductivity estimates by experiment. This could be done by making measurements on samples with different cross-sections, but with equal purities and surface finishes; it is discussed further in Chapter 7.

The above analysis indicates that, should it be necessary to reduce the overall heat load coming down a tungsten MR heat switch in its "off" condition, it would be more effective to reduce the cross-section dimension parallel to the magnetic field, as opposed to the one perpendicular to it. However, the quantitative estimation used to plot Figure 6.23 and Figure 6.24 suggests that the benefit of doing this over reducing the dimension perpendicular to the field will be relatively small (~ 10%).

6.6.3 Net Effect on Switching Ratio

The calculations and figures in the preceding section show that in reducing the cross-section to reduce the "off" conductivity of the switch, it is more effective to reduce the thickness (i.e. the dimensions parallel to the magnetic field) rather than the width. However, any reduction in cross-section will also reduce the "on" conductivity due to surface scattering, as shown in 6.6.1. The combination of these two effects on the switching ratio is plotted in Figure 6.25.

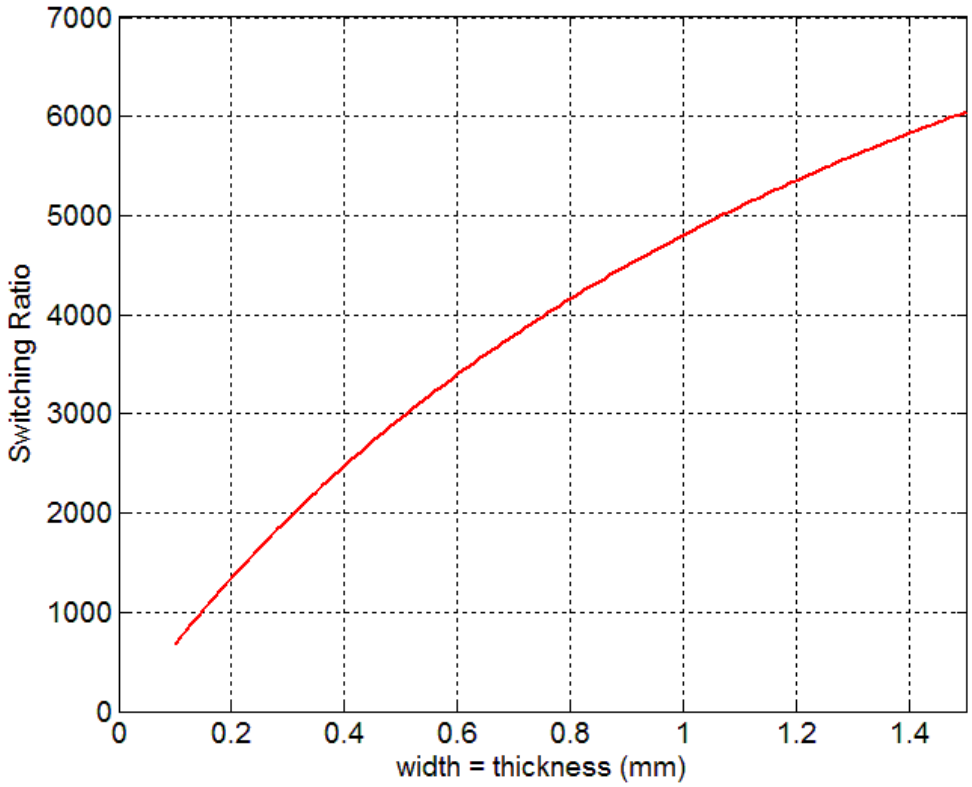

Figure 6.25: Effect on a tungsten MR heat switch's switching ratio of reducing the cross-section. The width and thickness are assumed equal.

As an example of the relative magnitudes of the effects, a reduction in sample width and thickness from 1 mm × 1 mm to 0.3 mm × 0.3 mm will reduce the "on" conductivity by ~ 59% (assuming diffuse scattering), while the 'off' conductivity (assuming a magnetic field

of 2 T) will increase by ~ 2%[32]. This translates to an overall reduction in switching ratio from ~ 4800 to ~ 2000. Clearly, then, reducing the switch cross-section to reduce the parasitic load in the "off" state will compromise the switching ratio and overall performance of the ADR.

6.7 Tungsten Thermal Bus

One way in which the overall mini-ADR design could be simplified (and thus further miniaturised) would be to use a tungsten thermal bus so that the paramagnetic refrigerant could be interfaced directly to the heat switch. A modified TMM has been produced to model this.

An additional effect that has to be accounted for when modelling the tungsten thermal bus is that it will be influenced by the magnetic field on the pill and magnetoresistive effects will limit its conductivity. This is modelled using the theory and data from Chapter 5 for the thermal conductivity of tungsten in a magnetic field that is aligned to the direction of heat flow. This resistance is then added in series to the heat switch resistance to create a combined thermal resistance. The resulting equation is shown below (for HSA2).

$$\dot{Q}_{C_{A-D}} = \int_{T_D}^{T_{HSA2-P}} \left\{ \frac{1}{\frac{L_{HSA2}}{\kappa_{HSA2} A_{HSA2}} + \frac{L_{BUS-A2}}{\kappa_{BUS-A2} A_{BUS-A2}}} \right\} dT \qquad (6.29)$$

The thermal conductivity of the bus (e.g. κ_{BUS-A2}) is found using the equation developed in Chapter 5:

$$\kappa_{BUS}(T,B) = b_0 T^2 + \frac{1}{\frac{a_1 + a_2 T^2}{T} + \frac{B^n}{a_{zz} T}}. \qquad (6.30)$$

Comparison with equation (6.10) shows that the a_4 term has been neglected (since it is negligible anyway) and the a_3 term has been replaced by the appropriate constant for the

[32] Note this increase could be lessened if the cross-section dimension parallel to the field is kept constant and only the other dimension is changed (see Figure 6.23).

longitudinal magnetoresistance, labelled a_{zz}. Based on the measurements described in Chapter 5 at 5.5 K, this has been estimated as $a_{zz} = 90$ since $aT \approx 500$ (c.f. Table 5.4) and $500/5.5 \approx 90$. The magnetic field exponent is taken, again from the results in Chapter 5, as $n = 1.15$.

The schematic for the thermal model incorporating tungsten thermal buses is shown in Figure 6.26.

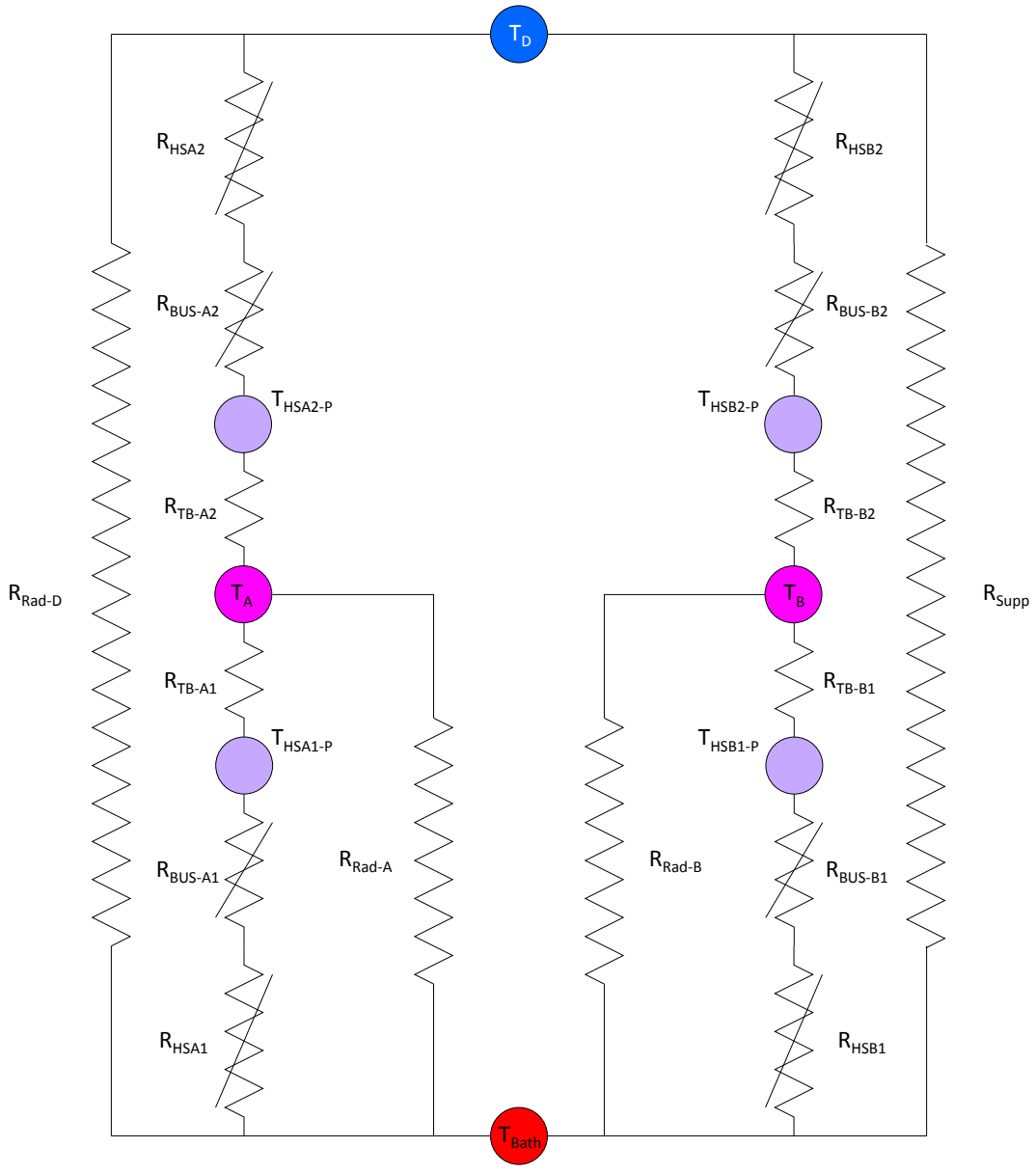

Figure 6.26: Thermal Model architecture incorporating a tungsten thermal bus.

To solve equation (6.30) it is necessary to know the magnetic field inside the pill (i.e. the field to which the tungsten thermal bus is exposed). The assumption that the pill's temperature changes linearly with field is not accurate enough in this case; instead, the value predicted by the linear assumption is adjusted iteratively by comparison with the free-ion approximation. If the entropy predicted by free-ion approximation for a given field is lower than the entropy calculated from the step method, the field is decreased and if the reverse is true, it is increased. The iteration stops when the two entropy values are within a specified tolerance[33]. Using the free-ion approximation for this correction leads to an overestimate of the field at low values of B and therefore causes an overestimation of any magnetoresistive effects in the thermal bus. The model is conservative in this respect. Once the field inside the pill has been calculated, equation (6.29) is integrated numerically in MATLAB.

The temperature of nodes $T_{HSA1\text{-}P}$, $T_{HSA2\text{-}P}$, etc. are again found iteratively by equating heat flows through the heat switch and across the thermal boundary between the switch and the pill (see 6.3.4). For this calculation it is assumed that the β value used in the baseline model will apply.

The parameters used were initially based on those listed in Table 6.4. However, several iterations were performed to find a combination that was consistent with a realistic mini-ADR concept. The conceptual design was developed in parallel and is illustrated in Figure 6.27 and Figure 6.28. It reflects the conceptual design described in 6.2, but incorporates a heat switch/thermal bus component that achieves the necessary A/L ratio for the heat switch and the required thermal boundary area for the thermal bus. The component is shown in detail in Figure 6.29. The heat switch section employs four layers to achieve a path length of 320 mm and has a cross-section of 1 mm × 1 mm; this is directly attached to a base and the thermal bus, which contains a total of 93 wires of 0.8 mm diameter and 15 mm in length.

[33] The tolerance is calculated based on the entropy and field limits for the particular model parameters. The expression used is $S_{tol} = (S_1 - S_2)/((B_f - B_i)/(dT_{mag}\Delta t))$ where S_1 is the zero field entropy at the bath temperature, S_2 is the entropy at full field and bath temperature, B_i and B_f are the initial and final fields, respectively, dT_{mag} is the magnetisation rate and Δt is the size of the time step.

The pattern of the wires is the same as described in 6.3.4, but a larger wire diameter was chosen to make manufacturing them from a single piece of tungsten more feasible. The design produces a thermal boundary contact area of 3500 mm^2. In comparison with the baseline design parameters, the heat switch is longer, but the thermal boundary area is reduced; this was found to be a good solution for minimising the overall ADR size because the extra layer in the heat switch only added just over 2 mm to the total height, while the smaller thermal boundary area allowed a reduction in length that was greater than this.

The design as shown could not be constructed from the spark erosion techniques used to make current heat switches. However, it has been designed to take advantage of the latest Additive Manufacturing (3D printing) techniques. Manufacturing aspects are discussed further in the following chapter.

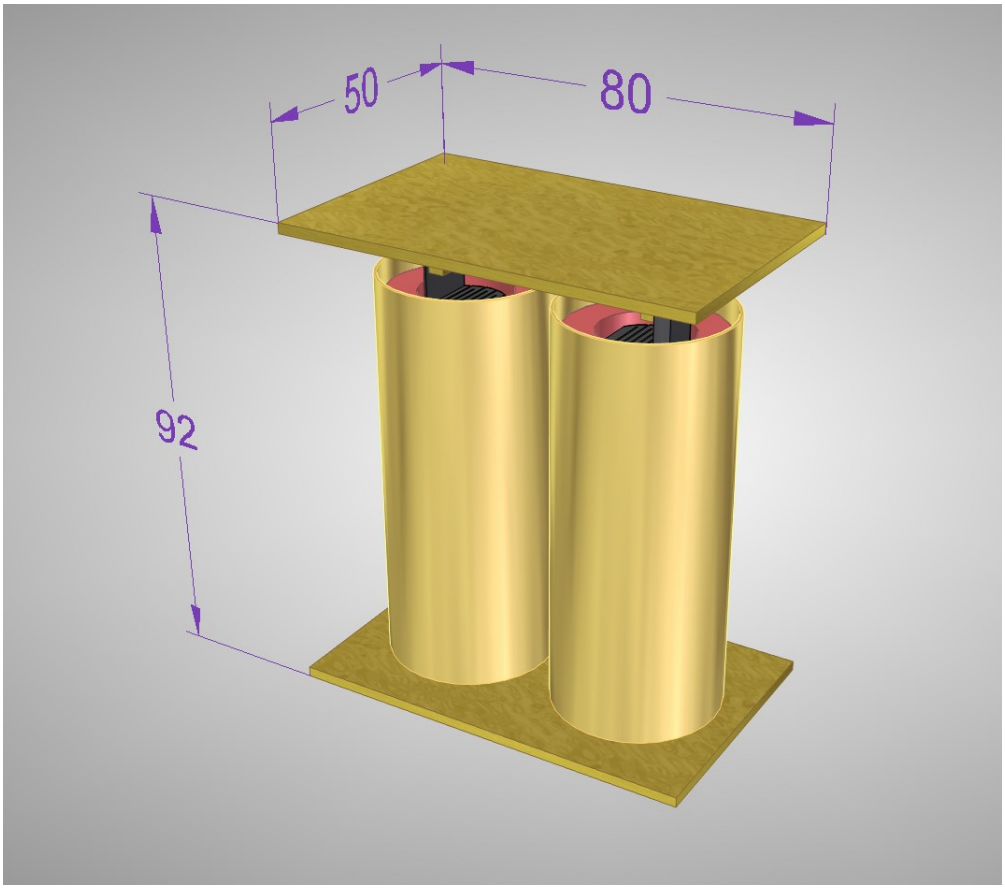

Figure 6.27: 3D conceptual design for mini-ADR showing overall dimensions.

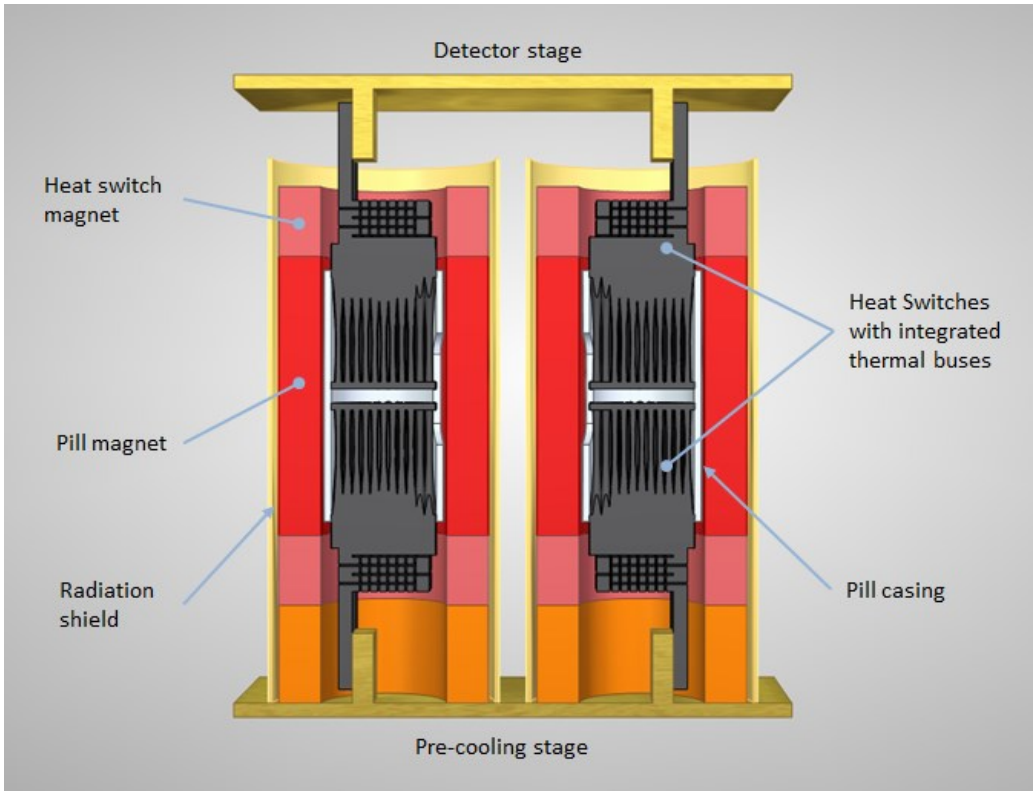

Figure 6.28: Section through mini-ADR concept showing main components.

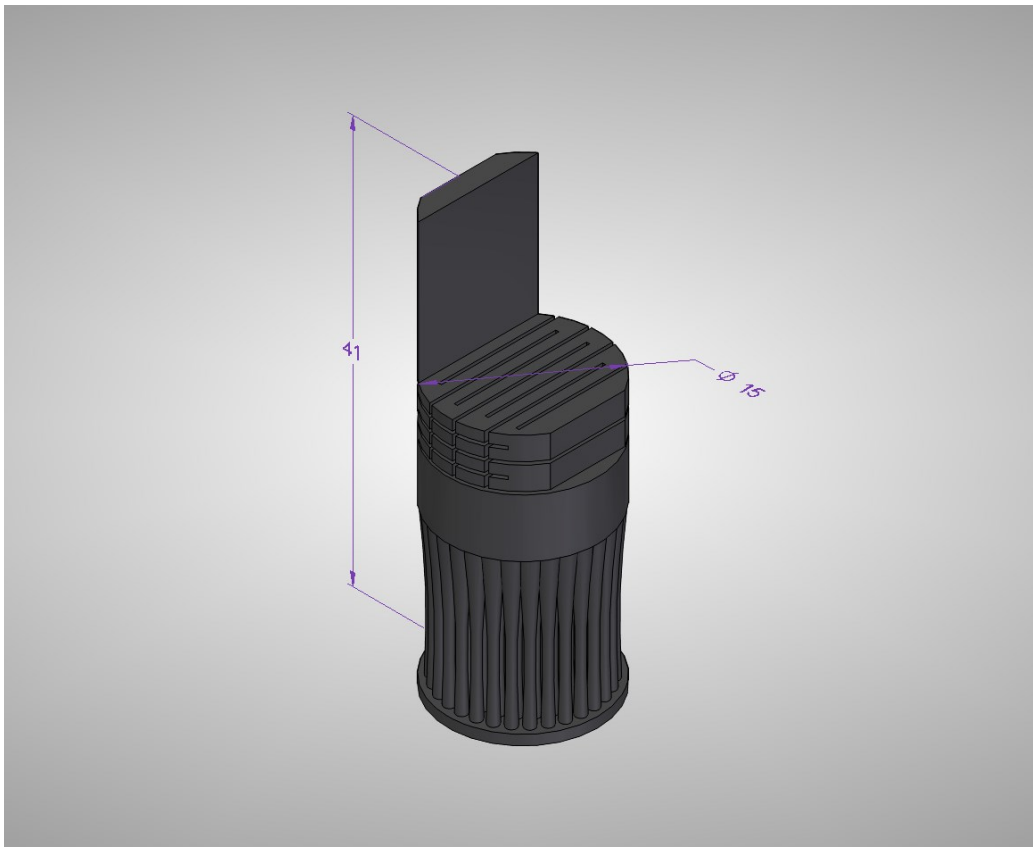

Figure 6.29: Conceptual design for a heat switch with integrated thermal bus.

The pill size was adjusted so that it could accommodate the thermal buses of both heat switches (as shown in Figure 6.28). This made it slightly longer than the pill in the baseline model, but the absence of bolted joints between the heat switches and pills reduces the overall size of the assembly. In spite of the larger pill, the need to include two thermal buses (one for each heat switch) means that the total amount of CPA is the same as in the baseline model. A full list of the parameters used in the modified model is given in Table 6.5.

Parameter	Value
Heat Switch cross-sectional area	1 mm^2
Heat Switch length	320 mm
Moles of CPA	0.014
Pill aspect ratio (length/diameter)	2.12
Pill length	36 mm
Pill diameter	17 mm
Support Structure cross-sectional area	5 mm^2
Support Structure length	90 mm
Area of thermal boundary	3500 mm^2

Table 6.5: Summary of mini-ADR design parameters when a tungsten thermal bus is used.

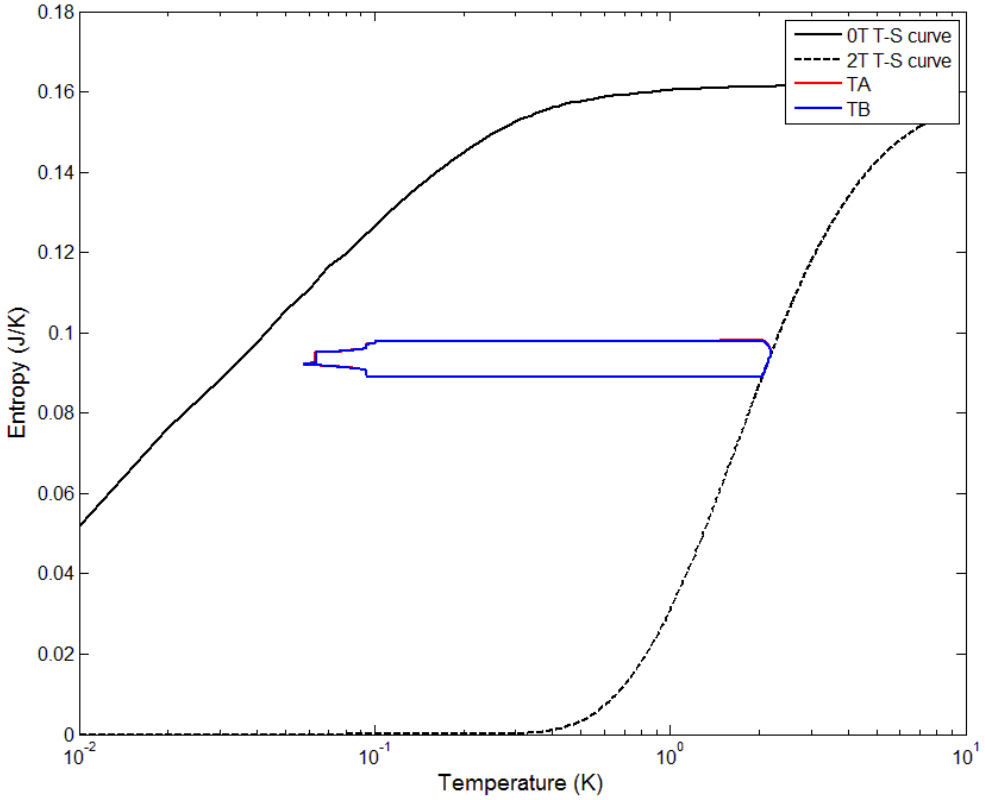

Figure 6.30: Temperature-entropy plot for the two pills with the thermal bus modelled as tungsten (the latter cycles, after stabilisation of the detector stage, are shown).

As with the baseline model described in 6.5, this ADR is only able to hold a stable base temperature of 100 mK after the first cycle. Once stability has been achieved, however, Figure 6.30 confirms that the pills have sufficient entropy capacity to meet the required hold time (although the margin is small).

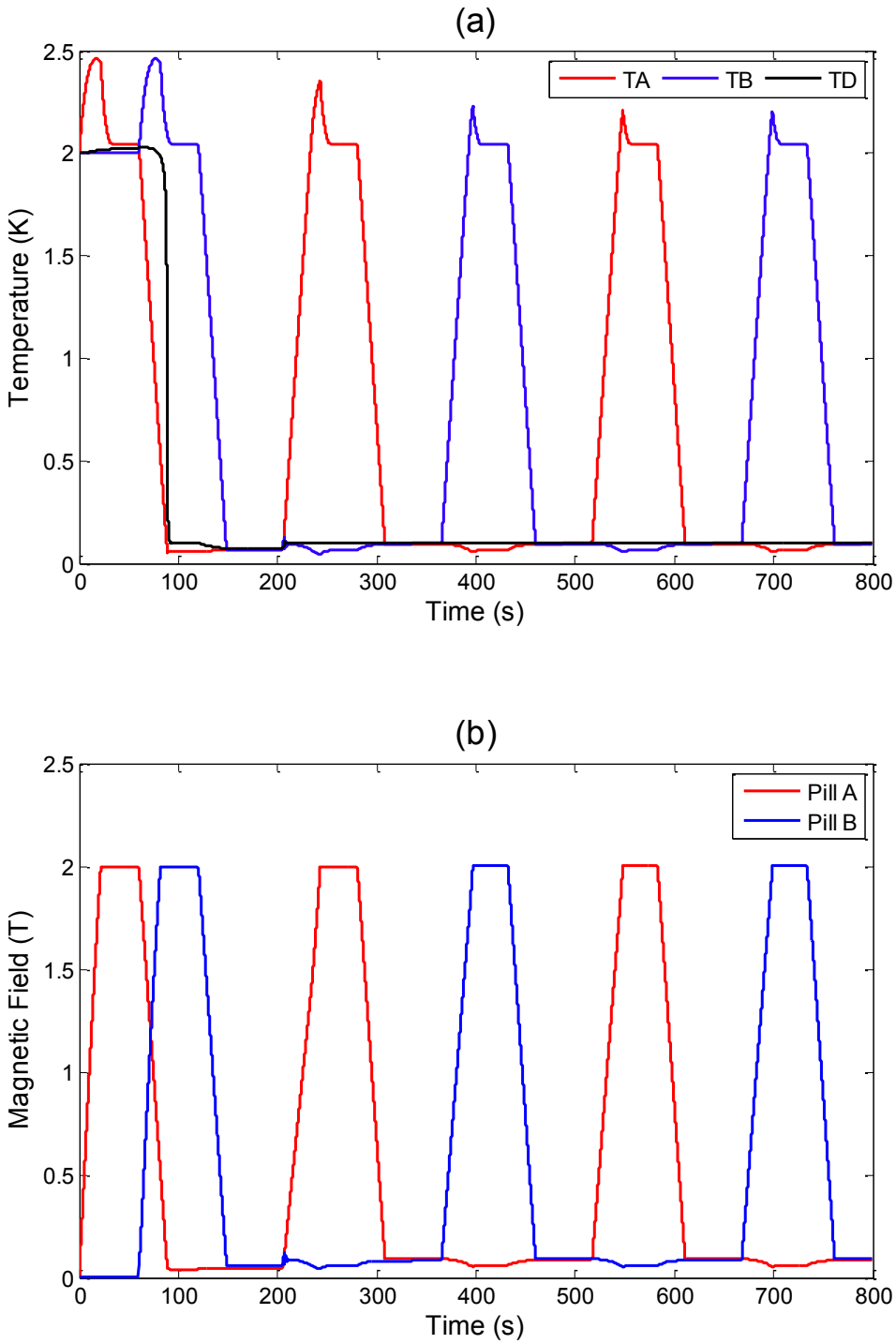

Figure 6.31: (a) Predicted pill and cold stage temperatures over first two cycles with thermal bus modelled as tungsten (b) Magnetic fields in the pills calculated from the free-ion approximation.

Figure 6.31(a) corroborates that a stable detector stage temperature can be maintained. It also demonstrates that the model's predictions for the each pill's field and temperature track each other very closely at all but the lowest fields. At these fields the model slightly over-predicts the magnetic field for a given temperature and this is a direct result of using the free-ion approximation: at low temperatures, the free-ion approximation predicts higher applied magnetic fields because it neglects any contribution from the interactions of the dipoles that are present in a real paramagnetic material (see 2.4.1).

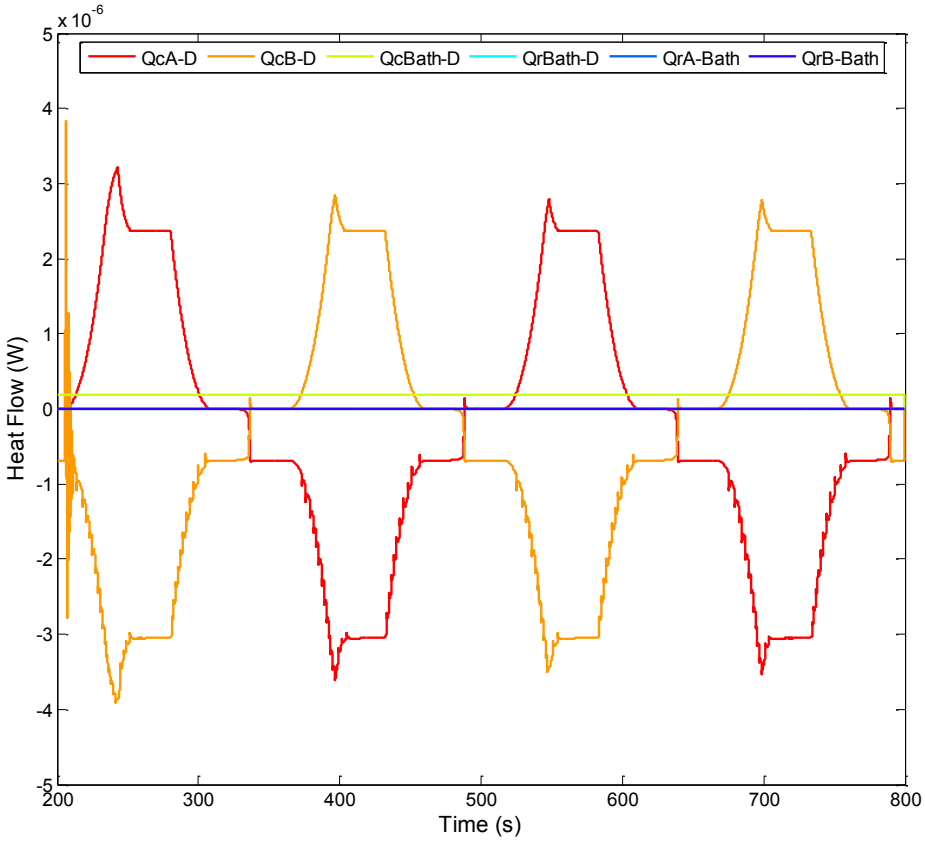

Figure 6.32: Heat loads on the cold stage after initial cool-down with a tungsten thermal bus. The first part of the line labels refer to the type of load - Qc = conduction, Qr = radiation; the second part refers to the nodes between which the heat flow occurs.

Figure 6.32 shows the heat loads for the latter cycles. On the first cycle shown, a spike of the type seen in Figure 6.19 is evident. As with the baseline model, this is a result of the temperature control algorithm attempting to compensate for the fact that in the first cycle the

pill has to completely demagnetise to extract the heat from the detector stage. As the algorithm matches the temperature of the pills for switchover, the active pill has to rapidly adjust once the target base temperature has been reached and it need only balance the heat loads on the stage.

Figure 6.32 also shows that the heat loads conducted through the switches are again the dominant contributors to the total heat load. The effect of the longer heat switch path length is evident, with loads down the switches peaking at less than 3 μW for this ADR.

The heat loads on the pre-cooling path follow the same trend as for the baseline design (see Figure 6.20). In the case of this ADR, the initial peaks are just over 8 mW dropping to below 4 mW in the latter cycles. As before, these are compatible with cooling powers that could reasonably be expected at 2 K.

6.8 Summary and Conclusions

The results presented in this chapter suggest a possible conceptual design for a miniaturised ADR. The key parameters in the design have been described and areas that will need further development have been identified – these are discussed in more detail in Chapter 7.

The baseline design uses the concept illustrated in Figure 6.1 and assumes that current pill and heat switch manufacturing techniques are to be used in its construction. The pill and its thermal bus would be constructed according to the methods described in Chapter 2 (2.4.1) where CPA crystals are grown around a thermal bus constructed of gold-plated copper wires. The heat switch would be a separate item and connected to the thermal bus through a bolted joint. This method of connection would also be used to make the connections to the cold stage and bath. Based on the pill and heat switch dimensions in the thermal model, and current 2 T magnets in use at MSSL [145], this concept would result in overall ADR dimensions in the region of 60 mm × 90 mm × 100 mm high.

Further miniaturisation may be possible by using a single piece of tungsten for both the heat switch and the thermal bus as described in 6.7. This could reduce the overall height of the ADR to ~ 90 mm by eliminating the need for bolted joints at the pill–heat switch interface. Perhaps more importantly, it removes an element of the design that cannot be miniaturised beyond a certain size. With this design, manufacture of the heat switch would be more challenging, particularly using the existing spark erosion technique. However, tungsten is already being manufactured using additive manufacturing techniques (3D printing) and production of heat switches in this way appears feasible. It would also be important to demonstrate that CPA crystals could be grown directly onto a tungsten crystal and to measure the boundary resistance of such an interface. These aspects are discussed further in Chapter 7.

Further size reductions in the heat switch would likely be aimed at maintaining the same A/L ratio in an even smaller space. One way to achieve this is reducing the cross-sectional dimensions of the switch, so that its length can be reduced accordingly. Based on the conclusions of section 6.6, it can be assumed that reducing the cross-section dimension parallel to the magnetic field will be most effective in reducing the "off" conductivity. Larger dimensions can be maintained in the perpendicular cross-sectional dimension without such a detrimental impact and this should be accounted for in heat switch geometries.

Another way to reduce the overall envelope of the heat switch would be to consider alternative geometries. This is already being investigated at MSSL in the form of coiled shapes (see Chapter 7).

Whilst the mini-ADR design presented in this chapter clearly requires further development, it shows that tungsten heat switches offer genuine potential to reduce the size of ADRs. An ADR design following the concepts described above would not be so out-of-proportion to the cryogenic detectors it was intended to cool as current sub-Kelvin coolers. Although it has been sized for a detector dissipation of 500 nW, the modelling results show that this is

nearly an order of magnitudes smaller than the parasitic heat loads from the heat switches and it is these that drive the size of the ADR. Increasing the detector dissipation beyond the 1 μW level would therefore only fractionally increase the amount of refrigerant and thus the overall size of the ADR.

The mathematical model described here should serve as a useful tool in refining mini-ADR designs. It is fully parameterised and thus allows investigation of any combination of pill size and heat switch geometry. It could also be augmented to include additional magnetic cooling stages, as might be required if the ADR was operated from a bath above 2 K.

Chapter 7 – Developing a mini-ADR

7.1 Introduction

The previous chapter showed how detailed knowledge of the behaviour of magnetoresistive heat switches could be used to design a miniature ADR. Such a cooler, incorporated as the final stage in a full cryogenic chain, would be an attractive solution to cooling the types of cryogenic detectors described in Chapter 1. If the entire cooling system were to be sufficiently small and easy to integrate with the detectors, the application of sub-Kelvin detectors has the potential to experience huge growth – both in space and ground applications. Transition Edge Sensors are already being used in the design of current X-ray (Athena+) and Infrared (SPICA) space missions. As MKIDs become a more mature technology, these are likely to become the detector of choice in the visible to UV and may even compete with TESs at other wavelengths. Regardless of the particular detector technology, the drive to increase array size will make scalable cooling more important. Miniature ADR units could be grouped together to achieve this aim, with each unit being a CADR of the type modelled in Chapter 6. The achievable cooling power from one of these units for a given size then becomes crucial. It has been shown in the preceding chapters of this thesis that understanding and controlling the heat flows in an ADR are central to optimising this. However, there are other areas of ADR technology that require development. The following sections take a broader view of the further research required.

7.2 Future Heat Switch Development

The work described in Chapters 4 and 5 of this thesis provides a good basis for understanding the behaviour of tungsten magnetoresistive heat switches in a range of fields and angles. It has been complemented by the work of other members of the Cryogenics Group at MSSL into how tungsten's thermal conductivity changes with temperature. Beyond this, there are a number of other avenues for investigation that would contribute to

an improved understanding of tungsten's thermal magnetoconductivity and might permit even better heat switches to be designed.

7.2.1 Further Investigation of the Static Skin Effect

The results in Chapter 4 were interpreted under the assumption that the Static Skin Effect was important in the samples measured. This was assumed on the basis that the experimental and sample conditions matched those in which the effect has been demonstrated to occur in tungsten [215]: high purity crystals with long electron mean free paths, in magnetic fields for which the Larmor radius is much less than the cross-section dimensions. However, all previous measurements have been on the electrical conductivity. It is therefore important to confirm that:

i. the effect occurs in thermal as well as electrical transport;
ii. the Static Skin Effect does indeed take place in the crystals used for heat switches.

The above questions could be answered by a relatively straightforward experiment. A tungsten sample should be procured that has a rectangular cross-section with significantly different dimensions – 4 mm × 1 mm is suggested based on the proportions of the samples used by Volkenshtein *et al.* [215]. The thermal conductivity as a function of magnetic field could then be measured with the long edge parallel to the field and the short edge parallel to the field. If the Static Skin Effect is taking place, the thermal conductivity in a magnetic field[34] should be much greater when the long edge is parallel to the applied field.

An additional test would be to measure a "Corbino disc" sample (see, for example, [213,215]). In this geometry, the sample is cut into a small disc with electrical (or thermal) current entering at the centre of the disc and leaving at the edges. The electrical (or thermal) potential difference is measured at these locations and the magnetic field is applied perpendicular to the plane of the disc. For the purposes of the Static Skin Effect, this creates

[34] It must be of sufficient strength that the Larmor radius is much less than the sample dimensions. Based on the calculation in Chapter 4, this would be any field in excess of a few mT.

an effectively infinite sample, since there are no surfaces that are parallel to both the magnetic field and the direction of current flow for electrons to interact with. Previous measurements of Corbino discs of tungsten have shown the conductivity to be much less than hexahedral geometries when the Static Skin Effect is present [213,215].

If the importance of Static Skin Effect is confirmed for thermal transport, it may be that the Corbino disc geometry offers a way of further reducing the "off" conductivity of a heat switch. However, the reduction in conductivity from eliminating the Static Skin Effect would be counteracted by the increased cross-sectional area.

7.2.2 Surface Preparation

It was shown in Chapter 3 that the long electron mean free paths in tungsten at 4 K and below lead to scattering at the sample surface playing an important role in the thermal conductivity. There is some evidence that with the right preparation, and for surfaces corresponding to certain crystallographic planes, specular reflection can take place in tungsten [176,216]. Measurements on polished samples are currently planned at MSSL and it would be of interest to continue this with the sample preparation methods employed by Mitrjaev *et al.* [176] – i.e. electro–polishing in a 3% sodium hydroxide solution. Both the zero-field effects and those in a magnetic field should be studied.

In zero-field, increasing the proportion of electrons that are specularly reflected at the surface should increase the conductivity and produce a heat switch with a higher "on" conductivity. Increased specular reflection could also increase the conductivity with magnetic field applied, although the extent to which this occurs may depend on the degree to which the Static Skin Effect plays a role in the samples (see 7.2.1). If this should lead to an increase in the "off" conductivity it would clearly be detrimental to performance.

It was found in Chapter 4 that the magnetic field exponent in the magnetoconductivity equation was lower than the theoretical value of 2 and it was concluded that sub-surface defects were likely to be responsible for this. If this were correct, it may be possible to

achieve an exponent much nearer 2 – and so increase the magnetoresistive effect – by removing such defects. In their investigations, Cherepanov *et al.* achieved this by electro-polishing in a 2% hydrogen peroxide solution [212]. Finding out if such a surface preparation could increase the field exponent in the crystals used in this work would be extremely valuable.

7.2.3 Longitudinal Magnetoresistance Effects

The thermal modelling of a miniature ADR with a tungsten thermal bus described in Chapter 6 made use of an equation for the longitudinal magnetoresistance of tungsten. While the longitudinal resistance has been measured over a range of fields (Chapter 5), it has not been measured as a function of temperature. In Chapter 6, a linear temperature dependence was assumed, which was deemed reasonable on the basis that impurity scattering would dominate at 5 K and below. Transverse conductivity measurements conducted at MSSL have shown that the a_3 term in equation (4.9) is much more dominant than the a_4 term, which might therefore be ignored. Nevertheless, if significant amounts of tungsten are to be used parallel to the magnetic field in future miniature ADR designs, this assumption should be verified.

If further longitudinal magnetoresistance measurements were to be made, it would also be of interest to determine whether different crystals orientations would lead to noticeable differences. The reasons for expecting different levels of magnetoresistance for different crystal orientations are detailed in Chapter 3 and in Chapter 5 it was suggested that the results obtained may be consistent with this effect. Unfortunately, definitive conclusions were impossible because the precise crystal orientation was only known for one of the samples measured. This could be addressed by measuring the magnetoresistance as a function of field for a selection of samples, each cut so that the length (and hence direction of heat flow) was aligned with different crystal axes. Since the sample C-3b investigated in this thesis had its length along the [100] direction, other directions should be considered – e.g. [111], [110].

Further measurements would also provide an opportunity to look for the theoretically predicted saturation which was not observed in Chapter 5.

7.2.4 Other Magnetoresistive Materials

Chapters 2 and 3 described the reasons why tungsten is considered such a good material for the construction of the magnetoresistive heat switches. Its key features are its closed Fermi surface and the fact that it is a compensated metal. Other materials that also have these properties are: molybdenum, indium, aluminium, the alkali metals and semi-metals of the bismuth group [232]. Semi-metals generally have a lower thermal (and electrical) conductivity than normal metals because they have a lower density of states at the Fermi surface and therefore fewer carriers for conduction processes. This makes them unattractive choices. Likewise, the highly reactive nature of the alkali metals makes them difficult to work with and probably unsuitable.

Of the remaining candidates it would be of interest to measure aluminium and molybdenum, although their relatively high superconducting transition temperatures (1.2 K and 0.92 K, respectively) would mean they would not be suitable for ADR stages operating below these temperatures. Illustrations of the Fermi surfaces of these materials are shown in Figure 7.1 with that of tungsten for comparison.

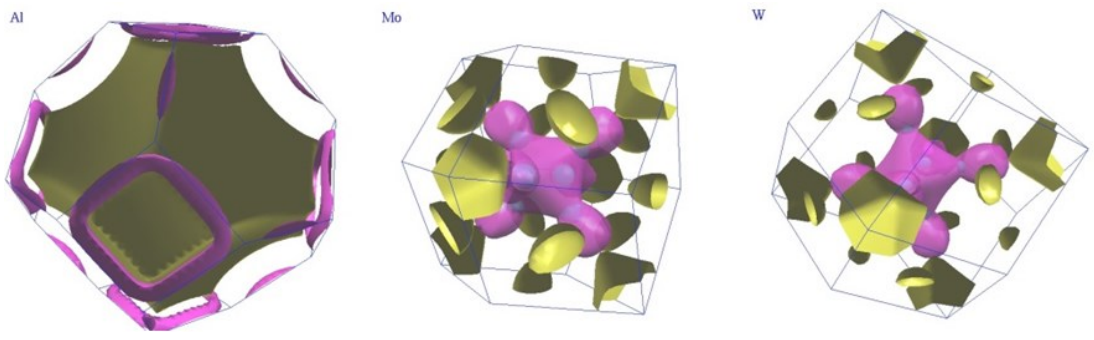

Figure 7.1: Fermi surfaces of aluminium (left), molybdenum (centre) and tungsten (right) [233].

There are also, of course, other considerations, such as availability of high purity single crystals, mechanical strength and ease of manufacture. For example, indium's lack of strength probably makes it an impractical choice.

7.2.5 Alternative Geometries

It was mentioned in Chapter 6 that a way to reduce the size of the heat switch whilst maintaining the same performance would be to conceive alternative geometries, which allow the same area/length (A/L) ratio to be achieved in a smaller overall volume. One such alternative geometry currently being investigated at MSSL is a coiled heat switch, shown in Figure 7.2.

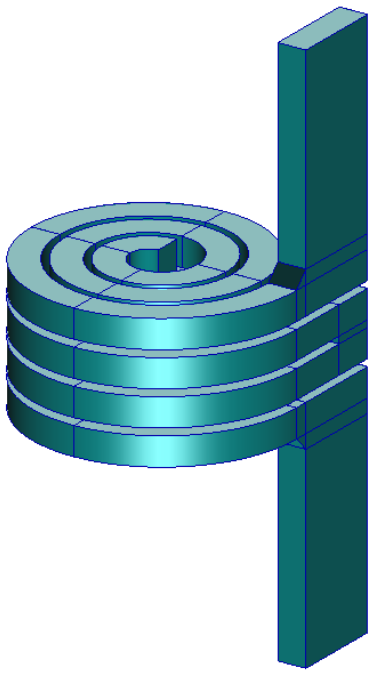

Figure 7.2: Coiled heat switch geometry
(courtesy of A. Green).

This geometry can be manufactured from a single crystal using existing spark erosion techniques and the shape makes good use of the cylindrical envelope within a solenoid magnet. It has also been the subject of mechanical analyses which indicate it is compatible with the launch loads on a spaceflight ADR. Other possibilities no doubt exist and the

constraints imposed by the spark erosion manufacturing method may be able to be relaxed by considering Additive Manufacturing techniques (see 7.4).

7.3 Pill and Thermal Bus Development

7.3.1 Boundary Resistance

The modelling performed in Chapter 6 highlighted the importance of the thermal boundary between the pill and the ADR's thermal bus – be it tungsten or some other material. It was shown that this can be a limiting factor in the miniature ADR design. Understanding heat transfer in this part of an ADR has also been shown to be crucial to accurately predicting the performance of other ADRs constructed at MSSL [152]. While the β value used in the thermal boundary resistance equation (6.20) has been verified against the real performance of the MSSL ESA ADR [152], it would be useful to confirm experimentally that this is still an appropriate value for the latest designs of CPA pill. Results from the milli-Kelvin Cryo-Cooler (mKCC) currently under construction at MSSL [145] should help to answer this question.

A further question is whether the same β value will be valid when the materials on either side of the boundary differ from copper and CPA. The use of a tungsten thermal bus was investigated in Chapter 6 and this has the potential to simplify a miniature ADR's construction. It was assumed in that chapter that the same value used for the copper–CPA boundary in the MSSL ESA ADR could be applied to a tungsten–CPA boundary. If the concept is to be pursued, it will be important to measure the thermal boundary resistance for this case and determine the β value experimentally. The practical implementation of the concept is discussed further below (7.4).

7.3.2 Pill Construction

Whatever the materials used in the pill and thermal bus, and whatever the β value for the interface, it will be important to maximise the contact area between the pill and thermal bus. In current MSSL pill designs [112], this has been successfully achieved with large numbers

of small diameter wires (see Figure 2.6). It is not certain, however, that a similar solution will still work as the size of the ADR is reduced further. Furthermore, current methods of containing the paramagnetic material may not be appropriate for smaller pills.

If a tungsten thermal bus were to be employed, a possible method of pill manufacture would be to grow the material (e.g. CPA) directly on to the tungsten and then seal it with a conductive epoxy that would provide an additional path for heat exchange between the pill and the bus. It would be worthwhile prototyping this method of manufacture and measuring the thermal resistance that results between the pill and the thermal bus. Making such a measurement at low temperature will not be trivial, because the true boundary resistance must be extracted from other effects. Correct positioning of the thermometers is crucial: the thermometer measuring the temperature on the pill side should ideally be within one phonon mean free path length of the boundary. This is complicated by the fact that the presence of the thermometer can influence the mean free path. The pill would preferably be constructed with a thermometer contained within it, while the other thermometer could be mounted on the bus as close as possible to the pill.

It may also be possible to miniaturise current pill designs that use G-10 outer housings [112]; this type of construction was assumed for ADR concept presented in Chapter 6, but, again, this should be prototyped.

7.4 Heat Switches with Integrated Thermal Buses

In Chapter 6 a conceptual design for a miniaturised ADR was presented that combined the heat switch and thermal bus into one tungsten component. As was pointed out in that chapter, such a component could not be produced using the current method of heat switch manufacture. This involves forming a single crystal of high purity tungsten by taking an initially very pure polycrystalline sample, and then melting and re-forming it around a "seed crystal" that sets the crystal orientation. The crystal is then "zone-refined" – a process of re-melting a portion of the crystal and moving the molten region gradually along the crystal.

Impurities concentrate in the melt and they therefore migrate to the ends of the crystal with the molten zone. The final geometry of the heat switch is spark eroded from the solid crystal. Ideally, this is done only from the purer central region.

It is the spark erosion which is the main barrier to the type of geometry proposed in Chapter 6 (see Figure 6.29); the wire arrangement used for the thermal bus would not be possible to produce using this method. However, it should be possible to produce such a geometry using Additive Manufacturing (3D printing) [234]. The heat switch part could be manufactured in the normal way to ensure a high purity, single crystal structure. This could then be placed in an Additive Manufacturing machine and used as a base from which to construct the complex thermal bus geometry. This part of the component would not have the same purity, or single crystal structure of the heat switch element, which would reduce the thermal conductivity. However, given sufficient purity, it should still retain a zero-field thermal conductivity that would compare well with copper. In fact, the comparative impurity and polycrystalline structure would reduce magnetoresistive effects and this would assist in extracting the heat of magnetisation.

Such a novel method of manufacturing would clearly require testing, but producing complex geometries in tungsten using Additive Manufacturing has already been demonstrated using Direct Metal Laser Sintering (DMLS) [235][35]. In this process, fine metal powder is fused together using a laser beam. The laser is accurately controlled to only fuse material where it is needed and the unsintered material can be removed. The geometry is built up in a series of very thin layers, each formed in this way. The technique is perfectly suited to the production of the type of small, intricate features in the heat switch design presented in Chapter 6.

[35] See www.smitroentgen.com/en/tungsten-parts-created-by-powder-bed-laser-melting/

7.5 Magnet Development

Throughout Chapter 6 it was assumed that miniaturisation of the pill and heat switches could be matched by miniaturisation of the magnets they require to operate. Engineering smaller superconducting magnets, however, is a significant challenge. Equation (7.1) below shows the expression for the field in a solenoid magnet [236]:

$$B = jaF(\alpha\beta), \tag{7.1}$$

where j is the current density, a is the solenoid inner radius and

$$F(\alpha\beta) = \mu_0\beta \ln\left(\frac{\alpha + (\alpha^2 + \beta^2)^{1/2}}{1 + (1 + \beta^2)^{1/2}}\right), \tag{7.2}$$

where μ_0 is the magnetic permeability, $\beta = l/a$, where $2l$ is the solenoid length, and α is the ratio of the outer and inner radii. Using sizes from the mini-ADR conceptual design presented in Chapter 6 (inner diameter = 18 mm, outer diameter = 30 mm, length = 40 mm) and specifying a 2 T field on axis, the required current density in the winding is ~ 300 A/mm^2. This is a manageable current for a superconductor such as niobium-titanium in fields of the order of 2–3 T [236], but the challenge is to achieve it with relatively low currents.

It is clearly desirable to reduce the current through the solenoid to minimise Joule heating in the normally conducting sections of the current leads and thus minimise loads on the higher temperature stages of the cryogenic system. However, reducing the current in the wire necessitates more turns in the coil pack and this sets a limit on the wire diameter if the overall magnet size is to be kept constant. To achieve the current density quoted above with 2 A in the conductor would require a wire diameter of < 90 μm; to limit the current to 1 A would demand a diameter < 60 μm. Winding with such small diameter wire requires specialist winding machines and clearly presents a significant challenge.

In addition to the difficulty of winding such small wires, increasing the number of turns to reduce the current has the drawback of increasing the inductance, L. This will impact on the ramp time:

$$\Delta t = L\frac{\Delta I}{V}. \tag{7.3}$$

As shown in Chapter 6, the ramping times for the magnets are the dominant factor in determining the recycle time for a miniature ADR. In a CADR, this impacts on the required hold time which then limits the size of pill that can be used. Equation (7.3) shows that the ramp time is proportional to both the inductance and the operating current; to reduce ramp times, therefore, either: the maximum operating current in the magnet can be reduced, or the inductance can be reduced. Of course, these demands are not compatible. It was shown above that reducing the operating current must be balanced by an increase in turns per unit length if the same field is to be maintained. This will increase the inductance of the solenoid:

$$L = \mu_0 \frac{N^2}{2l} A, \tag{7.4}$$

where N is the number of turns and A is the cross-sectional area of the solenoid. The trade-off between current and inductance is illustrated in Figure 7.3, where the required operating current and inductance are plotted against the number of turns for a solenoid of the dimensions above.

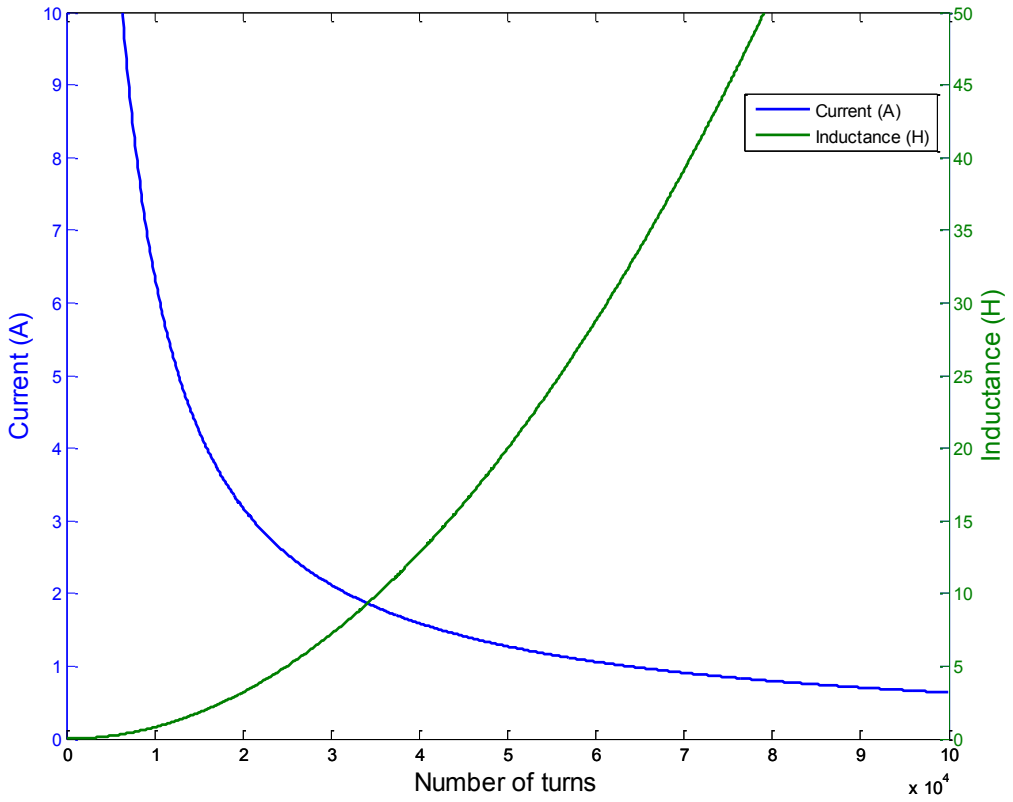

Figure 7.3: Effect of increasing the number of turns in a 2 T solenoid magnet on the operating current and inductance.
The plot is based on a solenoid of diameter 18 mm and 40 mm long.

Clearly there is a point at which any benefit from reducing the current is far outweighed by the increase in inductance, although it is likely that minimum wire size will be the limiting factor in practice.

7.6 Support Structure

A robust and thermally insulating supporting structure will be vital for a miniature ADR. Its design becomes especially challenging as the size of the ADR shrinks because it becomes more difficult to accommodate supports with the necessary A/L ratio to keep the conducted heat load manageable.

As well as geometry, the materials of construction must also be considered. Both G-10 fibreglass and Vespel® SP22 polyimide (as used in Chapter 6) are good candidate materials for the support structure, with Vespel® SP22 having slightly lower thermal conductivity in the range of interest (0.1–2 K). Vespel® is used as a support material in current ADRs at

MSSL. As described in Chapter 2, a more common material for supporting ADR pills is Kevlar® and this has been used in cord form to support pills in ADRs qualified for spaceflight [133,146]. Kevlar® cords cannot be used without some additional structure to wind or bond them to, however, and this increases the number of the parts required and potentially complicates the design and assembly of a miniature system.

The modelling in Chapter 6 showed that, as the size of the ADR continues to shrink, it is increasingly difficult to: (i) accommodate a support structure in the space available; and (ii) maintain the heat conducted through it at a low enough level that the cooler can still function. Two potential solutions are to either eliminate the support structure completely, or, for applications such as large detector arrays, construct a super-structure which supports a single cold stage whose cooling load is shared by multiple miniature ADRs. The first option requires supporting the cold stage directly from the heat switches that link it to the pill. Given the small A/L ratios needed in these switches, this only seems feasible for ground-based systems that could be very carefully handled. For systems operating in harsher environments, such as space, additional support would almost certainly be required. However, for space ADRs, the most severe loads are only experienced during launch and a temporary support system that could be disconnected before operations begin might be a possibility. A "launch lock clamp" serving this purpose has been constructed using a shape memory alloy (nickel-titanium) and used successfully on a previous space mission [60,237]. An alternative concept would be to use materials in the clamp with sufficiently different coefficients of the thermal expansion, such that the clamp would disengage as the system cooled down to its operating temperature.

The super-structure solution could employ thin walled tubes of G-10 or Vespel® around multiple miniature ADRs, all cooling a single cold stage for a large detector array. If necessary, the path length could be increased by using concentric tubes, joined alternately at top and bottom edges. Any design of support structure should be subject to proper mechanical analysis and, for space qualification, vibration tests would also be necessary.

7.7 Towards a micro-ADR

The research described in this chapter thus far points towards the possibility of manufacturing ADRs on the scale of tens of millimetres. To move beyond this, to ADRs on the millimetre scale and below, would require yet another technological jump. There are a number of barriers to building such devices at present.

As the work in this thesis has demonstrated, heat switches are central to ADR miniaturisation. The main challenge to further miniaturisation of magnetoresistive heat switches would be to maintain a sufficiently low "off" conductivity as the length of the switch is reduced. The obvious way to address this is smaller cross-sections (i.e. sub-millimetre), but the results in 6.6 show that this is likely to lead to a reduction in heat switch performance. Furthermore, sub-millimetre cross-sections make the heat switch mechanically weak and may introduce manufacturing issues. While it may be possible to produce the heat switch in the form of thin films, these would need to be manufactured on a substrate which would introduce an additional parasitic heat load.

Parasitic heat loads in general would become ever more important as the size of the ADR is reduced. Although it could be possible to support the paramagnetic refrigerant directly from the heat switch (as proposed in Chapter 6), it is likely that there will always need to be some additional support for the item to be cooled and the structure that serves this purpose will inevitably introduce a heat leak that is difficult to reduce beyond a certain point.

Perhaps the biggest obstacle to making ADRs on the millimetre to sub-millimetre scale is creating the necessary magnetic fields. The magnet development described in 7.5 is still based on miniaturising superconducting solenoids and this is limited by the size of superconducting wire that is commercially available. The recent production of superconducting magnets using multi-layer HTS coatings [141] offers some promise in this area.

Despite the fact that the paramagnetic refrigerant can, in theory, be shrunk to the molecular scale, it should not be neglected as a component for further development. Improving the cooling power per unit volume would still provide gains and, even if small, these may be sufficient to partially counteract the problems of smaller heat switches and excessive parasitic heat loads. The multiferroic materials described in 1.4.9.3 may prove to be extremely important in this area.

7.8 Summary and Conclusions

This thesis has described some initial steps towards the prospect of milli-Kelvin cooling of high sensitivity cryogenic detectors on the bench-top scale. The review of current photon detectors that require temperatures below 1 K contained in Chapter 1 showed that these detectors offer single photon sensitivity coupled with the ability to measure photon energy and hence provide spectroscopic information. The importance of being able to assemble large arrays of such detectors for astronomy was also highlighted. The prospect of using sub-Kelvin photon detectors, particularly in large arrays, is currently severely hampered by the large and unwieldy cooling systems required. Chapter 1 also reviewed these systems and the current technologies used within them to reach < 1 K from room temperature. Since most astronomical observations for which these detectors are applicable take place at wavelengths that are absorbed by the Earth's atmosphere (e.g. Far–Infrared, UV, X-ray), particular attention was given to those technologies that are suitable for spaceflight. To reach temperatures of 100 mK and below, there are only two candidates: Adiabatic Demagnetisation Refrigerators and Dilution Refrigerators. While DRs can generally provide slightly higher cooling powers without interruption, spaceflight versions have a finite life dependent on the amount of helium isotopes that can be accommodated on the spacecraft. Proposed designs that recycle the helium require pumps that add mass and complexity. ADRs, on the other hand, have no inherent lifetime limitations. The main drawback of the traditional version is that it cannot provide continuous cooling because once the entropy of the paramagnetic refrigerant has been used up, it must be recycled by a process of re-

magnetisation. This problem is addressed in Continuous ADRs and different concepts for these have been discussed in Chapter 2. It was shown that only the tandem CADR provides true continuous cooling and this arrangement will therefore have a higher gross cooling power. This was the concept chosen for development in the thesis.

Since the tandem concept consists of two separate ADRs in parallel to alternately cool a continuous cold stage, the hold time of the active side need only just exceed the recycle time of the inactive side. This means the cooling power for a given size is no longer dictated by the required hold time, but by how fast the recycling process can take place and how well parasitic heat loads are controlled. The emphasis of the design is then on how well heat is transferred within the ADR and the main components responsible for this are the heat switches.

Magnetoresistive heat switches made from tungsten have been shown to be very effective at controlling thermal currents at low temperatures. A short review of heat switch technologies in Chapter 2 illustrated that they compare favourably against other alternatives in terms of switching ratio and suitability for miniaturisation.

A review of the theory of magnetoresistance was reported on in Chapter 3, along with semi-classical transport theory as it applies to heat flow in all elements of ADRs, not only the heat switches. This led on to the use of semi-classical theory to develop the equation governing the thermal conductivity of tungsten at zero, low and high fields. Thermal conductivity measurements were performed to verify the form of this equation and excellent agreement was found. The field dependent part of the conductivity did not vary precisely quadratically with field – as was expected theoretically – and it was found that this could be explained with reference to surface effects in the samples. It was suggested that with a magnetic field applied to the tungsten, the major proportion of the electronic thermal current flows next to the surface (the Static Skin Effect) and that the region just below the surface is therefore expected to be extremely important for the overall thermal conductivity.

Further thermal conductivity experiments have been performed on tungsten samples oriented such the direction of heat flow varies with respect to the applied. These were reported in Chapter 5, where it was also shown that the zero to high-field equation could be generalised such that it would be applicable to measurements at arbitrary angles. A global fit to the data was largely within the measurement errors and the generalised equation is therefore considered accurate enough to be a useful predictive tool for modelling. It was found that no saturation of magnetoresistance occurred in the longitudinal case (magnetic field parallel to the thermal current), in contrast to theoretical predictions. It was concluded that small angle scattering might explain this. More importantly for ADR designs, the longitudinal effect, although smaller than the transverse, was found to give a reduction in conductivity of nearly two orders of magnitude between 0 and 2 T. This means that any tungsten parts used to transport heat an ADR will experience significant conductivity changes in applied fields regardless of their orientation.

The experimentally verified thermal conductivity equations for tungsten have been implemented in a Thermal Mathematical Model, which predicts the temperatures and heat flows in a tandem CADR. This model made possible an estimation of the size reduction of the CADR using current magnet technology. Using heat switches with the performance characteristics of the tungsten samples measured, the model predicts that it would be possible to construct a miniature ADR of the layout shown in Figure 6.1 with the following design parameters:

Parameter	Value
Heat Switch cross-sectional area	1 mm^2
Heat Switch length	200 mm
Moles of CPA	0.014
Pill aspect ratio (length/diameter)	1.5
Pill length	22.2 mm
Pill diameter	15.8 mm
Support Structure cross-sectional area	5 mm^2
Support Structure length	100 mm
Thermal bus wire diameter	0.4 mm

Table 7.1: Design parameters for a miniature ADR

An alternative design that incorporated the thermal bus and the heat switch into a single component was then put forward. The idea of this concept was to offer scope for even further size reductions by eliminating mechanical interfaces (e.g. bolted joints) which become impractical at very small scales. It was shown that using this concept a tandem CADR with the following parameters could be constructed.

Parameter	Value
Heat Switch cross-sectional area	1 mm^2
Heat Switch length	320 mm
Moles of CPA	0.014
Pill aspect ratio (length/diameter)	2.12
Pill length	36 mm
Pill diameter	17 mm
Support Structure cross-sectional area	5 mm^2
Support Structure length	90 mm
Area of thermal boundary	3500 mm^2

Table 7.2: Design parameters for a miniature ADR using an integrated thermal bus–heat switch component

The conceptual design of this ADR is shown in Figure 6.27 and Figure 6.28. It has overall dimension of 50 mm × 80 mm × 92 mm high.

This chapter has suggested further research that may lead to improved performance of magnetoresistive tungsten heat switches. Given the results of the Chapter 4 is would seem particularly important to find out more about the role of the Static Skin Effect in the thermal magnetoconductivity. This is closely linked to the influence of surface preparation and the impact of this should also be tested. Further research into longitudinal effects may also be of use, especially if tungsten is to be used as the ADR's thermal bus. The heat switches represent just one of the three main components of an ADR, of course, and development is also needed of the pills and the magnets. In the case of the pills, the main challenge is to make a good thermal link to the rest of the heat switch that minimises the thermal boundary resistance. Containing and growing the paramagnetic refrigerant must also be addressed. The magnet design for a miniature ADR is even more challenging. This requires thin (~ 100 μm) superconducting wire wound on formers of the order of 10 mm diameter.

Successfully winding such coils will require several stages of prototyping and a significant R&D effort in its own right.

In conclusion, Continuous ADRs are a key enabling technology for sub-Kelvin photon detectors. These detectors have a huge range of possible applications; one that must surely grow if the cooling technology they require does not hold them back. To realise this potential, the cooling system must not be so large that the practical difficulties associated with their use outweigh their benefits. The degree of cryogenic complexity that can be tolerated will naturally depend on the benefits the detectors offer to a particular application. As has been highlighted in this thesis, in astronomy they offer the ability to make measurements of a precision unrivalled by other technologies and therefore unwieldy cryogenic systems can be accepted. That is not to say, of course, that simpler and smaller systems would not be welcomed. For applications beyond this specialist field, simplification and miniaturisation is essential. This calls for R&D effort on all elements of a room temperature to sub-Kelvin cryogenic chain, but it is hoped that the work described here indicates a fruitful direction for this effort in the case of the lowest temperature stage.

Appendix A – Derivation of Magnetic Entropy According to the Free-Ion Approximation

Consider an assembly of non-interacting dipoles of magnetic moment $\boldsymbol{J}$, where J may take any integer or half-integer value. The partition function – defined as the sum of Boltzmann factors over all states of the system [14] – for this assembly is [101]:

$$Z = \sum_{m_J=-J}^{J} \exp\left(m_J \epsilon / k_B T\right), \tag{A.1}$$

where:

$$\epsilon = \mu_B \mathrm{g} B. \tag{A.2}$$

Let:

$$y = \mu_B \mathrm{g} B / k_B T, \tag{A.3}$$

so that the partition function may be written as:

$$\begin{aligned} Z &= \mathrm{e}^{-Jy} + \mathrm{e}^{(-J+1)y} + \mathrm{e}^{(-J+2)y} + \cdots + \mathrm{e}^{(-J+2J)y} \\ &= \mathrm{e}^{-Jy} + \mathrm{e}^{-Jy}\mathrm{e}^{y} + \mathrm{e}^{-Jy}\mathrm{e}^{2y} + \cdots + \mathrm{e}^{-Jy}\mathrm{e}^{2Jy}. \end{aligned} \tag{A.4}$$

This is a geometric progression of the form:

$$a + ar + ar^2 + \cdots + ar^{M-1} = \sum_{j=1}^{M} ar^{j-1} \tag{A.5}$$

with $a = \mathrm{e}^{-Jy}$, $r = \mathrm{e}^{y}$ and $M = 2J + 1$. Such a geometric progression can be summed using the formula [101]:

$$\frac{a(1 - r^M)}{1 - r}. \tag{A.6}$$

Substituting in the values for a, r and M:

$$Z = \frac{\mathrm{e}^{-Jy}\left(1 - \mathrm{e}^{(2J+1)y}\right)}{1 - \mathrm{e}^{y}}$$
$$= \frac{\mathrm{e}^{-Jy} - \mathrm{e}^{Jy+y}}{1 - \mathrm{e}^{y}}. \quad \text{(A.7)}$$

Multiplying through by $e^{-y/2}$ leads to:

$$Z = \frac{\mathrm{e}^{-Jy-\frac{y}{2}} - \mathrm{e}^{Jy+y-\frac{y}{2}}}{\mathrm{e}^{-\frac{y}{2}} - \mathrm{e}^{y-\frac{y}{2}}}$$
$$= \frac{\mathrm{e}^{-(2J+1)\frac{y}{2}} - \mathrm{e}^{(2J+1)\frac{y}{2}}}{\mathrm{e}^{-\frac{y}{2}} - \mathrm{e}^{\frac{y}{2}}} \quad \text{(A.8)}$$
$$= \frac{\sinh[(2J+1)\frac{y}{2}]}{\sinh[\frac{y}{2}]},$$

where the hyperbolic trigonometric identities $\sinh x = \frac{\mathrm{e}^{x}-\mathrm{e}^{-x}}{2}$ and $\sinh(-x) = -\sinh(x)$ have been used.

Now, the differential of the Helmholtz Free Energy, defined as $F = U - TS$, can be written:

$$dF = dU - TdS - SdT$$
$$= -SdT - pdV, \quad \text{(A.9)}$$

where the thermodynamic identity $TdS = dU + pdV$ [14] has been used. This leads to the following equation for the entropy:

$$S = -\left(\frac{\partial F}{\partial T}\right)_{B,V}. \quad \text{(A.10)}$$

This can be substituted back into the definition of the Helmholtz Free Energy to show that [14]:

$$F = -nk_B T \ln Z, \quad \text{(A.11)}$$

where n is the number of moles.

Using equations (A.10) and (A.11) together, the entropy of the system can be found:

$$\begin{aligned} S &= \frac{\partial}{\partial T}(nk_B T \ln Z) \\ &= nk_B \ln Z + nk_B T \frac{\partial(\ln Z)}{\partial T} \\ &= nk_B \ln Z + nk_B T \frac{\partial(\ln Z)}{\partial y}\frac{\partial y}{\partial T}. \end{aligned} \tag{A.12}$$

From equation (A.3):

$$\frac{\partial y}{\partial T} = -\frac{\mu_B \mathrm{g} B}{k_B T^2} = -\frac{y}{T} \tag{A.13}$$

and from equation (A.8):

$$\begin{aligned} \frac{\partial(\ln Z)}{\partial y} &= \frac{\partial}{\partial y}\left\{\ln\left[\frac{\sinh\left[(2J+1)\frac{y}{2}\right]}{\sinh\left[\frac{y}{2}\right]}\right]\right\} \\ &= \frac{1}{2}\left[\frac{\sinh\left[\frac{y}{2}\right](2J+1)\cosh\left[(2J+1)\frac{y}{2}\right] - \sinh\left[(2J+1)\frac{y}{2}\right]\cosh\left[\frac{y}{2}\right]}{\sinh^2\left[\frac{y}{2}\right]}\right] \\ &\quad \times \left[\frac{\sinh\left[\frac{y}{2}\right]}{\sinh\left[(2J+1)\frac{y}{2}\right]}\right] \\ &= \frac{1}{2}\left[\frac{\sinh\left[\frac{y}{2}\right](2J+1)\cosh\left[(2J+1)\frac{y}{2}\right] - \sinh\left[(2J+1)\frac{y}{2}\right]\cosh\left[\frac{y}{2}\right]}{\sinh\left[\frac{y}{2}\right]\sinh\left[(2J+1)\frac{y}{2}\right]}\right] \\ &= \frac{(2J+1)}{2}\coth\left[(2J+1)\frac{y}{2}\right] - \frac{1}{2}\coth\left[\frac{y}{2}\right]. \end{aligned} \tag{A.14}$$

Finally, substituting equations (A.13) and (A.14) into (A.12) gives:

$$S = nk_B\left\{\ln\left[\frac{\sinh\left[(2J+1)\frac{y}{2}\right]}{\sinh\left[\frac{y}{2}\right]}\right] - (2J+1)\frac{y}{2}\coth\left[(2J+1)\frac{y}{2}\right] + \frac{y}{2}\coth\left[\frac{y}{2}\right]\right\}. \tag{A.15}$$

Replacing $\frac{y}{2}$ with x and noting that $R = nk_B$ leads directly to equation (2.16).

Appendix B – Mean Energy of a Particle in a Classical Gas

The energy of a free particle of mass m is:

$$\epsilon = \frac{\hbar^2 k^2}{2m}. \tag{B.1}$$

The problem of finding the mean energy is thus one of finding the mean value of k^2. This is done by taking the mean of all the expected values of k^2: a sum is taken over all values of k and k^2 is multiplied by the number of states $s(k)$ containing the particular value of k and the expected number of particles in that state $\langle n_k \rangle$. This is normalised by dividing by the sum of $s(k)\langle n_k \rangle$:

$$\langle k^2 \rangle = \frac{\sum_k k^2 s(k)\langle n_k \rangle}{\sum_k s(k)\langle n_k \rangle}. \tag{B.2}$$

Classical particles obey the Maxwell-Boltzmann distribution function which defines the probability of finding a given state occupied as [161]:

$$\langle n_k \rangle = \mathrm{e}^{(\mu - \epsilon(k))/k_B T}. \tag{B.3}$$

Substituting (B.3) into (B.2):

$$\langle k^2 \rangle = \frac{\sum_k k^2 s(k) \mathrm{e}^{(\mu - \epsilon(k))/k_B T}}{\sum_k s(k) \mathrm{e}^{(\mu - \epsilon(k))/k_B T}}. \tag{B.4}$$

The factor $\mathrm{e}^{\mu/k_B T}$ cancels and, assuming the states are close in energy, the sums can be replaced by integrals. Treating the energy levels as a continuum, $s(k)$ can be replaced by the density of states and it can be shown that this is proportional to k^{j-1} where j is the number of dimensions[16] [16].[36] This leads to:

[36] It can be seen that this must be so without resorting to a complete proof (see [16]) since the number of states will be proportional to the k-space volume/area under consideration, which must be proportional to k^j. The density of states, $D(k)$, is defined such that the number of states (per unit volume of r-space), n, between k and $k + dk$ is $D(k)dk$ and hence $D(k) \equiv dn/dk \propto k^{j-1}$.

$$\langle k^2 \rangle = \frac{\int_0^\infty k^2 k^{j-1} \mathrm{e}^{-\hbar^2 k^2 / 2mk_B T}\, dk}{\int_0^\infty k^{j-1} \mathrm{e}^{-\hbar^2 k^2 / 2mk_B T}\, dk}. \tag{B.5}$$

Using standard tables of integrals, this can be evaluated as:

$$j \frac{mk_B T}{\hbar^2}, \tag{B.6}$$

which leads to:

$$\langle \epsilon \rangle = \frac{j}{2} k_B T. \tag{B.7}$$

Appendix C – Derivation of the Debye T^3 Law

The thermal average number of phonons in a mode with frequency ω_q is given by the same distribution function (Bose-Einstein) as for photons:

$$\langle s \rangle = \frac{1}{\mathrm{e}^{h\omega_q/k_B T} - 1}. \tag{C.1}$$

Debye's theory makes use of this along with the following assumptions:

i. The frequency of an elastic wave is independent of its amplitude;

ii. The velocities of all elastic waves are equal – independent of frequency, direction of propagation and polarisation.

The modes of an elastic wave in a cubic sample of side length L can be described by [14]:

$$E_{\mathrm{x}} = A_{\mathrm{x}} \sin(\omega t) \cos(\mathrm{q}_x \pi x/L) \sin(\mathrm{q}_y \pi y/L) \sin(\mathrm{q}_{\mathrm{z}} \pi \mathrm{z}/L), \tag{C.2}$$

$$E_{\mathrm{y}} = A_{\mathrm{y}} \sin(\omega t) \sin(\mathrm{q}_x \pi x/L) \cos(\mathrm{q}_{\mathrm{y}} \pi y/L) \sin(\mathrm{q}_{\mathrm{z}} \pi \mathrm{z}/L), \tag{C.3}$$

$$E_{\mathrm{z}} = A_{\mathrm{z}} \sin(\omega t) \sin(\mathrm{q}_x \pi x/L) \sin(\mathrm{q}_y \pi y/L) \cos(\mathrm{q}_{\mathrm{z}} \pi \mathrm{z}/L), \tag{C.4}$$

where A_{x}, A_{y}, A_{z} are the wave amplitudes and q_{x}, q_{y}, q_{z} are integers.

To count modes one should properly sum over all combinations of q_{x}, q_{y}, q_{z}, but this can be replaced by an integral over $d\mathrm{q}_{\mathrm{x}}$, $d\mathrm{q}_{\mathrm{y}}$, $d\mathrm{q}_{\mathrm{z}}$ in the space of the mode indices, where it is assumed that all modes lie within a sphere of radius q:

$$\sum_q (\dots) = \int_0^\infty 4\pi \mathrm{q}^2 d\mathrm{q} (\dots). \tag{C.5}$$

Unlike electromagnetic modes, the number of elastic modes in a finite solid is limited because of the finite number of independent oscillators (i.e. atoms in the crystal). For N atoms with 3 degrees of freedom (rotations ignored), there are $3N$ possible modes. This sets an upper limit on the integral in (C.5) which is referred to as q_D. There are also three

possible polarisations: two transverse and a longitudinal one in which the displacement of the atoms is parallel to the direction of propagation of the wave. The integral is multiplied by a factor of 3 to take account of the three possible polarisations and a factor of 1/8 to account for the fact that all applicable combinations are found in the positive octant of mode space.

The above arguments lead to:

$$\frac{3}{8}\int_0^{\mathrm{q}_D} 4\pi \mathrm{q}^2 d\mathrm{q} = 3N. \tag{C.6}$$

Carrying out the integration gives:

$$\frac{1}{2}\pi {\mathrm{q}_D}^3 = 3N, \tag{C.7}$$

or

$$\mathrm{q}_D = \sqrt[3]{6N/\pi}. \tag{C.8}$$

Each phonon mode has a frequency ω_q and an energy $h\omega_\mathrm{q}$. To find the total thermal energy of the phonons in the sample, the energy of each mode is multiplied by the average number of phonons in that mode (from equation (C.1)) and summed over all modes using (C.6).

$$U = \frac{3\pi}{2}\int_0^{n_D} \mathrm{q}^2 d\mathrm{q} \frac{h\omega_\mathrm{q}}{\mathrm{e}^{h\omega_\mathrm{q}/k_B T} - 1}. \tag{C.9}$$

From assumption ii, the velocity of waves of all modes will be equal to speed of sound in the sample, v. Therefore:

$$v = f_q \lambda_q = \omega_q \lambda_q / 2\pi \tag{C.10}$$

and using $\lambda_q = 2L/\mathrm{q}$:

$$h\omega_\mathrm{q} = \pi h v \mathrm{q}/L. \tag{C.11}$$

Substituting this into (C.9) gives:

$$U = \frac{3\pi^2 hv}{2L}\int_0^{n_D} \mathrm{q}^3 d\mathrm{q}\,\frac{1}{\mathrm{e}^{h\omega_\mathrm{q}/k_B T}-1}. \tag{C.12}$$

Making the substitution $x \equiv h\omega_\mathrm{q}/k_B T = \pi hv\mathrm{q}/Lk_B T$ allows (C.12) to be re-written as:

$$U = \left(\frac{3\pi^2 hv}{2L}\right)\left(\frac{Lk_B T}{\pi hv}\right)^4 \int_0^{x_D} dx\,\frac{x^3}{\mathrm{e}^x - 1}. \tag{C.13}$$

The upper limit of the integral can be written as $x_D = \theta_D/T$ where θ_D is the "Debye temperature". By making use of (C.8) and the definition of x, this can be expressed as:

$$\theta_D = \frac{hv}{k_B}\left(\frac{6\pi^2 N}{V}\right)^{1/3}, \tag{C.14}$$

where the substitution $L = V^{1/3}$ for the cubic sample has also been made. At this temperature $\mathrm{q} = \mathrm{q_D}$ and all possible modes in the sample are excited.

At low temperatures where $T \ll \theta_D$, it is valid to replace x_D with ∞, producing the following definite integral [14]:

$$\int_0^{\infty} dx\,\frac{x^3}{\mathrm{e}^x - 1} = \frac{\pi^4}{15}. \tag{C.15}$$

Using this result in (C.13) gives:

$$\begin{aligned} U &= \left(\frac{3\pi^2 hv}{2L}\right)\left(\frac{Lk_B T}{\pi hv}\right)^4 \frac{\pi^4}{15} \\ &= \left(\frac{\pi^6 hv}{10L}\right)\left(\frac{Lk_B T}{\pi hv}\right)^4 \\ &= \frac{3}{5}\pi^4 N k_B T^4 \left(\frac{k_B}{hv}\right)^3 \left(\frac{V}{6\pi^2 N}\right) \\ &= \frac{3\pi^4 N k_B T^4}{5{\theta_D}^3}, \end{aligned} \tag{C.16}$$

from which the heat capacity at low temperature is found as:

$$C = \frac{\partial U}{\partial T} = \frac{12\pi^4 N k_B}{5}\left(\frac{T}{\theta_D}\right)^3. \qquad \text{(C.17)}$$

Appendix D – Fermi Function Differentials

The equilibrium Fermi distribution function can be written:

$$f_{\mathbf{k}}^{0} = (\mathrm{e}^{x} + 1)^{-1}, \tag{D.1}$$

where $x = (\epsilon(\mathbf{k}) - \mu)/k_B T$.

The energy derivative can then be found using the chain rule

$$\frac{df_{\mathbf{k}}^{0}}{d\epsilon} = \frac{df_{\mathbf{k}}^{0}}{dx}\frac{dx}{d\epsilon} = -\frac{1}{k_B T(\mathrm{e}^{(\epsilon-\mu)/k_B T} + 1)^2}. \tag{D.2}$$

The temperature derivative can be found in a similar manner:

$$\frac{df_{\mathbf{k}}^{0}}{dT} = \frac{df_{\mathbf{k}}^{0}}{dx}\frac{dx}{dT}. \tag{D.3}$$

However, since the chemical potential μ is a function of temperature dx/dT must be evaluated using the quotient rule:

$$\begin{aligned}\frac{dx}{dT} &= \frac{d}{dT}\big((\epsilon - \mu(T)\big)/k_B T\big) \\ &= -\frac{d\mu}{dT}\frac{1}{k_B T} - \frac{\epsilon - \mu}{k_B T^2}.\end{aligned} \tag{D.4}$$

Substituting (D.4) into (D.3) then gives:

$$\begin{aligned}\frac{df_{\mathbf{k}}^{0}}{dT} &= -\frac{1}{(\mathrm{e}^{(\epsilon-\mu)/k_B T} + 1)^2} \times \frac{1}{k_B T} \times \left(-\frac{d\mu}{dT} - \frac{\epsilon - \mu}{T}\right) \\ &= -\frac{df_{\mathbf{k}}^{0}}{d\epsilon}\left(\frac{\epsilon - \mu}{T} + \frac{d\mu}{dT}\right).\end{aligned} \tag{D.5}$$

Appendix E – Evaluation of a Shockley Tube Integral [160]

First, it is necessary to limit the range of the inner integral. This is achieved by recognising that the velocities are periodic functions of ϕ and ϕ'. Hence the range of integration for ϕ'can be divided into stretches of 2π [160]:

$$\begin{aligned}
&\int_0^{\infty} \mathrm{e}^{-\phi'/\omega_c\tau} f(\phi') d\phi' \\
&= \int_0^{2\pi} \mathrm{e}^{-\phi'/\omega_c\tau} f(\phi') d\phi' + \int_{2\pi}^{4\pi} \mathrm{e}^{-\phi'/\omega_c\tau} f(\phi') d\phi' \\
&\qquad + \int_{4\pi}^{6\pi} \mathrm{e}^{-\phi'/\omega_c\tau} f(\phi') d\phi' + \cdots \\
&= \int_0^{2\pi} \mathrm{e}^{-\phi'/\omega_c\tau} f(\phi') d\phi' + \int_0^{2\pi} \mathrm{e}^{-(2\pi+\phi')/\omega_c\tau} f(\phi') d\phi' \\
&\qquad + \int_0^{2\pi} \mathrm{e}^{-(4\pi+\phi')/\omega_c\tau} f(\phi') d\phi' + \cdots \\
&= \sum_n \mathrm{e}^{-2\pi n/\omega_c\tau} \int_0^{2\pi} \mathrm{e}^{-\phi'/\omega_c\tau} f(\phi') d\phi'.
\end{aligned} \tag{E.1}$$

Using the geometric series result

$$\sum_{n=0}^{\infty} x^n = \frac{1}{1-x} \tag{E.2}$$

the sum can be simplified to give:

$$\frac{1}{1-\mathrm{e}^{-2\pi/\omega_c\tau}} \int_0^{2\pi} \mathrm{e}^{-\phi'/\omega_c\tau} f(\phi') d\phi' \approx \frac{\omega_c\tau}{2\pi} \int_0^{2\pi} \mathrm{e}^{-\phi'/\omega_c\tau} f(\phi') d\phi' \tag{E.3}$$

where the fraction has been simplified by expanding the exponential up to the linear term.

Substituting this into equation (3.132):

$$\kappa_{ij} = \frac{{k_B}^2 T}{12\pi\hbar^2} \int \frac{m_c^*\tau}{2\pi} \left\{ \int_0^{2\pi} \int_0^{2\pi} \mathrm{v}_i \mathrm{v}_j \mathrm{e}^{-\phi'/\omega_c\tau} d\phi d\phi' \right\} d\mathrm{k}_{\boldsymbol{B}}, \tag{E.4}$$

from within which the exponential can be expanded:

$$e^{-\phi'/\omega_c\tau} = 1 - \frac{\phi'}{\omega_c\tau} + \frac{1}{2}\left(\frac{\phi'}{\omega_c\tau}\right)^2 - \cdots \tag{E.5}$$

Appendix F – Pippard's Derivation of the Conductivity Tensor [183]

The following is based on treating the electric field as a rapid sequence of short pulses, whose overall effect can be determined by summing all the impulse responses. During a short interval, δt, each electron experiences a change in state, which can be written:

$$\delta\mathbf{k} = \frac{e\boldsymbol{E}\delta t}{\hbar}. \tag{F.1}$$

Hence, the distribution of filled states in k-space is shifted. Effectively, electrons are created on one side of the Fermi surface and destroyed on the opposite side. By assuming a sharp division between filled and unfilled states it is possible to calculate the number of electrons created[37] as follows.

Any elementary area on the Fermi surface, $\delta\boldsymbol{S_F}$, sweeps out a volume $\delta\boldsymbol{S_F}\cdot\delta\mathbf{k}$ which will contain $\delta\boldsymbol{S_F}\cdot\delta\mathbf{k}/4\pi^3$ electrons per unit volume of metal. Therefore, the number of "new" electrons created on an element of Fermi surface between t' and $t'+\delta t'$ is:

$$\delta^2 n = e\boldsymbol{E}\cdot\frac{\delta\boldsymbol{S_F}\delta t'}{4\pi^3\hbar}. \tag{F.2}$$

The *initial* current density due to these electrons is simply found from multiplying the number of electrons by their initial velocity (which must be the Fermi velocity) and unit charge:

$$\delta^2\mathbf{J}(t') = \frac{e^2\mathbf{v}_F(\boldsymbol{E}\cdot\delta\boldsymbol{S_F})\delta t'}{4\pi^3\hbar}. \tag{F.3}$$

A group of electrons generated on the same element of Fermi surface will start moving as a compact bunch, but will eventually be dispersed by scattering such that the velocity of their centroid, $\mathbf{v}$ (initially $\mathbf{v}_F$), falls to zero. This is independent of the starting time t' and only dependent on the time that has passed since their creation, $t-t'=\Delta t$ – i.e. $\mathbf{v}=\mathbf{v}(\Delta t)$.

[37] This is allowed because the smearing of the Fermi surface above 0 K does alter the number of states, but merely spreads them over an interval k_BT.

Substituting this for $\mathbf{v}_F$ in (F.3):

$$\delta^2\mathbf{J}(t') = \frac{e^2(\boldsymbol{E}\cdot\delta\boldsymbol{S_F})\mathbf{v}(\Delta\mathrm{t})\delta t'}{4\pi^3\hbar}. \tag{F.4}$$

To find the effect of a steady field t' is integrated from $-\infty$ to t (using the definition of Δt):

$$d\mathbf{J} = \frac{e^2(\boldsymbol{E}\cdot\delta\boldsymbol{S_F})}{4\pi^3\hbar}\int_0^{\infty}\mathbf{v}(\Delta\mathrm{t})\mathrm{d}(\Delta\mathrm{t})\,; \tag{F.5}$$

i.e.

$$d\mathbf{J} = \frac{e^2(\boldsymbol{E}\cdot\delta\boldsymbol{S_F})}{4\pi^3\hbar}\boldsymbol{L}. \tag{F.6}$$

L represents the integral; it is function of the position on the Fermi surface, the applied magnetic field and scattering mechanisms.

To obtain the total current due to the field, (F.6) is integrated over the whole Fermi surface:

$$\mathbf{J} = \frac{e^2}{4\pi^3\hbar}\int \boldsymbol{L}(\boldsymbol{E}\cdot d\boldsymbol{S_F}). \tag{F.7}$$

Then using Ohm's Law ($J_i = \sigma_{ij}E_j$), the conductivity tensor is found to be:

$$\sigma_{ij} = \frac{e^2}{4\pi^3\hbar}\int L_i dS_{F_j}. \tag{F.8}$$

Appendix G – Derivation of the Longitudinal Conductivity Integral [183]

An element of the projected k-space area shown in the top of Figure 3.19 is calculated as:

$$\delta A_k = \delta s \delta \mathrm{k}_\perp. \tag{G.1}$$

As the k-vector moves around the orbit, the area is swept out at a rate:

$$\frac{\delta A_k}{\delta t} = \frac{\delta s}{\delta t} \delta \mathrm{k}_\perp. \tag{G.2}$$

From equation (3.113) the rate at which the k-vector moves around the orbit can be calculated:

$$\frac{\delta s}{\delta t} = \frac{e \mathrm{v}_\perp B}{\hbar}. \tag{G.3}$$

Using this together with the fact that $\delta \mathrm{k}_\perp = \delta \mathrm{k}_z \cot\theta$ and $\mathrm{v}_\perp = \mathrm{v}\sin\theta$ (from the geometry of Figure 3.19):

$$\frac{\delta A_k}{\delta t} = \frac{e \mathrm{v} B}{\hbar} \delta \mathrm{k}_z \cos\theta = \frac{eB}{\hbar} \frac{\delta z}{\delta t} \delta \mathrm{k}_z, \tag{G.4}$$

since $\mathrm{v}\cos\theta = \mathrm{v}_z = \delta z / \delta t$. The distance travelled in z for one orbit (i.e. the pitch of helical orbit in real space) is then:

$$z = \frac{\hbar}{eB} \left(\frac{\partial A_k}{\partial \mathrm{k}_z} \right), \tag{G.5}$$

where A_k is entire projected area. The probability of being scattered for a particular real-space orbit is found – by comparing the mean free path in the plane normal to z ($= l \sin\theta$), with the distance around that orbit – to be:

$$\frac{\hbar}{eB} \oint \frac{ds}{l \sin\theta}. \tag{G.6}$$

Note that while ds is a distance in k-space, multiplication by the factor $\hbar/eB$ translates it into a distance in real-space. Combining (G.5) and (G.6) the mean free path in z is computed as:

$$L_z = \left(\frac{\partial A_k}{\partial k_z}\right) \Big/ \oint \frac{ds}{l \sin\theta}. \tag{G.7}$$

The Fermi surface in the slice $\delta \mathrm{k}_z$ has a projected area onto the plane normal to $\boldsymbol{B}$ given by:

$$\delta S_{F_z} = \left(\frac{\partial A_k}{\partial \mathrm{k}_z}\right)_E \delta \mathrm{k}_z. \tag{G.8}$$

Substituting these expressions into equation (3.151):

$$\sigma_{zz}(\infty) = \frac{e^2}{4\pi^3\hbar} \int d\mathrm{k}_z \left(\frac{\partial A_k}{\partial \mathrm{k}_z}\right)_E^2 \Big/ \oint \frac{ds}{l \sin\theta}, \tag{G.9}$$

which is simplified by noting that $dS_F = ds d\mathrm{k}_z \operatorname{cosec}\theta$ to give:

$$\sigma_{zz}(\infty) = \frac{e^2}{4\pi^3\hbar} \int \bar{l} C^2 dS_F, \tag{G.10}$$

where

$$C = \left(\frac{\partial A_k}{\partial S_F}\right)_E \tag{G.11}$$

and $\bar{l} = \langle 1/l \rangle^{-1}$ (the brackets denoting an average over those areas of the Fermi surface in the slice $\delta \mathrm{k}_z$ which give rise to the orbit in question).

Appendix H – Derivation of Specific Heat Capacity According to the Free-Ion Approximation

The entropy of a paramagnetic material (per mole) according to the free-ion approximation is given by:

$$S = R\left\{x\coth(x) - (2J+1)x\ \coth[(2J+1)x] + ln\left[\frac{\sinh[(2J+1)x]}{\sinh(x)}\right]\right\} \qquad \text{(H.1)}$$

where

$$x = \frac{g\mu_B B}{2k_B T}. \qquad \text{(H.2)}$$

The specific heat capacity is found from taking the derivative with respect to temperature and multiplying by temperature (see equation (6.6)). The part of equation (H.1) in braces can be differentiated term by term. Use is made of the following results:

$$\frac{d}{dx}(\coth x) = -\frac{1}{\sinh^2 x}, \qquad \text{(H.3)}$$

$$\frac{d}{dx}(\sinh x) = \cosh x, \qquad \text{(H.4)}$$

$$\frac{dx}{dT} = -\frac{x}{T}. \qquad \text{(H.5)}$$

The first term is differentiated using the product and chain rules as follows:

$$\begin{aligned}\frac{d}{dT}(x\coth x) &= x\frac{d}{dT}(\coth x) + \coth x\ \frac{dx}{dT}\\ &= x\frac{dx}{dT}\frac{d}{dx}(\coth x) + \coth x\ \frac{dx}{dT}\\ &= \frac{x^2}{T\ \sinh^2 x} - \frac{x\coth x}{T}.\end{aligned} \qquad \text{(H.6)}$$

The differential of the second term is found in a similar manner:

$$\begin{aligned}
&\frac{d}{dT}\big((2J+1)x\ \coth[(2J+1)x]\big)\\
&=(2J+1)x\frac{d}{dT}(\coth[(2J+1)x])+\coth[(2J+1)x]\frac{d}{dT}\big((2J+1)x\big)\\
&=(2J+1)x\frac{dx}{dT}\frac{d}{dx}(\coth[(2J+1)x])\\
&\qquad+\coth[(2J+1)x]\frac{dx}{dT}\frac{d}{dT}\big((2J+1)x\big)\\
&=\frac{(2J+1)^2x^2}{T\sinh^2[(2J+1)x]}-\frac{x(2J+1)\ \coth[(2J+1)x]}{T}.
\end{aligned} \tag{H.7}$$

Expressing the third term in the form $f\left(g\big(x(T)\big)\right)$ it is differentiated using the chain rule as follows:

$$\frac{df}{dT}=\frac{df}{dg}\frac{dg}{dx}\frac{dx}{dT}, \tag{H.8}$$

$$\frac{df}{dg}=\frac{d}{dg}(\ln g)=\frac{1}{g}\equiv\frac{\sinh(x)}{\sinh[(2J+1)x]}, \tag{H.9}$$

$$\frac{dg}{dx}=\frac{d}{dx}\left(\frac{\sinh[(2J+1)x]}{\sinh(x)}\right). \tag{H.10}$$

Using the quotient rule, this is found to be:

$$\frac{\sinh x\,(2J+1)\cosh\big((2J+1)x\big)-\sinh\big((2J+1)x\big)\cosh x}{\sinh^2 x}. \tag{H.11}$$

Hence,

$$\begin{aligned}
&\frac{df}{dT} \\
&= \frac{\sinh(x)}{\sinh[(2J+1)x]} \\
&\times \frac{\sinh x\,(2J+1)\cosh\big((2J+1)x\big) - \sinh[(2J+1)x]\cosh x}{\sinh^2 x} \times -\frac{x}{T} \qquad \text{(H.12)} \\
&= -\frac{x}{T}\left\{\frac{(2J+1)\cosh\big((2J+1)x\big)}{\sinh[(2J+1)x]} - \frac{\cosh x}{\sinh x}\right\} \\
&= -\frac{x(2J+1)\coth\big((2J+1)x\big)}{T} + \frac{x\coth x}{T}.
\end{aligned}$$

Combining terms and cancelling leaves:

$$\frac{dS}{dT} = \frac{R}{T}\left(\frac{x^2}{\sinh^2 x} - \frac{(2J+1)^2x^2}{\sinh^2[(2J+1)x]}\right). \qquad \text{(H.13)}$$

Thus, the free ion heat capacity, per mole, is given by:

$$C = R\left(\frac{x^2}{\sinh^2 x} - \frac{(2J+1)^2x^2}{\sinh^2[(2J+1)x]}\right). \qquad \text{(H.14)}$$

References

1. W. F. Giauque and D. P. MacDougall, Phys. Rev. **43**, 768 (1933).

2. N. Kürti and F. Simon, Nat. Lond. **133**, 907 (1934).

3. N. Kürti and F. Simon, Proc. R. Soc. Lond. Ser. Math. Phys. Sci. **149**, 152 (1935).

4. H. E. Hall, P. J. Ford, and K. Thompson, Cryogenics **6**, 80 (1966).

5. B. N. Esel'son, B. G. Lazarev, and A. D. Shvets, Cryogenics **2**, 279 (1962).

6. G. K. White, *Experimental Techniques in Low-Temperature Physics*, 3rd ed. (Clarendon Press, Oxford, 1979).

7. O. V. Lounasmaa, *Experimental Principles and Methods Below 1K* (Academic Press Inc. Ltd, London, 1974).

8. M. Linder, N. Rando, A. Peacock, and B. Collaudin, *Cryogenics in Space - A Review of the Missions and Technologies* (2001).

9. B. Collaudin and N. Rando, Cryogenics **40**, 797 (2000).

10. P. Verhoeve, in *AIP Conf. Proc.* (AIP Publishing, 2002), pp. 559–564.

11. C. L. Chang, P. Ade, K. Aird, J. Austermann, J. Beall, D. Becker, B. Benson, L. Bleem, J. Britton, J. Carlstrom, H. Cho, T. de Haan, T. Crawford, A. Crites, A. Datesman, M. Dobbs, W. Everett, A. Ewall–Wice, E. George, N. Halverson, N. Harrington, J. Henning, G. Hilton, W. Holzapfel, S. Hoover, J. Hubmayr, K. Irwin, R. Keisler, J. Kennedy, A. Lee, E. Leitch, D. Li, M. Lueker, D. P. Marrone, J. Mcmahon, J. Mehl, S. Meyer, J. Montgomery, T. Montroy, T. Natoli, J. Nibarger, M. Niemack, V. Novosad, S. Padin, T. Plagge, C. Pryke, C. Reichardt, J. Ruhl, B. Saliwanchik, J. Sayre, K. Schafer, E. Shirokoff, K. Story, K. Vanderlinde, J. Vieira, G. Wang, R. Williamson, V. Yefremenko, K. W. Yoon, and E. Young, Phys. Procedia **37**, 1381 (2012).

12. B. A. Mazin, K. O'Brien, S. McHugh, B. Bumble, D. Moore, S. Golwala, and J. Zmuidzinas, in *Proc. SPIE* (2010), p. 773518.

13. Infrared, Submillimeter, and Millimeter Detector Working Group, *Detector Needs for Long Wavelength Astrophysics* (NASA, 2002).

14. C. Kittel and H. Kroemer, *Thermal Physics* (W. H. Freeman and Company, 2000).

15. P. L. Richards, J. Appl. Phys. **76**, 1 (1994).

16. J. Singleton, *Band Theory and Electronic Properties of Solids* (Oxford University Press, 2001).

17. B. V. Rollin, Proc. Phys. Soc. **77**, 1102 (1961).

18. E. E. Haller, Infrared Phys. **25**, 257 (1985).

19. W. A. Holmes, J. J. Bock, B. P. Crill, T. C. Koch, W. C. Jones, A. E. Lange, and C. G. Paine, Appl. Opt. **47**, 5996 (2008).

20. F. S. Porter, M. D. Audley, R. P. Brekosky, R. J. Derro, M. J. DiPirro, K. C. Gendreau, J. D. Gygax, R. L. Kelley, D. McCammon, A. Morrell, S. D. Murphy, R. J. Paulos, T. Pham, C. K. Stahle, A. E. Szymkowiak, and J. G. Tuttle, in *EUV X-Ray Gamma-Ray Instrum. Astron. X* (Denver, CO, USA, 1999), pp. 729–740.

21. W. S. Holland, E. I. Robson, W. K. Gear, C. R. Cunningham, J. F. Lightfoot, T. Jenness, R. J. Ivison, J. A. Stevens, P. A. R. Ade, M. J. Griffin, W. D. Duncan, J. A. Murphy, and D. A. Naylor, Mon. Not. R. Astron. Soc. **303**, 659 (1999).

22. C. Enss, editor , *Cryogenic Particle Detection* (2005).

23. B. Cabrera, J. Low Temp. Phys. **151**, 82 (2008).

24. D. D. E. Martin, A. Peacock, P. Verhoeve, A. Poelaert, and R. Venn, Nucl. Instrum. Methods Phys. Res. Sect. Accel. Spectrometers Detect. Assoc. Equip. **444**, 115 (2000).

25. D. D. E. Martin, A. Peacock, P. Verhoeve, A. Poelaert, and R. Venn, Rev. Sci. Instrum. **71**, 3543 (2000).

26. D. Barret, J.-W. den Herder, L. Piro, L. Ravera, R. den Hartog, C. Macculi, X. Barcons, M. Page, S. Paltani, G. Rauw, J. Wilms, M. Ceballos, L. Duband, L. Gottardi, S. Lotti, J. de Plaa, E. Pointecouteau, C. Schmid, H. Akamatsu, S. Bagliani, S. Bandler, M. Barbera, P. Bastia, M. Biasotti, M. Branco, A. Camon, C. Cara, B. Cobo, L. Colasanti, J. L. Costa-Kramer, L. Corcione, W. Doriese, J.-M. Duval, L. Fabrega, F. Gatti, M. de Gerone, P. Guttridge, R. Kelley, C. Kilbourne, J. van der Kuur, T. Mineo, K. Mitsuda, L. Natalucci, T. Ohashi, P. Peille, E. Perinati, C. Pigot, G. Pizzigoni, C. Pobes, F. Porter, E. Renotte, J. L.

Sauvageot, Sciortino, S., G. Torrioli, L. Valenziano, D. Willingale, C. de Vries, and H. van Weers, *The X-Ray Integral Field Unit (X-IFU) for Athena+* (n.d.), p. 16.

27. D. Martin, *IXO Payload Overview Following MTR* (Paris, 2010).

28. T. M. Lanting, H.-M. Cho, J. Clarke, W. L. Holzapfel, A. T. Lee, M. Lueker, P. L. Richards, M. A. Dobbs, H. Spieler, and A. Smith, Appl. Phys. Lett. **86**, 112511 (2005).

29. P. A. J. de Korte, J. Beyer, S. Deiker, G. C. Hilton, K. D. Irwin, M. MacIntosh, S. W. Nam, C. D. Reintsema, L. R. Vale, and M. E. Huber, Rev. Sci. Instrum. **74**, 3807 (2003).

30. J. A. Chervenak, K. D. Irwin, E. N. Grossman, J. M. Martinis, C. D. Reintsema, and M. E. Huber, Appl. Phys. Lett. **74**, 4043 (1999).

31. D. Bintley, M. J. MacIntosh, W. S. Holland, J. T. Dempsey, P. Friberg, J. T. Kuroda, E. G. Starman, H. S. Thomas, C. Walther, X. Gao, P. A. R. Ade, R. V. Sudiwala, C. Dunare, W. Parkes, A. J. Walton, K. D. Irwin, G. C. Hilton, M. Niemack, M. Amiri, V. Asboth, B. Burger, E. L. Chapin, M. Halpern, M. Hasselfield, and A. L. Woodcraft, Proc. SPIE - Millim. Submillimeter Far-Infrared Detect. Instrum. Astron. VI **8452**, 845208 (2012).

32. M. Bühler and E. Umlauf, EPL Europhys. Lett. **5**, 297 (1988).

33. C. Enss, in *AIP Conf. Proc. - 9th Int. Workshop Low Temp. Detect.* (AIP Publishing, 2002), pp. 5–10.

34. A. Fleischmann, L. Gastaldo, S. Kempf, A. Kirsch, A. Pabinger, C. Pies, J.-P. Porst, P. Ranitzsch, S. Schäfer, F. v Seggern, T. Wolf, C. Enss, and G. M. Seidel, in *AIP Conf. Proc. - 13th Int. Workshop Low Temp. Detect.* (AIP Publishing, 2009), pp. 571–578.

35. J.-P. Porst, S. R. Bandler, J. S. Adams, M. Balvin, J. Beyer, S. E. Busch, D. Drung, M. E. Eckart, R. L. Kelley, C. . Kilbourne, F. S. Porter, J. E. Sadleir, G. M. Seidel, S. J. Smith, and T. R. Stevenson, IEEE Trans. Appl. Supercond. **23**, 2500905 (2013).

36. J.-P. Porst, S. R. Bandler, J. S. Adams, M. A. Balvin, S. E. Busch, M. E. Eckart, R. L. Kelley, C. A. Kilbourne, S. J. Lee, P. C. Nagler, F. S. Porter, J. E. Sadleir, G. M. Seidel, S. J. Smith, and T. R. Stevenson, J. Low Temp. Phys. **176**, 617 (2014).

37. B. A. Mazin, P. K. Day, J. Zmuidzinas, and H. G. Leduc, in *AIP Conf. Proc. - 9th Int. Workshop Low Temp. Detect.* (AIP Publishing, 2002), pp. 309–312.

38. P. K. Day, H. G. LeDuc, B. A. Mazin, A. Vayonakis, and J. Zmuidzinas, Nature **425**, 817 (2003).

39. B. A. Mazin, Microwave Kinetic Inductance Detectors, Ph.D., California Institute of Technology, 2005.

40. B. A. Mazin, B. Bumble, S. R. Meeker, K. O'Brien, S. McHugh, and E. Langman, Opt. Express **20**, 1503 (2012).

41. B. A. Mazin, S. R. Meeker, M. J. Strader, P. Szypryt, D. Marsden, J. C. van Eyken, G. E. Duggan, A. B. Walter, G. Ulbricht, M. Johnson, B. Bumble, K. O'Brien, and C. Stoughton, Publ. Astron. Soc. Pac. **125**, 1348 (2013).

42. B. Collaudin and T. Passvogel, in *SPIE Conf. Space Telesc. Instrum. V* (SPIE, Kona, Hawaii, 1998), pp. 1114–1126.

43. M. Donabedian, editor , *Spacecraft Thermal Control Handbook* (American Institute of Aeronautics and Astronautics/Aerospace Press, 2003).

44. C. Jewell, Adv. Cryog. Eng. Vols 55A 55B **1218**, 1487 (2010).

45. S. R. Breon, J. A. Gibbon, R. F. Boyle, M. J. DiPirro, B. A. Warner, and J. G. Tuttle, Cryogenics **36**, 773 (1996).

46. T. D. Eastop and A. McConkey, *Applied Thermodynamics for Engineering Technologists*, 5th ed. (Longman, 1998).

47. R. Radebaugh, in *Proc. Inst. Refrig.* (London, 2000).

48. R. S. Bhatia, S. T. Chase, W. C. Jones, B. G. Keating, A. E. Lange, P. V. Mason, B. J. Philhour, and G. Sirbi, Cryogenics **42**, 113 (2002).

49. T. Bradshaw, Sixth Eur. Symp. Space Environ. Control Syst. Vols 1 2 **400**, 465 (1997).

50. J.-M. Lamarre, J.-L. Puget, P. A. R. Ade, F. Bouchet, G. Guyot, A. E. Lange, F. Pajot, A. Arondel, K. Benabed, J.-L. Beney, A. Benoît, J.-P. Bernard, R. Bhatia, Y. Blanc, J. J. Bock, E. Bréelle, T. W. Bradshaw, P. Camus, A. Catalano, J. Charra, M. Charra, S. E. Church, F. Couchot, A. Coulais, B. P. Crill, M. R. Crook, K. Dassas, P. de Bernardis, J. Delabrouille, P. de Marcillac, J.-M. Delouis, F.-X. Désert, C. Dumesnil, X. Dupac, G. Efstathiou, P. Eng, C. Evesque, J.-J. Fourmond, K. Ganga, M. Giard, R. Gispert, L. Guglielmi, J. Haissinski, S.

Henrot-Versillé, E. Hivon, W. A. Holmes, W. C. Jones, T. C. Koch, H. Lagardère, P. Lami, J. Landé, B. Leriche, C. Leroy, Y. Longval, J. F. Macías-Pérez, T. Maciaszek, B. Maffei, B. Mansoux, C. Marty, S. Masi, C. Mercier, M.-A. Miville-Deschênes, A. Moneti, L. Montier, J. A. Murphy, J. Narbonne, M. Nexon, C. G. Paine, J. Pahn, O. Perdereau, F. Piacentini, M. Piat, S. Plaszczynski, E. Pointecouteau, R. Pons, N. Ponthieu, S. Prunet, D. Rambaud, G. Recouvreur, C. Renault, I. Ristorcelli, C. Rosset, D. Santos, G. Savini, G. Serra, P. Stassi, R. V. Sudiwala, J.-F. Sygnet, J. A. Tauber, J.-P. Torre, M. Tristram, L. Vibert, A. Woodcraft, V. Yurchenko, and D. Yvon, Astron. Astrophys. **520**, A9 (2010).

51. G. Morgante, Exp. Cosmol. Millimetre Wavel. **616**, 298 (2002).

52. T. W. Bradshaw, S. Brown, M. R. Crook, G. Gilley, M. Hills, T. Rawlings, S. Watson, and M. Linder, in *5th Eur. Space Cryog. Workshop* (ESTEC, Noordwijk, 2013).

53. L. Duband, in *Cryocoolers 11*, edited by R. G. Ross (Kluwer Academic Publishers, Boston, 2002), pp. 561–566.

54. R. S. Bhatia, S. T. Chase, S. F. Edgington, J. Glenn, W. C. Jones, A. E. Lange, B. Maffei, A. K. Mainzer, P. D. Mauskopf, B. J. Philhour, and B. K. Rownd, Cryogenics **40**, 685 (2000).

55. L. Duband, L. Hui, and A. Lange, Cryogenics **30**, 263 (1990).

56. L. Duband, L. Clerc, E. Ercolani, L. Guillemet, and R. Vallcorba, Cryogenics **48**, 95 (2008).

57. G. Ventura and L. Risegari, *The Art of Cryogenics: Low-Temperature Experimental Techniques*, 1st ed. (Elsevier, Oxford, 2008).

58. D. S. Betts, *Refrigeration and Thermometry below One Kelvin* (Sussex University Press, 1976).

59. A. Benoît and S. Pujol, Cryogenics **34**, 421 (1994).

60. S. Triqueneaux, L. Sentis, P. Camus, A. Benoit, and G. Guyot, Cryogenics **46**, 288 (2006).

61. P. Camus, G. Vermeulen, A. Volpe, S. Triqueneaux, A. Benoit, J. Butterworth, S. d'Escrivan, and T. Tirolien, J. Low Temp. Phys. **176**, 1069 (2014).

62. G. Chaudhry, A. Volpe, P. Camus, S. Triqueneaux, and G. Vermeulen, Cryogenics **52**, 471 (2012).

63. S. Jeong, Cryogenics **62**, 193 (2014).

64. G. V. Brown, J. Appl. Phys. **47**, 3673 (1976).

65. V. K. Pecharsky and J. Gschneidner K. A., Phys. Rev. Lett. **78**, 4494 (1997).

66. M. Khlifi, E. Dhahri, and E. K. Hlil, J. Alloys Compd. **587**, 771 (2014).

67. E. Bonnot, R. Romero, L. Mañosa, E. Vives, and A. Planes, Phys. Rev. Lett. **100**, 125901 (2008).

68. L. Mañosa, D. González-Alonso, A. Planes, E. Bonnot, M. Barrio, J.-L. Tamarit, S. Aksoy, and M. Acet, Nat. Mater. **9**, 478 (2010).

69. K. A. Müller, F. Fauth, S. Fischer, M. Koch, A. Furrer, and P. Lacorre, Appl. Phys. Lett. **73**, 1056 (1998).

70. J. F. Scott, Annu. Rev. Mater. Res. **41**, 229 (2011).

71. A. S. Mischenko, Q. Zhang, J. F. Scott, R. W. Whatmore, and N. D. Mathur, Science **311**, 1270 (2006).

72. B. Neese, B. Chu, S.-G. Lu, Y. Wang, E. Furman, and Q. M. Zhang, Science **321**, 821 (2008).

73. S. Kar-Narayan and N. D. Mathur, Ferroelectrics **433**, 107 (2012).

74. W. N. Lawless, Phys. Rev. B **16**, 433 (1977).

75. S. Kapphan and F. Lüty, Solid State Commun. **6**, 907 (1968).

76. G. Lombardo and R. O. Pohl, Phys. Rev. Lett. **15**, 291 (1965).

77. Y. V. Sinyavskii, Chem. Pet. Eng. **31**, 295 (1995).

78. S. Kar-Narayan and N. D. Mathur, J. Phys. Appl. Phys. **43**, 032002 (2010).

79. M. M. Vopson, Solid State Commun. **152**, 2067 (2012).

80. M. M. Vopson, J. Phys. Appl. Phys. **46**, 345304 (2013).

81. A. Midya, S. N. Das, P. Mandal, S. Pandya, and V. Ganesan, Phys. Rev. B **84**, 235127 (2011).

82. J. Hwang, E. S. Choi, H. D. Zhou, J. Lu, and P. Schlottmann, Phys. Rev. B **85**, 024415 (2012).

83. A. S. Starkov and I. A. Starkov, Ferroelectrics **483**, 102 (2015).

84. M. Nahum, T. M. Eiles, and J. M. Martinis, Appl. Phys. Lett. **65**, 3123 (1994).

85. M. M. Leivo, J. P. Pekola, and D. V. Averin, Appl. Phys. Lett. **68**, 1996 (1996).

86. P. A. Fisher, J. N. Ullom, and M. Nahum, Appl. Phys. Lett. **74**, 2705 (1999).

87. J. Pekola, Nature **435**, 889 (2005).

88. N. A. Miller, G. C. O'Neil, J. A. Beall, G. C. Hilton, K. D. Irwin, D. R. Schmidt, L. R. Vale, and J. N. Ullom, Appl. Phys. Lett. **92**, 163501 (2008).

89. A. M. Clark, A. Williams, S. T. Ruggiero, M. L. van den Berg, and J. N. Ullom, Appl. Phys. Lett. **84**, 625 (2004).

90. P. J. Lowell, G. C. O'Neil, J. M. Underwood, and J. N. Ullom, Cryogenics **52**, 130 (2012).

91. B. Wilson, M. Atlas, P. Lowell, S. Moyerman, N. Stebor, J. Ullom, and B. Keating, J. Low Temp. Phys. **176**, 243 (2014).

92. J. P. Pekola, T. T. Heikkilä, A. M. Savin, J. T. Flyktman, F. Giazotto, and F. W. J. Hekking, Phys. Rev. Lett. **92**, 056804 (2004).

93. P. J. Lowell, G. C. O'Neil, J. M. Underwood, X. Zhang, and J. N. Ullom, J. Low Temp. Phys. **176**, 1062 (2014).

94. V. Kotsubo and G. W. Swift, J. Low Temp. Phys. **83**, 217 (1991).

95. A. E. Jahromi and F. K. Miller, Cryogenics **62**, 202 (2014).

96. I. D. Hepburn and A. Smith, Wiley Encycl. Electr. Eectronics Eng. **12**, 91 (1999).

97. P. Debye, Ann. Phys. **81**, 1154 (1926).

98. W. F. Giauque, J. Am. Chem. Soc. **49**, 1864 (1927).

99. W. J. De Haas, E. C. Wiersma, and H. A. Kramers, Physica **1**, 1 (1933).

100. Ambler, E. and Hudson, R. P., Rep. Prog. Phys. **18**, 251 (1955).

101. S. Blundell, *Magnetism in Condensed Matter*, 1st ed. (Oxford University Press, 2001).

102. R. P. Hudson, *Principles and Application of Magnetic Cooling* (North-Holland Publishing Company, Amsterdam, 1972).

103. F. E. Simon, N. Kurti, J. F. Allen, and K. Mendelssohn, *Low Temperature Physics: Four Lectures* (Pergamon Press Ltd, London, 1952).

104. P. Wikus, E. Canavan, S. T. Heine, K. Matsumoto, and T. Numazawa, Cryogenics **62**, 150 (2014).

105. P. J. Shirron, Cryogenics **62**, 130 (2014).

106. C. Yeager, E. Maloof, S. Yano, and T. Shimzu, Nucl. Instrum. Methods Phys. Res. Sect. Accel. Spectrometers Detect. Assoc. Equip. **559**, 657 (2006).

107. C. Hagmann, D. J. Benford, and P. L. Richards, Cryogenics **34**, 213 (1994).

108. P. Wikus, G. Burghart, and E. Figueroa-Feliciano, Cryogenics **51**, 555 (2011).

109. I. Hepburn, in *Wiley Encycl. Electr. Electron. Eng.* (John Wiley & Sons, Inc., 2014).

110. C. Hagmann and P. L. Richards, Cryogenics **35**, 345 (1995).

111. P. J. Shirron and D. McCammon, Cryogenics **62**, 163 (2014).

112. J. Bartlett, G. Hardy, and I. D. Hepburn, Cryogenics **65**, 26 (2015).

113. J. H. Colwell, Rev. Sci. Instrum. **40**, 1182 (1969).

114. A. E. Jahromi and D. F. Sullivan, Rev. Sci. Instrum. **85**, 065118 (2014).

115. F. Pobell, *Matter and Methods at Low Temperatures*, 2nd ed. (Springer, Berlin, 2007).

116. M. J. DiPirro and P. J. Shirron, Cryogenics **62**, 172 (2014).

117. P. J. Shirron, E. R. Canavan, M. J. DiPirro, M. Jackson, J. Panek, and J. G. Tuttle, AIP Conf. Proc. **613**, 1175 (2002).

118. J. Tuttle, P. Shirron, M. DiPirro, M. Jackson, J. Behr, K. Kamiya, B. Warner, E. Kunes, and T. Hait, Cryogenics **41**, 781 (2001).

119. P. Wikus, S. A. Hertel, S. W. Leman, K. A. McCarthy, S. M. Ojeda, and E. Figueroa-Feliciano, Cryogenics **51**, 41 (2011).

120. O. E. Vilches and J. C. Wheatley, Rev. Sci. Instrum. **37**, 819 (1966).

121. A. Kent, *Experimental Low-Temperature Physics*, 1st ed. (The MacMillan Press Ltd, London, 1993).

122. M. Tinkham, *Introduction to Superconductivity*, 1st ed. (McGraw-Hill Book Company, 1975).

123. A. B. Pippard, Philos. Trans. R. Soc. Lond. Ser. Math. Phys. Sci. **248**, 97 (1955).

124. K. Mendelssohn and H. M. Rosenberg, Proc. R. Soc. Lond. Ser. Math. Phys. Sci. **218**, 190 (1953).

125. J. Laudy and A. Knol, Cryogenics **6**, 370 (1966).

126. F. W. Gorter and A. R. Miedema, Cryogenics **8**, 86 (1968).

127. J. M. L. Engels, F. W. Gorter, and A. R. Miedema, Cryogenics **12**, 141 (1972).

128. R. Radebaugh, J. Low Temp. Phys. **27**, 91 (1977).

129. C. Kittel, *Introduction to Solid State Physics*, 7th ed. (John Wiley & Sons, Inc., 1996).

130. J. Bartlett, G. Hardy, I. Hepburn, R. Ray, and S. Weatherstone, Cryogenics **50**, 647 (2010).

131. E. R. Canavan, M. J. Dipirro, M. Jackson, J. Panek, P. J. Shirron, and J. G. Tuttle, in *Adv. Cryog. Eng.* (American Institute of Physics, 2002), pp. 1183–1190.

132. J. Tuttle, S. Pourrahimi, E. Canavan, M. DiPirro, and P. Shirron, Cryogenics **46**, 196 (2006).

133. J. Bartlett, G. Hardy, I. D. Hepburn, C. Brockley-Blatt, P. Coker, E. Crofts, B. Winter, S. Milward, R. Stafford-Allen, M. Brownhill, J. Reed, M. Linder, and N. Rando, Cryogenics **50**, 582 (2010).

134. T. Prouvé, J. M. Duval, N. Luchier, and S. D'escrivan, Cryogenics **64**, 201 (2014).

135. U. Hishi, R. Fujimoto, T. Kunihisa, S. Takakura, T. Mitsude, K. Kamiya, M. Kotake, A. Hoshino, and K. Shinozaki, J. Low Temp. Phys. **176**, 1075 (2014).

136. I. D. Hepburn, C. Brockley-Blatt, P. Coker, E. Crofts, B. Winter, S. Milward, R. Stafford-Allen, R. Hunt, M. Brownhill, N. Rando, and M. Linder, AIP Conf. Proc. **710**, 1737 (2004).

137. S. Pourrahimi, J. Williams, W. Punchard, J. Tuttle, M. DiPirro, E. Canavan, and P. Shirron, Cryogenics **48**, 253 (2008).

138. M. DiPirro, E. Canavan, P. Shirron, and J. Tuttle, Cryogenics **44**, 559 (2004).

139. R. McFee, Rev. Sci. Instrum. **30**, 98 (1959).

140. E. R. Canavan, B. L. James, T. P. Hait, A. Oliver, and D. F. Sullivan, Cryogenics **64**, 194 (2014).

141. E. Maher, J. S. Abell, R. I. Chakalova, Y. L. Cheung, T. W. Button, and P. Tixador, Supercond. Sci. Technol. **17**, 1440 (2004).

142. M. R. Emes, I. D. Hepburn, R. J. Ray, and L. B. C. Worth, Cryogenics **41**, 771 (2001).

143. P. Shirron, M. Kimball, D. Wegel, and F. Miller, Cryogenics **50**, 494 (2010).

144. H. van Weers, in *5th Eur. Space Cryog. Workshop* (ESTEC, Noordwijk, 2013).

145. J. Bartlett, G. Hardy, I. Hepburn, S. Milward, P. Coker, and C. Theobald, Proc. SPIE - Int. Soc. Opt. Eng. **8452**, (2012).

146. P. J. Shirron, M. O. Kimball, B. L. James, D. C. Wegel, R. M. Martinez, R. L. Faulkner, L. Neubauer, and M. Sansebastian, Cryogenics **52**, 165 (2012).

147. C. Hagmann and P. L. Richards, Cryogenics **34**, 221 (1994).

148. P. Shirron, Cryogenics **62**, 140 (2014).

149. L. Duband, J. M. Duval, N. Luchier, and T. Prouve, Cryogenics **52**, 145 (2012).

150. L. Duband, J. M. Duval, and N. Luchier, Cryogenics **64**, 213 (2014).

151. P. J. Shirron, M. O. Kimball, D. J. Fixsen, A. J. Kogut, X. Li, and M. J. DiPirro, Cryogenics **52**, 140 (2012).

152. J. S. Bartlett, Design of a 50 mK Continuous Adiabatic Demagnetisation Refrigerator for Future Space Missions, PhD Thesis, Mullard Space Science Laboratory, University College London, 2008.

153. N. Luchier, J. M. Duval, L. Duband, P. Camus, G. Donnier-Valentin, and M. Linder, Cryogenics **50**, 591 (2010).

154. J. M. Ziman, *Electrons and Phonons* (Oxford University Press, 1960).

155. G. S. Kumar, G. Prasad, and R. O. Pohl, J. Mater. Sci. **28**, 4261 (1993).

156. J. R. Long, Phys. Rev. B **3**, 2476 (1971).

157. P. G. Klemens, in *Therm. Conduct.* (Academic Press Inc. Ltd, London, 1969), pp. 1–68.

158. H. J. Pain, *The Physics of Vibrations and Waves*, 6th ed. (John Wiley & Sons, Ltd., Chichester, England, 2005).

159. N. W. Ashcroft and D. N. Mermin, *Solid State Physics*, International (Holt-Saunders, Japan, 1981).

160. J. M. Ziman, *Principles of the Theory of Solids*, 2nd ed. (Cambridge University Press, 1972).

161. L. Girifalco, *Statistical Mechanics of Solids*, 1st ed. (Oxford University Press, New York, 2000).

162. J. M. Ziman, Can. J. Phys. **34**, 1256 (1956).

163. P. L. Taylor and O. Heinonen, *A Quantum Approach to Condensed Matter Physics*, 1st ed. (Cambridge University Press, Cambridge, 2002).

164. A. B. Pippard, Rep. Prog. Phys. **23**, 176 (1960).

165. R. J. M. van Vucht, H. van Kempen, and P. Wyder, Rep. Prog. Phys. **48**, 853 (1985).

166. M. Khoshenevisan, W. P. Pratt, P. A. Schroeder, and S. D. Steenwyk, Phys. Rev. B **19**, 3873 (1979).

167. *Brookhaven National Laboratory Materials Database* *Materialdatabase.magnet.fsu.edu* (Brookhaven National Laboratory, United States, 2015).

168. H. M. Rosenberg, Philos. Trans. R. Soc. Lond. Ser. Math. Phys. Sci. **247**, 441 (1955).

169. K. Mendelssohn and H. M. Rosenberg, Proc. Phys. Soc. Sect. A **65**, 388 (1952).

170. R. G. Chambers, Proc. R. Soc. Lond. Ser. Math. Phys. Sci. **202**, 378 (1950).

171. K. Fuchs, Math. Proc. Camb. Philos. Soc. **34**, 100 (1938).

172. R. B. Dingle, Proc. R. Soc. Lond. Ser. Math. Phys. Sci. **201**, 545 (1950).

173. E. R. Andrew, Proc. Phys. Soc. Sect. A **62**, 77 (1949).

174. H. B. G. Casimir, Physica **5**, 495 (1938).

175. R. Berman, F. E. Simon, and J. M. Ziman, Proc. R. Soc. Lond. Ser. Math. Phys. Sci. **220**, 171 (1953).

176. A. A. Mitrjaev, O. A. Panchenko, I. I. Razgonov, and V. S. Tsoi, Surf. Sci. **75**, L376 (1978).

177. V. E. Startsev, V. P. D'yakina, V. I. Cherepanov, N. V. Volkenshtein, R. S. Nasyrov, and V. G. Manakov, Sov. Phys. JTEP **52**, 675 (1980).

178. E. T. Swartz and R. O. Pohl, Rev. Mod. Phys. **61**, 605 (1989).

179. N. S. Snyder, Cryogenics **10**, 89 (1970).

180. E. Mendoza, in *Phenomenes Cryomagnetiques Langevin-Perrin Colloq.* (1948), pp. 53–76.

181. B. B. Goodman, Proc. Phys. Soc. Sect. A **66**, 217 (1953).

182. M. Kohler, Ann. Phys. **424**, 211 (1938).

183. A. B. Pippard, *Magnetoresistance in Metals* (Cambridge University Press, 1989).

184. F. Seitz, Phys. Rev. **79**, 372 (1950).

185. L. Davis, Phys. Rev. **56**, 93 (1939).

186. W. Shockley, Phys. Rev. **79**, 191 (1950).

187. M. I. Azbel, M. I. Kaganov, and I. M. Lifshitz, Sov. Phys. JTEP **5**, 967 (1957).

188. I. M. Lifshitz, M. I. Azbel, and M. I. Kaganov, Sov. Phys. JTEP **4**, 41 (1957).

189. V. V. Marchenkov, A. N. Cherepanov, V. E. Startsev, C. Czurda, and H. W. Weber, J. Low Temp. Phys. **98**, 425 (1995).

190. R. F. Girvan, A. V. Gold, and R. A. Phillips, J. Phys. Chem. Solids **29**, 1485 (1968).

191. D. R. Baer and D. K. Wagner, J. Low Temp. Phys. **13**, 445 (1973).

192. A. B. Pippard, Proc. R. Soc. Lond. Ser. Math. Phys. Sci. **305**, 291 (1968).

193. V. G. Peschanskii and M. Y. Azbel, Sov. Phys. JTEP **28**, 1045 (1969).

194. A. L. Woodcraft and A. Gray, in *AIP Conf. Proc. - 13th Int. Workshop Low Temp. Detect.* (AIP Publishing, 2009), pp. 681–684.

195. A. B. Batdalov and N. A. Red'ko, Sov Phys Solid State **22**, 664 (1980).

196. J. R. Long, Phys. Rev. B **3**, 1209 (1971).

197. D. K. Wagner, J. C. Garland, and R. Bowers, Phys. Rev. B **3**, 3141 (1971).

198. S. Olszewski, Acta Phys. Pol. A **120**, 525 (2011).

199. D. K. Wagner, Phys. Rev. B **5**, 336 (1972).

200. J. R. Long, Phys. Rev. B **3**, 1197 (1971).

201. E. Fawcett, Phys. Rev. **128**, 154 (1962).

202. D. R. Baer and D. K. Wagner, J. Low Temp. Phys. **13**, 445 (1973).

203. E. Fawcett and D. Griffiths, J. Phys. Chem. Solids **23**, 1631 (1962).

204. G. Heine and W. Lang, Cryogenics **38**, 377 (1998).

205. B. L. Brandt, D. W. Liu, and L. G. Rubin, Rev. Sci. Instrum. **70**, 104 (1999).

206. P. Bevington and D. K. Robinson, *Data Reduction and Error Analysis for the Physical Sciences*, 3rd edition (McGraw-Hill Science/Engineering/Math, Boston, 2002).

207. D. W. Marquardt, J. Soc. Ind. Appl. Math. **11**, 431 (1963).

208. D. I. Bolef and J. D. Klerk, J. Appl. Phys. **33**, 2311 (2004).

209. G. K. White and S. J. Collocott, J. Phys. Chem. Ref. Data **13**, 1251 (1984).

210. E. Lassner and W.-D. Schubert, *Tungsten: Properties, Chemistry, Technology of the Elements, Alloys, and Chemical Compounds* (Springer Science & Business Media, 1999).

211. F. J. Blatt, *Physics of Electronic Conduction in Solids* (McGraw-Hill Book Company, New York, 1968).

212. A. N. Cherepanov, V. V. Marchenkov, V. E. Startsev, N. V. Volkenshtein, and M. Glin'skii, Sov. J. Low Temp. Phys. **12**, 666 (1986).

213. A. N. Cherepanov, V. V. Marchenkov, V. E. Startsev, N. V. Volkenshtein, and M. Glin'skii, J. Low Temp. Phys. **80**, 135 (1990).

214. J. Kollár, Solid State Commun. **27**, 1313 (1978).

215. N. V. Volkenshtein, M. Glin'skii, V. V. Marchenkov, V. E. Startsev, and A. N. Cherepanov, Sov. Phys. JETP **68**, 1216 (1989).

216. V. S. Tsoi and I. I. Razgonov, JETP Lett. **25**, 26 (1977).

217. N. V. Volkenshtein, V. V. Marchenkov, V. E. Startsev, A. N. Cherepanov, and M. Glin'skii, JETP Lett. **41**, 458 (1985).

218. Y. A. Kolesnichenko, Sov. J. Low Temp. Phys. **11**, 641 (1985).

219. J. W. Gibson and R. A. Hein, Phys. Rev. Lett. **12**, 688 (1964).

220. K. P. Riley, M. P. Hobson, and S. J. Bence, *Mathematical Methods for Physics and Engineering*, 3rd ed. (Cambridge University Press, New York, 2009).

221. D. M. Sparlin and J. A. Marcus, Phys. Rev. **144**, 484 (1966).

222. J. O. Strom-Olsen, Proc. R. Soc. Lond. Ser. Math. Phys. Sci. **302**, 83 (1967).

223. L. F. Mattheiss, Phys. Rev. **139**, A1893 (1965).

224. V. J. Johnson, *A Compendium of the Properties of Materials at Low Temperatures (Phase I). Part II: Properties of Solids* (National Bureau of Standards, 1960).

225. P. de Bernardis, F. Bouchet, and J. Delabrouille, *COrE+ Mission Proposal* (2014).

226. M. Ferlet, N. Geis, J. Goicoechea, D. Griffin, A. Heras, K. Isaak, T. Nakagawa, N. Rando, B. Swinyard, N. Takahashi, and S. Vives, *SPICA Assessment Study Report* (European Space Agency, 2009).

227. O. E. Vilches and J. C. Wheatley, Phys. Rev. **148**, 509 (1966).

228. D. G. Kapadnis, Physica **22**, 159 (1956).

229. M. C. Runyan and W. C. Jones, Cryogenics **48**, 448 (2008).

230. M. Locatelli, D. Arnaud, and M. Routin, Cryogenics **16**, 374 (1976).

231. J. Bartlett, G. Hardy, and I. D. Hepburn, Cryogenics **72, Part 2**, 111 (2015).

232. C. P. Poole Jr, *Encyclopedic Dictionary of Condensed Matter Physics* (Academic Press, 2004).

233. T.-S. Choy, *The Fermi Surface Database (www.phys.ufl.edu/fermisurface/)* (2015).

234. K. V. Wong and A. Hernandez, Int. Sch. Res. Not. **2012**, e208760 (2012).

235. Smit Röntgen, *Tungsten Laser Sintered Products (http://www.smitroentgen.com/uploads/pdf/17_3_Leaflet_Smit Röntgen_Tungsten.pdf)* (2015).

236. M. N. Wilson, *Superconducting Magnets* (Oxford University Press, Oxford, 2002).

237. G. Algouy, P. Nobile, L. Sentis, and A. Huguet, in *Eur. Conf. Spacecr. Struct. Mater. Mech. Test.* (Noordwijk, 2005).